Growth, chamber formation, and microscale heterogeneity in planktic foraminifera: Implications for paleoclimate proxies

Elisa Angeles Bonnin

A dissertation

submitted in partial fulfillment of the

requirements for the degree of

Doctor of Philosophy

University of Washington

2019

Reading Committee:

Alexander C. Gagnon, Chair

Steven R. Emerson

Mark J. Warner

Program Authorized to Offer Degree:

School of Oceanography

University of Washington

Abstract

Growth, chamber formation, and microscale heterogeneity in planktic foraminifera: Implications for paleoclimate proxies

Elisa Angeles Bonnin

Chair of the Supervisory Committee:
Alexander C. Gagnon, Ph.D.
School of Oceanography

The calcite tests of planktic foraminifera contain a number of geochemical proxies, which are often used to determine past ocean conditions. However, the incorporation of these proxies into the test is often affected by growth and biomineralization processes, which cause biogenic calcite to behave differently from inorganic calcite. These are often called ‘vital effects’. The examination of foraminiferal tests at the microscale, using novel imaging and isotope labeling techniques, can further our understanding of the underlying mechanisms behind the incorporation of these proxies into calcite, reducing the impact of individual variability and aiding accurate paleoclimate reconstructions. This work examines three aspects of growth that may affect metal-to-calcium (Me/Ca) proxies in planktic foraminifera: (1) the incorporation of organic matrices into the test during chamber formation, (2) systematic diurnal heterogeneity throughout the test, and (3) gametogenic calcification, where an extra layer of calcite is

precipitated at the end of the organism's life. Using time-of-flight secondary ion mass spectrometry (ToF-SIMS), an imaging technique with a resolution of ~300 nm, we observe that Na and Mg are both high at the location of the primary organic sheet (POS) in *Orbulina universa*, and that during chamber formation, a new POS is laid down over all existing chambers in that species. We also observe Na banding throughout the test of *O. universa*, which may be linked to previously observed heterogeneity in Mg/Ca (Chapter 2). By making use of a novel, multi-isotope labeling technique and ICP-MS analyses to examine diurnal heterogeneity, we observe high Sr/Ca during the night, following a similar pattern as Mg/Ca heterogeneity. Sr/Ca and Mg/Ca also appear positively correlated during the night, a relationship consistent with Sr/Ca and Mg/Ca in inorganic calcite and other biominerals. This indicates that this positive relationship is due to a mineralogical property of calcite, and any shift away from this relationship is due to other processes, such as kinetics or Rayleigh fractionation (Chapter 3). Finally, by using the same isotope labeling technique to examine gametogenic calcite, we observe that gametogenic calcite is high in Mg/Ca and Sr/Ca, and has a similar chemical composition and mechanism as night calcification (Chapter 4).

TABLE OF CONTENTS

LIST OF FIGURES

LIST OF TABLES

ACKNOWLEDGEMENTS

This research was supported in part by the U.S. National Science Foundation under Grant NSF OCE 14-20689 (A.C.G), NSF OCE 12-32987 (B.H.), and NSF OCE 12-61519 (A.R., J.F.). ToF-SIMS analysis was supported through user proposal 48564 to A.C.G, part of a Special Science Call at the Environmental Molecular Sciences Laboratory, a DOE Office of Science User Facility sponsored by the Office of Biological and Environmental Research and located at Pacific Northwest National Laboratory. ICP-MS analyses were conducted at TraceLab, a mass spectrometry facility established through the generous support of the M.J. Murdock Charitable Trust. Part of this work was conducted at the Molecular Analysis Facility, a National Nanotechnology Coordinated Infrastructure site at the University of Washington which is supported in part by the National Science Foundation (grant NNCI-1542101), the University of Washington, the Molecular Engineering & Sciences Institute, and the Clean Energy Institute. We would like to thank all those who assisted with foraminifera capture and culturing during the summers of 2011, 2013 and 2014 on Catalina Island, the Wrigley Marine Science Center on Catalina Island for allowing us to use their facilities, Megan Kogut for her assistance in preparing ToF-SIMS samples for analysis, all those who assisted with ToF-SIMS, and Anne Gothmann and Tamas Ugrai for their assistance with spike calibration and ICP-MS analyses.

DEDICATION

For Mom, Tata, Isa, Mamá, Papá, and Rob for being there for me.

For Tita Diday, Tita Josefa, Tito Vic and the rest of my Seattle family for making me feel welcome in a new city.

In memory of Tito Vic, who was there at the start but left too soon. You are missed.

For everyone else that supported me through this whole process. You know who you are, and I could not have done it without you.

Chapter 1. INTRODUCTION

The addition of anthropogenic carbon dioxide into the atmosphere is altering Earth's climate at an unprecedented rate, leading to concerns about the effects of this environmental change on ecosystems (IPCC, 2013). In order to predict how climate will change in the future, it is important to understand how climate has changed in the past. This is often done by examining the chemistry of materials that formed during periods of Earth's history where climate has changed significantly. By relating the geochemistry of these materials with environmental parameters, we can examine how perturbations in the Earth system have affected global climate, and life's response to that perturbation.

Foraminifera are single-celled marine protists, which are ubiquitous across the global ocean. These organisms occupy a variety of habitats, ranging from the planktic foraminifera which occupy the photic zone, to the benthic foraminifera which live on the seafloor. These organisms are useful to the study of past climate changes not simply because of their widespread distributions, but also due to their ability to form calcium carbonate shells, or tests, which record information about the environment in which they are formed. The majority of foraminifera create their tests out of calcite, however, one notable species, *Hoeglundina elegans*, creates an aragonite test. These tests have a range of different morphologies which make them visually distinct from each other, usually determined by the arrangement of the chambers which form the test.

Foraminifera form their chambers gradually over the course of their life span, usually forming one chamber at a time (Reiss, 1957; Erez, 2003). An organic sheet, termed the primary organic sheet or POS, is formed prior to the formation of these chambers, and is used as a

template for calcification (Spero, 1988). At the end of the organism's life, after creating and thickening its final, or terminal chamber, the foraminifer undergoes gametogenesis, releasing its gametes into seawater and emptying its test of organic matter. During gametogenesis, some species of foraminifera, such as *O. universa*, are also observed to precipitate an extra layer of calcite over their tests (Bé, 1980; Caron et al., 1990; Brown and Elderfield, 1996; Nürnberg et al., 1996). This calcite layer is often called gametogenic calcite. After gametogenesis, these tests sink to the seafloor and are preserved in the sediment. The chemistry of these preserved tests can then be analyzed to determine information about the environment in which the organism lived (Katz et al., 2010). Many of these proxies are based on empirical calibrations, where the amount of a certain element or isotope within the calcite (often compared to Ca), is related to some environmental parameter such as temperature, salinity, or pH.

These proxies are incorporated into the calcite test during calcification, where foraminifera precipitate their shells from surrounding seawater. Calcification occurs in the calcifying space, which is sometimes thought to be comprised of seawater at the site of calcification. There are two major models for the delivery of seawater or ions to the calcifying space. The first, seawater vacuolization, suggests that seawater is delivered to the calcifying space by specialized vacuoles, which carry seawater into the cell (Bentov et al., 2009). The second, trans-membrane Ca transport, suggests that ions must cross a membrane in order to enter the calcifying space. Ca ions are transported across the membrane (Nehrke et al., 2013). The method of ion delivery to the calcifying space has implications for the overall chemistry of the calcite, as whether the calcifying space is a closed system or an open system may affect final shell chemistry. For example, if the calcifying space is a closed system which is occasionally 'flushed' by a fresh supply of seawater, Rayleigh processes may occur within the calcifying

space, where Ca becomes depleted in this internal closed pool, resulting in a steadily increasing concentration of other ions substituting for Ca in the calcite until the pool is flushed (Elderfield et al., 1996).

Foraminifera may also exert some control on the calcifying fluid. For example, during calcification, it has been suggested that foraminifera increase the pH of the calcifying space in order to promote calcite precipitation (Rollion-Bard and Erez, 2010). Similarly, the Mg/Ca ratio of foraminiferal calcite is lower than the Mg/Ca ratio of inorganic calcite grown under similar conditions (Katz, 1973; Duckworth, 1977; Mucci and Morse, 1983; Nürnberg et al., 1996; Bentov and Erez, 2006; Evans et al., 2018). This has led researchers to suggest that foraminifera are actively decreasing the amount of Mg in the calcifying space, possibly through the use of Mg-specific pumps. This would be advantageous to foraminifera because Mg increases the solubility of calcite and acts as an inhibitor to calcite nucleation.

During chamber formation, the foraminifera first secretes an organic envelope, which delineates the space into which the new chamber will be formed (Spero, 1988). Calcification then continues on either side of this organic template until the shell reaches its full thickness, although calcification rates are generally faster towards the exterior of the shell. This organic template is known as the primary organic sheet (POS), and remains embedded in the calcite after chamber formation is complete. The calcite associated with the POS may have a different chemical composition from non-POS-associated calcite (Bentov and Erez, 2005; Kunioka et al., 2006; Branson et al., 2013). It is thought that a new POS is formed prior to the formation of each new chamber. Some foraminiferal specimens, known as bilamellar foraminifera, lay this organic template over all older chambers, so that older chambers tend to be thicker than newer chambers

(Reiss, 1957). The extent to which certain species do or do not follow the bilamellar model is an area of active study (Fehrenbacher et al., 2017; Chapter 2).

In this thesis, we will focus on planktic foraminifera, which are the species of foraminifera that live in the photic zone. Planktic foraminifera can be further divided into spinose foraminifera, which have thin calcite spines that protrude outward from the test, and non-spinose foraminifera, which do not have spines and usually reside in the seasonal thermocline. Although benthic species are frequently used to understand past climate conditions, planktic foraminifera can provide unique information about surface ocean conditions during past climate changes, especially for low latitudes where other well-preserved archives may be scarce. In addition, it is easier to obtain samples of living planktic foraminifera for culture, using methods such as those described in Huber et al. (1996) and Lea et al. (1999). Culturing planktic foraminifera allows us to control the organism's environment, altering the conditions in which the organism is grown and reducing environmental variables in order to determine how changes in certain environmental properties change the chemistry of their shells.

At this point, we make an important note about the use of the term 'culturing', which has a slightly different meaning in the context of planktic foraminifera than in the context of algal or bacterial studies. Because planktic foraminifera have not been observed to reproduce in a laboratory setting, foraminiferal samples must be captured from the wild prior to their introduction into culture, and because new samples cannot be produced in culture, foraminiferal samples must be replenished frequently over the course of a culturing season. This means that in many cases, cultured foraminifera contain some amount of calcite that was grown in the wild, along with calcite grown under controlled conditions. We attempt to mitigate this by using samples from the species *Orbulina universa*, a spinose planktic foraminifer that forms a

distinctive sphere as its final chamber. This sphere is significantly larger than the previous, juvenile test, and completely envelops the juvenile test. By capturing specimens of *O. universa* prior to the formation of this sphere, we can ensure that the sphere grows entirely under cultured conditions. Because the sphere thickens over a period of 3-7 days, this sphere contains multiple days' worth of data. For species other than *O. universa*, which may have more complex morphologies, it is necessary to make accurate measurements of each foraminifer prior to introducing it into culture, in order to identify calcite grown in culture from calcite grown in the wild. Often, only chambers which are grown entirely in culture are used for these analyses.

Paleoclimate proxies are valuable tools for understanding earth's climate history, however, the incorporation of these proxies into foraminiferal calcite may not be straightforward. For example, previous studies have observed that the Mg/Ca ratio of the test, which is often used as a proxy for sea surface temperature, changes between day and night even in specimens that were cultured at constant temperature, in a way that has not yet been explained mechanistically (Eggins et al., 2004; Spero et al., 2015). While the sea surface temperature proxy still works in cases where multiple specimens are combined into a single sample in order to compensate for individual variability, diurnal heterogeneity is likely a strong contributor to internal variability in foraminiferal Mg/Ca. Heterogeneity in other metal-to-calcium (Me/Ca) ratios likely results in greater internal variability for those proxies as well. Also, the presence and regularity of this banding reflects a potential source of information about processes that occur on a diurnal timescale. If we could understand the causes of this heterogeneity, we would ideally be able to correct for the influence of this banding on the variability of existing proxies, and potentially make use of this unexplored source of information to better understand processes that occur on diurnal timescales.

Multiple processes have been proposed to explain Mg/Ca banding, such as banding being the result of high Mg in organic matrices (Erez, 2003; Kunioka et al., 2006), being associated in some way with chamber formation (Jonkers et al., 2016), being due to photosynthetic symbionts affecting the microchemistry of the environment on a diurnal scale (Eggins et al., 2004), or being due to diurnally modulated Mg uptake by mitochondria (Spero et al., 2015). However, none of these processes can explain Mg banding in all the species in which it has been observed. In this thesis, we examine processes that may be affecting intrashell heterogeneity at the microscale, in order to determine both how these processes are affecting trace metal incorporation into the foraminiferal calcite, and also to place constraints on the mechanism behind this heterogeneity. We explore three avenues by which foraminiferal growth processes have been suggested to affect metal-to-calcium (Me/Ca) ratios: (1) organic matrices and chamber formation (Chapter 2), (2) mineral growth kinetics (Chapter 3), and (3) gametogenic calcification (Chapter 4). We specifically ask how each of the named processes affects Me/Ca ratios in planktic foraminifera, as well as whether these processes can contribute to observed Mg/Ca heterogeneity. By measuring multiple Me/Ca ratios in each chapter, rather than simply focusing on Mg, we can examine how the behavior of other elements and proxies in foraminiferal calcite may be similar or different from the behavior of Mg, giving us more parameters which can be used to understand the entire system.

We use two major approaches to examine Me/Ca heterogeneity over the course of this thesis. First, we make use of isotope mapping and imaging techniques, such as time-of-flight secondary ion mass spectrometry (ToF-SIMS), which allows us to map the distribution of elements across a cross-section of the test wall of a foraminifer, and NanoSIMS, a similar technique to ToF-SIMS, which allows us to map the distribution of stable isotopes. These tools

enable us to determine how elements are arranged in space across the test wall. To lend further support to the results gained using ToF-SIMS, we also reference findings from atom-probe tomography (ATP), which allows us to spatially map atoms from a section of shell. These techniques are primarily used in Chapter 2 of this thesis, because they allow us to visualize Mg banding across the test wall of cultured foraminifera and examine how this banding is affected by organic matrices and chamber formation.

The second approach utilized in this thesis is drawn from the multi isotope spike technique described in Gagnon et al., (2012). This is a method that allows for the measurement of metal-to-calcium ratios of sections of a test wall with high precision, as long as the locations of interest are labeled with an enriched isotope of each of the elements in question (for example, labeling with ^{25}Mg and ^{43}Ca to measure Mg/Ca). In order to label the section of interest, the foraminifer is placed in enriched seawater during culture. Placing foraminifera into labeled seawater allows us to label only the portion of the test of interest, namely portions of the test that were grown during either the day or night (Chapter 3), or precipitated during gametogenesis (Chapter 4). After culture and collection of the foraminifer, whose test is made up of a combination of labeled and unlabeled calcite, the foraminifer is cleaned and dissolved for analysis. By measuring both the ratio between labeled and unlabeled calcite and the total Me/Ca ratio of the shell, the Me/Ca ratio of the labeled portion can be calculated.

This method is anticipated to have the high precision inherent in bulk analysis techniques, while retaining the small-scale spatial resolution necessary for the analysis of microscale processes. However, it should be noted that this method had never been applied to real foraminifera samples prior to this thesis and was previously only theoretical. The application of this method to our foraminiferal samples thus serves two purposes: the first, to gain information

about the composition of the shell in order to answer the questions described previously, and the second, to determine the effectiveness of this method in examining Me/Ca ratios in foraminiferal samples.

From our work with ToF-SIMS in cultured planktic foraminifera (Chapter 2), we observe that Mg/Ca and Na/Ca ratios increase at the location of the POS in *O. universa*, an observation that was further explored and confirmed with atom probe tomography (Branson et al., 2016). The POS in *O. universa* does not significantly contribute to the final mass of the shell. However, in *Orbulina bilobata*, a morphotype of *O. universa* that creates a second spherical chamber attached to its primary sphere, a second POS is observed to be embedded in the test during the formation of the second chamber. While *O. universa* and *O. bilobata* still have diurnal Mg/Ca banding external to the POS, the high Mg bands representative of the two POS in *O. bilobata* are distinct and account for two of the high Mg bands in this specimen (Figure 2.2). This increase in banding due to organic matrices has been observed in the shallow water benthic foraminifera *Amphistegina lobifera* and *A. lessonii* (Geerken et al., 2019) and in the planktic foraminifer *Pulleniatina obliquiloculata* (Kunioka et al., 2006). Na bands that are not associated with chamber formation are also observed in *O. universa*. External to the organic sheets, Na appears to be inversely linked to Mg during the first few days of test formation, with this pattern changing towards the end of the organism's life. This Na banding may have implications for emerging proxies that use foraminiferal Na/Ca to measure salinity (e.g: Wit et al., 2013), or past ocean calcium concentrations (Hauzer et al., 2018).

The remaining two chapters of the thesis (Chapters 3 and 4) examine the effects of diurnal cycles and gametogenic calcite on Me/Ca ratios in *O. universa.* Both of these chapters make use of the multi-isotope spike approach, however, in each chapter a different portion of the

test is labeled. Because these chapters represent the first use of the multi-isotope spike method to examine true foraminiferal samples, the effectiveness and precision of the method is also examined in Chapter 3. The method was found to be able to reliably reproduce ratios of Mg/Ca, Li/Ca, and Sr/Ca at high precision.

Mg/Ca, Li/Ca, and Sr/Ca were all observed to vary on a diurnal cycle. Because all samples were cultured at constant temperature in controlled environments, this variability cannot be explained by changes in temperature or pH. Variability in Mg/Ca was found to be comparable to previous observations of Mg/Ca variability, with significantly higher Mg during the night than during the day. Sr/Ca was observed to follow Mg/Ca, with high Sr during the night and low Sr during the day, however the variation in Sr/Ca was much lower in amplitude than that of Mg/Ca. In contrast, Li/Ca ratios displayed an opposite trend to Mg/Ca and Sr/Ca, with high Li/Ca during the day and low Li/Ca during the night.

By placing foraminifera into labeled seawater at the onset of gametogenesis, and by making use of the multi-isotope spike method, we are able to examine Mg/Ca and Sr/Ca ratios in gametogenic calcite (Chapter 4). We observe that gametogenic calcite in *O. universa* is high in Mg/Ca compared to non-gametogenic calcite, an observation similar to previous observations of the planktic foraminifer *Trilobatus sacculifer* (Brown and Elderfield, 1996; Nürnberg et al., 1996; Hathorne et al., 2003). However, we also observe that the chemical composition of gametogenic calcite appears indistinguishable from night calcification (Chapter 3). Thus, gametogenic calcite may be precipitated using a similar method as calcite precipitated at night. The observation that the Mg/Ca and Sr/Ca ratios of gametogenic calcification and night calcification share the same relationship as Mg/Ca and Sr/Ca ratios in inorganic calcite and other biogenic calcites (Mucci and Morse, 1983; Lea et al., 1999; Vielzeuf et al., 2013) further

indicates that similar geochemical processes govern night and gametogenic calcification. Day calcification Mg/Ca and Sr/Ca ratios have a slightly different relationship than observed in all other types of calcite, which may reflect the influence of kinetic and Rayleigh processes. We also observe an age effect, where Me/Ca ratios increase as the foraminifer ages This increase may indicate that the foraminifer's ability to discriminate between ions in the calcifying solution decreases with age.

The findings of this thesis reveal that much of the geochemical variability in *O. universa* can be explained by a handful of mechanisms and processes—organic-mineral interactions, mineralogical properties of calcite, kinetic effects due to growth rate changes, and Rayleigh processes. While this has so far been confirmed only in *O. universa*, these results may also apply to other species of foraminifera. This may also be complicated by species-specific differences in growth pattern and physical characteristics. For example, while organic matrices may have high Mg/Ca and high Na/Ca in *O. universa*, the nature of that species' terminal sphere means that organic matrices contribute very little to the overall Mg/Ca and Na/Ca ratios of the shell. However, other foraminifera which follow the bilamellar model of calcification may have more organic components in each chamber, especially if the POS of each chamber covers all previous chambers during chamber formation.

Similarly, if the diurnal patterns observed in Chapter 3 of this work also hold for other planktic foraminifera, the combination of diurnal heterogeneity and organic matrices may affect Me/Ca ratios more severely in species with multiple chambers, such as *Globigerinoides ruber, G. bulloides,* or *T. sacculifer*. The precipitation of a layer of calcite at the end of the organism's life, may also affect shell Me/Ca ratios. Even if, as observed in this study, gametogenic calcite is indistinguishable from night calcification, many other species of foraminifera have been

observed to precipitate a calcite crust, which has lower Mg than the remainder of the test and which affects proxy interpretation (e.g: Davis et al., 2017).

These observations highlight the importance of considering the effects of foraminiferal growth processes on the geochemical proxies contained within their shells. Foraminiferal proxies cannot be considered separately from the processes that form them, and record information not only about the environmental properties of the seawater in which the organism grew, but also about the way the organism affects the chemistry of the calcifying space. By understanding how proxies are incorporated into the calcite, we can hope to separate the effects of foraminiferal growth and biomineralization from the effects of environmental parameters, reducing variability in paleoclimate proxies and ultimately improving past climate reconstructions.

Chapter 2. SUBMICRON SODIUM BANDING IN CULTURED PLANKTIC FORAMINIFERA SHELLS

The calcite shells, or tests, of foraminifera provide a window into Earth history because they are archived in most marine sediments and contain useful geochemical proxies for paleoceanography. Previous observations of diurnal heterogeneity in proxies like Mg/Ca demonstrate a complex relationship between environmental conditions and test composition. The causes for this diurnal banding and the potential impact for proxy interpretation in systems other than Mg/Ca have yet to be determined. Recently, Mg and Na in shells of the planktic foraminifer species *Orbulina universa* have been observed to be high at the location of the primary organic sheet (POS), i.e. the organic template upon which the calcite test is formed. Here we use time-of-flight secondary ion mass spectrometry (ToF-SIMS), a chemical and isotope mapping technique with a spatial resolution of 300 nm, to show that Na banding is a consistent feature in the tests of 45 individual cultured *O. universa*. This banding occurs in two distinct forms: (1) sharp Na bands associated with organic sheets that are embedded in the calcite test after chamber formation; and (2) regular, thicker, but lower-amplitude Na bands that are found throughout the test. We use the pattern of the first type of banding to indicate the extent and sequence of calcite growth during chamber formation. Specifically, we show that new chamber formation involves growth over the previous chamber in *Orbulina bilobata*, a morphotype of *O. universa* that develops a second partial spherical chamber attached to the primary sphere. This is consistent with a bilamellar model of foraminiferal growth. However, a SIMS mapping survey of the morphologically more complex *Globigerina bulloides* and *Neogloboquadrina dutertrei* suggests that the pattern of growth during chamber formation and the prevalence of different types of Na bands may be species-specific. The wide, repeating Na bands that occur throughout the test of *O.*

universa generally occur in an inverse pattern with respect to Mg banding for the first few days of the foraminifer's life, but this pattern changes as the organism ages. We use the magnitude, timing, and coherency between Na and Mg bands to put constraints on various proposed mechanisms for banding, including antiport Mg^{2+}-$2Na^{+}$ exchange and kinetic growth rate effects.

2.1 INTRODUCTION

The calcium carbonate tests of foraminifera are widely used in paleoceanographic reconstructions because the elemental and isotope geochemistry of the tests contains a record of past environmental conditions (e.g. Katz et al., 2010). The majority of these geochemical proxies work on the principle that specific environmental properties affect the incorporation of trace elements or isotopes into the biomineral calcite, and that they follow a relationship that can be defined empirically. For example, the Mg/Ca temperature proxy is based on a calibration between calcification temperature and average test Mg content.

The discovery that Mg/Ca ratios vary by several-fold within a single test on a diurnal cycle independent of environmental temperature, with low Mg during the day and high Mg at night (Eggins et al., 2004; Spero et al., 2015; Fehrenbacher et al., 2017), but nevertheless still faithfully record temperature when analyzed in bulk, demonstrates a complex relationship between environmental conditions and test composition. While this micrometer-scale pattern of Mg/Ca variation is the best studied type of trace element (TE) banding in planktic foraminifera, there is growing evidence that other elements such as sulfur, boron, and uranium also display banding patterns (Erez, 2003; Allen et al., 2011; Paris et al., 2014; Holland et al., 2017). The causes for TE banding and its potential impact on paleoproxy interpretation in systems other than Mg/Ca have yet to be determined.

Na heterogeneity had previously been observed in a shallow water benthic species (Erez, 2003), but Branson et al., (2016) reported the first evidence for Na banding in the planktic foraminifer *Orbulina universa.* The study showed that high Na and high Mg are associated with the primary organic sheet (POS), the organic template upon which the calcite test is precipitated during chamber formation. During terminal sphere formation, *O. universa* secretes a cytoplasmic layer, which expands away from the pre-existing trochospiral test in a spherical pattern (Spero, 1988). Calcification begins on this layer within ~1 hour, suggesting that some elements of this cytoplasmic layer form the POS. Spines also begin to form from this POS shortly after initial calcification. Test growth occurs asymmetrically on both sides of the POS, with thicker calcite on the outer surface of the test. The presence of elevated Na and Mg in close association with the POS (Branson et al., 2016) suggests that (1) local test geochemistry can be influenced by organic components, and (2) coupled Na and Mg bands can potentially be used as geochemical markers for organic sheets within the test. This hypothesis links test geochemistry with foraminiferal growth models, which attempt to explain the pattern and timing of chamber formation.

The bilamellar growth model described by Reiss (1957) states that in the process of forming a new chamber, foraminifera also secrete a layer of calcite over all previous chambers in a regular pattern (Reiss, 1957; Erez, 2003; de Nooijer et al., 2014). This idea has been supported by etching and microscopic observations in some benthic (Reiss, 1957) and planktic (Bé and Lott, 1964) species, and by NanoSIMS observations of isotopically labeled chamber formation in shallow water benthic foraminifera (Nehrke et al., 2013). If the organic sheets that serve as the biomineralizing templates for new chambers also cover pre-existing chambers in the manner described above, then we would expect the number of organic sheets embedded into the calcite of each chamber and associated geochemical bands to increase with ontogeny.

A modification of this growth model was proposed by Fehrenbacher et al., (2017), who suggest that the non-spinose thermocline-dwelling species *Neogloboquadrina dutertrei* forms all of its chambers before adding calcite layers on pre-existing chambers. After the final chamber addition is completed, shell wall thickening and diurnal Mg-banding occurs around the entire test, in a process that is distinct from crust or gametogenic calcite formation, as the majority of specimens were not observed to develop a crust in culture. Fehrenbacher et al. (2017) developed this model based on observations that show the same number of Mg bands in all chambers of *N. dutertrei*. Such a growth model would result in a different pattern of organic sheet deposition than the bilamellar model, as the majority of the test would thicken after most chambers had formed and POS-associated banding may not be observed.

In this study, we use time-of-flight secondary ion mass spectrometry (ToF-SIMS) to map the relationship of Na and Mg banding to the shell formation process in laboratory-cultured individuals from planktic foraminifera with a variety of different morphologies. ToF-SIMS is a surface analysis technique with a spatial resolution of roughly 300 nm. This technique allows examination of small-scale variations in elemental composition to evaluate the role of test architecture in shell geochemistry, so that we can identify the sequence of calcification processes in foraminifera and attribute bands to either organic sheets or other mechanisms.

The foraminifer species studied herein were chosen because they represent a range of geometric complexities. We use the terminal spheres of 45 *O. universa* specimens as our simplest test case, because it is a complete sphere that is unattached from juvenile trochospiral chambers. We also present data from four (4) specimens of *Orbulina bilobata*, a rare morphotype of *O. universa* that develops a second partial spherical chamber attached to the primary sphere. These tests are used to represent a second level of geometric complexity. While the calcification

pattern of *O. bilobata* may not be the same as that of a typical multi-chambered species, this morphotype allows us to bridge the gap between the simple *O. universa* sphere and the multi-chambered geometries commonly seen in other planktic foraminifera species. In addition, we present results from a survey of *Globigerina bulloides* (N = 2) and *N. dutertrei* (N = 1), both of which are multi-chambered. Since Na/Ca is currently under consideration as a paleoproxy for salinity (Wit et al., 2013, Mezger et al., 2016, Bertlich et al., 2018, Mezger et al., 2018a, Mezger et al., 2018b), and past seawater calcium concentrations (Hauzer et al., 2018), the observations of Na banding observed here also contribute to the continued development and critical evaluation of these nascent proxies.

2.2 Materials and Methods

2.2.1 *Sample collection and culturing*

Specimens of *O. universa* and *G. bulloides* were captured using the blue-water collection method described by Huber et al., (1996) and cultured at the Wrigley Marine Science Center at Catalina Island, California, according to methods described by Lea and Spero, (1992). All *O. universa* and *G. bulloides* specimens were fed a single, day-old brine shrimp nauplius (*Artemia salina*) every two days. Only pre-sphere juvenile trochospiral *O. universa* were collected for this study in order to ensure all spherical tests were precipitated under controlled conditions in experimental seawater. The production of a second spherical chamber that yields the rare *O. bilobata* morphotype is not generally observed in culture experiments. Hence, *O. bilobata* specimens were not distinguishable from *O. universa* specimens until the end of an experiment. The reason why some individuals of *O. universa* form a second chamber is still debated (Caron et al., 1987; Robbins, 1988; Spero, 1988). Because *G. bulloides* does not have a terminal feature as distinctive as the *O. universa* sphere, the *G. bulloides* specimens used in this experiment were

chosen for their small size, and only those specimens that secreted additional chambers in the laboratory were selected for geochemical analyses. For *G. bulloides*, the longest dimension of each test was measured prior to the start of the experiment as a way to distinguish experimental from pre-experimental calcite growth.

While each individual foraminifer was maintained at constant seawater conditions (temperature, carbonate chemistry, and salinity) over the course of its time in culture, different individuals were drawn from a matrix of distinct experimental treatments, with individual conditions spanning from T = 18°C to 22°C, S = 30 to 36.6, pH_{NBS} = 7.90 to 8.59, and total alkalinity = 2091 to 2621 µmol/kg (Table 6.1). Samples were cultured on a constant 12 hr:12 hr light/dark cycle until specimens underwent gametogenesis. Each specimen was cultured in an individual glass jar filled completely with seawater and sealed with Parafilm and tight-fitting lids to minimize CO_2 gas exchange with the atmosphere. After gametogenesis, empty tests were rinsed in deionized water. Their largest diameter was measured, and tests were then stored in micropaleoslides until analyses. A single specimen of *N. dutertrei* (#152A from Fehrenbacher et al., 2017) included in this study was cultured and prepared for analysis according to the methods described in Fehrenbacher et al. (2017).

2.2.2 *Sample preparation for analysis*

In preparation for analysis by ToF-SIMS and to allow for thorough cleaning, *O. universa* spheres were fractured into roughly two halves using a scalpel. To maintain the fragile structures of *O. bilobata* and *G. bulloides*, these samples were not fractured prior to cleaning. Instead, they were cleaned and mounted as whole shells. Whole shells and shell fragments were individually cleaned in ~300 µL of a 1:1 solution of 30% hydrogen peroxide and 0.1 N sodium hydroxide for two minutes at room temperature. As the last step of chemical cleaning, the samples were rinsed

twice in 0.1 N NaOH, to buffer against dissolution, and dried in a trace-metal clean laminar flow hood. This cleaning method is modified from the method employed in Branson et al., (2016). It is shorter than some published procedures (Barker et al., 2003) and does not include a heating step, but was chosen for two reasons: (1) the cultured material in this study is relatively clean compared with sediment samples and (2) preliminary cleaning experiments using multiple heated H_2O_2 steps showed signs of dissolution as monitored through mass loss of individual tests (see Appendix A).

The use of NaOH during the cleaning step is a potential contamination concern, however, we believe that Na contamination does not affect our signal for the following reason. If Na contamination were to occur, it would be on the exterior of the shell, which was exposed to cleaning solution. However, after polishing, the exterior portion of the shell is removed, and the exposed section of the shell which is then analyzed was never exposed to NaOH. The observation that Na is anomalously high at the inner and outer edges of the shell may be an indication that the inner and outer surfaces are contaminated by NaOH (for example, see the inner edge of the *O. universa* image in Figure 2.1), however, this area is excluded from analyses using our sample processing script. Due to the presence of this high Na coating, we recommend that future studies to examine Na banding either avoid the use of NaOH during cleaning or to follow the NaOH step with multiple rinses in 18Ω ultrapure water.

O. universa fragments were mounted on glass slides or brass rounds in Araldite 502 resin and polished with progressively smaller diamond grit sizes ranging from 15 µm to 0.15 µm. In the case of *O. bilobata* and *G. bulloides*, samples were polished until a cross-section of the foraminifer was exposed, then more resin was added to fill the voids in the individual chambers. Polishing then continued in the same way as with *O. universa*.

2.2.3 *Time of Flight Secondary Ion Mass Spectrometry (ToF-SIMS) analyses*

A TOFSIMS.5-100 (IONTOF GmbH, Germany) time-of-flight mass spectrometer was used for all ToF-SIMS analyses. A 25 keV pulsed Bi^+ beam was used as the primary beam, which was focused to ~200 nm size on a 1000 mesh Cu grid. The resulting lateral resolution on the samples was found to be approximately 300 nm (see Appendix A for beam size analysis). The pulse width of the Bi^+ beam was 200 ns, and the pulse frequency was 33.3 kHz with a beam current of 0.6 pA on the sample. The time-of-flight was 30 µs, resulting in a full mass spectrum between 0-78 atomic mass units (amu) at each pixel. Specific peaks (Na^+, Ca^+ and Mg^+), were selected during post-analysis. A low energy electron flood gun was used to achieve charge compensation during measurement. A 10 nm Au coating was applied prior to analysis to promote charge compensation. Before analysis, each site was pre-sputtered at a 25x25 µm field of view for 60 seconds using continuous direct current (DC) beam (~200 pA beam current) to remove the Au coating and to reach a stable sputter interface. To ensure optimum Bi^+ beam focus for each location, a separate location with distinct topographic contrast near each site of analysis was selected and used for fine focus tuning. Measurements on foraminiferal samples were then taken across the test wall with a 20x20 µm field of view and 256x256 pixels per image. A total of 3200 scans were taken from each location. In cases where the thickness of the test wall exceeded the size of the image, more than one image was tiled together to capture the full thickness of the test.

2.2.4 *Post-analyses and standardization*

The image data were corrected for any translational stage movement as part of post processing. The yield of secondary ions changes over the course of each analysis, reaching steady-state sometime before the halfway point of the measurement (i.e., Scan 1600). Because of this, only the second half of scans (Scans 1600-3200) from each image was used. This same

cutoff scan number was applied to all samples and standards. The counts for the remaining scans were summed at each pixel to form intensity images for Na, Ca, and Mg. ^{40}Ca images are homogeneous throughout the imaged portion of the foraminifer with typical counts of ~2000 per pixel, suggesting that observed Mg/Ca and Na/Ca changes are due to changes in Mg and Na, rather than topography (see Appendix A).

Mg/Ca intensity ratios were converted to mmol/mol ratios using a suite of calcite mineral standards imaged under identical conditions as the foraminifera samples. The standards used in this study were previously analyzed using isotope dilution ICP-MS and are described in more detail in Gabitov et al., (2013). We use the same abbreviated naming scheme for these standards as Gabitov et al. (2013). The standards used for Mg/Ca in this study are: UCI, with a known Mg/Ca = 3.45 ±0.02mmol/mol and Blue Calcite, with a known Mg/Ca = 3.75 ±0.08 mmol/mol, which is comparable to the typical Mg/Ca values found in foraminifera during microanalysis(Sadekov et al., 2005). The standards used for Na/Ca in this study are: Blue Calcite and LAS-20. The Na/Ca calibration of these standards was performed by Branson et al. (2016), who used laser ablation ICP-MS referenced to NIST glass. According to that calibration, Blue Calcite has a Na/Ca ratio of 0.015 ±0.003 mmol/mol, while LAS-20 has a Na/Ca ratio of 0.48 ±0.03 mmol/mol. This is significantly lower than reported values of Na/Ca in foraminifera found during bulk analysis (Allen et al., 2016), which means that extrapolation is required for Na/Ca calibrations. While a sodium standard that better matches foraminifera would have been ideal, the fact that the magnesium standardization is linear over four orders of magnitude gives us confidence that the sodium extrapolation may also be linear over a smaller range (see Appendix A). The relative signals reported in this study are meaningful even in the absence of an accurate standardization.

The Mg/Ca intensity ratios of the standards were typically measured at the beginning and end of each experimental day, to account for instrumental drift. Within a typical analytical session (~13 hours), the mean Mg/Ca ratio of the standard varies by approximately 5-10%. The mean Na/Ca ratio of the standard is less stable, varying anywhere from 5-50% during a typical analytical session. While the high end of this variability is large, the signal in foraminifera can be large as well, which permits meaningful calibrations of Na/Ca. An average of the Mg/Ca or Na/Ca ratios across all standards during one analytical session is used for calibration.

As part of post-analysis processing, Mg/Ca and Na/Ca profiles were calculated perpendicular to the banding using the image data. This is done using a custom MATLAB script (see Appendix A) that traces the contour of each Mg/Ca band and then produces a profile with integer numbers of pixels normal to each contour line. Each point in the profile represents the sum of the pixels at that growth horizon. Mg/Ca and Na/Ca intensity ratios were calculated by dividing the intensity of the Mg and Na measurements by the Ca measurements (in counts) along the profile line. Because of its simple concentric growth pattern, a single *O. universa* specimen was chosen as a consistency standard and measured repeatedly over the course of different analytical sessions to examine the accuracy of the method and the ability of the method to reproducibly resolve Mg/Ca and Na/Ca features in a foraminifer. The mean Mg/Ca, averaged along a complete profile from inner edge to outer edge, has a relative standard deviation over the course of five different analytical sessions of 19%. Over the course of three analytical sessions with available Na/Ca calibration, the relative standard deviation of the mean Na/Ca ratio of the consistency standard is 6%. This shows that the mean foraminiferal Na/Ca was standardized reproducibly despite variability in the external calibrations.

The analytical noise in Na/Ca profiles was assessed by examining the range of Na/Ca variability in regions within the profile where Na/Ca was not changing systematically. Over the course of five different analytical sessions, Na/Ca noise levels in the foraminifera consistency standard vary from 5-35%. When compared with the typical amplitude of Na/Ca bands (7-20%), this noise can affect the amount of Na/Ca banding visible in each analytical session.

The overall pattern of Mg/Ca banding is visible and consistent in all measurements taken, making it possible to examine one distinct Mg/Ca band and observe how its amplitude changed from session to session (peak to trough). Over the course of five analytical sessions, the relative standard deviation of this amplitude is 4%, with exception of a clear outlier, which raises the RSD to 15% when included in our statistical analysis. We thus conservatively report a relative uncertainty of 15%. The reproducibility of banding in the consistency standard across several analytical sessions suggests that the ToF-SIMS method can faithfully image Mg and Na banding in foraminifera.

Across all individuals where Na/Ca calibration was available, the mean Na/Ca ratio of *O. universa* calcite in this experiment was found to be 2.02 ±1.20 mmol/mol. This is lower than previous measurements of Na/Ca in bulk planktic foraminifera (Bender et al., 1975; Delaney et al., 1985; Allen et al., 2016; Mezger et al., 2016), which typically show Na/Ca values for *O. universa* of approximately 6 mmol/mol. While this discrepancy is unresolved, the fact that we measure lower Na/Ca than previous studies suggests that our sample processing method does not introduce a major new source of Na contamination. Because the absolute Na/Ca of LAS-20 was calibrated after some initial foraminiferal samples were analyzed, Na/Ca calibration was not possible for all of the samples analyzed.

Cracks in the calcite or other topographic features are sometimes introduced as part of the polishing process. These features typically stand out in the ^{40}Ca intensity images, which are otherwise homogenous. While Na is occasionally elevated in cracks in the calcite or along the inner and outer edges of the test as mentioned above, this is usually detectable as bright spots in Na images in areas of topographically low calcite. High intensity Na features that appear as a result of these edge effects do not have the same regular, systematic pattern found in intra-chamber Na banding. Additionally, they are not consistent across different individuals or analytical sessions and tend to exhibit distinct features in the ^{40}Ca intensity image, so are easily diagnosed. Thus, the Na bands described in this study do not appear to be a result of cracks or topography.

2.3 RESULTS

2.3.1 *Unique Na band observed in O. universa*

ToF-SIMS images of 45 individual *O. universa* specimens reveal a thin (< 1μm) high Na band near the inner edge of the test wall that occurs between the closely spaced inner Mg bands and more widely spaced outer bands (labeled 'POS' in Figure 2.1A,B). The sharp Na band described here was observed in 91% of the individuals analyzed by ToF-SIMS and is often visible even in cases where analytical noise is too large to resolve other, more subtle, Na bands. In 54% of the samples, this Na band occurred in the same location as a distinct high Mg band. In the remaining samples, the high Na band occurred either between two small Mg peaks (7%) or was offset from a nearby Mg peak (30%). Mg banding on both sides of this sharp Na band appears to be symmetrical, with an equal number of Mg bands on either side of this Na band. Furthermore, intra-wall spines appear to originate from this sharp band (Figure 2.1B, D).

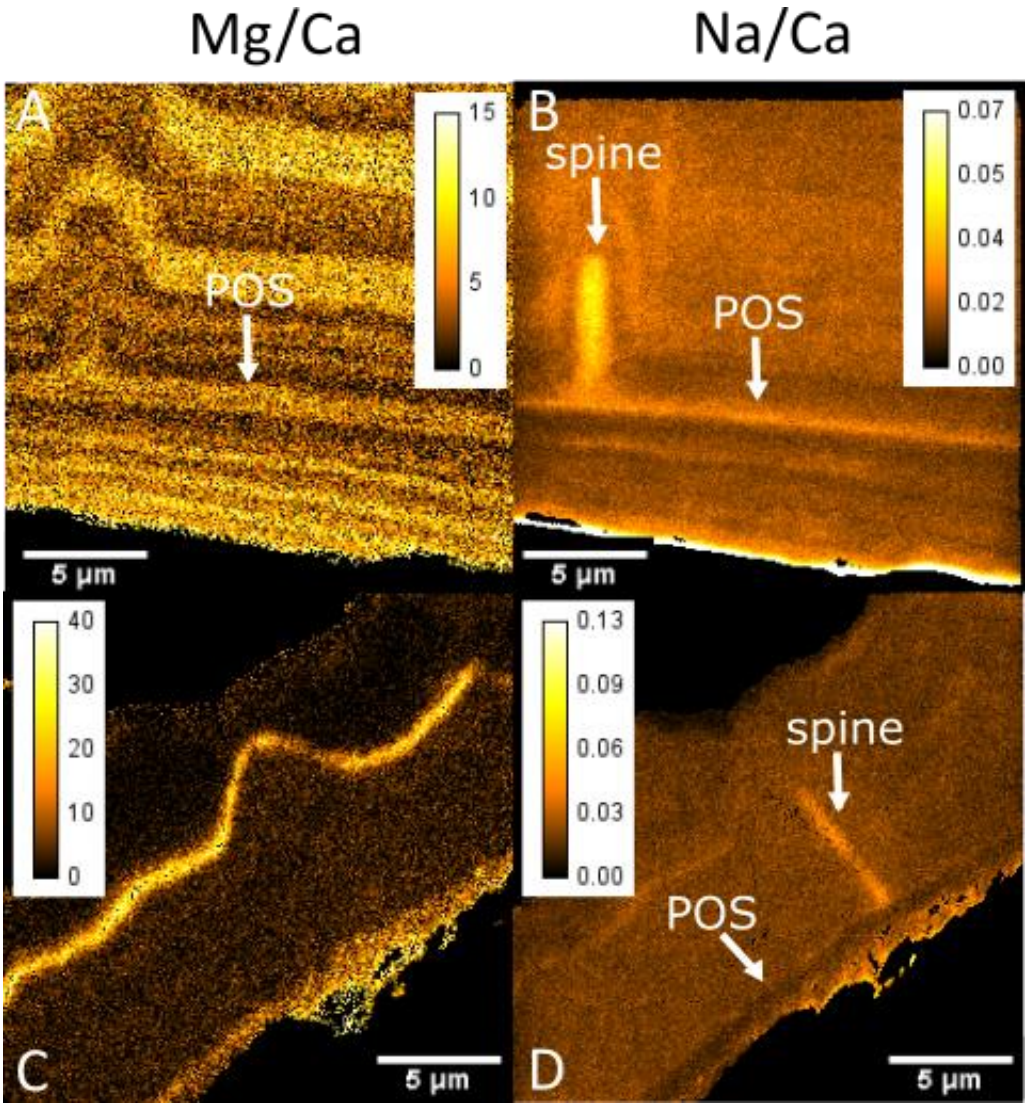

Figure 2.1. A thin high Na band is associated with the location of the embedded primary organic sheet (POS) in *O. universa* (A, B). In *G. bulloides* (C, D), all bands are thin with both high Na and high Mg (bottom images). Intra-shell wall spines (bright lines that are orthogonal to the POS) that originate at the POS in *O. universa* and *G. bulloides* are high in Na and thought to be associated with the intra-spine organic matrix. Regions of the sphere with spines are easily identified because the normally parallel Mg banding pattern is distorted around the spines. Na/Ca ratios are presented in uncalibrated intensity as counts/counts. Mg/Ca ratios are presented in mmol/mol.

The sharp Na band is compositionally distinct from other Na and Mg bands in the *O. universa* test. The Mg and Na bands that correspond to the sharp band are thin, with a mean

width of 0.6±0.3 µm, and often represent dramatic increases in Na (15% to as much as 98% in some cases). This large increase in Na/Ca ratios makes the sharp band the largest amplitude transition in most images, measured from minimum to maximum Na concentration. In contrast, Na bands not associated with the sharp band are often much wider, with a mean width of 2.0±1.4 µm. While there is some overlap between the change in Na/Ca magnitude associated with other Na banding and the change in magnitude at the sharp band, it is possible to identify this feature as a single distinct band in 91% of all cases examined.

2.3.2 *Sharp Na bands in bilobata and other multi-chambered foraminifera*

ToF-SIMS images were acquired across four different cultured *O. bilobata*, and images from a characteristic specimen are displayed in Figure 2.2. The images focus on the suture region between the two chambers, and the region of the primary sphere immediately adjacent to the second chamber. These images reveal an additional narrow high Na and high Mg band towards the outside of the primary sphere that continues into the secondary 'bilobata' chamber (Figure 2.2C). This second sharp band has similar characteristics to the sharp Na band in the primary spherical chamber of *O. universa* and to the sharp band of *O. bilobata*'s older chamber. For example, the outer sharp Na band in *O. bilobata* has a mean width of 0.6±0.3 µm. In addition, spines also appear to radiate outward from this outer sharp Na band (Figure 2.2B). This outer sharp Na band forms a continuous band that is present in the second chamber, extends across the suture site between the primary sphere and second chamber, and continues around the primary sphere. In the interior region below the second chamber wall, the outer sharp band is conspicuously absent (Figure 2.2A).

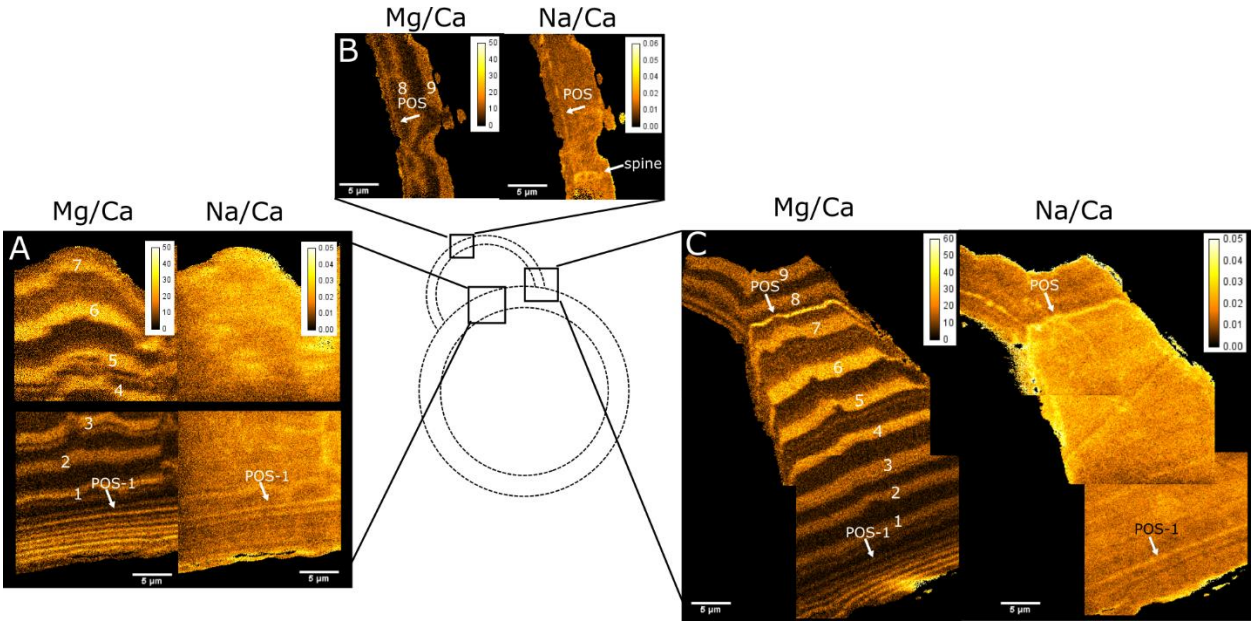

Figure 2.2. The formation of a new chamber wall attached to the *O. universa* sphere characterizes the test structure in *O. bilobata.* The formation of a second chamber involves the deposition of a new POS that extends completely around the primary spherical chamber (C). Calcification of the second chamber (B) begins at the POS and is similar to the calcification process documented between the POS and primary sphere. The second chamber POS is consistently located between bands 7 and 8 in the primary sphere of this specimen, with bands 8 and 9 displaying continuity with the second chamber. Note that the region of the primary sphere beneath the second chamber (A) does not contain the second chamber POS, nor Mg bands 8 and 9 although this foraminifer lived 9 days in culture. In this particular specimen, the POS is significantly brighter than the POS-1, indicating a higher Na concentration. Mg/Ca ratios are in mmol/mol. Na/Ca ratios are in uncalibrated counts/counts intensity units.

The remaining individuals of *O. bilobata* show similar patterns consistent with their life histories, with the exception of the fourth specimen, where undulating banding patterns obscure the relationship between different features, but do not contradict the above observations (see Appendix A). Such undulating banding is characteristic of over-polished samples where the polishing plane is too oblique.

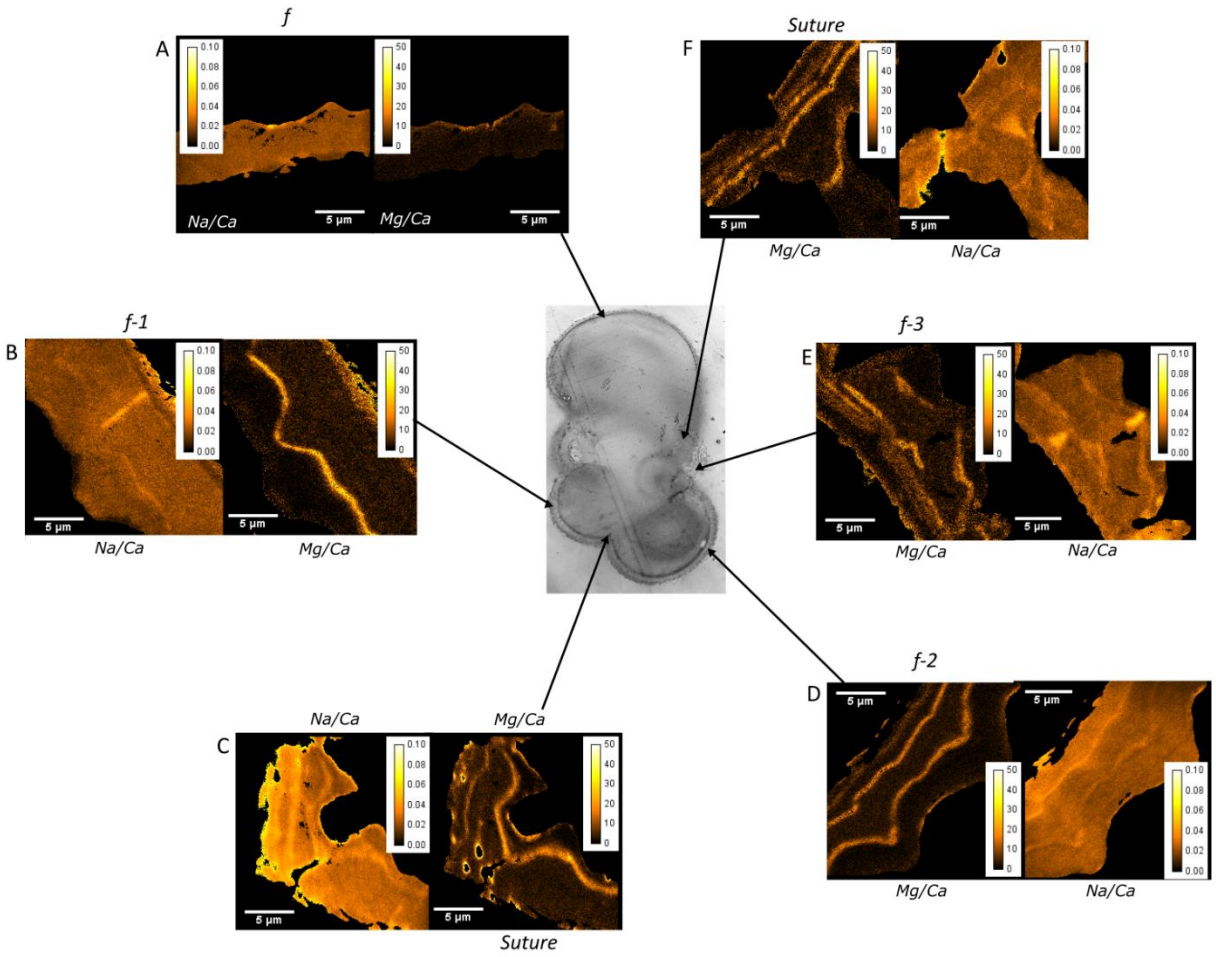

Figure 2.3. Each high Mg band observed in *G. bulloides* (pictured) appears to coincide with a high Na band. Mg/Ca and Na/Ca images are derived from ToF-SIMS images. Designation '*f*' represents the final chamber, *f-1* the penultimate chamber…etc. The number of bands appears to increase with age, with the exception of the final chamber (A), where no bands are visible. The lack of observed banding in the final chamber may be due to oblique sectioning through the chamber, or due to ablation of the chamber edge during polishing. The remaining chambers (B, D,E) and sutures between chambers (C,F) show increasing numbers of bands with ontogeny. Mg/Ca ratios are reported in mmol/mol. Na/Ca ratios are in counts/counts.

Specimens of *G. bulloides* and *N. dutertrei* were also examined in this study. In *G. bulloides*, all high Mg bands appear to coincide with high Na bands, similar to the sharp Na bands described above (Figure 2.3). In addition, the number of bands in the final three chambers

appears to increase with ontogeny (Figure 2.3A, B,D). In *N. dutertrei*, all high Mg bands coincide with high Na bands, however, the number of high Mg/high Na bands is the same across all measured chambers (Figure 2.4).

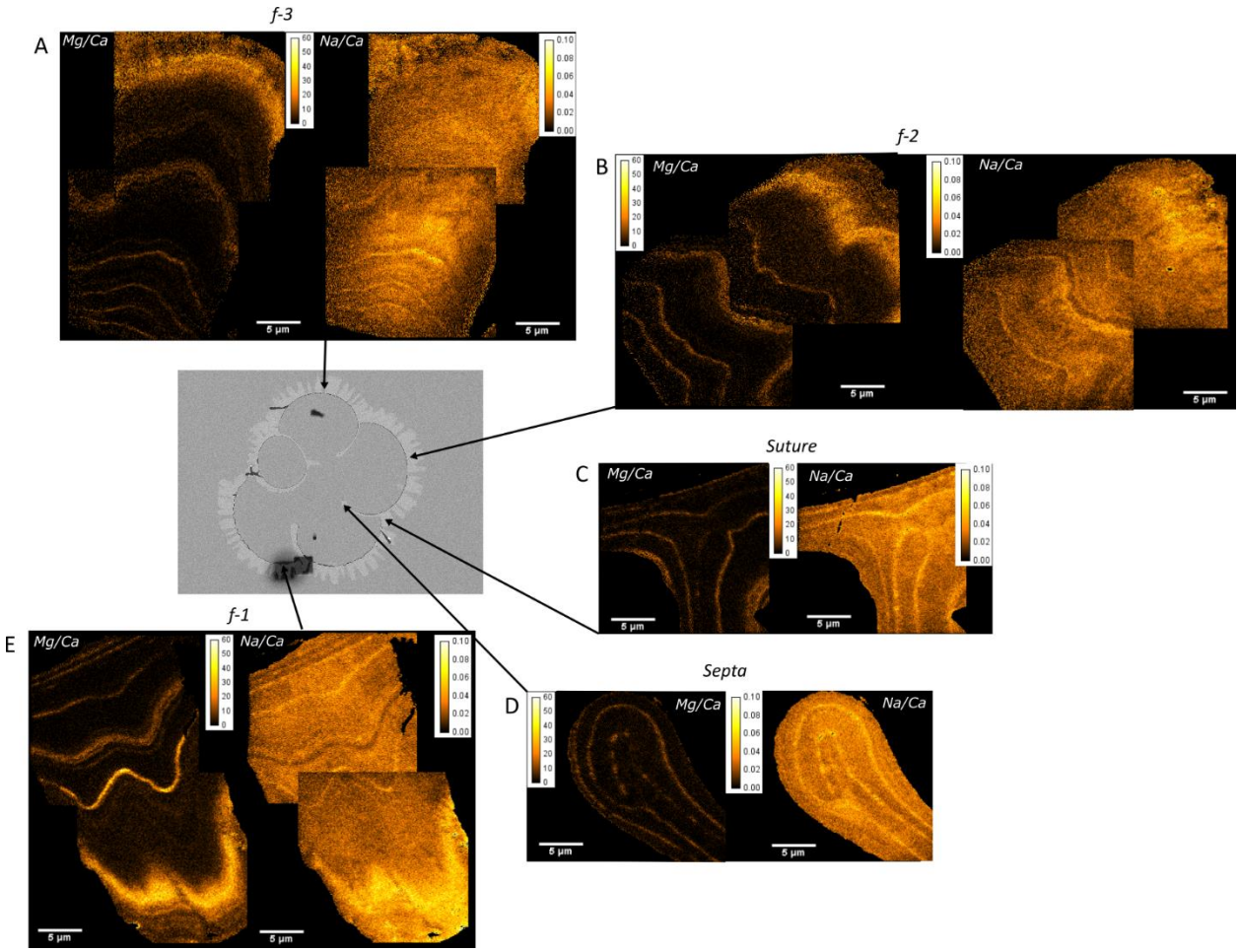

Figure 2.4. Each high Mg/Ca band observed in *N. dutertrei* is also accompanied by a Na/Ca band. The number of bands is roughly equal across all chambers (A, B, E), similar to the growth pattern described by Fehrenbacher et al. (2017). However, there are no inverse bands, making this pattern distinct from *O. universa* and *O. bilobata.* Images of the suture region (C) between the chambers imaged in (B) and (E) show one Mg band traveling through the septa (D) while another Mg band bypasses the septa entirely. Mg/Ca and Na/Ca images are derived using ToF-SIMS. Chamber designations are the same as in Fig. 2.3. Mg/Ca ratios are in mmol/mol. Na/Ca ratios are in uncalibrated counts/counts. The individual imaged in this figure is Foram 152A, the same specimen imaged with NanoSIMS in Fehrenbacher et al. (2017) (Fig. 6.21).

2.3.3 *Systematic inorganic Na heterogeneity in O. universa*

External to the sharp Na bands, Na heterogeneity in *O. universa* is organized into additional repeating bands throughout the test (Figure 2.5). These bands generally have a smaller amplitude than the sharp Na bands and are often wider. They are also not associated with a sharp Mg peak. While the amplitude or width of some of the repeating Na bands may be similar to the magnitude or width of the sharp Na bands, or they may be associated with an Mg peak, the combination of these three features (width, amplitude, and association with Mg) allows us to distinguish between sharp and repeating Na banding. These repeating Na bands are observed in all examined *O. universa* and *O. bilobata* specimens, except where analytical Na background noise exceeded 10%, a value that is comparable to the magnitude of this banding.

The repeating Na bands display similar patterns to previously observed Mg diurnal banding, but the timing is not necessarily similar between Na and Mg bands. The relationship between Mg and Na banding was examined to assess the coherency of these features. The relationship between each individual Na band and the corresponding Mg band was placed into one of three categories: inverse, synchronous, or out-of-phase. 'Synchronous' indicates that a high Mg band corresponds to a high Na band, (Figure 2.6B), 'inverse' means a high Mg band is associated with a Na band minimum (or vice versa, Figure 2.6A), and 'out of phase' occurs when a Mg band peak does not align with either a peak or a trough of a Na band (Figure 2.6C). Most (89%) of the 45 *O. universa* specimens studied display an inverse banding pattern during the first few days of sphere formation. This inverse pattern then shifts to another pattern (synchronous or out of phase) as the individual ages. The inverse pattern shifts to synchronous in 60% of all foraminifera studied or to 'out of phase' in 23% of samples. The remaining 12% of foraminifera are divided fairly evenly among the following banding patterns: inverse throughout the entire

sphere, 'out-of-phase' for the first few bands but inverse towards the edge of the test, and synchronous throughout the entire sphere. Overall, for most *O. universa*, Na and Mg bands start with an inverse relationship, which then typically evolves into synchronized or out-of-phase patterns. There was no resolvable difference in the pattern or amplitude or timing of Na banding between specimens cultured under different salinity and pH conditions (see Appendix A).

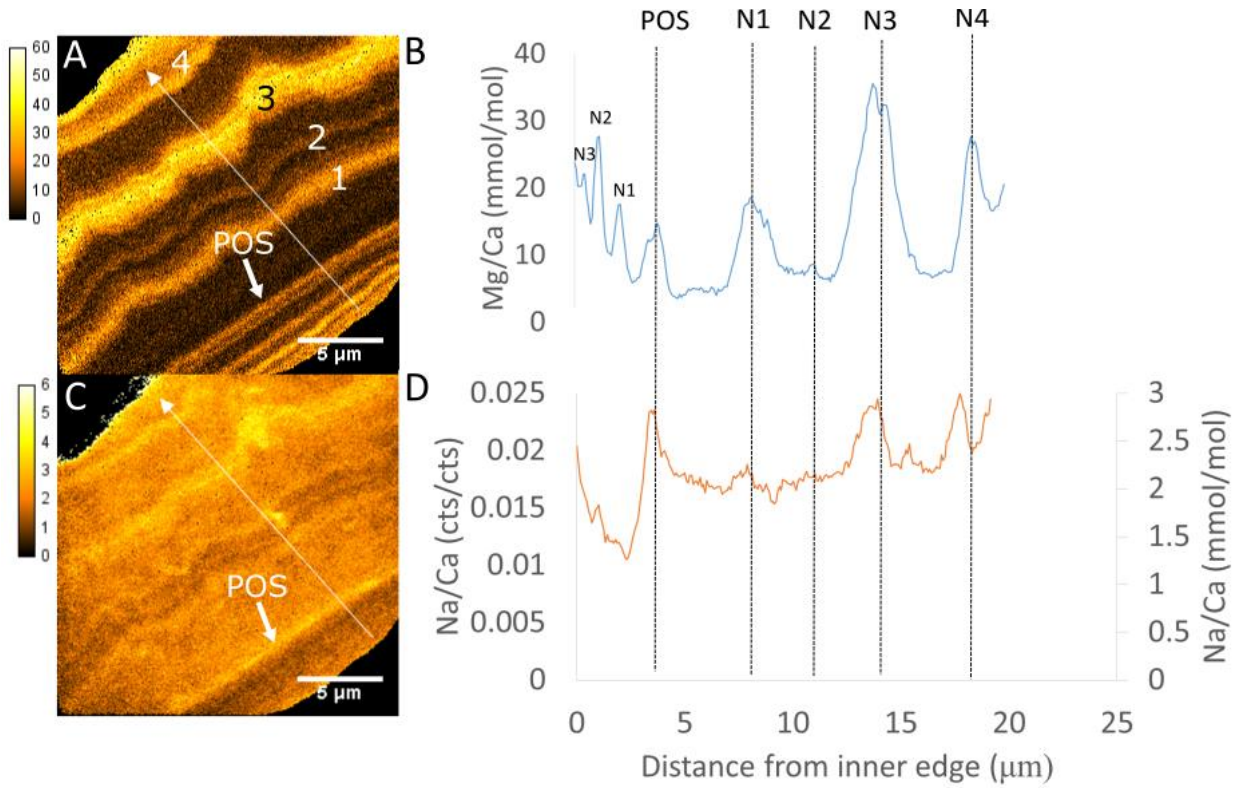

Figure 2.5. A) Mg/Ca intensity image showing banding, with Mg/Ca ratios recorded in units of mmol/mol. Note that Mg bands appear thicker towards the outer edge of the test. B) Profile of Mg/Ca across the foraminifer test. C) Na/Ca intensity image from the same foraminifer, with Na/Ca presented as uncalibrated counts/counts. D) Profile of Na/Ca throughout the foraminifer test at the same location as the Mg/Ca profile in (B), with Na/Ca ratios in both cts/cts and mmol/mol. The relationship between Mg/Ca and Na/Ca in this individual is synchronous. This individual was chosen because of its clear inner lamella banding, but is an example of an atypical relationship between Mg/Ca and Na/Ca. The POS and all corresponding night bands (high Mg) are labeled. These profiles begin on the inner shell surface as indicated by the white arrow. Bidirectional calcification around the POS is evident.

The diurnal timing of Na banding in *O. universa* was assessed using ToF-SIMS by examining two foraminifera whose culture media had been enriched with ^{43}Ca during night periods (see Appendix A). In these specimens, high ^{43}Ca peaks correspond to high Mg bands, as predicted from previous experiments with *O. universa* (Spero et al., 2015). In both these individuals, the initial Na bands were formed during the day (inverse pattern relative to Mg). One of the foraminifera continued this pattern while the other shifted to an "out of phase" relationship. This suggests that during initial sphere calcification, high Na bands are laid down during the day and occur roughly every 24 hours, however, at some point in the foraminifer's life, the pattern shifts so that high Na bands are laid down either at night or during the transition period between day and night. Because feeding occurred regularly every two days, the rough diurnal timing of Na banding does not indicate any connection between Na banding and feeding.

2.4 DISCUSSION

2.4.1 *Sharp Na bands as indicators of organic sheets in O. universa*

We hypothesize that the sharp Na band observed in *O. universa* is the elevated Na layer previously observed within the primary organic sheet (POS) using atom probe tomography (APT) (Branson et al., 2016). For the sharp Na band to be a unique indicator of the POS, at least two characteristics must be true: (1) the sharp Na band must occur in the location where the POS is independently known to occur, and (2) the sharp band must be unique and distinct from other compositional features in the test.

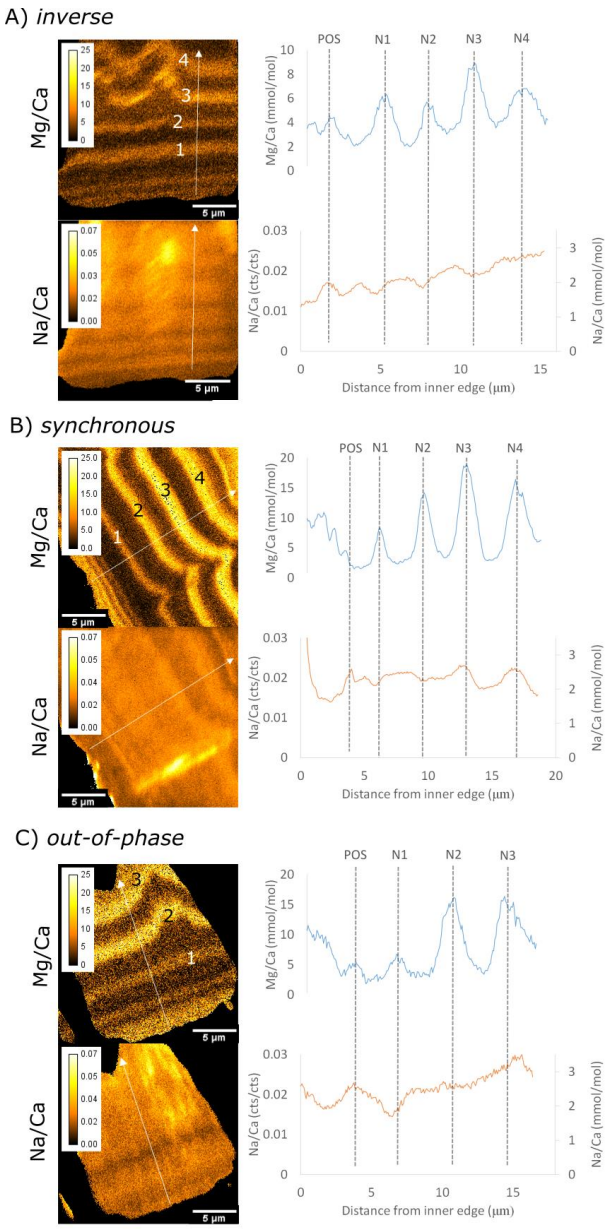

Figure 2.6. Different relationships between Mg/Ca and Na/Ca banding in *O. universa*: (A) inverse, where Na and Mg maxima and minima are ~180 degrees out of alignment (Table 6.1, #316), (B) synchronous, where Na and Mg extrema are aligned (Table 6.1, #555), and (C) out-of-phase, where the relationship between Na and Mg extrema does not appear to be aligned or varies between inverse and synchronous (Table 6.1, #645). This figure shows characteristic examples of each of the three categories. Mg/Ca ratios are recorded in mmol/mol. White arrows indicate the direction of growth. All corresponding night bands (based on Mg/Ca maxima) are marked and numbered.

Three pieces of evidence support the hypothesized correspondence between the sharp Na increase in our ToF-SIMS images and the POS in *O. universa*. First, when the inner Mg bands are resolvable, the number of Mg bands on either side of the sharp band is symmetrical, suggesting that growth occurs inward and outward from this band. This pattern is consistent with the sharp Na band being associated with the position of the POS in microscopic observations on living foraminifera (Spero, 1988). Second, intra-wall spines originate at the sharp band (Figure 2.1). This connection between spines and the sharp band is also consistent with the pattern expected for new sphere chamber spines originating at the POS reported by Spero (1988). Third, APT (Branson et al., 2016) identified a thin 10 nm layer of elevated Na and a thicker layer of Mg at the interface between the POS and initially deposited shell calcite. The concentration of Na and Mg in the POS layer observed at the nm scale using APT is consistent with the elevated Na and Mg concentrations in the sharp band using ToF-SIMS. Collectively, these data support our notion that the sharp Na band is co-located with the POS.

In addition to high Na at the POS, Na is also elevated in the center of spines (Figure 2.1). It is interesting to note that in spines, the high Na core appears to be confined to the area of initial growth, before the first observed Mg band. These features may be the result of oblique sectioning through the spine regions, although this pattern is consistent across all observed spines in this study. If elevated Na is associated with the organic sheet that was previously reported from TEM images of spines (Spero, 1988), then this may suggest that spine calcification utilizes Na ions at the organic-inorganic $CaCO_3$ crystallization interface similar to the APT observations of shell wall POS-Na association reported by Branson et al. (2016). Sodium is also elevated in the spines of *G. bulloides* (Figure 2.1C, D).

2.4.2 *Organic sheets in O. bilobata and other multi-chambered foraminifera*

Because of the similarity between the outer sharp Na band observed in *O. bilobata* (Figure 2.2B) and the Na band associated with the POS in *O. universa* (Figure 2.5), we hypothesize that the second sharp Na band observed in *O. bilobata* indicates the presence of a new organic sheet that provided the template for the second chamber. The location of this organic sheet can indicate where new growth occurs during second chamber formation. To uniquely identify the two POS in *O. bilobata*, we name the POS associated with the outermost chamber "POS". The inner POS associated with the primary sphere is named POS-1. This scheme follows the convention used to classify chambers in foraminifera.

The relationship between POS formation and second chamber formation is supported by the number of Mg bands on either side of the POS and by chamber thickness. In the primary sphere, the outer POS is bracketed by 6 prior high Mg night bands and followed by 2 subsequent high Mg night bands (Figure 2.2C). Thus, calcification continues on the outer surface of the primary sphere after the second chamber has started to calcify. In the second chamber, we also observe two high Mg bands, which is again consistent with two nights of calcification after the second chamber formed (Figure 2.2B). The spherical chamber beneath the second chamber shell wall is thinner (~34 μm) than the primary sphere (~46 μm) that is not covered by the second chamber. The second chamber wall has a thickness of ~11 μm, roughly equal to the difference between the thicknesses of the two regions of the primary sphere. The difference in thickness in the test below the second chamber wall compared to the primary sphere, and the fact that only 6 Mg bands are visible in the interior region (Figure 2.2A), show that upon secretion of the second chamber, calcification ceases on the primary sphere where it is now covered by the second chamber. Taken together, our data show that the formation of *O. bilobata* from an *O. universa*

specimen involves the production of a new primary organic sheet across the entire exposed outer surface of the test, corresponding to the time that the new second chamber starts calcifying. Our data also suggest that organic sheets are not used in the bands between POS and POS-1. This geochemical observation is consistent with the bilamellar growth model proposed in previous studies (Reiss, 1957; Erez, 2003; de Nooijer et al., 2014).

Previous micro-analytical studies have suggested that Mg banding in multi-chambered species may be related to the arrangement of organic sheets (Kunioka et al., 2006) or to the process of chamber formation (Jonkers et al., 2016). Indeed, Mg banding has also been observed in the benthic foraminifera *Amphistegina lobifera* and *A. lessonii*, and it has been proposed that this banding is associated with the POS (Erez, 2003; Bentov and Erez, 2005). SEM observations in these species have also revealed alternating dark and light areas, which has been attributed to layers of POS-associated primary calcite alternating with non-POS associated secondary calcite (Rollion-Bard et al., 2008). The examination of Na banding using SIMS may help constrain patterns of growth and chamber formation for many other species of foraminifera, not simply the ones discussed in this work. If banding and organic layers are indeed associated, then it follows that the pattern of Mg banding in these species should be similar to that observed in *O. bilobata*, with the formation of a new organic sheet in each chamber and multiple organic sheets visible in older chambers. An initial survey of the planktic foraminifera *G. bulloides* and *N. dutertrei*, however, shows both similarities and differences in Mg and Na banding patterns compared with *O. bilobata*.

In *G. bulloides*, all high Mg bands appear to coincide with sharp Na bands (Figure 2.3). The width and Na intensity of the *G. bulloides* bands make them appear more like the Na bands associated with the POS in *O. universa* than the wider bands associated with regular Na banding.

In the *G. bulloides* specimen pictured in Figure 2.3, the number of bands also appears to increase corresponding to the age of the last three chambers (Figure 2.3A, B,D). If the high Na bands in these images are derived from organic sheets, we would expect that *G. bulloides* lays down an organic sheet across all exposed surfaces with the formation of each new chamber. This is consistent with a recent study by Hori et al., (2018) which used isotope labeling during chamber formation to suggest that *G. bulloides* follows the bilamellar growth model. However, the widths of the isotope labels in that reference are much broader than the observed Mg/Ca bands within the labeled portions of the calcite. Thus, it is difficult to say based on that study whether the timing of Mg/Ca banding in *G. bulloides* is associated with chamber formation and the associated POS, or with shell thickening processes that occurred before the organism was removed from labeled seawater.

Also, some of the characteristics we use to identify organic sheets in *O. universa* and *O. bilobata* may not translate directly to all multi-chambered foraminifera. An example of such differences can be seen in *N. dutertrei*. NanoSIMS and laser ablation-ICP-MS analyses show that most of the chamber thickening in this species occurs after the formation of the final chamber (Fehrenbacher et al., 2017). Specifically, the organism produces all of its chambers first, and then subsequently adds calcite to thicken them across the entire exposed surface of the test. ToF-SIMS analysis of one of the *N. dutertrei* specimens analyzed in the Fehrenbacher et al. (2017) study (#152A) confirms that each chamber is covered by the same number of Mg bands (Figure 2.4 and Appendix A). This suggests that thickening occurred simultaneously across all chambers, rather than *N. dutertrei* thickening all existing chambers with the formation of each new chamber.

This pattern of Mg banding is not consistent with the Reiss (1957) bilamellar growth model. Instead, *N. dutertrei* produces diurnal day/night Mg bands that are similar to chamber wall thickening in *O. universa* (Spero et al., 2015). However, in apparent contradiction, the thickness of the bands and the fact that all high Mg bands coincide with high Na bands is more consistent with the organic matrix driven pattern associated with the POS and new chamber formation in *O. universa, O. bilobata* and potentially *G. bulloides.* It is important to note, however, that we have not yet independently verified the association between sharp Na bands and the POS in *G. bulloides* and in *N. dutertrei.* We interpret this variety of banding patterns as an indication that the geochemical signatures of the POS that we established in *O. universa* and *O. bilobata* may not necessarily apply to all multi-chambered foraminifera.

2.4.3 *Potential mechanisms for non-POS Na and Mg banding*

Separate from POS-associated bands, repeating Na bands in *O. universa* appear to occur inverse to Mg bands for the first few days of sphere formation. This suggests that the underlying mechanism for Mg and Na banding may be linked, and that understanding the mechanism which causes this inverse relationship could provide insight into the cause of Mg banding. However, any mechanism proposed to explain Na and Mg bands must also be consistent with the observation that Na bands often shift to become decoupled in time from Mg bands as the foraminifera grows older. The observed shifts could indicate that completely different physiological mechanisms are responsible for Na and Mg banding. Alternatively, one mechanism could dominate for the first few days of test growth before it is overcome by another mechanism.

One possible explanation for an inverse relationship between Na and Mg is related to ion pumping. Foraminifera are thought to form their calcite tests by precipitating calcium carbonate

from a calcifying fluid. Some models suggest that foraminifera such as *O. universa*, which have a much lower Mg/Ca ratio than inorganic calcite precipitated from seawater, could actively decrease the Mg/Ca ratio of the calcifying solution through active export pumping during calcification (Katz, 1973; Duckworth, 1977; Mucci and Morse, 1983; Nürnberg et al., 1996; Bentov and Erez, 2006; Evans et al., 2018). Pumping of only Mg^{2+} results in charge imbalance and an energetically costly membrane potential. Exchanging 2 Na^{+} ions for each Mg^{2+} as part of an antiport scheme could alleviate this charge imbalance problem. While the antiport exchange of any cation (e.g. Ca^{2+} or K^{+}) would alleviate this charge imbalance, sodium ions are abundant, which makes this scenario plausible but not unique.

An exchange of one Mg^{2+} ion from the calcifying fluid with 2 Na^{+} ions from seawater would cause a stoichiometric change in cation chemistry, with the Mg/Ca ratio of foraminiferal calcite decreasing as Na/Ca increases; an inverse relationship. However, the Na/Ca ratio of seawater (45.62 mmol/mol) is roughly 9 times greater than the Mg/Ca ratio of seawater (5.14 mol/mol), resulting in a smaller relative change in Na/Ca than for Mg/Ca. To estimate the relative change in these ratios, we test a simple model where we assume that (1) the calcifying fluid is predominantly seawater, (2) the Mg and Na partition coefficients between the test and the calcifying solution remain constant, and (3) [Ca^{2+}] remains constant throughout the exchange. Under these assumptions, a five-fold decrease of test Mg/Ca, as observed in some *O. universa* specimens, implies a five-fold decrease of this ratio in the calcifying fluid, resulting in removal of ~42 mmol Mg/kg. Restoring charge balance would require importing ~84 mmol Na/kg. This results in an 18% increase in the Na/Ca ratio of both the calcifying fluid and shell calcite. This increase is the right magnitude for changes observed in Na/Ca. Active Mg export pumping

coupled to Na antiport exchange is therefore consistent with, but may not be the only valid explanation for, the banding patterns observed during the first few days of sphere formation.

Of course, observed shifts in the relationship between Mg and Na throughout the rest of the test cannot be explained by this antiport mechanism alone. Our spatially resolved data allow us to evaluate which mechanisms could decouple Na from Mg. A Rayleigh process (Elderfield et al., 1996; Evans et al., 2018) where the calcium concentration of the calcifying fluid varies on a diurnal cycle, with increasing diurnal Ca amplitude as the foraminifer ages, is one mechanism that would drive Mg/Ca and Na/Ca bands to become more synchronous with time. This process would affect both Mg/Ca and Na/Ca similarly because both ratios are measured relative to Ca. However, the apparent lack of banding in Sr/Ca (Holland et al., 2017), another ratio that should change with changing [Ca], puts an upper bound on the magnitude of a Rayleigh-based *banding* effect.

Another common explanation for shifts in the metal-to-calcium ratio (Me/Ca) of $CaCO_3$ is kinetic effects during co-precipitation. Inorganic calcite experiments have shown strong mineral growth rate effects for a number of tracers, such as Sr/Ca and $\delta^{44}Ca$ (Tang et al., 2008a; Tang et al., 2008b; DePaolo, 2011). The large and regular changes in diurnal growth rate over distances of a few micrometers within a foraminifera means that the spatial resolution of ToF-SIMS is well matched to look for kinetic growth rate effects. On the other hand, bulk measurements average banding effects, so even if kinetic effects are present at this small scale, they may be muted or absent in bulk measurements (for example, Hauzer et al. 2018). If Na/Ca in planktic foraminifera were influenced by growth rate, and if this postulated effect were of sufficient magnitude, then we could expect shifts in growth rate to override a default inverse pattern caused by $Mg^{2+}/2Na^{+}$ exchange, as we observe that bands generally grow thicker as the

organism ages (Figure 2.5A,B). Here, we focus on processes that could shift Na behavior because Mg continues to exhibit regular banding throughout most of the *O. universa* chamber, but both elements could be influenced by kinetics. For kinetics to explain the shift in Na banding, (1) the partition coefficients for Na must be sensitive to growth rate at typical foraminifera calcification rates; and (2) mineral growth rates must change during test formation in a way that allows kinetics to dominate Na incorporation during the later part of chamber growth.

Interestingly, a correlation may exist between changes in growth rate and shifts in Na banding in *O. universa*, but this pattern is opposite to what we would expect for a mechanism based on kinetics. We start with the simplifying assumption that growth rate is constant within each 12-hour day or night period, as supported by sub-diurnal isotope labeling experiments (Vetter et al., 2013). In our study, where Mg/Ca and Na/Ca occurred inverse to each other, low Mg/Ca day bands were observed to grow 89 ±88% larger than their corresponding high Mg/Ca night bands. In contrast, in the last few bands of growth or in other situations where Mg/Ca and Na/Ca banding was not inverse of each other, day Mg/Ca bands were only 48±67% thicker than their corresponding night bands, with no observable difference in band thickness between synchronous and out-of-phase banding patterns (Figure 2.7). Thus the contrast in growth rates between day and night decreases with test age, which would suggest that kinetic differences between the bands should become less significant rather than more significant towards the outer surface of the spherical chamber. This pattern argues against a kinetic growth rate effect as the cause for a shift in the timing between Na and Mg bands.

In summary, Mg^{2+}-$2Na^{+}$ exchange may explain part of the Na banding we observe. Any mechanism proposed to explain the remaining aspects of foraminiferal geochemistry must be consistent with the magnitude, timing and synchronous nature of Mg, Na, and other elemental

bands seen in *O. universa* (Allen et al., 2011; Paris et al., 2014; Holland et al., 2017). While the complete mechanism for repeating Na banding is unsolved, our examples show how the combination of geochemical data and micrometer scale growth rates revealed by ToF-SIMS can constrain and evaluate particular hypotheses for banding.

The observed variability in the pattern and timing of Na and Mg banding between individuals of the same species and the difference in patterns of Na banding observed across multiple planktic species show that the relationship between Na and Mg in foraminifera is complex. Thus, any proposed mechanism for banding that is consistent for *O. universa* will need to be evaluated in other foraminiferal species, as different species of foraminifera may utilize different mechanisms of growth and chamber formation.

The presence of Na banding in planktic foraminifera, both in banding associated with organic sheets and systematic banding external to these organic bands, has potential implications for the recently proposed Na/Ca salinity (Wit et al., 2013; Mezger et al., 2016) and past seawater [Ca] (Hauzer et al., 2018) proxies. On one hand, we show here that Na/Ca can vary dramatically at the micrometer scale for reasons that are not associated with changing seawater chemistry. On the other hand, for the mean or the variability of a bulk proxy to be affected, the amplitude or relative proportion of these day-night bands would have to shift, respectively. For shifts in the amplitude of banding to bias a proxy, Na banding would have to be modulated systematically as a function of some environmental parameter. This sort of modulation is observed for Mg banding in *O. universa*, where amplitude increases at lower pH (Spero et al., 2015). We do not observe this sort of amplitude modulation for Na banding for salinity, within analytical error (Figure 6.12). Furthermore, if this bias does exist it may already be incorporated into empirical bulk calibrations.

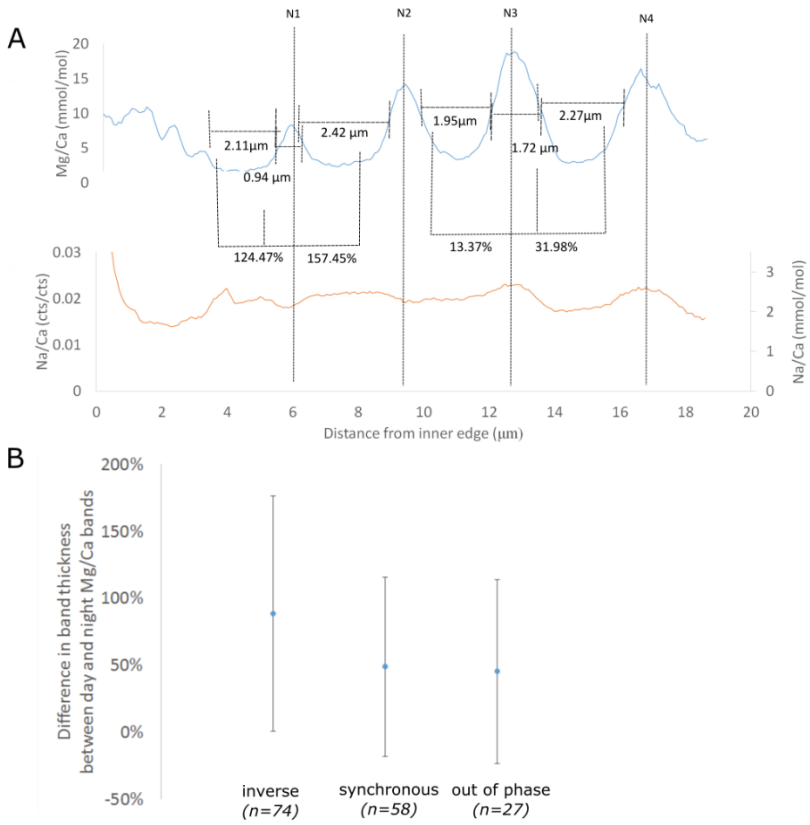

Figure 2.7. Relationship between Na banding and day/night growth in *O. universa*. We compare the width of each high Mg peak with its corresponding low Mg troughs, then sort these values depending on the relationship of the Mg band to its corresponding Na band. A) An example of this process performed on the same specimen displayed in Figure 2.6B. N1, which is an inverse band, is significantly thinner than its corresponding low Mg troughs, whereas N3, a synchronous band, is only slightly thinner than the corresponding troughs. B) A summary of the results when this analysis is applied to every observed Mg/Ca band. Note that in this case, 'inverse', 'synchronous', and 'out of phase' refer to individual bands, and not to the entirety of the test.

In contrast, internal variability, which could be influenced by banding, is known to cause uncertainty in other proxies, such as Cd/Ca (Boyle, 1995) and Mg/Ca (Anand and Elderfield, 2005), where the propagated effect of this internal variability can be diminished through the pooled analysis of many individuals. Since the amplitude of non-POS Na banding is up to 1-3 mmol/mol and this is close in magnitude to the reported change in shell Na/Ca due to salinity (Mezger et al., 2016), banding has more of a potential to impact the proposed salinity proxy

rather than the past seawater Ca proxy. For the seawater Ca proxy, several-fold changes in past calcium concentrations imply similarly large changes in test Na/Ca, and suggest that banding may not have much potential to bias this proxy (Hauzer et al., 2018).

2.5 CONCLUSIONS

Systematic Na banding is a consistent feature in *O. universa* tests and occurs in two different forms: (1) a distinct band of elevated Na associated with the POS, and (2) regularly spaced thick and lower magnitude Na bands that are found throughout the test. This latter form of Na banding is typically inversely related to Mg banding for at least the first few days of terminal test formation in *O. universa,* suggesting elevated Na occurs during the daytime. While a $Mg^{2+}/2\ Na^{+}$ exchange mechanism can explain the timing and magnitude of this inverse pattern, such a mechanism cannot explain why the relationship between Mg and Na often diverges later in the test thickening process. To explain this shift in timing, additional or alternative mechanisms should be present. The presence of Na banding further shows that elemental banding is a common feature for a wide range of cations and anions in foraminifera shells (see Paris et al. 2014, Allen et al. 2011, and Holland et al. 2017 for further examples).

A second high Na and high Mg band similar to the POS associated band that initiates primary sphere formation in *O. universa* was observed in *O. bilobata*, suggesting that this morphotype lays down a new POS over the terminal sphere when it creates this new chamber. The presence of this second organic sheet indicates that *O. universa* follows the bilamellar growth model described by Reiss et al. (1957), with an organic sheet laid down over all existing calcite at the formation of each chamber. While the co-location of a high-Na band with the POS suggests a promising geochemical indicator for organic layers in modern non-diagenetically altered foraminifera, it is unclear whether the co-location of Na and Mg bands relates to organic

sheets in all species. A survey of Na banding in *G. bulloides* and *N. dutertrei* may indicate the presence of species-specific patterns for Na banding.

Chapter 3. TESTING THE EFFECT OF CRYSTAL GROWTH RATE ON FORAMINIFERAL CALCITE MICROCHEMISTRY USING SR/CA OF INDIVIDUAL DAY/NIGHT BANDS

The Mg/Ca paleotemperature proxy in planktic foraminifera is one of the most widely-used proxies for sea surface temperature. However, over the past decade, studies have shown that this ratio is not constant throughout the test, varying systematically by several fold independent of temperature. This phenomenon has yet to be explained mechanistically, however, changing calcification rates may be a contributing factor. Observing the relationship between calcification rate and trace metal incorporation for multiple proxies will allow us to better understand the contribution of kinetic effects to this heterogeneity. In this study, we examine Me/Ca ratios on a diurnal cycle, utilizing a novel approach based on multiple isotopic spikes that allows us to measure Sr/Ca with the precision of isotope dilution while still maintaining the time resolution of microanalytical techniques. We measure Sr/Ca, Li/Ca and Mg/Ca in specimens of *Orbulina universa* that have been cultured in isotopically enriched seawater during either "day" or "night" periods. This allows us to examine the Me/Ca ratios of day and night calcite separately. Using independently measured growth rates derived from NanoSIMS measurements of diurnal Mg/Ca heterogeneity, we examine the effect of crystal growth rate on foraminiferal Sr/Ca and Li/Ca. We observe that Sr/Ca ratios in foraminifera are ~3% higher during the night than during the day, which initially appears opposite to the expected signal based on growth rate. However, we also observe a positive correlation between Sr and Mg in foraminiferal calcite, which falls on the same line as the Sr/Ca and Mg/Ca of various other biogenic and inorganic calcites from the literature. Kinetic effects appear to shift calcite composition away from this line. Interpreted within that framework, day Sr/Ca ratios appear more affected by kinetics than night Sr/Ca ratios,

which is consistent with observed calcification rates. We also observe high Li/Ca during the day, which is correlated to day Mg/Ca and may be reflecting Rayleigh processes within the calcifying fluid, which also act to shift calcite composition away from the mineralogical line. This indicates that the difference between any given data point and the mineralogical line may be explained by Rayleigh or kinetic processes, which may allow researchers to separate temperature, growth rate, pH, and other effects from the paleorecord.

3.1 INTRODUCTION

Foraminifera, single-celled marine protists, are important recorders of Earth history. As foraminifera calcify, they incorporate information about their environment into the chemistry of their calcite shells, or tests. Empirical relationships between chemical indicators in foraminiferal calcite and environmental parameters can be used to understand past climate changes (e.g. Katz et al., 2010). Because foraminifera are widespread across the world's ocean, and because their tests are preserved in the sediment, foraminiferal paleoproxies are valuable tools for understanding Earth history. Some of the most common types of foraminiferal proxies are derived from the metal-to-calcium (Me/Ca) ratios of the test.

Of these Me/Ca proxies, one of the most widely used is the Mg/Ca paleotemperature proxy in planktic foraminifera, which is used as a proxy for past sea surface temperature (SST). This proxy is based on the empirical observation that more Mg is incorporated into foraminiferal tests at higher calcification temperatures (Nürnberg et al., 1996; Rosenthal et al., 1997; Lea et al., 1999), a relationship that was first observed in inorganic calcite experiments (Katz, 1973; Burton and Walter, 1987; Mucci, 1987; Oomori et al., 1987). However, it has been observed that Mg/Ca varies by several-fold within the foraminiferal test between day and night independent of temperature (Eggins et al., 2004; Spero et al., 2015). The presence of this heterogeneity suggests

that temperature is not the primary control of Mg/Ca incorporation into calcite. This heterogeneity or other aspects of biomineralization may contribute to the sensitivity of foraminiferal Mg/Ca to several environmental parameters beyond temperature. For example, the Mg/Ca proxy has been observed to be biased by pH (Russell et al., 2004), where Mg/Ca increases at low pH and decreases at high pH. Similarly, Mg/Ca ratios have been observed to increase with salinity, with higher Mg/Ca at higher salinities (Hönisch et al., 2013). While Mg/Ca banding is the best-studied form of this heterogeneity, banding has been observed in other elements and proxies, such as sodium (Chapter 2), sulfur (Paris et al., 2014), boron (Hönisch et al., 2011), and uranium (Holland et al., 2017). The definitive mechanism behind this heterogeneity is still unresolved. Understanding the causes behind this heterogeneity and what it tells us about foraminifera biomineralization in general could help us better interpret paleoproxies.

Numerous factors have been suggested to contribute to Mg/Ca heterogeneity in foraminifera. It has previously been suggested that Mg banding could be caused by Mg being enriched in organic matrices (Erez, 2003; Kunioka et al., 2006), or that banding otherwise occurs due to high Mg calcite being precipitated during chamber formation (Jonkers et al., 2016). This mechanism can explain some of the geochemical patterns observed adjacent to organic layers (Branson et al., 2016) but does not explain banding observed separate from organic-associated calcite (Chapter 2). Others have suggested that banding could be due to photosynthetic symbionts affecting the chemistry of the foraminiferal microenvironment (Eggins et al., 2004), although this does not explain why banding is observed even in species without photosynthetic symbionts. Rayleigh fractionation of the internal calcium pool (Elderfield et al., 1996), which may act to set some of the overall Me/Ca ratio of the shell (Evans et al., 2018), is also unable to

explain the observed intratest banding on its own (Hathorne et al., 2009). The removal of Mg from the calcifying solution through active pumping, possibly through mitochondrial uptake, has been suggested to contribute to Mg banding (Spero et al., 2015), and indeed foraminiferal Mg/Ca has been observed to be lower than Mg/Ca of inorganic calcite grown under the same conditions Katz, 1973; Duckworth, 1977; Mucci and Morse, 1983; Nürnberg et al., 1996; Bentov and Erez, 2006; Evans et al., 2018). However magnesium pumping on its own does not explain why there is banding for several elements other than magnesium, nor does it quantitatively explain the robust temperature relationship that is the basis of the Mg/Ca paleo thermometer. The pumping of calcium to the site of calcification together with some amount of passive seawater transport, as posited in the transmembrane Ca transport model (Nehrke et al., 2013) may explain banding in elements other than Mg. However, through changes in calcium, this mechanism predicts that almost every Me/Ca should exhibit large and correlated shifts, which are not observed (Evans et al., 2018). Each of these proposed mechanisms can only explain a portion of the observations associated with Mg banding, meaning that the full mechanism behind this heterogeneity is still unknown.

Kinetic effects may also contribute to Mg/Ca banding. In inorganic mineral growth experiments, precipitation rate has been shown to affect trace metal incorporation into calcite, with various Me/Ca ratios showing a dependence on precipitation rate, such as Sr/Ca (Lorens, 1981; Tesoriero and Pankow, 1996; Tang et al., 2008a; Gabitov et al., 2014), Li/Ca (Füger et al., 2019), Ba/Ca (Mavromatis et al., 2018), and Mg/Ca (Mavromatis et al., 2013). Of these kinetic effects, the kinetic effect observed in Sr/Ca is the most studied. Calcite Sr/Ca increases relative to solution Sr/Ca at higher calcification rates (Lorens, 1981; Tesoriero and Pankow, 1996; Tang et al., 2008a; Gabitov et al., 2014), which has been explained as the balance between equilibrium

and kinetic partitioning (DePaolo, 2011). This makes Sr in particular a good candidate to use to evaluate the role of kinetic effects on foraminiferal heterogeneity. If we can make predictions for how calcification rates change in planktic foraminifera, then we can determine how much Sr/Ca can be expected to change based on kinetic effects.

Previous observations of planktic foraminifera (Lea et al., 1999; Kisakürek et al., 2011), have suggested that the amount of Sr incorporated into calcite is at least partially affected by calcification rate, although the signal is small and can be hard to discern from other factors during bulk analysis. This is because during whole shell measurements, intrashell heterogeneity in both Sr/Ca ratios and calcification rate is averaged. However, if we could measure both Sr/Ca ratios and growth rates at similar scales, for example between individual day or night bands within a foraminifer, we may be able to determine whether shell Sr/Ca ratios are changing with kinetics. Microanalysis using laser-ablation inductively-coupled mass spectrometry (LA-ICP-MS) has revealed very little variability in foraminiferal Sr/Ca ratios (Hathorne et al., 2009), however, limitations in precision and spatial resolution of these methods may be preventing the observation of small variations in Sr/Ca.

For this study, we use *Orbulina universa*, a species of planktic foraminifer, as a model. *O. universa* creates a terminal sphere as its final chamber, which envelops all previous chambers and thickens for ~3-7 days in a culture experiment. This ensures that several day and night bands are available for measurement, ensures a consistent growth axis across the entire test, and removes other variables that may be affecting intrashell Me/Ca ratios, such as chamber formation. This species has also been observed to calcify more during the day than at night (Lea et al., 1995; Bijma et al., 1999), a growth rate change that can be quantified because the diurnal timing of Mg/Ca banding is well-established in this species, and because in culture, the day-night

cycle of *O. universa* can be fixed at 12:12 hours. However, in order to test whether kinetics are affecting Me/Ca ratios in this species, it is necessary to measure Me/Ca ratios of individual day and night bands. For some elements that have lower concentrations in foraminiferal calcite than Mg, such as Li and Sr, this requires a high level of analytical precision.

In order to overcome this challenge, we use a novel multi-spike approach, which uses multiple isotopic spikes to increase the precision with which we measure analytical ratios (Gagnon et al., 2012). This approach is predicted to have the precision of bulk analysis, while being able to resolve the composition of features at the microscale. The use of this approach on cultured *O. universa* specimens will allow us to separate the composition of day and night bands from the remainder of the test. The precision of this approach is expected to be higher than previous methods of examining intrashell Sr variability, such as LA-ICP-MS or secondary ion mass spectrometry (SIMS). This approach would allow us to examine smaller variations in Sr/Ca and other Me/Ca ratios than have been analyzed using previous analytical techniques.

If a kinetic effect is present for Sr/Ca, we should expect to see high Sr/Ca when growth rates are high, such that Sr/Ca is high during the day and low during the night. For example, an expected calcification rate increase of ~60% would imply an Sr/Ca change of ~10%, based on the relationship of Sr/Ca to calcification rate in inorganic calcite (Tang et al., 2008a; DePaolo, 2011). Because Mg/Ca has been observed to be low during the day and high at night, this would result in an inverse relationship between Mg/Ca and Sr/Ca, where Sr/Ca is high when Mg/Ca is low and vice versa. A similar effect would also be expected for Li/Ca, which has been observed to increase as growth rate increases (Füger et al., 2019), but which may be also responding to one or more carbonate system parameters in foraminifera (Lear and Rosenthal, 2006; Vigier et al., 2015; Doss et al., 2018; Roberts et al., 2018). Observing these relationships would suggest that

kinetics play a role in intrashell heterogeneity, which could be used to explain the variability of other Me/Ca if they too respond to kinetic effects. However, even if these relationships are not observed, the results of this experiment will still provide us with information about diurnal heterogeneity in three separate elements and proxies. The relationships between these three elements and proxies, which may be responding to similar mechanisms, will provide useful insights into the mechanisms of foraminiferal calcification and any potential differences in biomineralization between day and night, ultimately providing constraints on the mechanisms driving diurnal heterogeneity and proxy incorporation in general.

3.2 MATERIALS AND METHODS

3.2.1 *Overview of multi-spike analysis technique*

The goal of the multi-isotope method is to analyze the Sr/Ca, Mg/Ca, and Li/Ca of just the day or night portion of a cultured planktic foraminifer and to make this measurement at high precision. To specifically label the day portion of a foraminifer, an individual is cultured in a seawater solution enriched in stable isotopes of calcium, strontium, lithium, and magnesium during the day. At night the same individual is transferred to natural abundance seawater. This process is repeated for several days, which results in a foraminifer where the isotopically labeled portion of the test corresponds only to day calcite and the natural abundance portion of the test corresponds to both night calcite and unlabeled calcite from days prior to the labeling sequence.

Bulk isotope analysis of this single foraminifer can then be used to isolate the composition of only the labeled portion of the test. Through the power of isotope dilution, this approach has the potential to produce high precision and high accuracy metal-calcium ratios. Although the approach is outlined theoretically in Gagnon et al., (2012) it has yet to be

demonstrated in practice. Thus, prior to applying this method to cultured foraminifera, we first test the method and assess precision using synthetic samples.

The method requires accurate isotope abundances of the two end members: the enriched culture solution (referred to as "X") and the natural abundance portion of the foraminifer (referred to as "O"). A dissolved sub-sample of each foraminifer is then isotopically analyzed to determine the mixing ratio between the labeled and unlabeled portion of the test for each element of interest. A second isotope dilution experiment is then applied to an aliquot of the dissolved foraminifer. This second isotope dilution experiment uses an enriched isotope spike (referred to as "XX") different than the culture media to determine the total amount of each element of interest in the mixture. Because mixed spikes are used throughout this study, where the term "mixed spike" indicates that isotopes of several elements are enriched simultaneously, element ratios can be calculated at high precision without having to know the exact amounts of spike added, as long as the isotope ratios in the mixed-spike are known for each element of interest. These ratios can be calibrated through one measurement or a series of measurements, and the same solution can then be used for the entire experiment.

Algebraically, the Me/Ca ratio of the labeled portion of the test is calculated using the following set of equations from Gagnon et al., 2012, which are demonstrated here using Sr/Ca as an example:

$$\left(\frac{\mathrm{Sr}}{\mathrm{Ca}}\right)_x = \left(\frac{{}^{48}A_x\,({}^{48}F+1)}{{}^{86}A_x\,({}^{86}F+1)}\right)T \tag{3.1}$$

where $(Sr/Ca)_x$ refers to the Sr/Ca of the labeled calcite; ${}^{48}A_x$ refers to the isotopic abundance of the reference calcium isotope (^{48}Ca) in the labeled calcite; ${}^{86}A_x$ refers to the abundance of the reference strontium isotope (^{86}Sr) in the labeled calcite; F refers to the mixing ratio between labeled and unlabeled calcite; and T refers to the total Sr/Ca of the sample. The equation for

calculating F for a specific element is shown below. ^{48}F is used for this example, however, other F-values use analogous equations.

$$^{48}F = \frac{^{48}n_o}{^{48}n_x} = \left[\frac{\left(\frac{^{43}Ca}{^{48}Ca}\right)_m - \left(\frac{^{43}Ca}{^{48}Ca}\right)_x}{\left(\frac{^{43}Ca}{^{48}Ca}\right)_o - \left(\frac{^{43}Ca}{^{48}Ca}\right)_m}\right] \quad (3.2)$$

Here, $^{48}n_o$ refers to the number of moles of ^{48}Ca in natural calcite, and $^{48}n_x$ refers to the number of moles of ^{48}Ca in the enriched culture solution. It is this ratio or F-value that is calculated. (^{43}Ca/^{48}Ca)$_m$ refers to the ratio of enriched isotope to reference isotope in the sample being measured, which is a mixture of both labeled and unlabeled calcite, where the reference isotope is an unenriched isotope that is measured at the same time as the enriched isotope. This ratio is determined for each dissolved foraminiferal test using mass spectrometry. Similarly (^{43}Ca/^{48}Ca)$_x$ refers to the isotopic ratio of the culture solution, and (^{43}Ca/^{48}Ca)$_o$ refers to the isotopic ratio of unlabeled calcite. Both of these values can be determined just once using mass spectrometry, and applied to all foraminifera. For simplicity, these terms will be referred to as R_m, R_x, and R_o in the remainder of this manuscript, where R refers to an isotope ratio defined as the enriched isotope divided by the reference isotope.

T is calculated using a second isotope dilution step and the equation below, again using Sr/Ca as an example:

$$T = \frac{^{86}n_T}{^{48}n_T} = \left(\frac{\mathrm{Sr}}{\mathrm{Ca}}\right)_{xx} \frac{^{86}A_{xx}}{^{48}A_{xx}} \left[\frac{^{Sr}R_{ID} - ^{Sr}R_{xx}}{^{Sr}R_m - ^{Sr}R_{ID}}\right] / \left[\frac{^{Ca}R_{ID} - ^{Ca}R_{xx}}{^{Ca}R_m - ^{Ca}R_{ID}}\right] \quad (3.3)$$

where (Sr/Ca)$_{xx}$ refers to the Sr/Ca of the isotope dilution spike (XX); $^{86}A_{xx}$ refers to the abundance of ^{86}Sr in the isotope dilution spike; $^{48}A_{xx}$ refers to the abundance of ^{48}Ca in the isotope dilution spike; R_{ID} refers to the ratio of enriched isotope to reference isotope in the mixture of isotope dilution spike and sample; R_m refers to the isotope ratio of the calcite sample

without the isotope dilution spike; and R_{xx} refers to the isotope ratio of the isotope dilution spike alone. The creation and measurement of these solutions are described in the following sections.

Because the spiked seawater from which the labeled calcite grew is likely to have a slightly different Me/Ca ratio than natural seawater (see for example, Table 1 in Gagnon et al., 2012), mean Me/Ca ratios obtained using this method were converted into partition coefficients (D_{Me}) between calcite and solution, using the following equation, here presented for Sr:

$$D_{Sr} = (Sr/Ca)_{calcite} / (Sr/Ca)_{seawater}. \quad (3.4)$$

The use of partition coefficients normalizes for changes in solution composition, allowing the compositional results of this study to be compared with other culture studies and with the geochemical results of inorganic mineral growth experiments.

To calculate the partition coefficient, Equation 3.4 was modified slightly by multiplication with $(^{86}A/^{48}A)_{calcite} / (^{86}A/^{48}A)_{seawater}$, the percent abundance ratio of ^{86}Sr, the reference isotope of Sr and ^{48}Ca, the reference isotope of Ca, to yield $D_{Sr} = (^{86}Sr/^{48}Ca)_{calcite} / (^{86}Sr/^{48}Ca)_{seawater}$. If we assume that there is no fractionation between spiked seawater and calcite, the term $(^{86}A/^{48}A)_{calcite} / (^{86}A/^{48}A)_{seawater}$ equals to 1, and the two equations for D_{Sr} are equivalent (see Appendix C).

The isotopically enriched seawater (X) was created by my thesis advisor prior to my involvement in this project (Section 3.2.2). All foraminifera culturing for this and the following chapter (Sections 3.2.3 and 4.2.1), and NanoSIMS imaging of the mixed-spike foraminifera (Section 3.2.9) were also conducted before my involvement. All other steps in this project, including cleaning and fracturing of foraminifera shells, spike calibration, the creation of a natural isotope consistency standard, and re-interpretation of available NanoSIMS data, were done by me.

3.2.2 *Preparation and calibration of the isotopically enriched seawater*

A recipe for isotopically enriched seawater was designed to maximize the level of enrichment while minimizing changes to total elemental concentrations, as described in Gagnon et al. (2012). The culture solution (referred to as YYH, which corresponds to 'X' in above equations) was created using the following enriched isotope batches: Oak Ridge National Laboratory (ORNL) 1803-307A Series SS (^{6}Li), ORNL Batch # 158591 (^{25}Mg), Trace Sciences International (TSI) Lot # 1-04 (^{43}Ca), ORNL Series NJ Batch # 163191 (^{84}Sr), and ORNL Batch # 174990 (^{135}Ba). Note that YYH contains ^{135}Ba, but barium will not be discussed in this study because the low concentration of barium in calcite precluded single foraminifera analysis at sufficient precision.

Carefully weighed amounts of each solid enriched isotope batch were dissolved in ultrapure 10% HCl to create primary solutions. Nitric acid was avoided during spike preparation to limit the introduction of the major nutrient NO_3^- to the culture solution. Following this initial dissolution step, serial dilution and subsequent mixing was used to create a mixed isotope spike that was then dried and stored (Table 3.1).

Five (5) days prior to the culture experiment, surface seawater was collected from an open ocean site ~2 km NNE of Catalina Island, California, USA. This same location was used to collect natural abundance seawater and was also the site of blue-water foraminifera collection. The collected seawater was filtered with 0.8 µm nitrate cellulose filters in a large glass side-arm Erlenmeyer vacuum flask. A 500 g portion of the filtered seawater was mixed with the YYH spike, which had been reconstituted using ultrapure HCl, and the mixture was stored in an acid leached low density polyethylene (LDPE) bottle. After the addition of the spike to seawater, solution pH was found to be 6.233 (NBS scale). Approximately 250µL of 2N NaOH was added

to the culture solution to raise the pH to 8.15 after equilibration, close to the initial pH value of the natural collected seawater of 8.17.

Samples of the natural abundance filtered seawater together with the isotopically enriched mixture X, made of seawater and primary elemental spikes, were collected in acid leached plastic vials, acidified to pH 2 using ultrapure HCl, and stored for later analysis (described below). A full breakdown of the isotope composition of the culture solution can be found in Table 3.2.

A number of steps were taken to minimize contamination and were followed throughout the study unless otherwise noted. Acids are ultrapure and were either prepared using a Teflon double distillation apparatus or purchased (Aristar Ultra). Ultrapure "Q water" is 18.2 MΩ. Dissolution, dilutions, and other solution manipulations were conducted in a HEPA filtered laminar flow bench (class 10 workstation) housed in a trace-metal class 1,000 clean lab. Solutions were stored in low density polyethylene (LDPE) bottles that had previously been leached in boiling acid, rinsed 4-6 times in Q water, and dried in the laminar flow bench.

3.2.3 *Sample collection and culturing*

Orbulina universa specimens were captured using the blue-water collection method described by Huber et al. (1996) and cultured at the Wrigley Marine Science Center at Catalina Island, California, according to the method outlined in Lea and Spero, (1992). All specimens were fed a single, day-old brine shrimp (*Artemia nauplius*) every two days, and were monitored through daily observation. The foraminifera were cultured at constant temperature (T = 20°C) with a 12hr:12hr light/dark cycle. Specimens were cultured in individual glass vials, which were filled completely with seawater and sealed with Parafilm and tight-fitting lids to minimize CO_2 gas exchange with the atmosphere. To minimize the use of expensive enriched culture solution,

the foraminifera were cultured in 20 mL glass scintillation vials (VWR) during the enriched isotope portion of the day. At all other times, foraminifera were cultured in similarly sealed 120 mL glass jars. One individual was cultured in each jar or vial. At the end of their natural life cycle, after gametogenesis, foraminiferal tests were collected, rinsed in deionized water and stored in micropaleoslides for future analysis.

Table 3.1. Sources and masses of isotope spikes dissolved to create the pure primary spikes used in the creation of the mixed-spike culture solution (YYH). The total mass of each spike solution is the sum of the mass of source dissolved and the mass of the acid used to dissolve the spike.

Spike Designation	**Spiked Isotope**	**Source**	**Compound**	**Mass of source dissolved (g)**	**Mass of acid used to dissolve spike (g)**
YYA	^{6}Li	ORNL (SS) 1803-307A	$^{6}Li_2CO_3$	0.0248	4.132
YYA_1B*	^{6}Li	YYA	-	0.0410	4.122
YYD	^{135}Ba	ORNL #174990	$^{135}BaCO_3$	0.00333	3.066
YYD_B*	^{135}Ba	YYD	-	0.0407	4.119
YYE*	^{43}Ca	TSI #1-04	$^{43}CaCO_3$	0.0415	5.266
YYF*	^{25}Mg	ORNL #158591	^{25}MgO	0.357	11.06
YYG*	^{84}Sr	ORNL (NJ) #163191	$^{84}SrCO_3$	0.000320	2.433

* Designates spikes that were directly used as sources for the YYH spike.

'Day-spiked' foraminifera were transferred from filtered seawater to isotopically-labeled seawater (YYH) at the beginning of each 12-hour light period, and transferred back into filtered seawater at the beginning of each 12-hour dark period. The reverse is true of 'night-spiked' foraminifera, which were transferred into labeled seawater (YYH) at the beginning of each 12-hour dark period, and transferred back into filtered seawater at the beginning of each 12-hour light period. The time taken for the isotope label to be incorporated into calcite is fast in *O. universa*, referenced to Mg/Ca diurnal banding, thus we can assume that each labeled band within the shell represents a period of 12 hours in culture (see Appendix C).

Table 3.2. Composition and measured isotope ratio of the mixed-spike culture solution (YYH).

Primary spike used	Spiked isotope	Mass of primary spike added to YYH (g)	Moles of spiked isotope in YYH	Moles of spiked isotope after addition of seawater	Isotope ratio	Calculated isotope ratio of YYH (R_x)
YYA_1B	^{6}Li	0.9818	1.393E-06	1.987E-06	^{6}Li/^{7}Li	0.272
YYD_B	^{135}Ba	5.748	4.356E-09	1.708E-08	^{135}Ba/^{138}Ba	0.123
YYE	^{43}Ca	4.913	2.945	2.945	^{43}Ca/^{48}Ca	0.800
YYF	^{25}Mg	0.6486	0.000423	0.00324	^{25}Mg/^{24}Mg	0.145
YYG	^{84}Sr	0.07163	1.820E-06	2.091E-06	^{84}Sr/^{88}Sr	0.431

Foraminifera were transferred between culture solutions using glass Pasteur pipettes that had been cut above the taper point and flame annealed to soften the edges. Using this modified pipette it is possible to move foraminifera without damaging their spines, following a procedure like that of Vetter et al., (2013). An individual foraminifer is first taken up by the pipette, then the foraminifer naturally falls to the meniscus of the hanging drop. Briefly touching the surface of the target solution with this drop transfers the foraminifer while minimizing the transfer of the host solution. During transfers, foraminifera are ported into a transfer vial containing the destination solution prior to being transported into the enriched culture solution. A dedicated pipette is used for each step to minimize cross-contamination between isotopically enriched and natural abundance culture solutions. Even if 50 µL of solution were moved into each 20 mL portage vial during transfers, the use of a transfer vial means that the total impact on the isotope ratio of the culture solution on Sr/Ca would be >1‰, which is not significant compared with the observed 2.6% signal.

3.2.4 *Natural abundance foraminifera standard*

A natural abundance solution of dissolved foraminifera was created in order to serve as a consistency standard and to act as the natural abundance end member of synthetic samples. Core

top foraminiferal samples from a variety of species collected from the Ontong Java Plateau (ODP Leg 130, Site 806) were sieved using a 125μm mesh size and cleaned according to the procedure outlined in Barker et al., (2003). After cleaning, a set of samples (pre-cleaning mass = 2.523g) were dissolved in 50 mL 2% HNO_3. The approximate [Ca] of the solution was measured using an iCap RQ Quadrupole ICP-MS and a dissolved calcium external standard and found to be ~2 mM. To replicate the estimated concentration of foraminifera samples in our analyses, the standard was diluted down to a [Ca] concentration of 0.2 mM for analysis, representing a 20 μg foraminiferal sample dissolved in 1 mL of HNO_3. The calibrated isotope ratios of the natural abundance standard are listed in Table 3.6.

3.2.5 *Creation and calibration of isotope dilution spike (XX)*

The isotope dilution spike (XX), which is used to determine the total amount of each element in solution during the multi-spike experiment, was created by A. M. Gothmann using the following spike batches: Oak Ridge National Laboratory (ORNL) 1803-307A Series SS (^{6}Li), ORNL Batch # 217201 (^{25}Mg), ORNL Batch #169191 (^{43}Ca), ORNL Batch # 136990 (^{87}Sr), and ORNL Batch # 142890 (^{135}Ba). All spike compounds except for ^{25}Mg were dissolved in 2% HNO_3. ^{25}Mg was dissolved in concentrated HCl, then dried down and brought back into solution in 2% HNO_3. Due to availability, an ^{87}Sr isotope spike was used rather than an ^{84}Sr spike. The masses of dissolved spike compounds and approximate concentrations are listed in Table 3.3. During spike calibrations, 30 μL of xx-spike were added for every 1 mL of sample. During analyses of foraminiferal samples, 20 μL of a 1:13 dilution of the xx-spike were added for every 550 μL of solution, which contained roughly 10μg of dissolved foraminifer (~0.2 mM [Ca]). This was done in order to achieve an optimal isotope ratio to minimize measurement error.

Table 3.3. Sources and masses of isotope spikes used to create the isotope dilution spike solution (xx-spike).

Spiked Isotope	Batch Number	Compound	Mass of solid spike dissolved (g)	Mass of acid added (g)	Moles of spiked isotope in primary	Mass of solution added to xx-spike (g)
^{6}Li	ORNL (SS) 1803-307A	$^{6}Li_2CO_3$	0.00104	44.962	2.73E-05	0.0809
^{25}Mg	ORNL (RN) #217201	^{25}MgO	0.00652	40.492	1.57E-04	11.044
^{43}Ca	ORNL (NX) #169191	$^{43}CaCO_3$	0.0167	21.088	1.40E-04	12.998
^{87}Sr	ORNL (LH) #136990	$^{84}SrCO_3$	0.0127	3.062	7.85E-05	1.914
^{135}Ba	ORNL (LV) #142890	$^{135}BaCO_3$	0.00443	5.069	2.10E-05	0.0135

3.2.6 *Re-creation of culture spike (X') for method testing*

A second isotope spike solution (X') was made to serve as the spiked endmember during the creation of synthetic samples. In order to ensure that our synthetic samples were of a similar composition as the foraminifera analyzed in this study, the isotopic composition of the spiked endmember was adjusted to be as close to that of the culture solution (X) as possible. The same dissolved spikes as in the isotope dilution (XX) spike (Table 3.3) were used to create the X' spike solution, with the exception of the ^{84}Sr spike, which was dissolved from ORNL Series NJ Batch # 163191. Because the culture solution was less isotopically enriched than the isotope dilution spike because it was mixed with seawater, it was necessary to dilute each of the dissolved spike primaries used in the isotope dilution spike, in order to create spiked solutions with isotopic compositions close to that of the culture solution. To do this, the isotope ratio of each spike primary was adjusted using High Purity Standards (HPS), which were found during spike calibration to be at natural abundance for the isotopes of interest. The target ratio of enriched isotope to unenriched isotope was calculated by using the isotope dilution equation:

$$n_o = n_x \frac{R_x - R_m}{R_m - R_o} * \frac{A_x}{A_o} \quad (3.5)$$

where n_o = moles of the element of interest in the natural analyte (HPS), n_x = moles of the element of interest in the enriched analyte (spike primary); R_x = isotope ratio of the enriched analyte (spike primary); R_o = isotope ratio of the natural analyte (HPS); R_m = target isotope ratio, or the calculated isotope ratio of the culture spike; A_x = isotope abundance of the reference isotope in the enriched analyte; and A_o = isotope abundance of the reference isotope in the natural analyte.

Rearranging the equation to solve for n_x/n_o we obtain the target mixing ratio of enriched isotope to unenriched isotope in order to achieve a solution with the same isotopic composition as YYH:

$$\frac{n_x}{n_o} = \frac{R_m - R_o}{R_x - R_m} * \frac{A_o}{A_x} \tag{3.6}$$

In order to use this solution for method testing, it was necessary to match the concentration of the solution to the expected concentration of each element of interest in *O. universa* (Hönisch et al., 2011; Allen et al., 2016), assuming that [Ca] = 0.2 mM to represent 20µg of $CaCO_3$ dissolved in 1mL of HNO_3. This results in a solution with the same isotope ratio as the culture solution, with a concentration equivalent to the spiked portion of a foraminifer. The concentrations used were as follows: [Li] = 1.33 nM, [Mg] = 3.76 µM, [Sr] = 0.272 µM, and [Ba] = 0.120 nM, with Mg/Ca being twice as high as the average value of 8 mmol/mol to represent the increase of Mg in a high Mg/Ca night band. The number of moles from each primary to add to the solution (n_x) was then calculated by using the above equation and using the concentrations of HPS to calculate n_o. Isotope ratios for the x' solution and the final concentrations of the natural isotope in solution are listed in Table 3.5.

3.2.7 *Spike calibration*

All isotope spikes were calibrated prior to use in this experiment, because the mixed-spike method requires us to know the isotopic composition of all spikes prior to measurement. Isotope standards (see Appendix C) were used for calibration, and the isotope ratios of all spikes were compared to these standards. The coral standard JCp-1 was used as an isotope standard for the following ratios: $^{6}Li/^{7}Li$ (Huang et al., 2010), $^{25}Mg/^{24}Mg$ (Wombacher et al., 2011) and $^{87}Sr/^{86}Sr$ (Krabbenhöft et al., 2009). JCp-1 was also used as an isotopic standard for $^{135}Ba/^{138}Ba$, however, because of the lack of absolute isotopic standards for Ba, JCp-1 was assumed to have a $^{135}Ba/^{138}Ba$ equal to natural abundance ($^{135}Ba/^{138}Ba = 0.0919$). SRM 915a was used as an isotope standard for $^{43}Ca/^{48}Ca$ (Russell et al., 1978; DePaolo, 2004) in the calibration of the XX-spike. For the calibration of the X'-spike, JCp-1 was used as an isotopic standard for Ca. The $^{43}Ca/^{48}Ca$ ratio of JCp-1 was measured during calibration of the XX-spike and found to be 0.712. The Sr isotope standard NIST SRM 987 and the Mg isotope standard DSM-3 were also measured and used to check the accuracy of obtained Me/Ca ratios. The concentration of the natural reference isotope in the isotope spike was calculated using reverse isotope dilution with the equation:

$$[C]_n = [C]_x * \left(\frac{A_x m_x}{A_n m_n}\right)\left[\frac{R_x - R_m}{R_m - R_n}\right] \quad (3.7)$$

where $[C]_n$ refers to the concentration of C in the natural standard; $[C]_x$ refers to the concentration of C in the enriched sample; A_x refers to the abundance of the natural isotope in the enriched sample; A_n refers to the abundance of the natural isotope in the natural sample; m_x refers to the mass of the enriched sample; m_n refers to the mass of the natural sample; R_x refers to the isotope ratio of the enriched sample; R_n refers to the isotope ratio of the natural sample; and R_m refers to the measured isotopic ratio of the mixed sample.

Using values obtained from spike calibration, we solved for the concentration of the natural isotope in the isotope spike by rearranging the equation to solve for $[C]_x * A_x$, as follows:

$$[C]_x * A_x = [C]_n * \left(\frac{A_n m_n}{m_x}\right)\left[\frac{R_m - R_n}{R_x - R_m}\right] \quad (3.8)$$

High Purity Standards (HPS) were used as the natural abundance standard for the reverse isotope dilution equation. The concentration of HPS ($[C]_n$) was obtained by recording the weight of acid (2% HNO_3) added to standard during serial dilution. HPS standards were kept at a concentration roughly equal to the concentration expected for foraminiferal samples (Hönisch et al., 2011; Allen et al., 2016). V_x and V_n were obtained by weight, using a Sartorius MSA6.6S0TRDM Cubis Micro Balance. The isotope ratio of HPS was calibrated using the same procedure used to calibrate the x' spike and xx spike, and was found to be at natural abundance for all isotopes of interest. Tables 4 and 5 lists all calibrated isotope ratios and concentrations.

Table 3.4. Calibrated isotope ratios of the isotope dilution spike (xx).

Isotope Ratio	**Isotope Standard**	**Isotope ratio of standard**	**Isotope ratio of xx-spike**	**Isotope ratio of natural standard**	**Natural isotope**	**Concentration of natural isotope in xx-spike (mmol/kg)**
$^{6}Li/^{7}Li$	JCp-1	0.0838	16.24	0.0859	^{7}Li	1.56E-05
$^{25}Mg/^{24}Mg$	JCp-1	0.127	90.80	0.127	^{24}Mg	2.66E-03
$^{43}Ca/^{48}Ca$	SRM	0.731	899.00	0.731	^{48}Ca	5.27E-04
$^{87}Sr/^{86}Sr$	JCp-1	0.709	55.25	0.705	^{86}Sr	5.30E-03
$^{135}Ba/^{138}Ba$	JCp-1*	0.0919	6.53	0.0919	^{138}Ba	8.46E-05

* Assumed natural abundance

Table 3.5. Calibrated isotope ratios of the recreated culture solution (x').

Isotope Ratio	Isotope Standard	Isotope ratio of JCp-1	Isotope ratio of x'-spike	Isotope ratio of HPS	Natural isotope	Concentration of natural isotope in x'-spike (mmol/kg)
$^{6}Li/^{7}Li$	JCp-1	0.0838	0.2368	0.0836	^{7}Li	1.07E-05
$^{25}Mg/^{24}Mg$	JCp-1	0.127	0.1453	0.127	^{24}Mg	3.21E-02
$^{43}Ca/^{48}Ca$	JCp-1	0.712	6.667	0.714	^{48}Ca	3.90E-03
$^{84}Sr/^{86}Sr$	JCp-1	0.0565	0.2575	0.0581	^{86}Sr	5.37E-04
$^{135}Ba/^{138}Ba$	JCp-1*	0.0919	0.09872	0.0916	^{138}Ba	8.28E-06

* Assumed natural abundance

Table 3.6. Calibrated isotope ratios of the natural abundance standard.

Isotope Ratio	Isotope Standard	Isotope ratio of JCp-1	Isotope ratio of natural abundance standard
$^{6}Li/^{7}Li$	JCp-1	0.0838	0.0825
$^{25}Mg/^{24}Mg$	JCp-1	0.127	0.128
$^{43}Ca/^{48}Ca$	JCp-1	0.712	0.707
$^{84}Sr/^{86}Sr$	JCp-1	0.0565	0.0567
$^{135}Ba/^{138}Ba$	JCp-1*	0.0919	0.0922

* Assumed natural abundance

3.2.8 *ICP-MS analysis*

Analyses of all samples were conducted using a ThermoScientific Element-2 ICP-MS. Prior to analysis, foraminiferal shells were fractured into two halves using a scalpel. Half of the shell (roughly 20µg) was subjected to an oxidative cleaning step prior to analysis, to remove excess organic material. Fragments were cleaned in individual 1 mL micro-centrifuge vials, which had previously been boiled in 10% Trace-Metal Grade HCl for 1-2 hours. After this step, vials were rinsed in MilliQ water and dried in a trace-metal clean laminar flow-bench. During cleaning, fragments were heated at 65°C for 10 minutes in a 500µL 1:1 solution of 30% H_2O_2 and 0.1 M NaOH. Following this, fragments were rinsed 3 times in 0.1 M NaOH and once in MilliQ water, and then immediately transferred to a second vial for dissolution. Fragments were

dissolved in 2% HNO_3 for analysis. The remaining half of the foraminifer was set aside for NanoSIMS imaging.

Each foraminiferal sample represents a small amount of material (20 µg of material in 1 mL of 2% HNO_3), which is then divided into two samples in order to obtain values for both F, the mixing ratio between labeled and unlabeled calcite, and T, the total Me/Ca of the shell. In order to perform analyses on these small samples, an ESI microFast autosampler and low-flow nebulizer were used to inject sample at a rate of 20 µL/min. Each measurement consisted of 270 µL of sample. A Jet sample cone (Ni) and X-skimmer cone (Ni) were used for this analysis. The following isotopes of each element were measured: ^{6}Li, ^{7}Li, ^{24}Mg, ^{25}Mg, ^{26}Mg, ^{43}Ca, $^{87}Sr^{++}$, ^{48}Ca, ^{83}Kr, ^{84}Sr, ^{85}Rb, ^{86}Sr, ^{87}Sr, ^{135}Ba, ^{137}Ba, and ^{138}Ba.

Because this represents a wide range of masses, measuring each of these isotopes using a single method file would result in multiple magnet hops between masses for each measurement. For example, to measure ^{6}Li. ^{7}Li, ^{24}Mg, ^{25}Mg, and ^{26}Mg, the magnet would first settle on ^{6}Li and ^{7}Li until data is collected, then 'hop' to the mass range of Mg to measure ^{24}Mg, ^{25}Mg, and ^{26}Mg. The magnet would then return to ^{6}Li and begin measurements again. This would continue until the number of cycles specified by the method is complete. However, magnet hops across this mass range represent a potential source of error, as plasma conditions may have changed in the time taken by the magnet to return to a single isotope. Thus, in order to minimize magnet hopping, we instead collect data sequentially, using a separate method file for each mass range. This means that rather than the situation described above, the magnet would instead first settle on ^{6}Li and collect all of the required data for Li isotopes without ever shifting mass, instead using E-scan, which changes the acceleration voltage. Only after all data has been collected for Li for a particular sample does the magnet 'hop' to a different mass and begin collecting data for all

isotopes of interest. This approach has another advantage, as it allows us to optimize each collection method for the element of interest, increasing the number of cycles of data collection for elements such as Li and Ba, which have low concentrations in foraminiferal calcite.

To correct for the doubly charged $^{86}Sr^{++}$ peak, which is an interference on ^{43}Ca that cannot be optically resolved, we also measure $^{87}Sr^{++}$. This peak can be found at mass 43.5, and can be measured in the same method as ^{43}Ca and ^{48}Ca. If we assume that $^{86}Sr^{++}$ and $^{87}Sr^{++}$ are being produced at the same rate, the ratio of $^{87}Sr^{++}/^{86}Sr^{++}$ should be the same as the ratio of $^{87}Sr/^{86}Sr$. Thus, by using the $^{87}Sr/^{86}Sr$ ratio of the same sample, a correction for $^{86}Sr^{++}$ can be applied. A similar correction is also applied for ^{84}Kr, which is an interference on the ^{84}Sr peak. By measuring ^{83}Kr and making the assumption that the $^{83}Kr/^{84}Kr$ ratio is equal to natural abundance (0.202), it is possible to correct for the ^{84}Kr interference.

Isotopes of Li, Ca, Sr, and Ba were measured in low resolution in all samples except seawater samples ($M/\Delta M$ = ~250). Mg isotopes were measured in medium resolution ($M/\Delta M$ = ~4000) for all samples, because of the interference of the NaH^+ peak on the ^{24}Mg peak. At medium resolution, the NaH^+ peak can be optically resolved and is distinct from the ^{24}Mg peak. Ca and Sr isotopes were measured for 400 cycles during each measurement. Because increasing the resolution also increases measurement time, Mg was only measured for 150 cycles. Due to the small amounts of Li and Ba in foraminifera (~6μmol Li/mol Ca and ~0.6μmol Ba/mol Ca respectively), Li and Ba were analyzed for longer, with Li analyzed for 4000 cycles and Ba analyzed for 1000 cycles. Five data points were collected from a region representing 10% of the center of the flat-topped low resolution peak during each cycle for each isotope of interest. In medium resolution, the entire peak was collected once per cycle for each isotope of interest with a mass window around the peak of 300%. Data across the entire peak was collected during post-

processing, which typically amounted to 25 data points. The total collection time for each data point per cycle was 10ms, with a settling time of 1ms.

For all seawater samples, including YYH, Ca isotope ratios were measured at medium resolution, due to an interference of $^{32}S^{16}O$ on the ^{48}Ca peak, which is optically resolvable in medium resolution. All other isotopes were measured using the same resolution as in carbonate samples. Seawater also has a significantly higher concentration of Rb than carbonate samples, which becomes an issue because one of the two stable isotopes of Rb, ^{87}Rb, is an interference on the ^{87}Sr peak. This interference cannot be optically resolved in medium resolution. Thus, to correct for ^{87}Rb interference, we collect measurements of ^{85}Rb. Using the natural abundance ratio of $^{87}Rb/^{85}Rb$ (0.386), and by assuming that the ^{87}Rb concentration of seawater is at natural abundance, we can correct for the influence of ^{87}Rb on the ^{87}Sr peak. Sample runs were conducted using standard-sample bracketing, with 5-6 samples bracketed by JCp-1 (see Appendix C). To ensure internal consistency among the isotope ratios required for the multi-spike method (R_o, R_x, R_{xx}, R_m, R_{ID}), measurements were taken of these ratios during every run. A dissolved foraminifer that had been cultured at constant temperature in natural abundance filtered seawater was used to measure R_o. R_m resulted from the direct measurement of each dissolved foraminifera sample, whereas R_{ID} resulted from the measurement of a dissolved foraminifera sample spiked with 20μL of a 1:13 dilution of the isotope dilution spike. R_x was calculated by measuring an aliquot of the culture solution (YYH, 1:1000 dilution) collected before the start of the culture experiment. The natural abundance consistency standard was also measured during each analysis. Each solution yielded two replicate measurements.

Instrumental mass fractionation (IMF) occurs because isotope ratios measured by ICP-MS are enriched in the heavier isotope with respect to the true isotope composition of the

sample. The magnitude of IMF can be estimated and corrected for by an isotopic standard, however, IMF changes with time. To correct for this drift, only the standards that bracket each sample are used to correct the isotope ratio of that sample. This ensures that standard and sample are experiencing the same amount of drift. Long-term reproducibility of standards was monitored by comparing isotopic ratios measured on a calibrated IMF-standard using JCp-1. Results from this analysis are shown in Figures 3.1 and 3.2.

Measurements are also subject to some amount of internal error, which reflects the precision by which the instrument can measure each isotope. One source of internal error is the theoretical limit of Poisson counting statistics. Counting statistics defines the smallest possible internal error for any given measurement, as $\sigma^2_x = x$, where x equals the number of counts from each measurement. This can be converted into relative error, such that:

$$\sigma_x^{rel} = \frac{1}{\sqrt{x}} \tag{3.9}$$

Equation 3.9 represents the theoretical internal error due to counting statistics. The actual relative internal error of each measurement can also be determined, by dividing the mean intensity of each element by the standard deviation of that mean. Typical ion intensities for the natural reference isotope of each element in foraminiferal samples, along with typical magnitudes of IMF and both theoretical and measured internal error are described in Table 3.7. Measured internal error will always be larger than the theoretical internal error, as the theoretical internal error represents the error only due to counting statistics, or the smallest possible error over the course of the run.

Synthetic samples were run in the same way as foraminiferal samples, with each solution treated as a mixed sample (R_m), and X' (Table 3.5) treated as R_x. Although the isotope ratios of the natural abundance standard, the isotope dilution spike, and X' were all previously calibrated,

they were measured concurrently with the samples together with a suite of isotopic standards, to ensure that corrections for any day-to-day instrumental variation is internally consistent for all isotope ratios. R_{ID} values were obtained by performing an isotope dilution where 30μL of the xx-spike was added to 1mL of R_m solution and then measured. The isotope dilution spike (XX) was also analyzed during each instrumental run to yield $R_{xx,}$ which was compared to the calibrated values (Table 3.4) to ensure that this measurement was accurate within uncertainty.

Table 3.7. Typical ion intensities for the natural reference isotopes of foraminiferal standards, along with typical internal error and instrumental mass fractionation.

Reference isotope	**Intensity (counts)**	**Isotope ratio**	**Measured internal error (‰)**	**Theoretical internal error (‰)**	**IMF (‰)**
^{7}Li	500	$^{6}Li/^{7}Li$	80	10	150
^{24}Mg	50000	$^{25}Mg/^{24}Mg$	25	2	50
^{48}Ca	500000	$^{43}Ca/^{48}Ca$	7	<1	125
^{86}Sr	100000	$^{84}Sr/^{86}Sr$	10	1	50
		$^{87}Sr/^{86}Sr$	8	2	25
^{138}Ba	5000	$^{135}Ba/^{138}Ba$	20	5	20

The final isotope ratio for each solution was calculated using a custom MATLAB script, which calculated the average intensity of each peak (counts/cycle) for Mg, Ca, Sr, and Ba. Because of the low number of counts of Li, the 4000 Li cycles measured were divided into eight blocks of 500 cycles each. ^{6}Li and ^{7}Li counts were summed within each block, and then the summed intensities in each block were averaged to yield the final $^{6}Li/^{7}Li$ ratio. This procedure was adapted from work done to reduce bias in SIMS, where bias was shown to decrease when the estimated ratio results from the sum of all counts in the numerator isotope divided by the sum of all counts in the denominator isotope, rather than the average of all ratios collected (Ogliore et al., 2011).

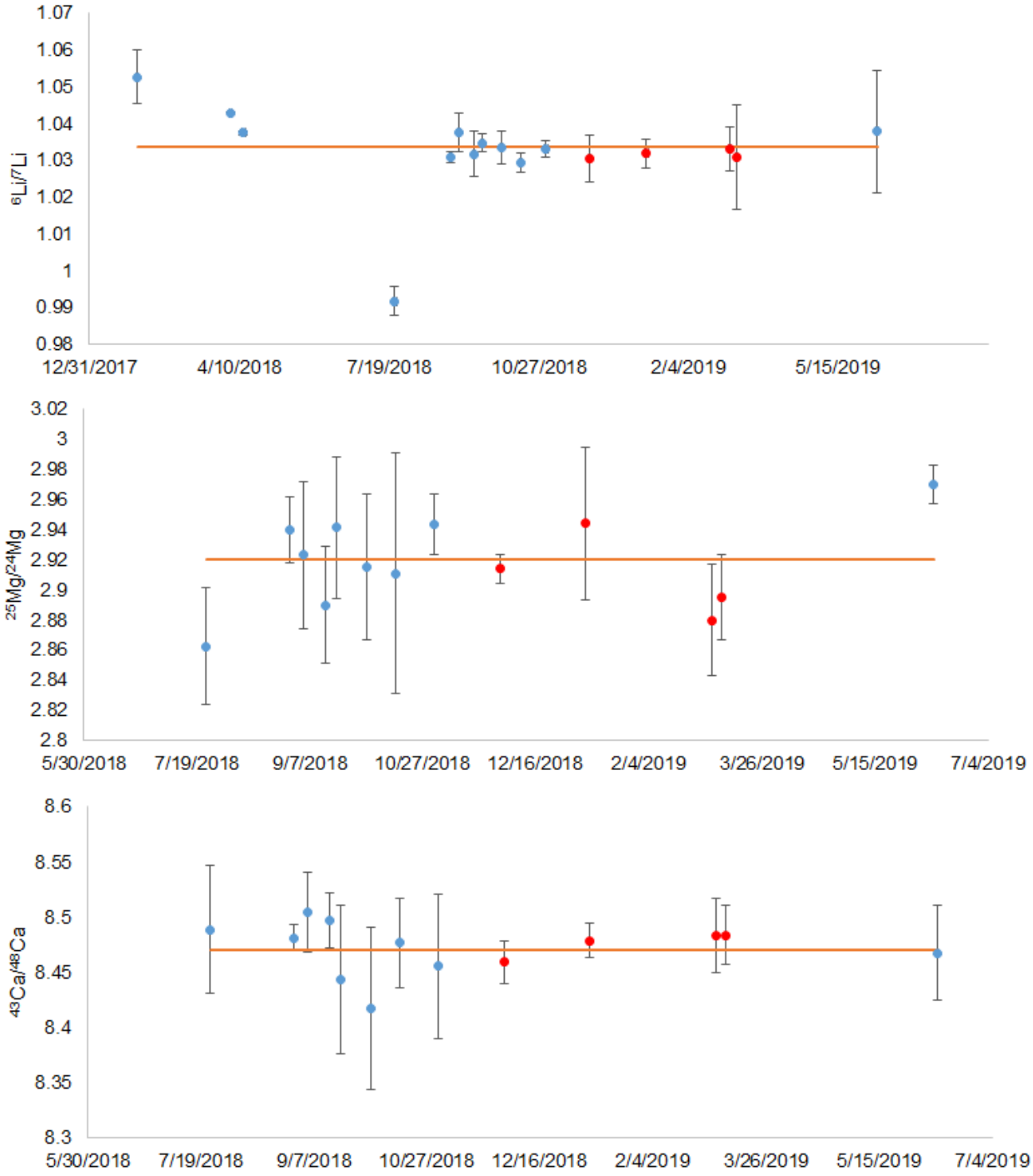

Figure 3.1. Measurements of a single IMF-standard (XG) over the course of all experimental runs for $^{6}Li/^{7}Li$, $^{25}Mg/^{24}Mg$, and $^{43}Ca/^{48}Ca$. Orange line represents the calibrated isotope ratio of the standard. Each point represents the measured value of the standard at each given date. Error bars represent one standard deviation. Red data points represent runs during which foraminiferal samples were analyzed.

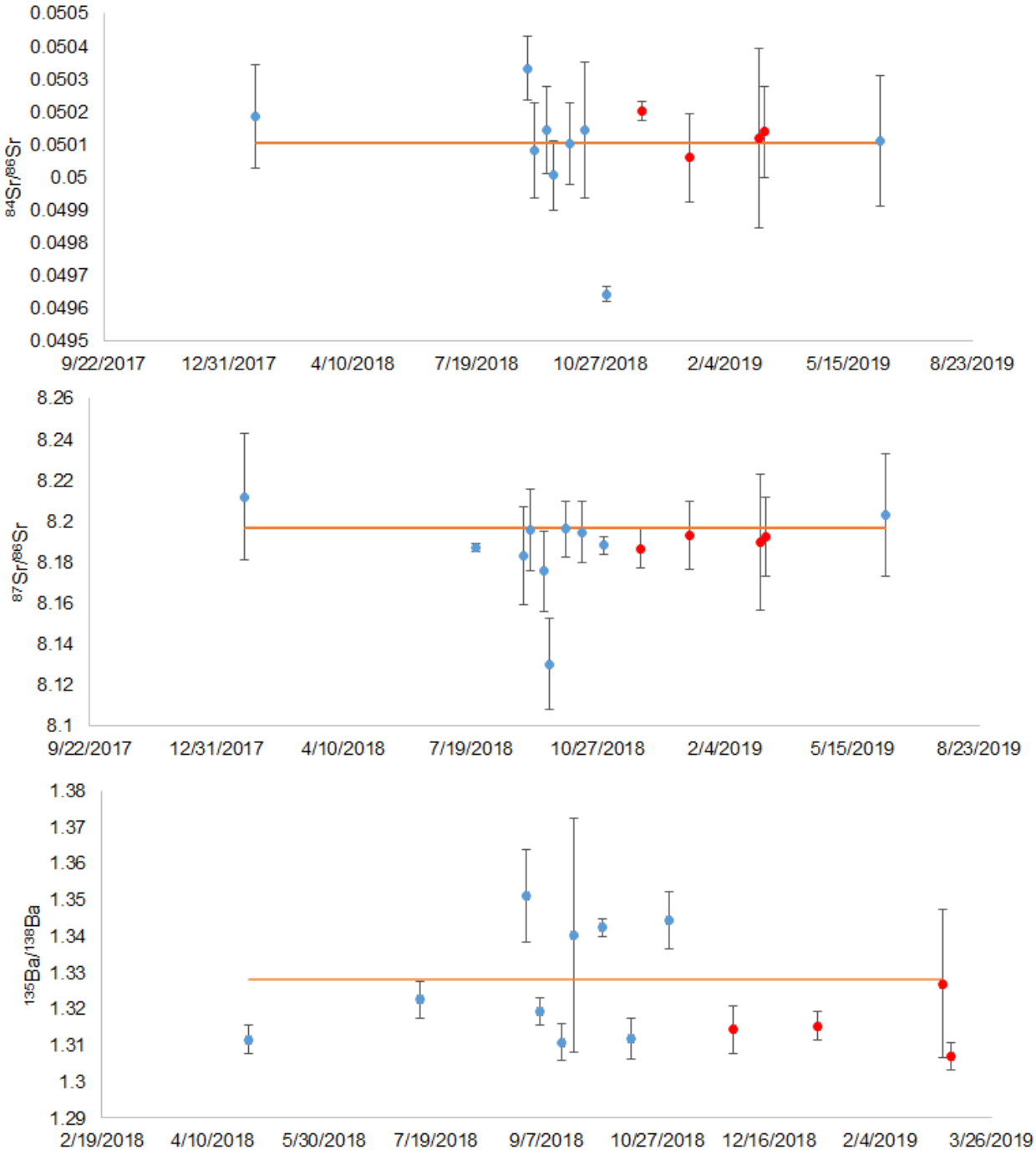

Figure 3.2. Measurements of a single IMF-standard (XG) over the course of all experimental runs for $^{84}Sr/^{86}Sr$, $^{87}Sr/^{86}Sr$, and $^{135}Ba/^{138}Ba$. Orange line represents the calibrated isotope ratio of the standard. Each point represents the measured value of the standard at each given date. Error bars represent one standard deviation. Red data points represent runs during which foraminiferal samples were analyzed.

3.2.9 *NanoSIMS imaging*

NanoSIMS imaging was conducted primarily by A. C. Gagnon on select samples in order to examine the detailed pattern of banding across a cross-section of an individual. NanoSIMS imaging allows the user to obtain images of multiple elements and isotopes at once, allowing us to determine whether the appropriate region was labeled with all isotopes of interest. Also, by focusing the beam on a smaller area of the shell, within a labeled portion, Mg/Ca ratios can be obtained through spot analysis. The Mg/Ca ratios obtained using NanoSIMS can then be compared with Mg/Ca ratios obtained through the multi-isotope method, to ensure consistency between analysis methods.

Samples for NanoSIMS imaging were cleaned using a similar oxidative cleaning step as samples processed using ICP-MS. However, after cleaning, samples fixed in Araldite-502 epoxy resin for analysis rather than dissolved. The mounted samples were then polished using a series of progressively smaller diamond grit sizes, ranging from 15µm to 0.125µm.

NanoSIMS images were obtained using a similar analysis method as in Gagnon et al., (2013). Briefly, samples were imaged using a 5pA primary beam (800nm O^- beam size), which was rastered over a 20µm x 20µm area during image collection to spread power evenly. During spot analysis, the primary beam was rastered over a 1µm x 1µm surface area. To limit edge effects, counts were collected within the inner 90% of the rastered area. Prior to analysis, areas of interest were pre-sputtered for several to tens of minutes using a primary beam with approximately twice the probe current as that used in analysis. Seven secondary electron multiplier detectors were arranged to monitor various isotopes of magnesium and calcium, and sputtered ions were collected in these detectors. Typical mass resolving power (MRP) was found

to be 10,000 M/ΔM (5%-95% peak-edge definition). This MRP is sufficient to distinguish $^{23}NaH^{+}$ from $^{24}Mg^{+}$.

Mg/Ca ratios were standardized using a suite of known calcite standards (Gabitov et al., 2013), including Blue Calcite (BCC, Mg/Ca = 3.75), LAS-20 Calcite (LAS-20, Mg/Ca = 45.3), Rensselaer Polytechnic Calcite (RPI, Mg/Ca = 0.396), and UC Irvine Calcite (UCI, Mg/Ca = 3.446). Due to differences in pre-sputter dose and source brightness between analytical sessions, new calibration curves were constructed during each session or when source brightness changed by more than a few percent. All other Me/Ca ratios (Sr/Ca, Li/Ca, and Ba/Ca) could not be imaged with high precision using NanoSIMS.

3.3 RESULTS

3.3.1 *Analysis of synthetic samples to test the precision of the multi-spike method*

Prior to this study, the mixed-spike method was an unproven tool that had only been developed theoretically. To evaluate the method, assess the real-world precision, and to quantify whether calculated Me/Ca ratios are affected by the percentage of labeled calcite in each sample, a set of synthetic samples were analyzed. The synthetic samples were made by mixing two dissolved standards, an isotopically enriched standard (X') designed to simulate the labeled portion of a cultured foraminifera, and a natural abundance foraminiferal consistency standard designed to simulate the rest of the unlabeled skeleton. If the method works as expected, then the mixed spike method should return the same Me/Ca ratio for any combination of these two standards, with the scatter around this constant value representing methodological precision.

Five (5) gravimetric solutions were created, each composed of a different ratio of the standards: 10X (10% X', 90% natural abundance consistency standard), 25X (25% X', 75% consistency standard), 50X (50% X', 50% consistency standard), 65X (65% X', 35% consistency

standard), and 80X (80% X', 20% consistency standard). While we do not expect foraminiferal samples to be more than 30-40% labeled, we examined the higher percentages to determine the behavior of the method under a range of conditions. Although the exact weights of these mixtures were recorded, this information was not used during subsequent analysis. Instead the synthetic dissolved foraminifera were analyzed using the mixed spike technique as if they were unknown samples. ICP-MS analyses were conducted at concentrations corresponding to those expected from foraminifera samples (roughly 1/4 of a test per sample, which corresponds to ~10 µg of $CaCO_3$ in 550 µL of 2% HNO_3, per analysis). Synthetic samples were analyzed using the same procedure as foraminiferal samples.

This experiment was designed as a precision test rather than an assessment of accuracy, so a foraminifera standard of uncalibrated composition was used and the absolute isotopic abundances of X' were also uncalibrated. The absolute isotopic abundances of X' were estimated from the mass of each primary isotope spike component. Errors in these estimates affect accuracy but not precision.

The results of this test are shown in Figure 3.3. Across the five different solutions Sr/Ca values are within 0.8% of each other (1 standard deviation). Mg/Ca and Li/Ca values are also resolvable with good precision, with Mg/Ca values being within 6.4% of each other and Li/Ca values being within 4.7%. Precision errors are large for Ba/Ca (32%). Precision errors are larger for samples with lower levels of isotope enrichment, and typically decrease as isotope enrichment increases, consistent with the analytical error models developed in Gagnon et al. (2012). The precision of this method provides an indication of the minimum signal that we can expect to resolve in our foraminiferal samples. Thus, we can expect to recover any change in Sr/Ca larger than 0.8%.

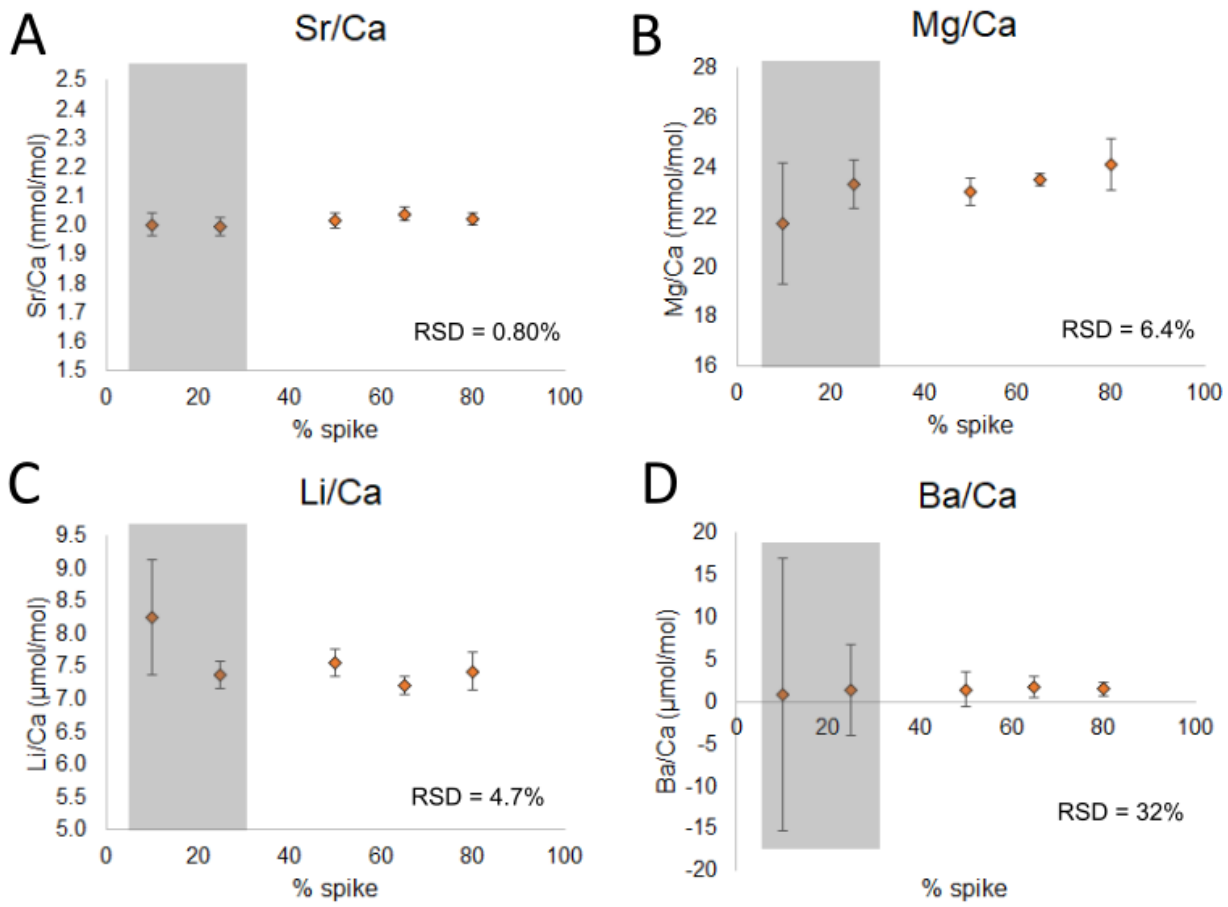

Figure 3.3. Results of the multi-spike method test. A) Sr/Ca ratios, B) Mg/Ca ratios, C) Li/Ca ratios, D) Ba/Ca ratios. Shaded areas reflect the level of enrichment observed for foraminiferal samples.

3.3.2 *Sources of methodological error in the mixed-spike technique*

The high precision of Sr/Ca values (0.8%) demonstrates that the multi-isotope spike technique can measure small variations in Sr/Ca. Li/Ca values are measurable within 4.7% of each other, thus, any change in Li/Ca between day and night will be visible if the change is greater than 4.7%. Error in Mg/Ca is larger (6.4%), however, this error is relatively small when compared to the natural variability of Mg/Ca in *O. universa*. In addition, Mg/Ca is measurable using techniques such as NanoSIMS, allowing for an external verification of foraminiferal Mg/Ca. The large precision error in Ba/Ca (>30%) likely results from a combination of the low

amount of Ba in foraminifera calcite and the relatively small amount of enrichment in this element from the isotope spike. Thus, although we measure Ba/Ca in our samples and those results are reported, they should be treated with caution.

The method appears sensitive to both the value and uncertainty of R_o, especially in the case of Sr/Ca. This is likely because the denominator of the term used to calculate ^{86}F is calculated as $R_o - R_m$. At lower levels of enrichment (10% and 25%) when R_o is close to R_m, small variations in R_o can cause large variations in ^{86}F, and thus, in the final Sr/Ca value. To mitigate this, we measure R_o within the same run as other parameters, to prevent day-to-day instrumental variations from affecting final results. In all samples of cultured foraminifera, R_o measurements were taken from dissolved *O. universa* that were also captured at and cultured at Catalina Island at the same temperature as our labeled foraminifera.

This observation, that error is amplified both at lower concentrations of spike in the culture solution and at lower percentages of labeled to unlabeled calcite, is consistent with the prediction of Gagnon et al., (2012), which states that error should increase as enrichment levels decrease. Although it is difficult to control the percentage of labeled calcite in each foraminifer, higher levels of enrichment in the spiked culture solution will likely improve the precision of this method, particularly in the case of Ba/Ca. The spiked culture solution (YYH, Table 3.2) is shown to be more isotopically enriched in ^{25}Mg and ^{135}Ba than X' which was used to test the method. Based on the estimates in Gagnon et al., (2012), this would result in an improvement of analytical error from >2.0% at the fraction of labeled calcite expected for foraminifera, to ~0.4% in foraminiferal samples, similar to all other isotope ratios. This error is smaller than the actual variability between samples, which may be reflecting individual variability.

3.3.3 *Me/Ca ratios of day/night samples*

In total, seven (7) day-spiked individuals and seven (7) night-spiked individuals were measured (Figure 3.4, Tables 3.8 and 3.9). The means of Sr/Ca measurements show a slight difference between day and night bands, with day Sr/Ca (1.27 ±0.03 mmol/mol) being 2.6% lower than night Sr/Ca (1.31 ±0.02 mmol/mol). Li/Ca shows a distinct difference between day and night, with mean day Li/Ca (10.42 ±1.60 μmol/mol) being 37% higher than mean night Li/Ca (7.60 ±1.09 μmol/mol). This trend is larger than our observed error in Li/Ca measurements during the test of the method (RSD = 4.7%), and is also larger than individual variability in Li/Ca between foraminiferal samples (RSD = ~15%). The means of Mg/Ca measurements showed a strong difference between day and night, with mean day Mg/Ca (3.62 ±0.58 mmol/mol) being as much as 54% lower than mean night Mg/Ca (7.88 ±0.86 mmol/mol). Ba/Ca ratios show no significant difference between day and night. However, because of the high error associated with Ba/Ca measurements of synthetic samples during the method test (RSD = 32%), and a high amount of individual variability between foraminiferal samples (RSD = 27% for day-spiked foraminifera and RSD = 35% for night-spiked foraminifera), this observation should be treated with caution. The percentage of calcite labeled (1/(F+1)) is approximately 25 ± 10% for day-spiked samples and 17 ± 6% for night-spiked samples.

A statistical analysis was conducted using a custom MATLAB script to test whether the observed mean Me/Ca ratios corresponding to day calcite and night calcite could have come from the same population, or whether these means indicate that day and night calcite are distinct because they come from different statistical populations. For this test, the null hypothesis is that the day and night calcite measurements come from the same population, so that the observed differences in mean between these two categories occurs only because of random variability.

This test is analogous to a one-tailed t-test, which, when performed on our data, suggests that the difference in means for Mg/Ca is significant at the 99% level of confidence (p = 0.00075), the difference in means for Li/Ca is significant at the 90% level of confidence (p = 0.086) and the difference in means for Sr/Ca is significant at the 80% level of confidence (p = 0.16). When the non-parametric Mann-Whitney U test (one-tailed) is used instead of the t-test because of our small sample size, we observe the same levels of significance for Mg/Ca (99% C.I.), and Li/Ca (90% C.I.). Sr/Ca was observed to not be significant at the 90% level of confidence, which is the lowest level of confidence we were able to test using the one-tailed Mann-Whitney U test.

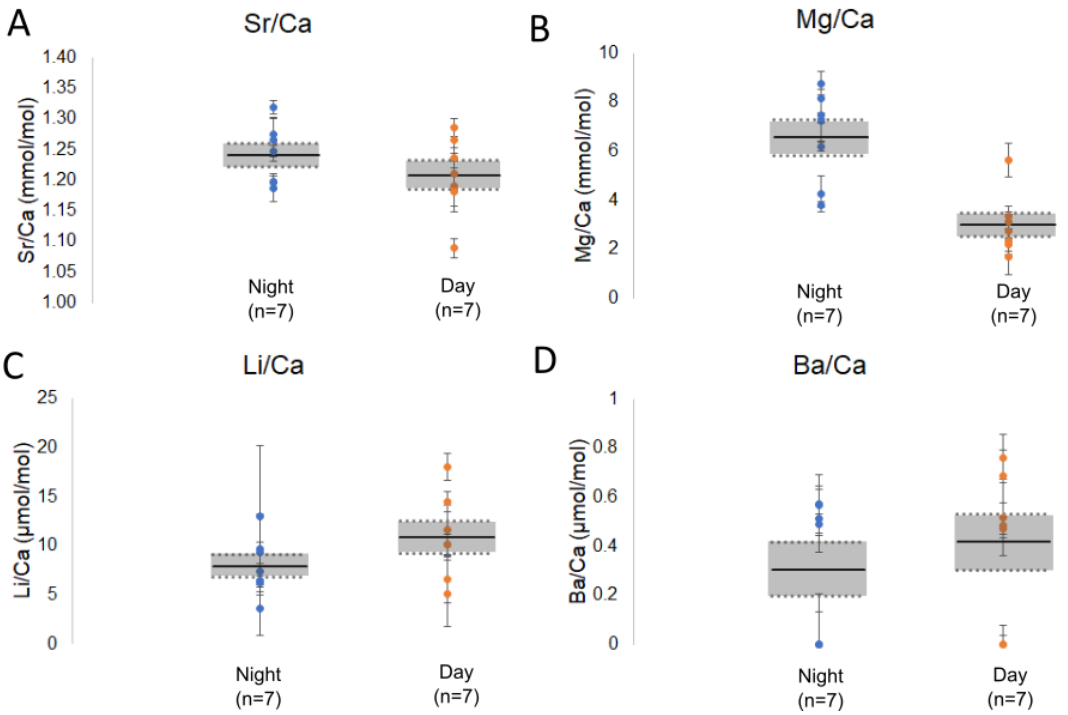

Figure 3.4. Me/Ca ratios of day (n=7) and night (n=7) foraminiferal samples. A) Sr/Ca ratios, with night Sr/Ca 2.6% higher than day Sr/Ca. B) Mg/Ca ratios, with day Mg/Ca ratios 54% lower than night Mg/Ca. C) Li/Ca ratios, with day Li/Ca ratios 37% higher than night Li/Ca. D) Ba/Ca ratios, with no significant difference between day and night. Error bars for Ba/Ca are cut off at zero. Solid lines refer to the means of each group. Shaded areas and dashed lines mark the standard error of the mean. Error bars reflect uncertainty in each individual measurement, as calculated using the procedure outlined in Gagnon et al., (2012).

Table 3.8. Me/Ca ratios of labeled calcite from individual day-spiked foraminifera. Uncertainties represent estimated error within a single sample, based on two replicate measurements (Gagnon et al., 2012). Errors are comparable to the level of uncertainty between each replicate measurement.

Foram #	**Li/Ca** (μmol/mol)	**Mg/Ca** (mmol/mol)	**Sr/Ca** (mmol/mol)	**Ba/Ca** (μmol/mol)
401	13.9 ±1.0	3.13 ±0.28	1.21 ±0.02	0.94 ±0.07
407	9.73 ±1.30	2.18 ±0.28	1.29 ±0.01	0.66 ±0.10
413	17.3 ±1.4	5.63 ±0.68	1.19 ±0.04	0.99 ±0.03
519	11.1 ±2.5	3.34 ±0.19	1.27 ±0.02	0.45 ±0.04
524	4.91 ±3.24	2.35 ±1.19	1.09 ±0.02	0.49 ±0.15
531	9.73 ±0.99	2.76 ±0.34	1.24 ±0.02	0.73 ±0.10
533	6.30 ±2.29	1.70 ±0.06	1.18 ±0.02	0.47 ±0.04

Table 3.9. Me/Ca ratios of labeled calcite from individual night-spiked foraminifera. Uncertainties represent estimated error within a single sample, based on two replicate measurements (Gagnon et al., 2012). Errors are comparable to the level of uncertainty between each replicate measurement.

Foram #	**Li/Ca** (μmol/mol)	**Mg/Ca** (mmol/mol)	**Sr/Ca** (mmol/mol)	**Ba/Ca** (μmol/mol)
311	3.47 ±2.63	7.23 ±0.11	1.27 ±0.03	0.55 ±0.06
312	9.28 ±3.34	8.15 ±0.58	1.20 ±0.01	0.92 ±0.12
325	6.15 ±0.43	4.27 ±0.74	1.20 ±0.01	0.54 ±0.06
331	5.94 ±1.20	3.82 ±0.10	1.19 ±0.02	0.47 ±0.04
431	8.88 ±1.05	7.47 ±1.07	1.25 ±0.01	1.06 ±0.20
518	7.04 ±1.94	8.76 ±0.48	1.32 ±0.01	0.90 ±0.20
520	12.5 ±6.9	6.18 ±0.18	1.27 ±0.04	0.49 ±0.13

In this case, we use the one-tailed test because we are specifically testing the possibility that a difference between day and night greater than the observed difference could be attributed to random variability. For all Me/Ca ratios, the mean difference between day and night ($\Delta mean = mean_{day} - mean_{night}$) is either positive (day > night) or negative (night > day). For example, in the case of Sr/Ca and Mg/Ca, where night Me/Ca ratios are greater than day Me/Ca ratios, $\Delta mean < 0$, and we are testing the possibility that a more negative $\Delta mean$ could result from random

variability. The remaining possibilities—that random variability could result in a Δmean = 0, where day and night populations are equal, or Δmean > 0, where we would observe higher Mg/Ca and Sr/Ca ratios during the day than during the night, opposite to our observations, are not of interest in this study.

For each element, 14 random Me/Ca were sampled from a population with a mean equal to the mean of all measured foraminiferal samples and a standard deviation equal to the standard deviation across all measured samples. A log-normal distribution was used to produce this population, to avoid physically unreasonable negative Me/Ca ratios (Limpert and Stahel, 2011). From within this random sample, seven Me/Ca values were randomly assigned to be day-spiked samples, and seven were randomly assigned to be night-spiked samples. The mean of all 'day' samples was then compared to the mean of all 'night' samples. The difference between these means (Δmean) was calculated. This process was repeated 10,000 times, and a histogram of all Δmeans plotted.

The observed Δmean from the actual mixed spike measurements was then plotted on each histogram as a red line. The integrated probability beyond that line (farther from zero) represents the likelihood that a single population could result in the observed Δmean by chance. If this probability is smaller than the level of confidence, then the null hypothesis of a single population can be rejected. Histograms from this set of analyses are displayed in Figures 3.5, 3.6, and 3.7 (see Appendix C for Ba/Ca). Although the observed diurnal difference in Sr/Ca ratios is small, the observed difference is inconsistent with a single population at the 85% level of confidence. The difference between mean day and mean night Li/Ca and Mg/Ca is indicative of two different populations at the 90% confidence interval at the 99% confidence interval, respectively. These results are consistent with the results of both the t-test and the Mann-Whitney U-test, except in

the case of Sr/Ca, which has been observed to have a difference significant at the 80% confidence interval using the t-test. For the remainder of this dissertation, we state that the diurnal difference in Sr/Ca is significant at the 85% confidence interval, however, we note this discrepancy here. A lack of statistical significance in the diurnal difference of Sr/Ca would suggest that Sr/Ca ratios between day and night are equal, which is still inconsistent with the prediction that Sr/Ca should be higher during the day than during the night because of kinetic effects.

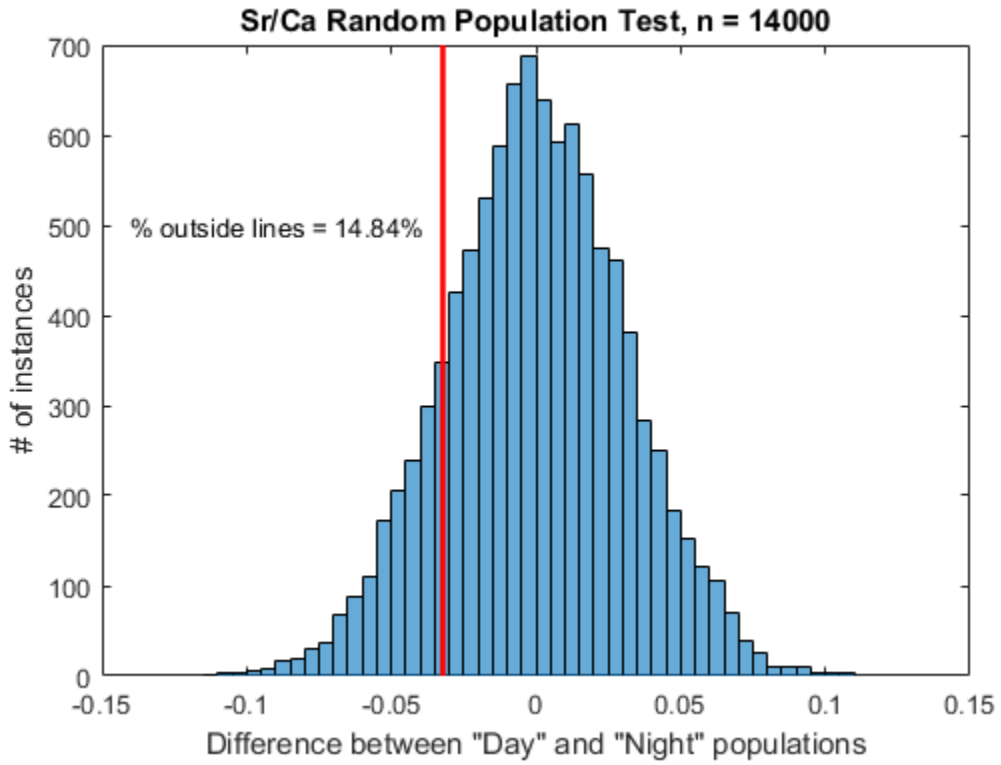

Figure 3.5. Histogram of Sr/Ca ratios calculated using the Monte Carlo analysis described in the text, from a randomly generated population of 14,000 samples with the same mean and standard deviation as the measured samples. The percent of the histogram outside the red line (farther from zero) represents the probability that a mean (difference between day and night) is greater than the observed Δmean.

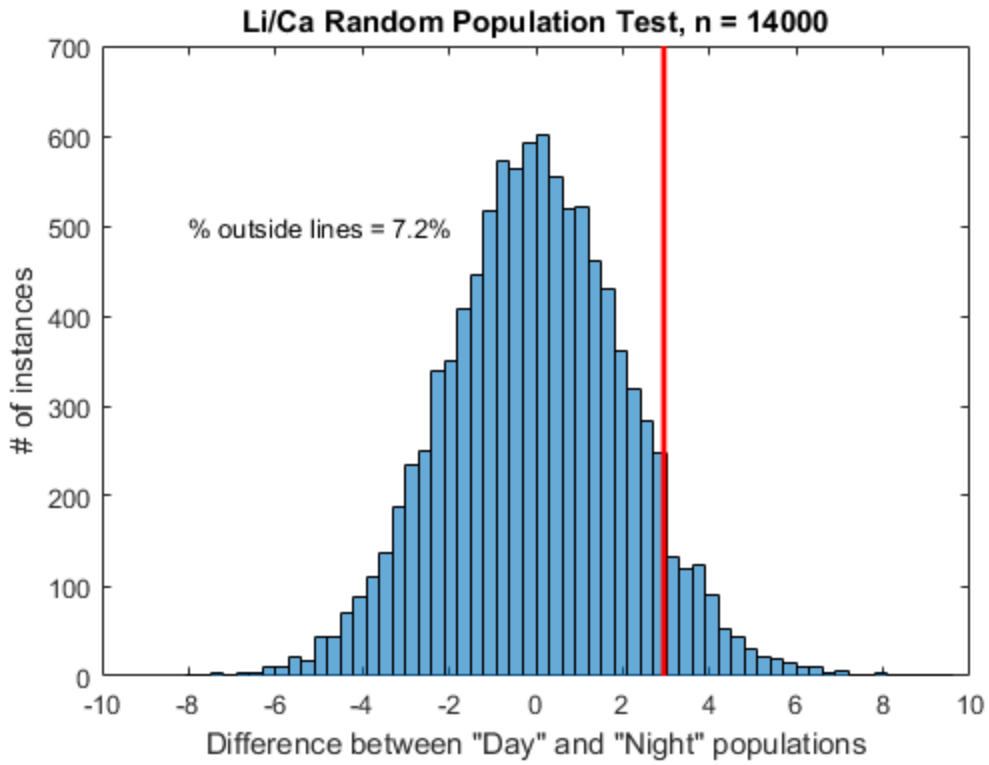

Figure 3.6. Histogram of Li/Ca ratios calculated using the Monte Carlo analysis described in the text, from a randomly generated population of 14,000 samples with the same mean and standard deviation as the measured samples. The percent of the histogram outside the red line (farther from zero) represents the probability that a mean (difference between day and night) is greater than the observed Δmean.

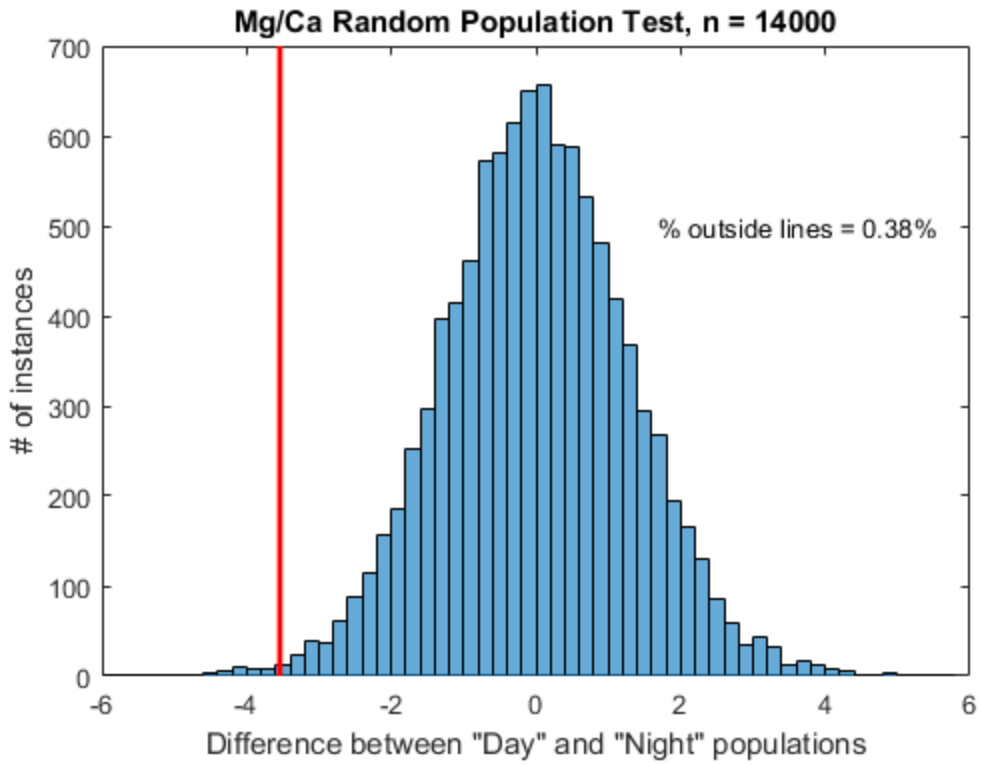

Figure 3.7. Histogram of Mg/Ca ratios calculated using the Monte Carlo analysis described in the text, from a randomly generated population of 14,000 samples with the same mean and standard deviation as the measured samples. The percent of the histogram outside the red line (farther from zero) represents the probability that a mean (difference between day and night) is greater than the observed Δmean.

3.3.4 *Correlations between Me/Ca ratios*

Li/Ca and Mg/Ca for each individual analyzed in this experiment were plotted against each other (Figure 3.8). This figure shows that Li/Ca and Mg/Ca are positively correlated to each other during the day ($R^2 = 0.76$). However, there is no apparent correlation between Mg/Ca and Li/Ca ratios at night ($R^2 = 0.031$). Similarly, a slight positive correlation appears to exist for Mg/Ca and Sr/Ca during the night ($R^2 = 0.42$) but not during the day ($R^2 = 0.0012$) (Figure 3.9). There is no apparent correlation between Sr/Ca and Li/Ca, either during the day or during the night (Figure 3.10).

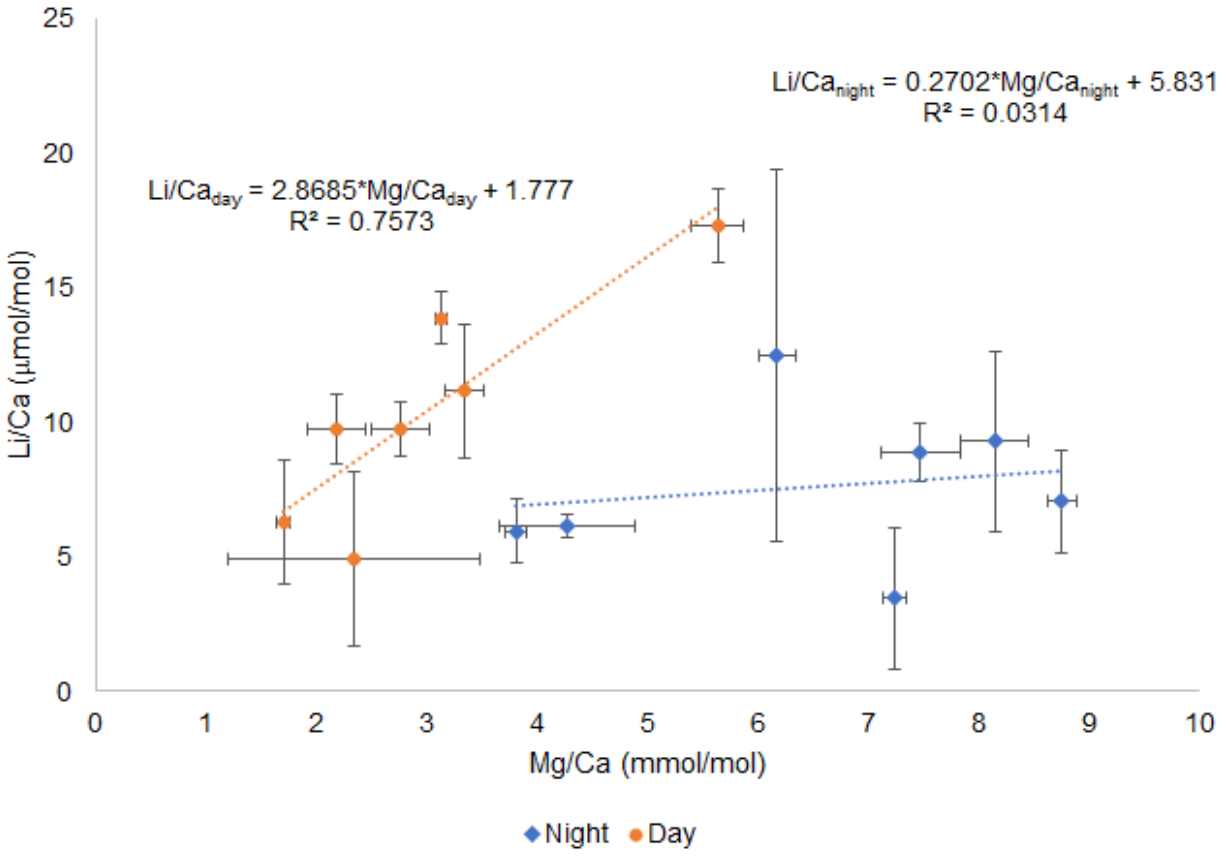

Figure 3.8. Mg/Ca and Li/Ca ratios plotted against each other for calcite grown during the day (orange points) and calcite grown during the night (blue points). Error bars correspond to analytical error for both Li/Ca and Mg/Ca ratios.

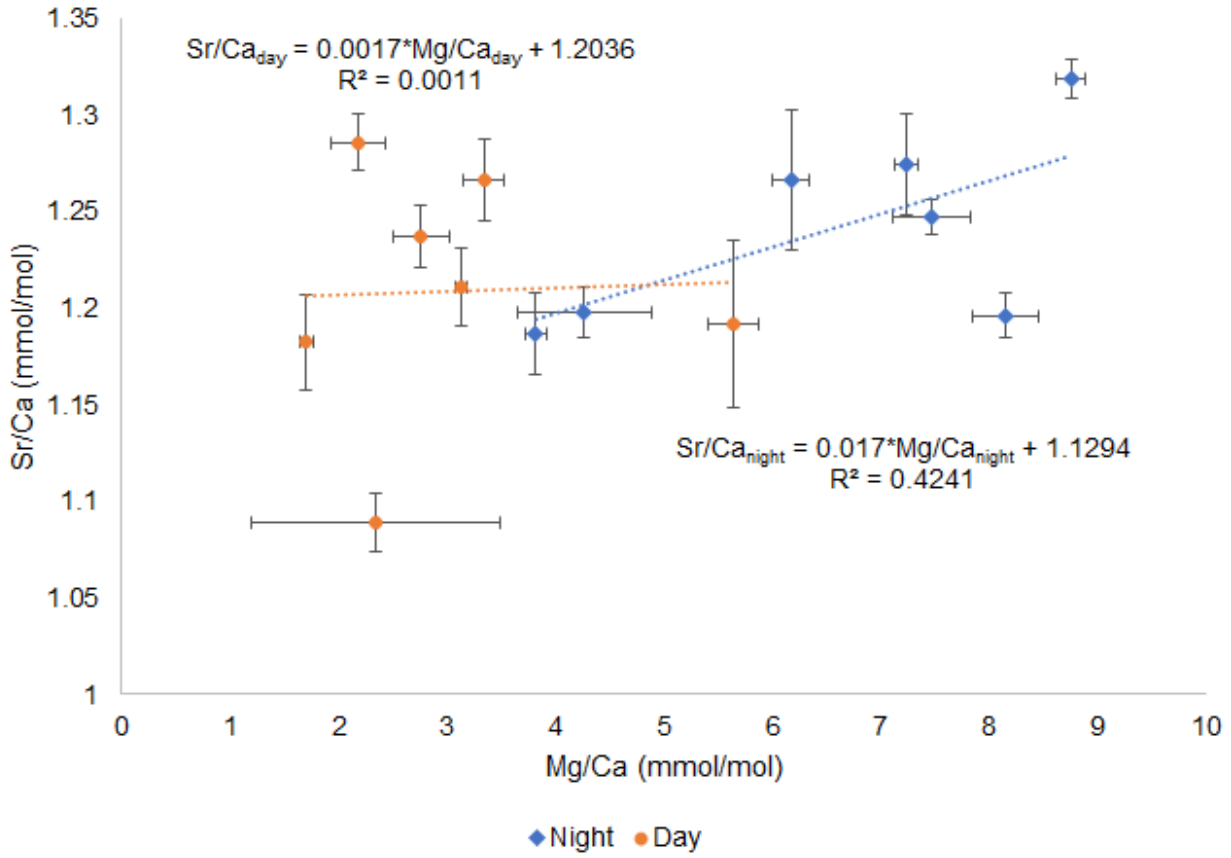

Figure 3.9. Mg/Ca and Sr/Ca ratios plotted against each other for calcite grown during the day (orange points) and calcite grown during the night (blue points). Error bars correspond to analytical error for both Sr/Ca and Mg/Ca ratios.

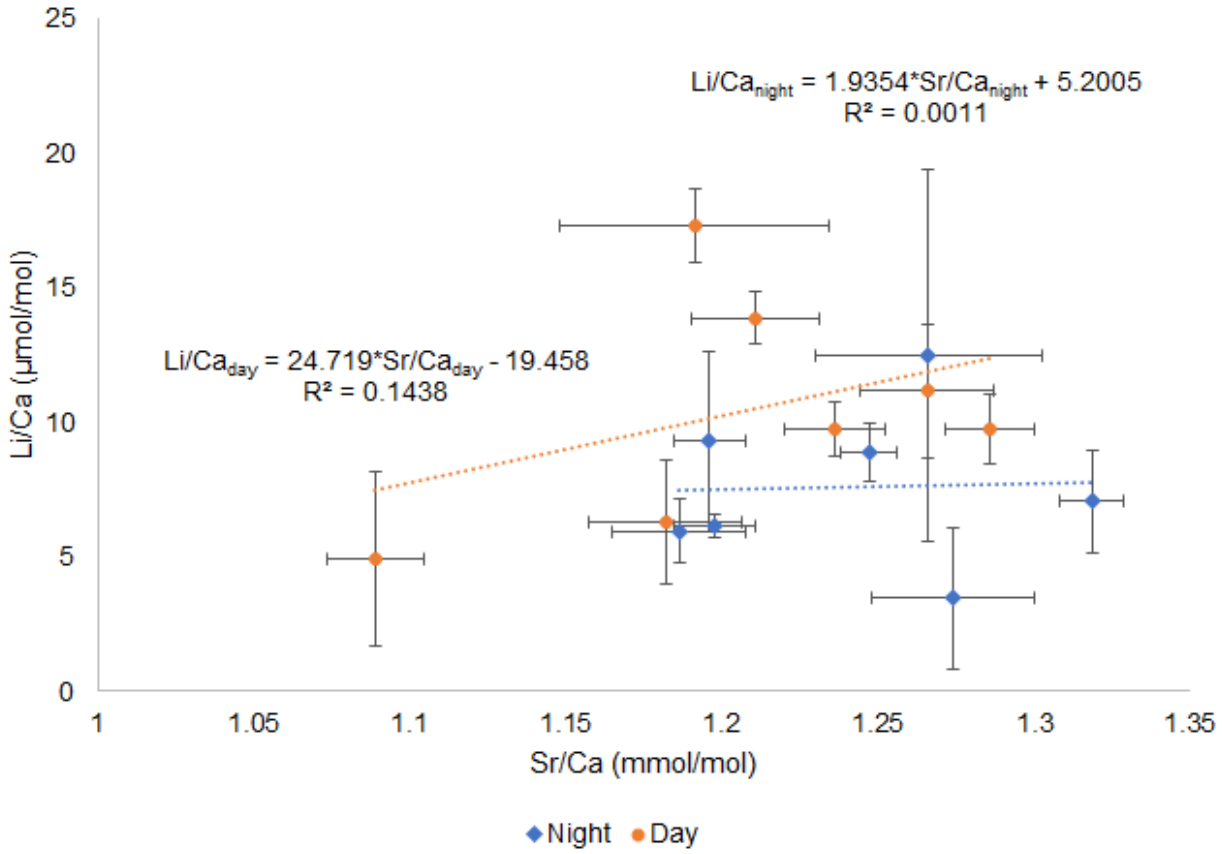

Figure 3.10. Sr/Ca and Li/Ca ratios plotted against each other for calcite grown during the day (orange points) and calcite grown during the night (blue points). Error bars correspond to analytical error for both Li/Ca and Sr/Ca ratios.

3.3.5 *NanoSIMS and ToF-SIMS images of cultured foraminifera*

Small pieces of three of the same foraminifer tests that were analyzed using the mixed-spike method were set aside prior to dissolution for complementary imaging using NanoSIMS. Chemical imaging of cultured foraminifer tests at the nano-scale can indicate the exact pattern of isotope labeling and provide an independent estimate of Mg/Ca for day or night bands. Furthermore, nano-scale images of day and night bands across many individuals can provide a statistical picture of day and night calcification rates. These rate data are crucial for testing kinetic models of foraminifera geochemistry because they allow for a direct comparison between our geochemical measurements and inorganic mineral growth experiments (Section 3.4.2). The

images also give a statistical picture of the relative proportion of day calcite to night calcite in a typical foraminifera, which provide a way to translate our band-resolved measurements into predictions about bulk test composition and proxy variability (Section 3.3.5.1).

3.3.5.1 NanoSIMS images confirm targeted isotope labeling of day or night bands

Figure 3.11 shows NanoSIMS images from a foraminifer that was spiked during the day, compared to a foraminifer spiked during the night. The position of the isotope label in the night-spike individual matches the position of the high Mg/Ca night bands. Similarly, the position of the isotope label in the day-spiked individual matches the position of the low Mg/Ca night bands. This pattern is consistent with the labeling experiments of Spero et al. (2015) and indicates that the appropriate time period was labeled in this study. The number of bands labeled with isotope spike also corresponds to the number of days or nights that each foraminifer was placed into labeled seawater, showing that all days or nights of interest were labeled.

Profiles of $^{43}Ca/^{40}Ca$ were collected across the test wall of the foraminifer and compared with profiles of $^{25}Mg/^{24}Mg$ and $^{24}Mg/^{40}Ca$ from the same location (see Appendix C). A close examination of the Mg/Ca bands compared to the ^{43}Ca spike incorporation reveals a slight discrepancy between the incorporation of the ^{43}Ca spike and the ^{25}Mg spike into foraminiferal calcite, and a similar offset between the location of high Mg/Ca bands and areas spiked with ^{43}Ca. These offsets represent a potential source of error, with up to 20% of the labeled calcite possibly spilling over into the next day or night band. The actual amount by which this may bias Me/Ca ratios varies depending on the Me/Ca ratios of each individual band. Using typical values for the Mg/Ca of day and night banding from spot analyses in the three foraminifera measured using NanoSIMS, we estimate that this offset could correspond to a relative change in Mg/Ca ratios of ~10-15% for the night-spiked specimens, and ~50% for the day-spiked foraminifer.

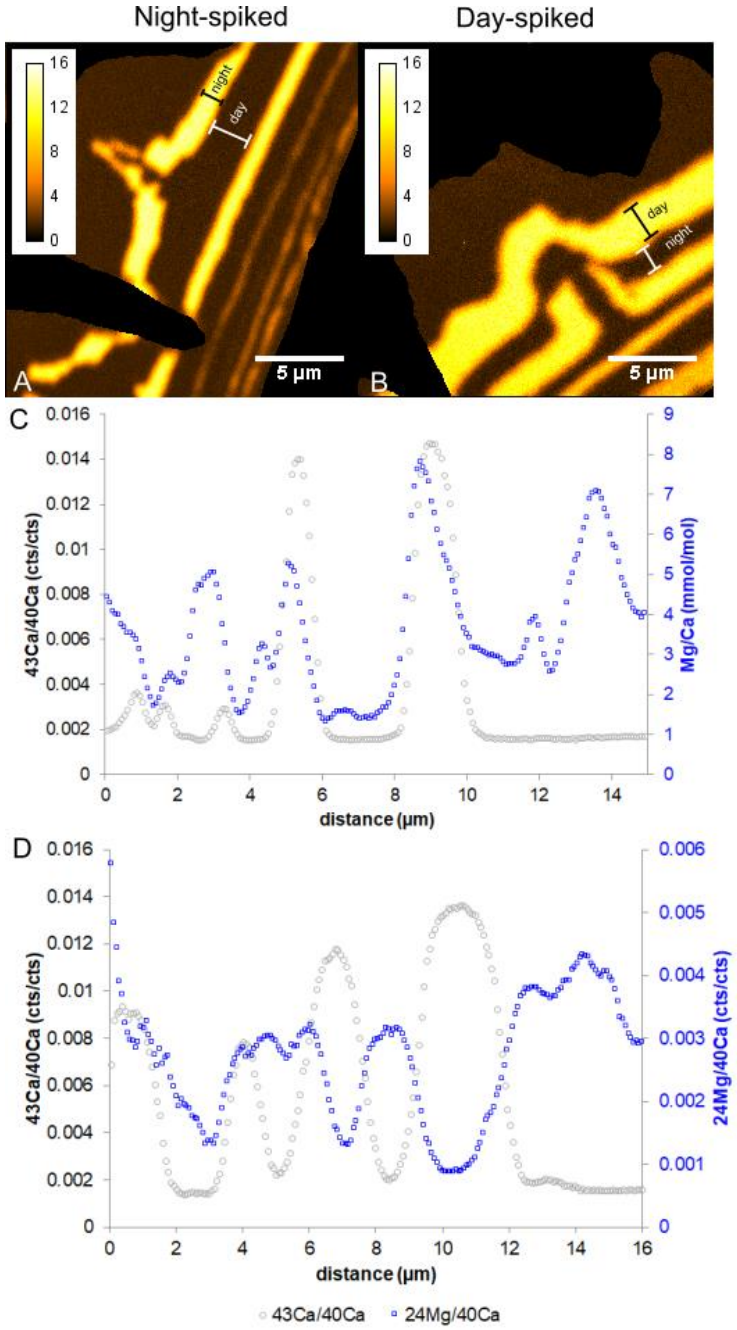

Figure 3.11. A) $^{43}Ca/^{40}Ca$ NanoSIMS image taken across the shell wall of an *O. universa* specimen placed in spiked seawater during night periods. B) $^{43}Ca/^{40}Ca$ NanoSIMS image taken across the shell wall of an *O. universa* specimen placed in spiked seawater during day periods. Bright colors indicate higher concentrations of ^{43}Ca in both images. The color scale represents ^{43}Ca cts x 10^3 /^{40}Ca cts. C) $^{43}Ca/^{40}Ca$ and Mg/Ca profiles of Foram #311, also pictured in A. Mg/Ca ratios are calibrated from spot analysis within this same foraminifer. $^{43}Ca/^{40}Ca$ ratios are in uncalibrated counts/counts. D) $^{43}Ca/^{40}Ca$ and $^{24}Mg/^{40}Ca$ ratios from the day-spiked individual imaged in B. Ratios are in uncalibrated counts/counts.

Potential errors are stronger for day Mg/Ca ratios than for night Mg/Ca ratios, because night Mg/Ca is typically significantly larger than day Mg/Ca. These potential errors are smaller for Sr/Ca, with these offsets resulting in a possible change of Sr/Ca ratios of ~0.5-0.7% during the night and ~0.5-1.3% during the day. For Li/Ca, these errors are of similar magnitude as for Mg/Ca, with a possible change in Li/Ca of ~7-10% during the night and ~4-12% during the day. However, we note that these errors would act to bring day and night Me/Ca values from the mixed spike method closer to each other, as this would result in a mixing of day and night Me/Ca ratios. Our results using the mixed-spike method show significant differences in the Me/Ca ratios between day and night, even with this source of error, suggesting that although the potential diurnal differences in *O. universa* may be greater than reported, this source of error does not significantly change our results.

3.3.5.2 Measurement of day and night calcification rates from NanoSIMS and ToF-SIMS images

Mg/Ca bands are observed to be much thinner than day Mg/Ca bands in the above NanoSIMS images. Further analysis of ToF-SIMS images from 45 *Orbulina universa* (Chapter 2), show that low Mg day bands are usually, but not always thicker than high Mg night bands (Figure 3.12A). Although these samples were drawn from culture treatments at a range of different temperatures, carbonate concentrations, and salinities (T = 18°C to 22°C, S = 30 to 36.6, pH_{NBS} = 7.90 to 8.59, and total alkalinity = 2091 to 2621 µmol/kg), we do not resolve a significant change in overall growth rates based on any of these factors. This may be because individual variability between each day and night bands was too large to observe any growth rate effects.

Calcification rates can be estimated from growth measurements by assuming that *O. universa*'s final chamber is a sphere of uniform thickness, with a surface area of $4\pi r^2$ and a

volume of $4/3\pi r$, where r is the radius of the sphere. We can then use the thickness of each band to calculate the amount of new growth, by calculating the change in the volume of the sphere. When the foraminifer first begins precipitating, it starts with a sphere whose radius is the distance from the point of initial growth to the center of the sphere. When the foraminifer has finished precipitating, its radius will have grown, commensurate to the amount of material added onto the surface of the sphere. The thickness of the band, then, is the differences of the radii of the sphere before and after growth: $\Delta r = r_1 - r_o$. The amount of material added to the sphere can be approximated as the difference in the sphere's volume before and after calcification, as follows:

$$\Delta V = V_1 - V_0 = 4/3\pi(r_1^3 - r_o^3) \tag{3.10}$$

The change in sphere volume, ΔV, can be converted into units of μmol by making use of the density ($\rho_{calcite}$ = 2.71 g/cm^3) and the molar mass (100.08 g/mol) of calcite. Porosity, due to regularly spaced pores within the test wall, can be corrected for by assuming a porosity of 7.5%, the approximate average empirically measured porosity for *O. universa* at ~20°C (Bé et al., 1973). By dividing the change in volume by the initial surface area of the sphere and the calcification time (12 hours), one can calculate an estimate of the growth rate. Based on measurements of diameters prior to sectioning, foraminiferal radii vary from 210 to 343.5 μm, with a mean of 274 ±4 μm. Across this range, growth rates do not appear sensitive to the value of the initial radius (r_o) and are rather driven by the thickness of the band.

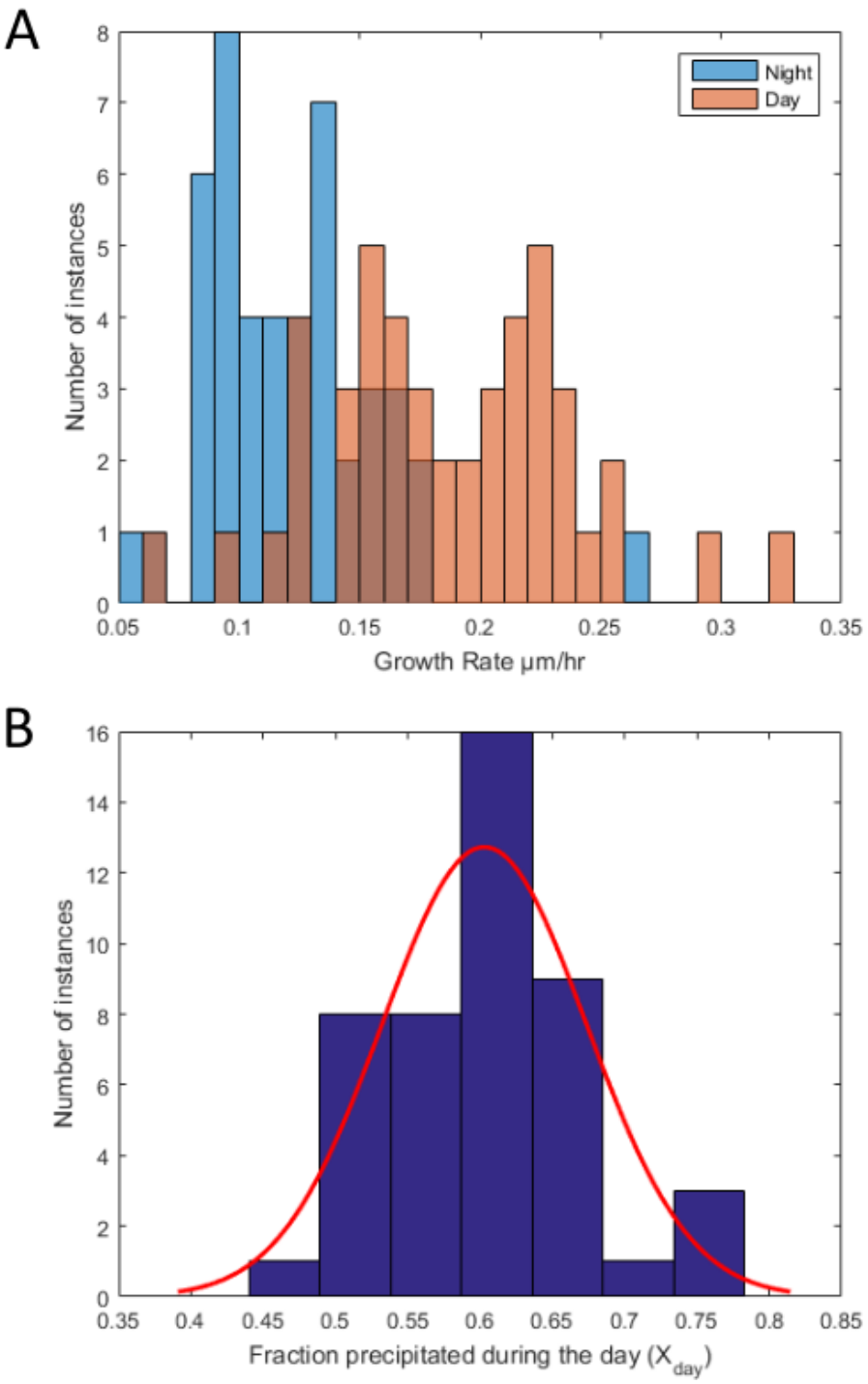

Figure 3.12. A) A histogram of day growth rates averaged over the course of an individual foraminifer's life, compared to night growth rates from the same time period. Although some overlap exists between day and night growth rates, in general, day growth rates are higher. B) A histogram of X_{day}, the fraction of calcite formed during the day, is plotted for same set of foraminifera. If X_{day} is fit to a normal distribution, the mean is 0.60 and the standard deviation is 0.071.

Oblique sectioning, where the foraminifera sample was not fractured exactly through the center of the sphere, can affect these growth rate estimates. However, based on measurements of the sphere radius pre- and post-polishing and the thickness of the shell, the mean angle of sectioning is observed to be 68 ±10º, which corresponds to a broadening of all features by 1.1 ±0.1, where all estimated growth rates could be 1.1 times higher than estimated (Branson et al., 2016). This correction would not change the relative growth rates between day and night, as all growth rates within a single individual would be affected by the same magnitude of broadening, however, it is worth noting that the uncertainty due to oblique correction is on the same order of magnitude as the uncertainty in the fraction of the foraminifer precipitated during the day (Figure 3.12B), which may be significant.

In the case of the night-spiked foraminifer (Figure 3.11), the calcification rate of the last high Mg/Ca night band is estimated to be 3540 μmol/m^2/hr or -6.01 $\log_{10}$(mol/m^2/s), and the calcification rate of the low Mg/Ca day band immediately preceding this band is estimated to be 6915 μmol/m^2/hr or -5.72 $\log_{10}$(mol/m^2/s), with the night growth rate being roughly 50% of the day growth rate. An examination of a range of day and night Mg/Ca banding in ToF-SIMS measurements of *O. universa* (Chapter 2) shows that on average, night Mg/Ca bands are 53% thinner than day Mg/Ca bands.

3.3.5.3 Direct comparison between mixed spike method and NanoSIMS within a cultured foraminifera

In total, three foraminifera were imaged using NanoSIMS—two night-spiked foraminifera and one day-spiked foraminifera. Of the two night-spiked foraminifera, one (#311, Table 3.8) was also analyzed using the mixed-spike experiment, because the tests of the other two foraminifera were destroyed accidently during cleaning. Spot analyses were conducted for all three samples, yielding Mg/Ca ratios of day and night bands (Figure 3.13).

Across the three samples analyzed by NanoSIMS, mean day Mg/Ca values were found to be 2.0 ±0.5 mmol/mol. Mean night Mg/Ca was found to be 7.6 ±1.1. This is comparable to mean Mg/Ca ratios observed using the mixed-spike experiment, which were 3.0 ±0.5 mmol/mol for day Mg/Ca values and 6.6 ±0.7 mmol/mol for night Mg/Ca, even though most of the individuals were different between the two methods. Overall, the large difference in Mg/Ca observed between day and night using both methods show that both methods can be used to examine Mg/Ca banding.

One individual cultured foraminifera (#311) was analyzed using both the mixed spike and the NanoSIMS spot method. Comparing the results of these two methods, which are calibrated in different ways, provides an independent check on the accuracy of the methods. For this comparison, the NanoSIMS image data from foraminifera #311 must first be converted into a quantitative and calibrated Mg/Ca map. Then the Mg/Ca of the isotopically labeled regions of the image can be integrated to compare with the mixed spike method. A two-point calibration was performed on the NanoSIMS image displayed in Figure 3.11, in order to convert intensity images to measurements of Mg/Ca in units of mmol/mol. The calibration points were based on two NanoSIMS spot measurements, each 1 μm in diameter, taken directly next to the NanoSIMS image (Figure 3.14). These spots were entirely within one Mg/Ca night band and one Mg/Ca day band, as confirmed by the fact that the isotope ratios of calcium and magnesium for these spots matched endmember values for spike and natural, respectively. Both spots were bracketed by bands with contrasting isotope ratios, so if the spot overlapped an adjacent band, then the isotope ratio would not match an endmember value. The spot measurements are calibrated using the standards described in Gabitov et al. (2013) and are traceable to isotope-dilution multi-collector-ICP-MS analysis of matching grains.

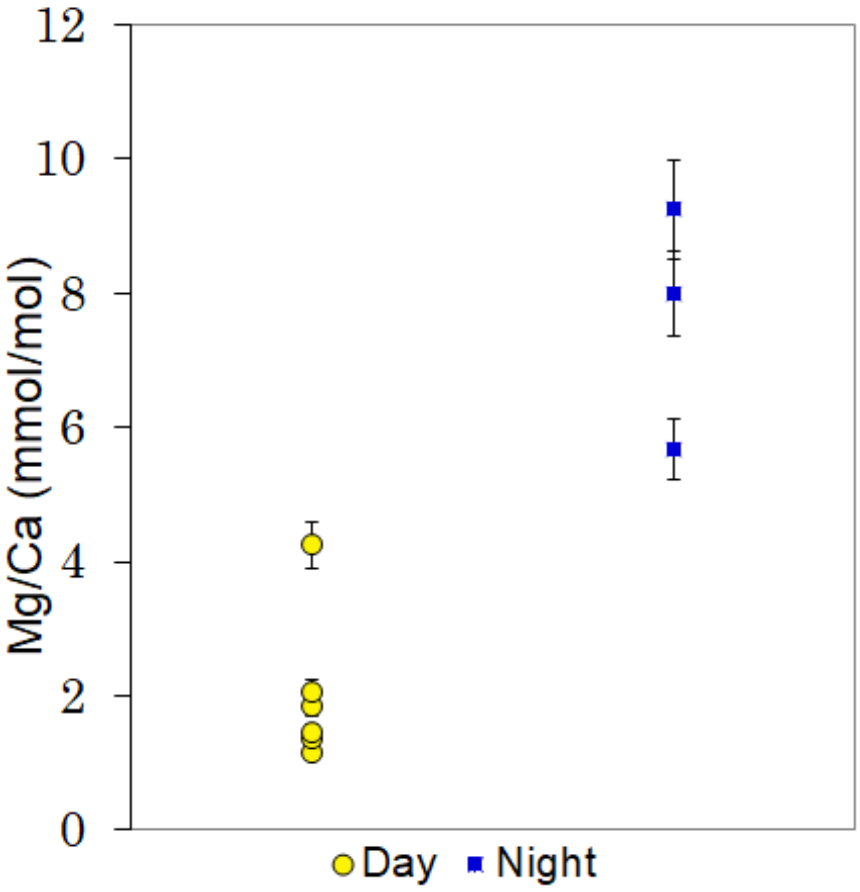

Figure 3.13. Mg/Ca ratios measured using spot analyses of day- and night- Mg/Ca bands from NanoSIMS samples. Mg/Ca ratios are calibrated to mmol/mol using mineral calcite standards traced to grain matched ID-MC-ICP-MS measurements. Standards are described in Gabitov et al., (2013).

After establishing a calibrated image map, a profile of Mg/Ca was measured across the test wall, and the Mg/Ca ratio of the two high Mg/Ca night bands that had been labeled with isotope spike was examined. The first band was observed to have an Mg/Ca ratio of 5.16 mmol/mol, with an estimated width of 0.96 μm. The second band had an Mg/Ca ratio of 8.81 mmol/mol, with an estimated width of 1.43 μm. This results in an average Mg/Ca ratio of 7.34 mmol/mol, when weighted using the width of the bands. This ratio is statistically the same as the observed Mg/Ca ratio using the mixed spike method (7.23 ± 0.11 mmol/mol), showing that the

two methods of examining Mg/Ca ratios are consistent with each other. Since the two methods are calibrated in different ways and use very different physical methods, this agreement would be unlikely unless both were accurate. This comparison suggests that a mixed spike method may be used to calibrate the Me/Ca ratios of intentionally labeled samples in order to create matrix-matched standards for micro- and nano-analysis.

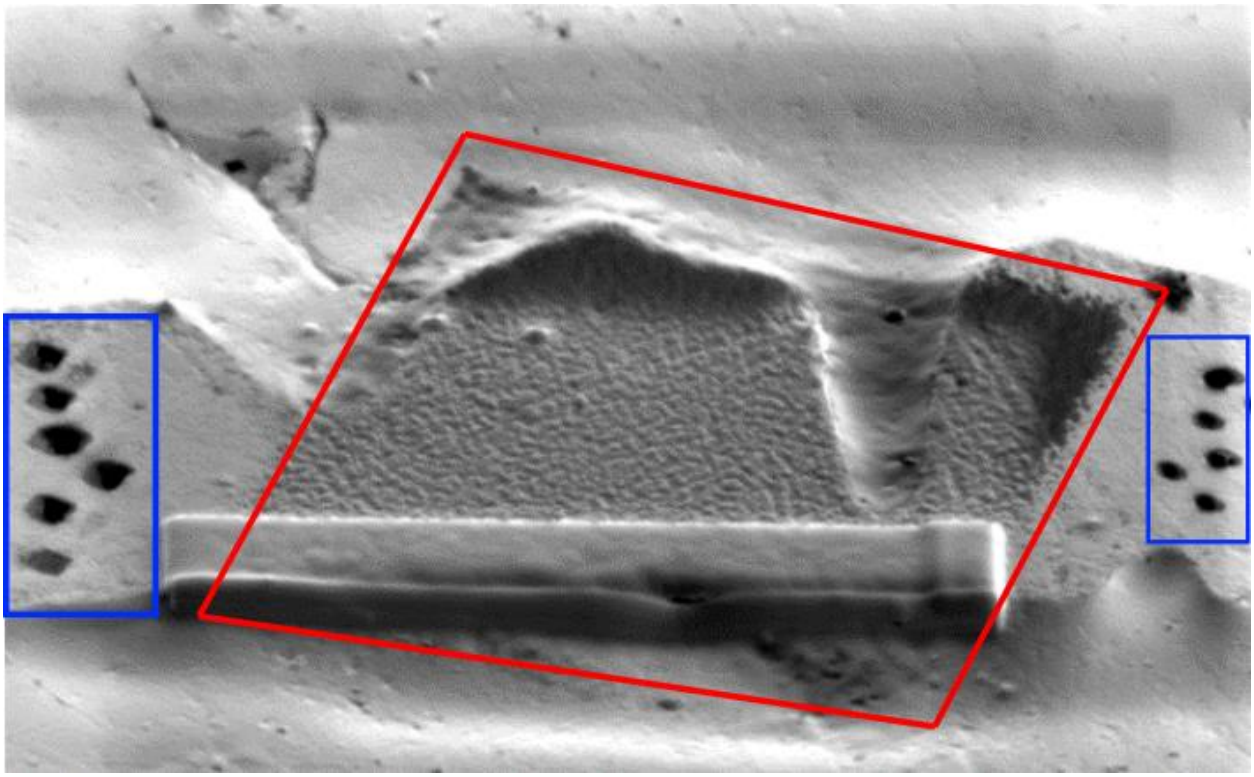

Figure 3.14. Location of NanoSIMS image (square burn mark, red rectangle) and adjacent spot analysis locations (dark circles, blue rectangles) across the test wall of #311, which was analyzed using both NanoSIMS and the mixed-spike method. The rectangular block in the foreground was placed after NanoSIMS analysis as part of focused ion beam (FIB) sampling, in support of Branson et al. (2016). Image from Branson et al., (2016).

The NanoSIMS image of #311 also allows a direct comparison of the portion of the labeled skeleton between the two methods. Using the multi-isotope spike method, the percentage

of calcite labeled in Foram #311 is 16.3%. A similar estimate can be obtained using the NanoSIMS image, by counting the number of points along the profile line that are labeled with an isotope spike, compared to the overall number of points along the profile line. When this calculation is performed, the percentage of calcite labeled is 15.3%. Thus, the two measurements return similar estimates for the ratio of labeled to unlabeled calcite.

3.3.5.4 Li/Ca intrashell heterogeneity observed using NanoSIMS

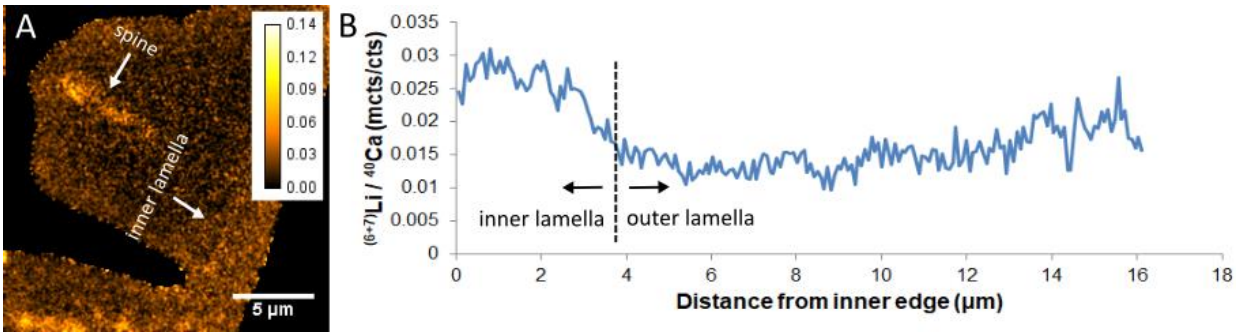

Figure 3.15. A) Intensity image of Li/Ca across the test wall of a cultured *O. universa* created from NanoSIMS data. Spine and inner lamella regions are labeled. This specimen is the same as that imaged in Figure 3.11A. Intensity ratios are reported in ^{7}Li cts x 10^{3} /^{40}Ca cts. B) A $^{(6+7)}$Li/^{40}Ca profile drawn across the test wall of the same foraminifer imaged in (A). The boundary between the inner and outer lamellae is labeled. The spine region is excluded from this profile.

Although Li counts using NanoSIMS are too low to resolve diurnal heterogeneity using this technique, ^{7}Li/^{40}Ca images acquired using NanoSIMS do reveal some patterns in intrashell Li that are consistent across all three individuals. NanoSIMS images of Li/Ca in foraminifera show high Li/Ca around the spine region in all three foraminiferal specimens (Figure 3.15 and Appendix C). Li is also observed to be high in the innermost ~3µm of the test, which we describe as the inner lamella. Here, Li is almost two-fold higher than in the remainder of the test.

3.4 DISCUSSION

The precision of the synthetic sample experiments as well as the agreement between NanoSIMS analysis and mixed spike analysis of the same foraminifer indicate that we can accurately and precisely measure select Me/Ca of day or night bands within a cultured foraminifer. Data collected using this approach indicate that the mean Sr/Ca, Li/Ca, and Mg/Ca differ between day and night bands. Although the magnitude of this difference varies for different elements, it is always larger than either the precision of the method or the variability between foraminifera. Furthermore, a statistical approach shows that day and night Me/Ca represent different populations at the 99% level of confidence (Mg/Ca), 90% level of confidence (Li/Ca) and 85% level of confidence (Sr/Ca).

3.4.1 *Sr/Ca of day and night calcite as compared with kinetic effects in experimentally precipitated inorganic calcite*

There is a well-established relationship between Sr/Ca and calcification rate in inorganic calcite, where Sr/Ca has been observed to increase as calcification rate increases (Tang et al., 2008a; DePaolo, 2011). In order to test whether our measurements of Sr/Ca using the multi-spike method are consistent with a kinetic effect, we must first obtain an independent measurement of calcification rate between day and night. Our NanoSIMS and ToF-SIMS images of Mg/Ca banding in *O. universa* allow us to obtain these independent measurements, because the diurnal timing of Mg banding is known (Eggins et al., 2004; Spero et al., 2015), and because our cultured foraminifera were grown at a consistent 12hr:12hr light/dark cycle (Figure 3.12). Based on these calcification rate changes, we predict that if Sr/Ca were being driven only by rate, Sr/Ca should be ~7% higher during the day than during the night.

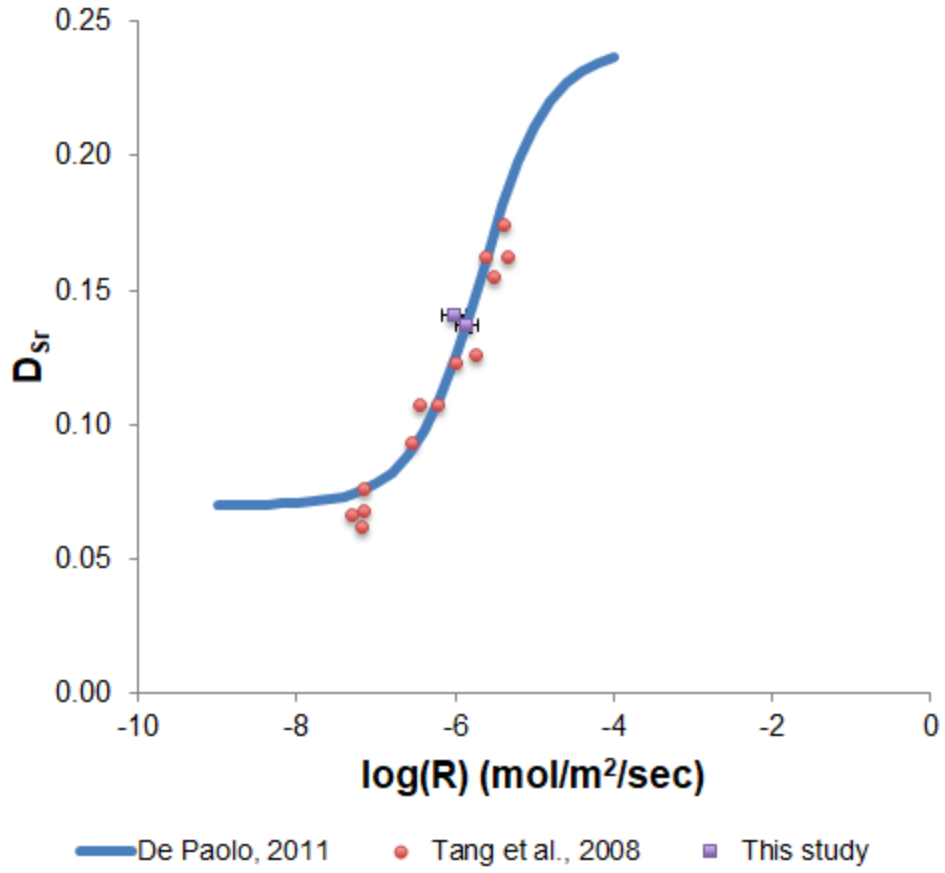

Figure 3.16. D_{Sr} values from this study compared to the inorganic model described in De Paolo, 2011, and the inorganic precipitation experiments performed by Tang et al., 2008a. Growth rates are reported in mol/m^2/sec. Foraminiferal growth rates are estimated from the average day and night growth rates plotted in Figure 3.12A, assuming a shell radius of 500µm. Horizontal error bars reflect the standard deviation of day and night growth rates. Errors in the vertical direction are smaller than the size of the marker.

By using our NanoSIMS and ToF-SIMS based day and night calcification rates, we can compare our measurements to the inorganic data and test this prediction. However, because the inorganic results come from calcite that formed in a fluid with a different composition from seawater, it is necessary to first convert our results to D_{Sr}, the partition coefficient between the mineral and the calcifying solution (see Equation 3.4). Using D_{Sr} allows us to directly compare our results with the inorganic data, without needing to consider the impact of the Sr concentration of the calcifying fluid. The results of this comparison are displayed in Figure 3.16.

On one hand, our data appear to be consistent with the inorganic data, falling very close to the model line and being within the scatter of the inorganic calcite experiments by Tang et al., (2008a). However, on the other hand, the implied diurnal changes in Sr/Ca as a function of growth rate are not visible, with night Sr/Ca being higher than day Sr/Ca, the opposite direction as would be predicted from calcification rates alone.

Performing an analogous statistical test as the one used to determine whether the day and night Me/Ca ratios are from the same population, we can test the possibility that mean Sr/Ca ratios are determined only by kinetics. In this case, the null hypothesis of the test is that the observed mean difference between day and night of Sr/Ca (Δmean = day – night) can be explained by kinetic effects. In order to perform this test, we first convert the observed calcification rates into D_{Sr} by using the relationship reported in Tang et al., (2008a). We then generate a random population of 100,000 individuals from two different populations, one with the same mean and standard deviation as our population of day D_{Sr} values, and one with the same mean and standard deviation as our population of night D_{Sr} values. We calculate Δmean for this random population. This gives us an estimate of the possible range of Δmeans that may be expected based on kinetics. Comparing our observed Δmean from the multi-spike method, we find that to the 99% level of confidence, we can reject the null hypothesis that the mean D_{Sr} of day and night are controlled solely by kinetics in foraminifera (Figure 3.17).

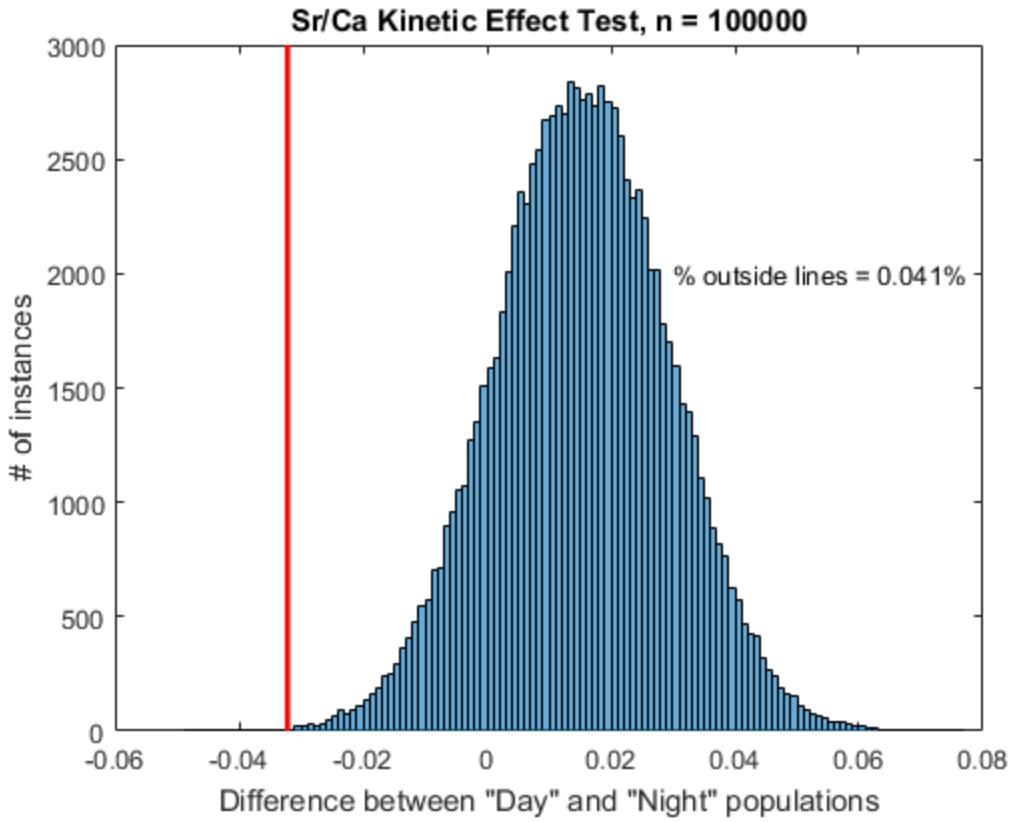

Figure 3.17. Histogram calculated using the Monte Carlo analysis described in the text, from a randomly generated population of 100,000 samples with the same mean calcification rates and standard deviation as the observed day and night growth rates in foraminifera. The percent of data points outside the red line (farther from zero) represents the probability that the observed Δmean can be explained using kinetic effects.

This reveals an important discrepancy between the bulk Sr/Ca ratios of the test and intrashell Sr/Ca. What causes the overall Sr/Ca of the test to follow the inorganic calcite trend, but not show a similar effect on a diurnal scale? Examination of the relationship between Sr/Ca and Mg/Ca in our samples as compared with other biominerals and inorganic calcites may help resolve this apparent contradiction.

3.4.2 *Robust Sr/Ca vs. Mg/Ca correlation in marine calcite: Mineralogical control*

Sr/Ca and Mg/Ca are strongly correlated when inorganic calcite is experientially precipitated from natural seawater, artificial seawater, and seawater with modified Mg/Ca (Mucci and Morse, 1983). This same relationship is seen in biomineral calcite formed by a wide range of taxa (Carpenter and Lohmann, 1992). Even organisms that are vastly different genetically, such as precious red coral (Vielzeuf et al., 2013), and a diverse set of different foraminiferal species (Evans et al., 2015), all plot surprisingly close to this inorganic line (Figure 3.18). This same relationship is found in our measurements of foraminiferal calcite, our measurements of gametogenic calcite (described in Chapter 4), as well as the single foraminifera measurements of *O. universa* cultured by Lea et al. (1999). We find that regardless of origin, calcite samples appear to fall on this same line. A similar relationship between Sr/Ca and Mg/Ca has been observed between D_{Sr} and Mg/Ca in the high-Mg foraminifer *Operculina ammonoides*, and this has also been observed to be consistent with inorganic calcite and other foraminifera measurements (Evans et al., 2015). This implies that the positive correlation observed between Mg/Ca and Sr/Ca is a consistent, mineralogical property of calcite, and does not differ between inorganic calcite or biogenic calcite, even when the biogenic calcite is formed under a range of physiological conditions. This mineralogical effect can explain much of the correlated variability in Sr/Ca and Mg/Ca in foraminifera.

How do we reconcile the robust mineralogical relationship between Sr/Ca and Mg/Ca in calcite with the clear existence of an inorganic kinetic effect that should be impacting the Sr/Ca of calcite? The canonical experiments of Mucci and Morse (1983), which define the mineralogical line have generally been interpreted as having no kinetic effect. However, Morse and Bender, (1990) suggested that when the data from different experimental conditions are

plotted separately, there may be evidence for a Sr/Ca vs. growth rate relationship. Inspired by this observation, we plotted the residual Sr/Ca as compared to the mineralogical line vs. calcification rate for the inorganic experiments of Mucci and Morse (1983), where high quality calcification rate data are available (Figure 3.19). Across a wide range of solution Mg/Ca, this residual follows the same positive relationship, which also follows the trend of the inorganic calcite kinetic effect at similar calcification rates. This reanalysis suggests that departures from the mineralogical line can be explained by the known kinetic effect. These two phenomena can explain the inorganic data and potentially the foraminifera data as well.

Re-examination of the Sr/Ca vs. Mg/Ca data shown in Figure 3.18 shows that some types of marine calcite are more tightly distributed along the mineralogical line than others. Speculatively, this scatter may represent the relative importance of the same two effects: mineralogical control and kinetics. For example, the tight relationship found for precious red coral (*Corallium rubrum*; Vielzeuf et al., 2013) may indicate either the absence of kinetic effects or a constant level of kinetic effects. If this is the case, then geochemical analysis of readily available samples like *C. rubrum* could be used to identify putative mineralogical effects for a range of proxies without having to conduct inorganic precipitation experiments.

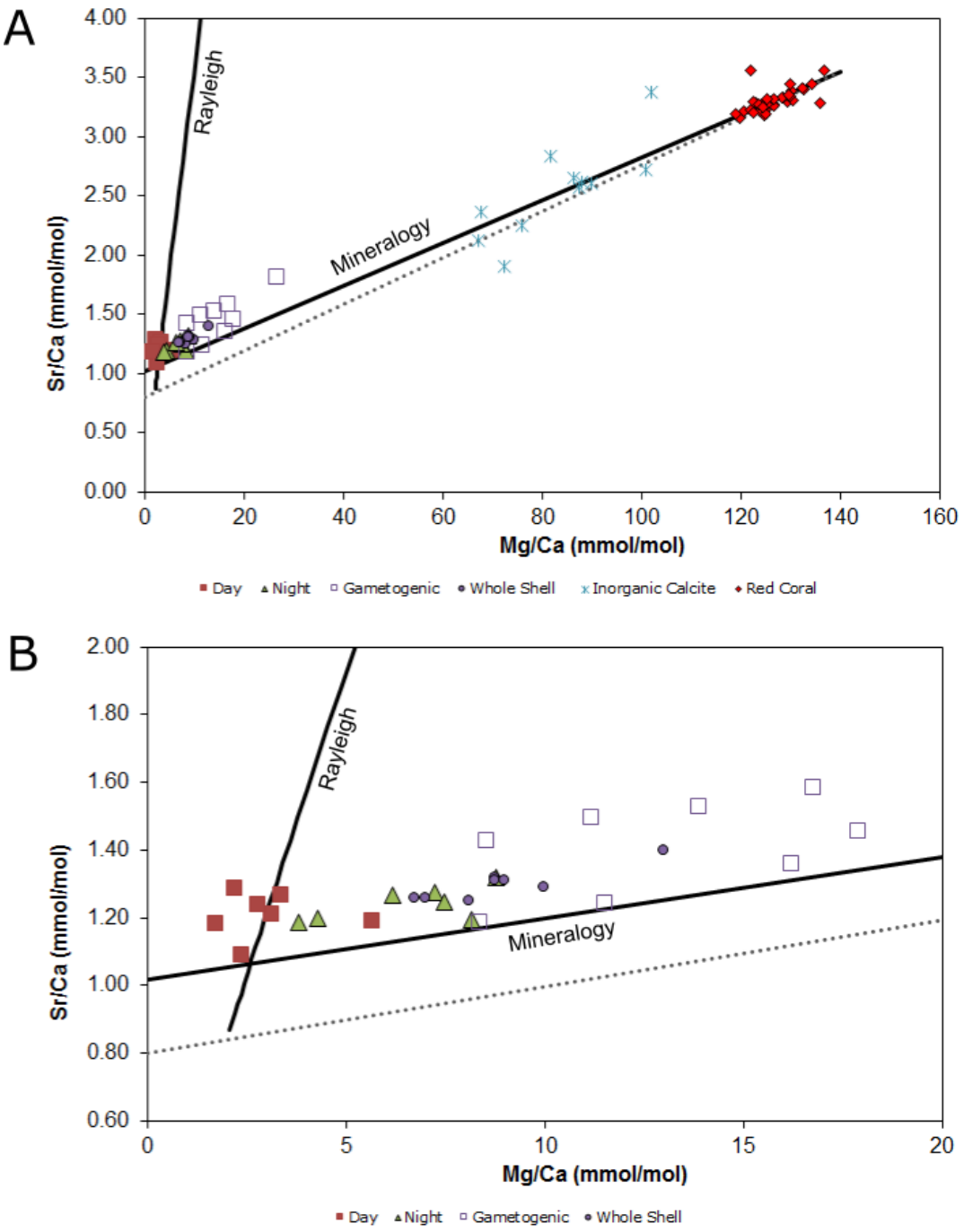

Figure 3.18. Night Mg/Ca and Sr/Ca values from this study plotted with whole shell *O. universa* measurements (Lea et al., 1999), gametogenic calcite (Chapter 4), inorganic calcite (Mucci and Morse, 1983), and red coral (Vielzeuf et al., 2013). A) Mg/Ca and Sr/Ca of our samples compared to sample data from literature. Dashed line represents a shift of the Rayleigh line downward to be more consistent with day Sr/Ca measurements. B) Mg/Ca and Sr/Ca of foraminiferal measurements only, in comparison to the mineralogical and Rayleigh lines.

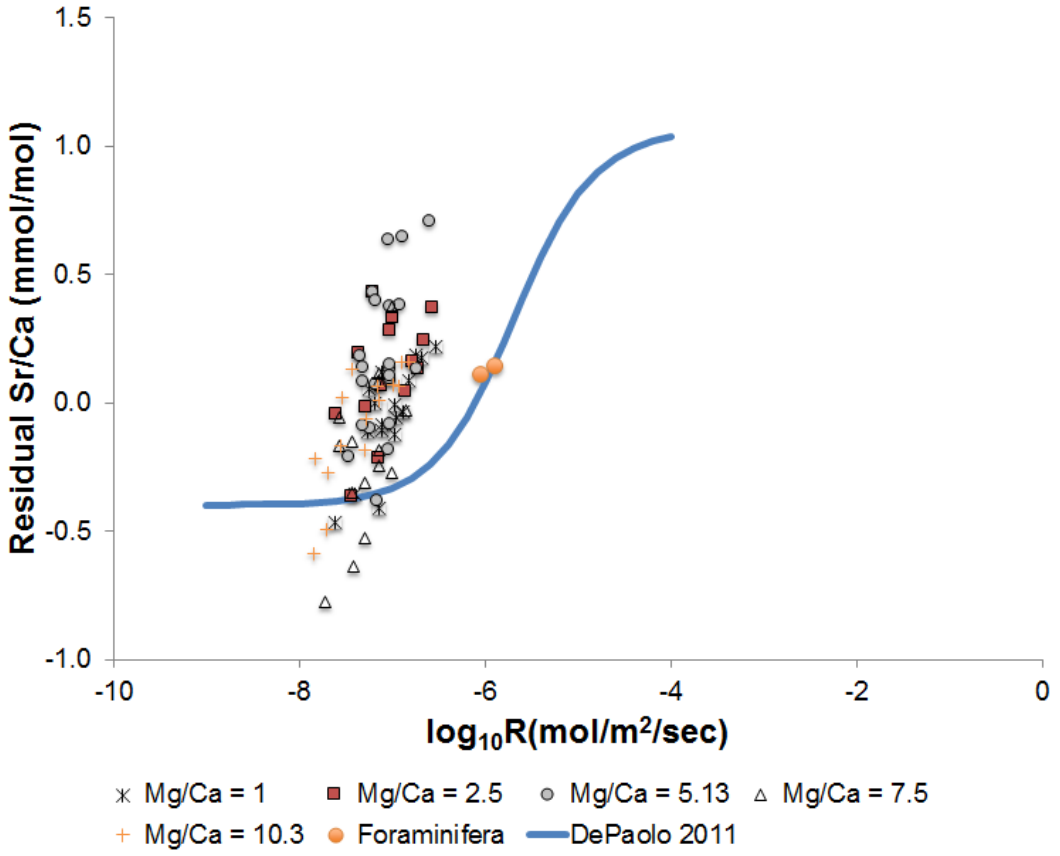

Figure 3.19. Residual Sr/Ca values (y-axis) plotted against precipitation rate for inorganic calcite experiments precipitated from seawater solutions of various Mg/Ca (mol/mol) (Mucci and Morse, 1983) and our foraminiferal samples. The kinetic effect is estimated from DePaolo, (2011).

This interpretation does not yet take into account the possibility of a similar kinetic effect on Mg/Ca. It has previously been suggested (Mavromatis et al., 2013) that Mg/Ca increases as calcification rate increases. If true, the apparent Sr/Ca residual from the line would decrease, as the Mg/Ca kinetic effect would shift calcite composition closer to the mineralogical line. This may be contributing to the observed offset from the kinetic line in Figure 3.19, where some points appear to plot below the kinetic line. If a Mg/Ca kinetic effect due to precipitation rate were decreasing Sr/Ca residuals, a correction for this kinetic effect would increase the Sr/Ca residual, potentially lifting points above the kinetic line. However, we note that this cannot

account for the offset along the x-axis, which is a result of changes in precipitation rate. Instead, this offset may result from the choice of mineralogical fit used to plot the inorganic curve, or some other process not yet accounted for.

A close examination of the foraminiferal samples in Figure 3.18 reveals that while the night bands and the *O. universa* specimens from Lea et al., (1999) all appear to fall on the same trend, Sr/Ca and Mg/Ca ratios obtained during the day appear to have a different relationship. This suggests that some process other than mineralogical processes is affecting Me/Ca incorporation during the day. Based on the trend observed in Figure 3.19, it is possible that day calcification is influenced by both kinetic and mineralogical effects. Then, extending the mineralogical line and calculating a residual would give an estimate of the day kinetic effect. If this is the case, we might expect the residual Sr/Ca of day calcification to be of a similar magnitude as the inorganic calcite kinetic effect. The mean residual of day Sr/Ca ratios from the mineralogical line is 0.14. If this is due to kinetics, it would imply a 0.14 increase in mean day Sr/Ca due to kinetic effects. If the magnitude of the residual reflects kinetic effects, we should expect to see a smaller residual for mean night Sr/Ca, because growth rates decrease between day and night. Indeed, we observe that the mean residual for night Sr/Ca ratios is 0.11, indicating a 0.11 increase in mean night Sr/Ca due to kinetics. This is consistent with the inorganic trend, and implies that kinetic effects may be contributing to this offset in Sr/Ca, consistent with the growth rate differences between day and night. Together, the mineralogical line and kinetic effects can explain our observations of foraminiferal Mg/Ca and Sr/Ca.

3.4.3 *Alternate explanation: Rayleigh fractionation*

Rayleigh fractionation of the internal calcium pool, such as presented by Elderfield et al., (1996), is an alternative mechanism that can contribute to the divergence of day Sr/Ca ratios

from the mineralogical line. This mechanism is based on the idea that foraminifera calcify from an internal pool where the concentration of Ca represents a balance between precipitation and replenishment. As calcification rates increase, relative to flushing, the [Ca] of the internal pool becomes depleted, causing the foraminifer to incorporate trace elements in different ratios as a function of the partition coefficient (D). Because the magnitude of this effect would depend entirely on the fraction of Ca remaining in the internal pool, we can predict how Rayleigh fractionation would affect test Me/Ca ratios (Gagnon et al., 2007). This prediction, based on day values of foraminiferal Mg/Ca, is plotted in Figure 3.18 as the Rayleigh line. The Rayleigh process moves Me/Ca ratios off the mineralogical line, much like kinetics.

The relationship between day Mg/Ca and Sr/Ca initially appears shifted in the same direction as the Rayleigh line. However, the large amount of scatter in day Mg/Ca and Sr/Ca measurements makes it difficult to attribute this observation solely to Rayleigh fractionation. The potential impact of Rayleigh fractionation can also be examined using Mg/Ca and Li/Ca, which have been observed to have a strong positive correlation during the day (Figure 3.20). By making predictions for the changes in Mg/Ca and Li/Ca due only to changes in *f*, the fraction of calcium remaining in the internal calcium pool, we find that this positive correlation is consistent with Rayleigh processes, however, this consistency is observed only during the day, similar to Mg/Ca and Sr/Ca. These observations, combined with the observations that Mg/Ca and Sr/Ca ratios at all other times fall on the same curve as other calcite samples, appears to suggest a different balance between the drivers of Me/Ca incorporation into foraminiferal calcite during day and night, where Rayleigh fractionation or kinetics, if present, is more significant during the day than during the night.

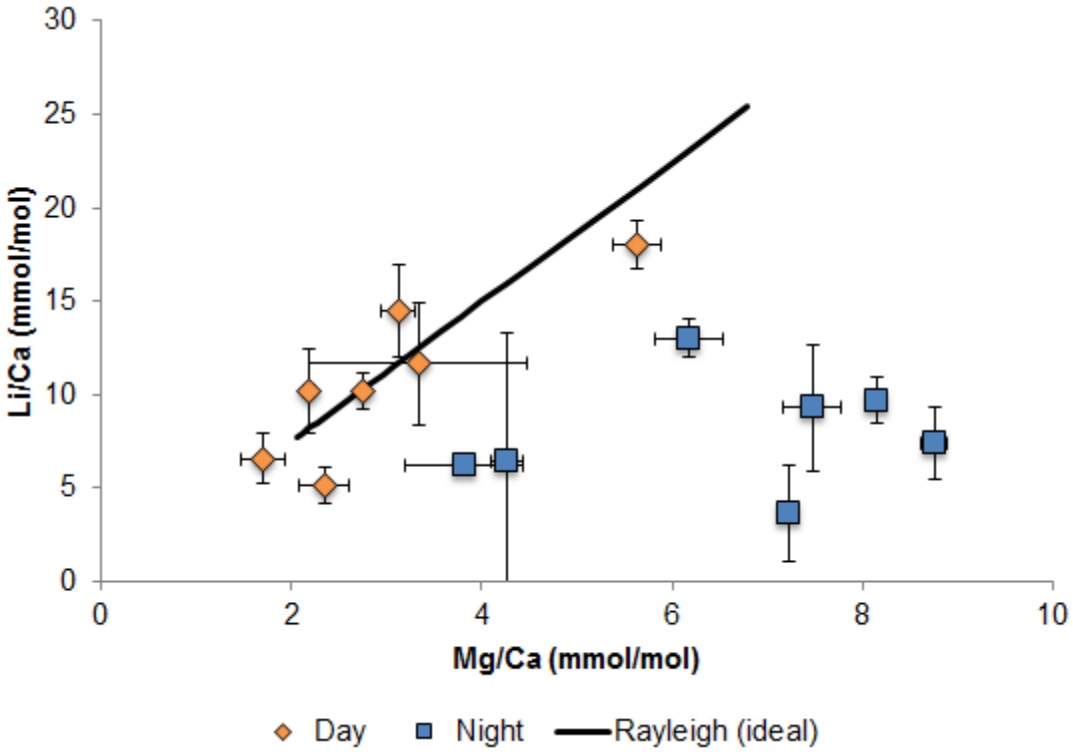

Figure 3.20. Li/Ca and Mg/Ca ratios of day- and night-spiked samples compared to the calculated change in Li/Ca and Mg/Ca based on Rayleigh processes (solid line). Rayleigh effect is calculated using the approach described in Elderfield et al., (1996) and Gagnon et al., (2007).

One caveat to this alternate explanation is that if Rayleigh processes are truly governing the Mg/Ca and Li/Ca trend during the day, the same magnitude of an effect should also be observed for day Sr/Ca ratios. While we do find that day Sr/Ca ratios appear to fall along the same Rayleigh line, the relative magnitude of this effect does not appear to match the magnitude of this effect for Li/Ca. The relationship implied in Figure 3.20 suggests that at $f = 0.63$ (meaning that 63% of the original Ca content of the internal pool remains), Sr/Ca should equal 1.7 mmol/mol. However, the highest Sr/Ca value we observe for day calcification is 1.3 mmol/mol. This can be adjusted by shifting the Rayleigh line downward, so that it crosses the mineralogical line. If this relationship were true, it would suggest that Me/Ca ratios of *O. universa* during the day are strongly influenced by Rayleigh processes. However, if this were the case, it would

imply that the mineralogical line is also shifted downward, as Rayleigh processes cannot move Me/Ca ratios below the inorganic line. This second potential mineralogical line (Figure 3.18B, dotted line), still appears to capture the relationship between inorganic calcite and red coral, and so is possible within error. A shifting of the mineralogical line, however, would imply a stronger contribution of Rayleigh processes to Me/Ca ratios in foraminifera at all times of day, as these ratios are now all moved further away from the line. It may be that both Rayleigh fractionation and kinetic effects are acting on foraminifera at the same time, driving Mg/Ca and Sr/Ca ratios away from the mineralogical line. At present, we cannot definitively distinguish between the two effects, but the overall effect is likely to be some combination of the two.

The discovery that Li/Ca differs between day and night in a way that is inversely proportional to variations in Mg/Ca has implications for the Mg/Li method of correcting for Mg/Ca variation, proposed by Bryan and Marchitto, (2008) for benthic species. This is based on the idea that foraminiferal Li/Ca is indirectly related to saturation state due to changes in the internal calcification pool, and that at high saturation states, taking the Mg/Li ratio removes the suppression of Mg/Ca by saturation state, similarly removing some of the variability in Mg/Ca ratios. However, if Li/Ca and Mg/Ca banding occur inversely to each other in *O. universa* and other species, dividing Mg/Ca by Li/Ca may increase the variability imposed by the vital effect in those species, rather than decrease it. This may be mitigated by the observed positive correlation between Mg/Ca and Li/Ca in calcite precipitated during the day (Figure 3.8), which would suggest that Mg and Li incorporation into calcite is responding to similar mechanisms. The correlation between Mg and Li in day-grown calcite, possibly due to Rayleigh effects, suggests that the Mg/Li temperature correction may indeed decrease variability in Mg/Ca,

assuming that day-grown calcite represents a larger portion of shell Mg and Li than night-grown calcite.

3.4.4 *Model for Me/Ca of foraminifera during biomineralization*

The correlation between Mg and Sr in calcite (Figure 3.18) appears to suggest a strong mineralogical control on the incorporation of these elements into calcite. Rayleigh fractionation and/or kinetic processes may both act to shift the Mg/Ca and Sr/Ca content of calcites away from the mineralogical line. Our observations of diurnal calcification in planktic foraminifera appear to suggest that the Me/Ca ratio of night calcite is more strongly controlled by the mineralogical line. In contrast, day calcification exhibits a stronger kinetic or Rayleigh effect, as expected from calcification rates. If the inorganic line is extrapolated only from the inorganic calcite and red coral data (Figure 3.18B, solid line), all foraminiferal measurements fall slightly above this line. This may suggest that all foraminiferal measurements, regardless of the timing of calcification, are shifted away from this line, indicating some basal level of kinetics or Rayleigh processes. If this is the case, then the position of any given sample between the mineralogical and Rayleigh/kinetic lines outlined in Figure 3.18B is set by the relative magnitude of these effects acting on each sample.

In order to understand this correlation, it is important to understand which processes result in movement along the mineralogical line. Changes in the Mg/Ca of the precipitation fluid would also result in changes in the Mg/Ca of the calcite (Figure 3.19 for example; Mucci and Morse, 1983). If the Sr/Ca content of any given sample of calcite is set by Mg/Ca, these shifts would result in commensurate changes in Sr/Ca. Foraminifera have a much lower Mg content than inorganic calcite (Katz, 1973; Duckworth, 1977; Mucci and Morse, 1983; Nürnberg et al., 1996; Bentov and Erez, 2006; Evans et al., 2018). If magnesium were actively being pumped out

of the calcifying fluid, this would also result in a lower Sr/Ca than inorganic calcite, as the entire system moves along the mineralogical line.

In this scenario, Mg heterogeneity is at least in part a result of increased Mg pumping during the day, which affects other Me/Ca ratios accordingly. Importantly, this mechanism implies that only magnesium pumping is necessary to affect the behavior of other elements such as strontium, without invoking the need for special pumps or the promiscuity of pumps for less physiologically relevant ions. This mechanism can also explain our findings without the need to invoke trans-membrane transport of Ca, one proposed model for the biomineralization of foraminifera (Nehrke et al., 2013).

Mechanistically, the cause of this mineralogical line is not fully understood. Hypotheses include deformations caused in the mineral lattice by the incorporation of Mg^{2+}, which create sites where Sr^{2+} can be accommodated (Mucci and Morse, 1983). This could mean that multiple independent processes could cause shifts along the mineralogical line, for example, pumping or changes in the partition coefficient of Mg (D_{Mg}) due to changes in temperature. Attempts to resolve the basis of this mechanism through a combination of solid-solid solution thermodynamics and atomistic calcite surface growth models are promising (Nielsen et al., 2013; Lammers and Mitnick, 2019). Kinetic effects and Rayleigh effects would then both act separately from this mechanism, to shift Me/Ca ratios away from the mineralogical line (Figure 3.19).

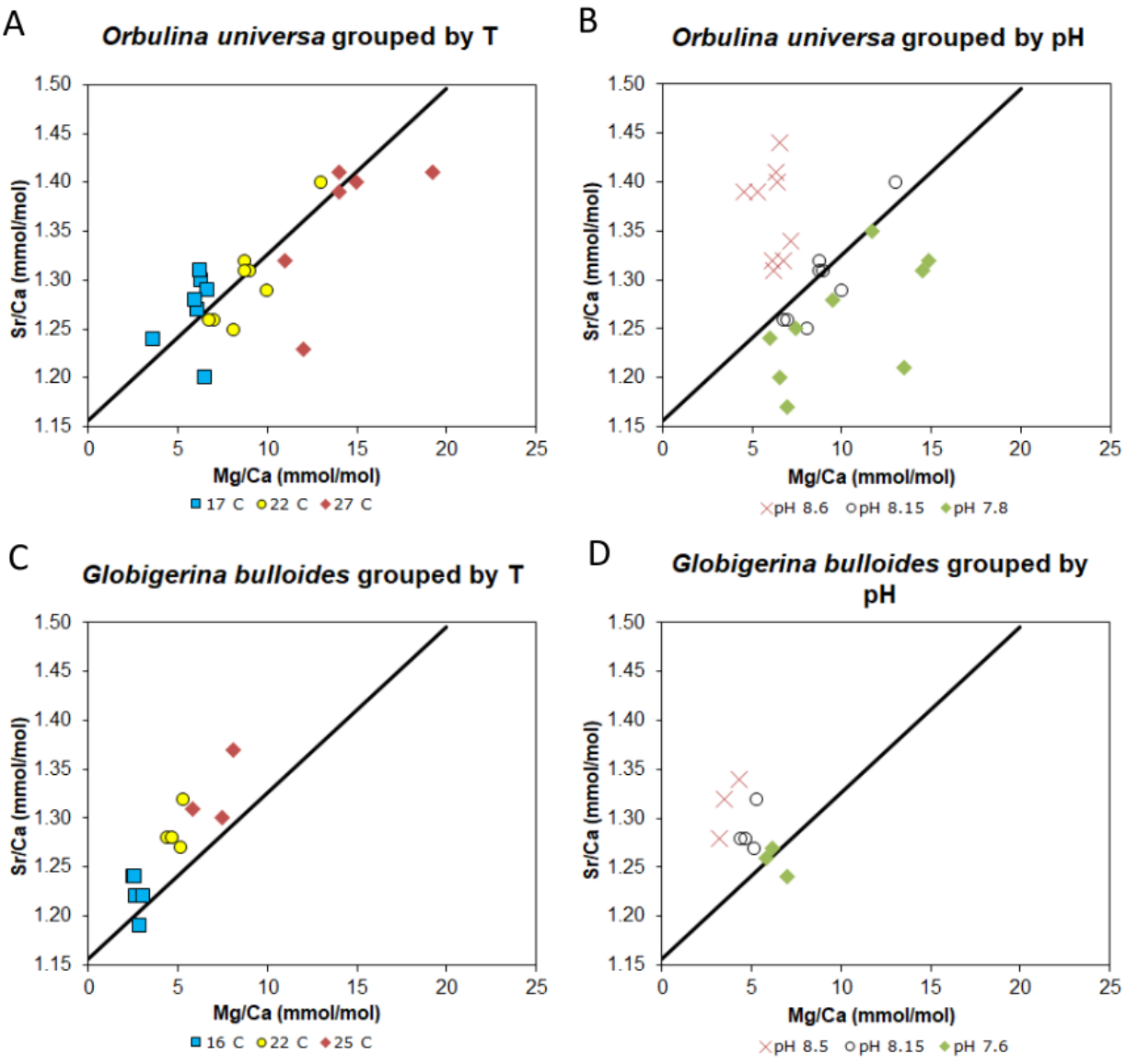

Figure 3.21. A) Mg/Ca and Sr/Ca ratios of *O. universa* samples cultured in treatments of varying temperature. B) Mg/Ca and Sr/Ca ratios of *O. universa* samples cultured in treatments of varying pH. C) Mg/Ca and Sr/Ca ratios of *G. bulloides* samples cultured at varying temperature. D) Mg/Ca and Sr/Ca ratios of *G. bulloides* cultured at varying pH. All foraminiferal data taken from Lea et al., (1999). Black lines represent the mineralogical line (Figure 3.18)

Examining the influence of temperature and pH on Mg/Ca and Sr/Ca ratios from *O. universa* and *Globigerina bulloides* measured by Lea et al., (1999), we observe that both Mg/Ca and Sr/Ca appear to increase with temperature in these two species (Figure 3.21). This increase

in temperature is consistent with the mineralogical line in *O. universa* (Figure 3.21A), and is raised slightly above the mineralogical line in *G. bulloides* (Figure 3.21C), albeit with a similar slope. This may indicate a species-specific difference in kinetic processes, however, temperature in both species appears to move Me/Ca ratios along the mineralogical line. In contrast, pH appears to shift Me/Ca away from the mineralogical line, with Me/Ca ratios being shifted downward at low pH and Me/Ca ratios being shifted upward at high pH in both *O. universa* (Figure 3.21B) and *G. bulloides* (Figure 3.21C).

It should be noted that these observed trends may be due to changes in the saturation state of calcite in seawater (Ω_{sw}) rather than pH. Raitzsch et al., (2010) observed that as saturation state is increased through the addition of [Ca^{2+}] into seawater, foraminiferal Sr/Ca increases and foraminiferal Mg/Ca decreases. However, changes in pH would also result in changes in saturation state, as the concentration of carbonate ion in seawater ([CO_3^{2-}]) is generally coupled to pH. Thus, even if saturation state is the primary driver of the shifts away from the mineralogical line, if pH is changed while $[Ca]_{sw}$ remains constant, the same effect as in Figure 3.21 would be observed. This potential correction merits further investigation, in order to distinguish pH and Ω_{sw} from other processes active in calcification.

The observed increase in Sr/Ca with increasing saturation state may be reflecting a kinetic effect, where growth rate increases as Ω_{sw} increases. Calcification rate has been observed to increase in inorganic calcites as the ratio of [CO_3^{2-}]/[Ca^{2+}] approaches 1, thus, as saturation state increases while [Ca^{2+}] is held constant (Nehrke et al., 2007). A similar observation has been noted in foraminifera (Allen et al., 2016), with the assumption that foraminifera raise the pH of the calcifying fluid to ~9 in order to promote calcification (Bentov et al., 2009; de Nooijer et al., 2014). It may be possible to test whether this increase is due to growth rate by measuring shell

^{44}Ca, which has been observed to decrease in inorganic calcite at increasing growth rates and to be correlated with D_{Sr} (Tang et al., 2008b). The multi-spike method can be adapted to measure Ca isotopes (Gagnon et al., 2012), and examining whether similar shifts in $\delta^{44}Ca$ are present in samples cultured at varying Ω_{sw} may allow researchers to quantify the effect of pH and Ω_{sw} on foraminiferal calcification rate.

If the observed shifts away from the mineralogical line are due to changes in precipitation rate as a function of Ω_{sw}, and if Mg/Ca is similarly affected by kinetic effects, we would expect to also see changes in the Mg/Ca ratio as a function of Ω. If Mg/Ca were increasing with precipitation rate such as suggested by Mavromatis et al., (2013), we would expect to see calcite composition shifted to the right (closer to the line) at higher Ω, and to the left (further away from the line) at lower Ω. However, we observe the opposite. Calcite composition is shifted to the left (away from the line) at higher Ω and to the right (closer to the line) at lower Ω (Figure 3.21). This is consistent with the observation that Mg/Ca decreases with increasing saturation state (Lea et al., 1999; Russell et al., 2004; Raitzsch et al., 2010) and may indicate that Mg/Ca decreases as precipitation rate increases. This relationship would be consistent with the growth-entrapment model of trace element incorporation described in DePaolo, 2011 and restated in Allen et al., 2016, which states that as mineral growth rates increase, the incorporation of cations larger than Ca^{2+}, such as Sr^{2+}, would increase while the incorporation of ions smaller than Ca^{2+}, such as Mg^{2+}, would decrease.

The observation by Spero et al., (2015) that the decrease in Mg/Ca with increasing pH is primarily driven by a decrease in the Mg/Ca ratio of night calcite suggests that the interpretation of these processes may not be straightforward. For example, if Mg/Ca is positively correlated with precipitation rate, as suggested by Mavromatis et al., (2013), a decrease in precipitation rate

during the night at high pH would ultimately result in a decrease in shell Mg/Ca. However, we do not observe a decrease in night precipitation rate in foraminiferal specimens that were cultured at variable pH (Table 7.1). Rather, we observe a slight increase in night precipitation rate with increasing pH leading to a decrease in the fraction of calcite precipitated during the day (Figure 8.18). This is consistent with our observations that Sr/Ca increases as pH increases, and indicates that foraminiferal Mg/Ca may decrease as precipitation rate increases.

So far, this model only takes into account the portions of the foraminiferal calcite that are not being affected by the organic sheet from which the calcite forms. The geochemistry of the layer of calcite around the organic sheet can be different, as observed in Branson et al., (2016) and Chapter 2, which show that Na and Mg are high in organic sheets. This effect is local and does not impact whole test composition significantly. Organic sheets may also be influencing the incorporation of Li into calcite. Li/Ca is observed to be high around the spine region in all three foraminiferal specimens examined using NanoSIMS. This is similar to previous observations of Na/Ca (Chapter 2), which show that Na is also high around the spine region, an observation that was previously attributed to high Na in the organic sheath that surrounds the spines during their formation (Spero, 1988). However, we do not observe high Li/Ca in the primary organic sheet (POS) using NanoSIMS. This may be because of the low number of Li counts and low resolution of Li using NanoSIMS, which also makes this imaging technique unable to resolve diurnal Li/Ca banding. A correlation between Li and Na in organic sheets would not be unexpected, as both Li and Na are monovalent cations and it has previously been stated that the two likely incorporate into calcite using the same mechanisms and pathways (Füger et al., 2019).

Organic constituents have been shown to change the rates of molecular exchange in growing calcite (Stephenson et al., 2008), and precipitation rate can be affected by the presence

of impurities such as Mg and Sr in the calcifying solution (Morse et al., 1997; Wasylenki, Dove, Wilson, et al., 2005; Wasylenki, Dove and De Yoreo, 2005). Thus, the organic-mineral interactions could be another process that acts to shift Me/Ca ratios away from this mineralogical line, but would most likely do so within a kinetic framework that could be interpreted in the context of the inorganic kinetic effect.

However, despite the influence of all of these other processes, the correlation between Mg/Ca and Sr/Ca in our samples with inorganic and other biogenic samples, both in terms of mineralogical effects (Figure 3.18) and kinetic effects (Figure 3.19) is both surprising and promising. Given the complex physiology of minerals, and the localized effect of organic-mineral interactions, observing such a good correlation is unexpected, and gives hope that it may be possible to model the complex process of biomineralization using a geochemical approach.

3.4.5 *Scaling up from banding to whole test composition*

The impact of internal variability on proxies such as the Mg/Ca sea surface temperature proxy is often reduced by averaging multiple individuals into a single data point. This variability can be inferred from plots of standard deviation versus the number of individuals included in a sample, and appears to follow the expected curve for standard error rather than that of analytical variability (Boyle, 1995; Anand and Elderfield, 2005; Sadekov et al., 2008). These observations of internal variability can be inverted to estimate the predicted variability within a single foraminifer. In *O. universa* specimens cultured under ambient seawater conditions (Lea et al., 1999; Russell et al., 2004; Hönisch et al., 2013), the internal variability in Mg/Ca, measured as the relative standard deviation between individuals, is ~20%.

Our growth rate data provide us with the unique opportunity to examine the contribution of diurnal growth rate to internal variability. For example, in the case of Mg/Ca, the mean Mg/Ca

of a single *O. universa* test will be a function of the Mg/Ca ratio of calcite grown during the day, the Mg/Ca ratio of calcite grown during the night, and the relative proportion of day- and night-grown calcite. Expressed as an equation, this is:

$$(Mg/Ca)_{foram} = X_{day} * (Mg/Ca)_{day} + X_{night} * (Mg/Ca)_{night} \quad (3.11)$$

where X_{day} refers to the fraction of the foraminifer grown during the day, X_{night} refers to the fraction of the foraminifer grown during the night, $(Mg/Ca)_{day}$ refers to the Mg/Ca ratio of day-grown calcite, and $(Mg/Ca)_{night}$ refers to the Mg/Ca ratio of night-grown calcite. Because the sum of X_{day} and X_{night} must be equal to 1, this equation can also be written as:

$$(Mg/Ca)_{foram} = X_{day} * (Mg/Ca)_{day} + (1 - X_{day}) * (Mg/Ca)_{night} \quad (3.12)$$

For simplicity, we will refer to $(Mg/Ca)_{foram}$ as F, $(Mg/Ca)_{day}$ as D, and $(Mg/Ca)_{night}$ as N for the remainder of the text. Using this terminology, we can rearrange the above equation so that:

$$F = X_{day} * (D - N) + N \quad (3.13)$$

Variability in F (σ_F) will then be a function of the variability in X_{day}, the variability in D, and the variability in N:

$$\sigma_F^2 = \left(\frac{\delta F}{\delta X}\right)^2 \sigma_X^2 + \left(\frac{\delta F}{\delta D}\right)^2 \sigma_D^2 + \left(\frac{\delta F}{\delta N}\right)^2 \sigma_N^2 \quad (3.14)$$

If we assume, for the purposes of this thought experiment, that the error associated with D and N is small, we find that the error in F becomes dominated by the error in X_{day}, as follows:

$$\sigma_F^2 \approx (D - N)^2 \sigma_X^2 \quad (3.15)$$

$$\sigma_F \approx (D - N)\, \sigma_X \quad (3.16)$$

Our previous study (Chapter 2), which imaged 45 *O. universa* specimens using ToF-SIMS, provides us with a useful dataset to test whether the relationship described above can be used to estimate the contribution of banding to individual variability. Based on this dataset, we

observe that X_{day} has a mean of 0.60 across 45 individuals, with a standard deviation (σ_X) of 0.071 (Figure 3.12B). If we assume that a typical value for $(Mg/Ca)_{day}$ is ~3 mmol/mol, and a typical value for $(Mg/Ca)_{night}$ is ~10 mmol/mol, not unreasonable based on our observations in this study, the calculated Mg/Ca of this foraminifer would be 5.80 mmol/mol, based on Equation 3.12. Similarly, based on Equation 3.15, σ_F = 0.50 mmol/mol. This results in a relative error of ~9%, or roughly half of the observed individual variability. The remaining half may be accounted for by variability in $(Mg/Ca)_{day}$ and $(Mg/Ca)_{night}$, however, this simple calculation shows that the propagated variability in the relative growth rate between day and night in *O. universa* can explain a large portion of observed individual variability, resulting in uncertainty in paleotemperature reconstructions.

This model predicts that foraminiferal Mg/Ca ratio changes as a function of two factors: (1) the amplitude of banding, and (2) the relative fraction of day growth versus night growth. The first factor may be driving the observed increase in Mg/Ca as pH decreases (Russell et al., 2004), because the amplitude of night Mg/Ca banding has also been observed to decrease with increasing pH, and vice versa (Spero et al., 2015). A decrease in the magnitude of night Mg/Ca ratios would result in a decrease in F, which is consistent with observations. The observation that X_{day} also decreases with increasing pH (Figure 8.18) would ordinarily act to increase F, as this would result in a decrease in the X_{day} * (D-N) term, however, because night Mg/Ca ratios are also decreasing as pH increases, the overall effect appears to be an increase in F. Similarly, a decrease in the amplitude of banding would result in a decrease in D-N, which would result in a decrease in variability. Thus, we would expect individual variability to decrease at high pH, and indeed, this is observed in cultured foraminifera (Russell et al., 2004).

Salinity is also observed to affect Mg/Ca ratios (Hönisch et al., 2013), with Mg/Ca ratios increasing at higher salinity. Similarly, in samples that were cultured at different salinities (30.0 to 36.0 psu, see Table 6.1), X_{day} is observed to decrease as salinity increases (Figure 8.19). A decrease in X_{day} would result in an overall decrease in the X_{day} * (D-N) term, which would increase total Mg/Ca ratios as whole shell Mg/Ca ratios become more influenced by the comparatively higher Mg/Ca of night calcite.

This framework can also be used to predict how other elements and proxies will be affected by internal variability. For example, this study has shown that both Li/Ca and Sr/Ca vary between day and night in foraminiferal samples. Assuming that this variability is reflective of typical variability in *O. universa*, diurnal heterogeneity appears to contribute to internal variability by 2.1% for Li/Ca and ~0.22% for Sr/Ca. The relatively smaller amplitude of banding for both Li/Ca and Sr/Ca compared to Mg/Ca results in a smaller contribution of banding to internal variability in these elements. By examining the response of relative error to sample size in other species of foraminifera, and by considering the difference in growth rate between day and night in these species, we can also use this method to gain a better understanding of the significance of diurnal banding in other species of foraminifera more commonly used for paleoceanography.

3.5 CONCLUSIONS

The multi-spike method described Gagnon et al., (2012) is an effective way of resolving Me/Ca in cultured planktic foraminifera, with high precision for Mg/Ca, Sr/Ca, and Li/Ca. When measured using this high precision, Sr/Ca appears to show a slight difference between day and night, with higher Sr/Ca during the night. This difference is significant at the 85% level of confidence. This result appears to run counter to the observation that Sr/Ca should increase with

growth rate in calcite (Tang et al., 2008a), as growth rates are high during the day and low at night, however, comparing our measurements of D_{Sr} to the inorganic calcite data from Tang et al., 2008a and De Paolo, 2011 shows that our data may still be consistent with a kinetic effect on Sr incorporation at the bulk scale. However, a kinetic growth rate effect cannot explain diurnal Sr/Ca banding.

Li/Ca is also observed to change between day and night, with high Li during the day and low Li during the night. This trend is anti-correlated to the observed trend in Mg. This trend may be due to changes in the carbonate chemistry of the foraminiferal microenvironment due to photosynthesis and respiration, or may possibly be due to changes in precipitation rate. Using the multi-spike method to examine Li/Ca in species without photosynthetic symbionts may help determine whether this trend is more likely to be due to carbonate chemistry or due to growth rate.

Mg/Ca and Sr/Ca appear correlated during the night, while Mg/Ca and Li/Ca are correlated during the day. The correlation between Mg/Ca and Sr/Ca during the night is consistent with other measurements of Mg/Ca and Sr/Ca in calcite samples reported in the literature, suggesting that this relationship is some inherent, mineralogical property of calcite. Rayleigh and kinetic processes can shift Me/Ca ratios away from this mineralogical line, and appear to be driving the correlation between Mg/Ca and Li/Ca during the day. This indicates that the difference between any given data point and the mineralogical line may be explained by Rayleigh or kinetic processes. This model may provide a possible way to separate temperature, growth rate, pH, and other effects from the paleorecord.

The observation that Me/Ca ratio changes between day and night has implications for internal variability, as it appears that some types of internal variability may be dependent on the

fraction of the shell precipitated during the day (X_{day}). Calculating internal variability based on X_{day} alone can account for up to half of observed individual variability in *O. universa*, showing a strong dependence of Me/Ca ratios in *O. universa* on diurnal patterns.

Chapter 4. MG/CA AND SR/CA OF GAMETOGENIC CALCITE IN O. UNIVERSA

The Mg/Ca sea surface temperature proxy in planktic foraminifera is one of the most widely-used proxies for past ocean temperature, however, previous studies have shown that Mg/Ca varies throughout the test independent of temperature in a way that cannot be explained mechanistically. This heterogeneity can be divided into three main categories: (1) systematic diurnal heterogeneity throughout the organism's life, (2) high Mg/Ca at the location of the primary organic sheet (POS) of each chamber, and (3) gametogenic calcification. In this study, we examine cultured specimens of *Orbulina universa*, a species of planktic foraminifer, that were placed into isotopically labeled seawater at the onset of gametogenesis. Examining the metal-to-calcium (Me/Ca) ratios of the labeled calcite using a novel multi-isotope technique, we find that this calcite is high in both Mg/Ca and Sr/Ca. However, this observed increase may also be due to diurnal heterogeneity, as all foraminifera underwent gametogenesis during night periods and both Mg/Ca and Sr/Ca have been observed to be high in calcite grown at night. The amplitude and width of Mg banding support the suggestion that this observed increase is due to night calcification. If true, this suggests that foraminiferal Me/Ca ratios increase towards the end of the organism's life.

4.1 INTRODUCTION

The previous chapter described a general set of mechanisms, which can explain much of the Me/Ca variability observed in foraminifera. However, other specific stages of growth may override these mechanisms, or alter them in different ways. For example, organic-mineral interactions can influence the Me/Ca ratios of associated calcite (Branson et al., 2016; Chapter

2). Various additional growth processes, corresponding to different stages in a foraminifera's life history could also affect whole shell Me/Ca ratios, which would ultimately affect the geochemical proxies derived from these ratios. In order to correct for these effects, it is necessary to understand how Me/Ca ratios are affected by various growth processes, and to which extent these growth processes are active in different species of foraminifera.

To further understand how the biomineralization process affects Me/Ca ratios, we examine gametogenic calcite, a layer of calcite precipitated over the shell of the organism at the final stage of its life cycle. For this study, we focus on *Orbulina universa*, a spinose planktic foraminifer, whose simple shape and spherical geometry allows us to examine intrashell heterogeneity without needing to consider variables such as chamber formation and morphology. As it reaches the end of its life, *O. universa* shortens its spines and fills its terminal sphere with dense cytoplasm, causing it to sink in the water column (Bé, 1980). At the end of its life cycle, *O. universa* undergoes gametogenesis, and precipitates a layer of calcite over the entirety of this test. This layer is referred to as 'gametogenic calcite'. In the remainder of the text, we will refer to the calcite grown earlier in the organism's life as 'ontogenic calcite', to distinguish it from gametogenic calcite. This gametogenic calcite has been observed to represent 4-17% of final shell weight (Hamilton et al., 2008), and has been suggested to have a different Mg/Ca ratio from ontogenic calcite. However, there are contradictions in the literature about the direction of the effect of gametogenic calcite on Mg/Ca, with gametogenic calcite being reported to have high Mg/Ca compared to ontogenic calcite in one study (Nürnberg et al., 1996), and low Mg/Ca compared to ontogenic calcite in another (Sadekov et al., 2005). Thus, although gametogenic calcite may represent an important source of variability in Mg/Ca ratios in *O. universa*, the exact extent of that variability is still uncertain. Gametogenic calcite has also been observed in

Trilobatus sacculifer and *Globigerinoides conglobatus* (Bé et al., 1973; Bé, 1980; Caron et al., 1990; Brown and Elderfield, 1996; Nürnberg et al., 1996), both species of spinose planktic foraminifera. In *T. sacculifer*, gametogenic calcite has been observed to have higher Mg/Ca than ontogenic calcite (Brown and Elderfield, 1996; Nürnberg et al., 1996; Hathorne et al., 2003).

Gametogenic calcite is distinguished from crust calcite, which forms over the test close to the end of the organism's life, and is observed in species such as *Neogloboquadrina dutertrei, Globigerinoides ruber, Globorotalia menardii, G. truncatulinoides, N. pachyderma,* and *N. incompta* to have lower Mg/Ca than ontogenic calcite (Sadekov et al., 2005; Sadekov et al., 2009; Bolton and Marr, 2013; Jonkers et al., 2016; Davis et al., 2017; Fehrenbacher et al., 2017). Unlike gametogenic calcite, which is formed at the moment of gametogenesis, crust calcite can begin to form days before gametogenesis (Fehrenbacher et al., 2017). However, both crust calcite and gametogenic calcite can have similar physical characteristics, such as a thicker shell with distinct euhedral textures (Sadekov et al., 2005). In species that precipitate crust calcite as opposed to gametogenic calcite, not all individuals are observed to form crusts. It has previously been speculated that crust formation is triggered by temperature changes, as foraminifera sink to deeper depths, however, a study by Jonkers et al., (2016) argues against a temperature trigger during crust formation. The exact reason why some individuals from the species listed above form crust calcite while some do not is still unknown. Gametogenic calcite, in contrast, begins forming ~16 hours prior to gametogenesis, and is presumed to form during gametogenesis in all individuals that form this type of calcite, although it varies in thickness from a 'thin veneer' to something that more resembles a calcite crust (Bé, 1980).

In uncultured foraminifera, the difference in Mg/Ca ratios between gametogenic or crust calcite and ontogenic calcite may be due to at least two different factors: (1) differences in the

physiology and biomineralization process involved in forming each type of calcite and (2) differences in environmental conditions, for example temperature, which would affect Mg/Ca ratios if the calcite is formed in different parts of the water column. An effect on Mg/Ca ratios from either of these two factors would result in complications for paleoproxy interpretation, as whole shell Mg/Ca ratios would not entirely reflect sea surface temperature. Separating the influence of these two factors on wild foraminifera is difficult, as both factors may have influenced overall test composition to some unknown degree. However, the impact of water column depth and changes in calcification environment does not need to be considered in cultured foraminifera, which form gametogenic calcite under the same environmental conditions as ontogenic calcite. Thus, the use of cultured foraminifera allows us to assess the impact of changes in physiology or biomineralization pathways on the Mg/Ca ratios of gametogenic calcite, separate from environmental changes. Examining these processes can allow us to examine whether gametogenic calcite is formed through the same process as ontogenic calcite or forms from a different mechanism, which is important in order to understand how gametogenic calcite contributes to foraminiferal variability.

In order to assess the impact of gametogenic calcification on *O. universa*, it is necessary to isolate gametogenic calcite from ontogenic calcite, to analyze the chemical composition of gametogenic calcite separately. However, measuring only gametogenic calcite using imaging techniques such as ToF-SIMS and NanoSIMS, or analytical techniques such as laser ablation is difficult, as the thickness of gametogenic calcite is small to begin with and has been observed to vary between individuals. This makes it difficult to separate gametogenic calcite from the well-characterized phenomenon of Mg/Ca banding, as without a way to positively identify gametogenic calcite, it is possible to mistake gametogenic calcite for either a day or night Mg

band. This may have contributed to previous contradictions about the relative Mg/Ca of gametogenic calcite (Nurnberg et al., 1996; Sadekov et al., 2005). Thus, to measure gametogenic calcite separately from ontogenic calcite, we utilize a technique similar to that used in Hamilton et al., (2008), where cultured foraminifera are placed in isotopically enriched seawater at the onset of gametogenesis. The inclusion of an isotope label into the gametogenic calcite, but not into the ontogenic calcite, will allow us to reliably separate these two types of calcification.

We combine this approach with a novel multi-isotope spike technique (Gagnon et al., 2012), which allows us to use bulk analysis techniques such as ICP-MS to measure the Me/Ca ratios of only the isotopically labeled portion of the test, provided that the stable isotopes used to label the gametogenic calcite are stable isotopes of the metal of interest. This approach, also used in Chapter 3 to examine diurnal variability in Me/Ca ratios in *O. universa*, can be used to obtain Me/Ca ratios of gametogenic calcite with a high level of analytical precision. Using this approach, we aim to answer three questions: (1) to what extent is the Mg/Ca ratio, and possibly other Me/Ca ratios, of gametogenic calcite different from ontogenic calcite, (2) what does this difference indicate about the method of calcification of gametogenic calcite, and (3) how would these differences affect the interpretation of the Mg/Ca paleoclimate proxy?

4.2 Materials and Methods

4.2.1 *Foraminifera culturing*

The *Orbulina universa* specimens used in this experiment were captured using the blue-water collection method described by Huber et al., 1996, and cultured at the Wrigley Marine Science Center at Catalina Island, California according to the method outlined in Lea and Spero, 1992. All specimens were captured after the formation of their terminal sphere, but prior to gametogenesis. After collection they were fed a single day-old *Artemia salina* (nauplii) every

two days and were cultured at constant temperature with a 12hr:12hr light/dark cycle. The foraminifera used in this study were typically cultured for ~5 days in the laboratory before they underwent gametogenesis (range: 4 to 6 days).

The status of individual foraminifera was closely monitored and recorded through daily observations. As individuals reached the end of their life cycle, they tended to shorten their spines, fill their terminal spheres with cytoplasm, and sink to the bottom of the jar (Bé, 1980; Spero, 1988). Individuals in which spine shortening was observed were transferred to seawater labeled with enriched isotopes of lithium, magnesium, strontium, calcium, and barium, and observed hourly. Only specimens that underwent gametogenesis in labeled seawater were set aside for use in this experiment. After gametogenesis was observed, foraminiferal tests were collected, rinsed in deionized water, and stored in micropaleoslides for future analysis.

4.2.2 *Overview of analysis methods*

This study uses the multiple isotope spike technique described in Gagnon et al., (2012), which uses the addition of an enriched isotope label to growing calcite in order to measure Me/Ca ratios with a high level of precision. This method was used because it allows the researcher to label the area of interest in a living foraminifer, in effect performing an isotope dilution experiment within a living foraminifer. Bulk analysis of each individual sample can then be used to calculate the Me/Ca ratio of the labeled portion by making two measurements. One measurement is necessary to obtain the mixing ratio between labeled and unlabeled calcite, while the second uses isotope dilution to obtain the total Me/Ca ratio of the shell. In order to obtain the mixing ratio, this method requires the analysis of both the enriched culture solution ('X', representing the spiked endmember), and a natural abundance sample ('O', representing the

unspiked end member). To obtain a measurement of the total Me/Ca ratio of the shell, a second isotope dilution spike ('XX') must be used for isotope dilution.

The first application of this method to cultured foraminifera is described in Chapter 3, and this analysis uses the same culture solution and isotope spikes as created in that study. Prior to the analysis of foraminiferal samples, the effectiveness of this method was tested using synthetic samples, which were prepared by creating gravimetric mixtures of an isotope spike created to have a similar composition as the labeled portion of a foraminifer, and a consistency standard composed of dissolved coretop foraminifera. This was done at various ratios of spiked solution to natural abundance solution, and the method was applied to these samples in order to calculate the concentration of the spiked solution. Because the same isotope spike solution was used for each synthetic sample, the precision of the method can be determined by examining the distribution of the resulting Me/Ca ratios from each other. If the method were perfectly precise, one would expect the resulting Me/Ca ratios to be equal.

This test was conducted in Chapter 3, and the method was found to have high precision for both Mg/Ca and Sr/Ca, with Mg/Ca having a precision of 6.4% and Sr/Ca having a precision of 0.8%. Li/Ca ratios were also returned with high precision using this method (4.7%), however, precision errors were observed to be large for Ba/Ca (~32%). Because of this, although each of the foraminifera labeled in this experiment was also labeled with a barium isotope spike, we do not discuss the analysis of Ba in this study. Error was also observed to increase as the percentage of the solution that had been enriched decreased, consistent with the predictions of Gagnon et al., (2012).

Foraminiferal samples were cleaned and measured as described in Chapter 3. Because the *O. universa* specimens used in this study were captured as spheres and had grown some of their

calcite in the wild, a foraminifer that had been captured as a sphere and cultured at constant temperature in filtered seawater was dissolved and used as a natural abundance standard (R_o), as this would produce an isotope ratio most similar to the ratio of the unlabeled calcite in the foraminifera used in this study.

Me/Ca ratios of the spiked portion of the calcite were calculated using the same procedure as in Gagnon et al., (2012) and in Chapter 3. Because we assume that the labeled portion of the calcite represents gametogenic calcite in this case, while the unlabeled portion of the calcite represents ontogenic calcite, we calculate the Me/Ca ratios of the *ontogenic* calcite by rearranging the equation presented in Gagnon et al., (2012):

$$\left(\frac{\mathrm{Me}}{\mathrm{Ca}}\right)_x = \left(\frac{{}^{48}A_x\,({}^{48}F+1)}{{}^{ref}A_x\,({}^{ref}F+1)}\right)T \tag{4.1}$$

where T refers to the total Me/Ca ratio of the shell, and F refers to the fraction of labeled calcite in the shell. $(Me/Ca)_x$ refers to the Me/Ca of the labeled calcite, ${}^{48}A_x$ refers to the isotopic abundance of ^{48}Ca, the Ca reference isotope, in the labeled calcite, and ${}^{ref}A_x$ refers to the abundance of the Me reference isotope in the labeled calcite.

This equation is derived from the following expression:

$$\left(\frac{\mathrm{Me}}{\mathrm{Ca}}\right)_x = \frac{{}^{48}A_x}{{}^{ref}A_x}\frac{{}^{ref}n_x}{{}^{48}n_x} \tag{4.2}$$

where ${}^{ref}n_x$ refers to the number of moles of the reference isotope of the metal (Me) in the labeled portion of the calcite, and ${}^{48}n_x$ refers to the number of moles of ^{48}Ca in the labeled calcite. Using the same reasoning as in the expression above, in order to determine the isotope ratio of the unlabeled calcite (o), the following expression can be written:

$$\left(\frac{\mathrm{Me}}{\mathrm{Ca}}\right)_o = \frac{{}^{48}A_o}{{}^{ref}A_o}\frac{{}^{ref}n_o}{{}^{48}n_o} \tag{4.3}$$

where $^{ref}n_o$ refers to the number of moles of the reference isotope of the metal (Me) in the unlabeled calcite, and $^{48}n_o$ refers to the number of moles of ^{48}Ca in the unlabeled calcite. $^{48}A_o$ refers to the isotopic abundance of ^{48}Ca in the unlabeled calcite, $^{ref}A_o$ refers to the abundance of the Me reference isotope in the unlabeled calcite. Because we assume that the unlabeled calcite is at natural abundance, something that can be tested by measuring a natural abundance foraminifer, we can estimate $^{48}A_o$ and $^{ref}A_o$ using natural abundance isotope ratios.

Solving for $^{ref}n_o/^{48}n_o$, we find that:

$$\frac{^{ref}n_o}{^{48}n_o} = \frac{\left(\frac{^{ref}n_o}{\left(^{ref}n_o + ^{ref}n_x\right)}\right)}{\left(\frac{^{48}n_o}{\left(^{48}n_o + ^{48}n_x\right)}\right)} \frac{^{ref}n_o + ^{ref}n_x}{^{48}n_o + ^{48}n_x} \tag{4.4}$$

Because:

$$T = \frac{^{ref}n_o + ^{ref}n_x}{^{48}n_o + ^{48}n_x} \tag{4.5}$$

as written in Gagnon et al., (2012), we can simplify this equation to:

$$\frac{^{ref}n_o}{^{48}n_o} = \frac{^{ref}X_o}{^{48}X_o} T \tag{4.6}$$

where X_o refers to the mole fraction of the reference isotope in the unlabeled material.

F is defined as:

$$^{48}F = \frac{^{48}n_o}{^{48}n_x} \tag{4.7}$$

for ^{48}Ca, however, analogous expressions can be written for other isotopes. Here, $^{48}n_o$ refers to the number of moles of ^{48}Ca in the unlabeled calcite, and $^{48}n_x$ refers to the number of moles of ^{48}Ca in the labeled calcite. Thus, $^{48}X_o$ can be written as:

$$^{48}X_o = \frac{^{48}n_o}{^{48}n_o + ^{48}n_x} = \frac{1}{1 + ^{48}n_x/^{48}n_o} = \left[\frac{^{48}n_x}{^{48}n_o} + 1\right]^{-1} = \left[\frac{1}{^{48}F} + 1\right]^{-1} \quad (4.8)$$

The full equation for the Me/Ca of ontogenic, unlabeled calcite then becomes:

$$\left(\frac{\mathrm{Me}}{\mathrm{Ca}}\right)_o = \left(\frac{^{48}A_o\,(\frac{1}{^{48}F}+1)}{^{ref}A_o\,(\frac{1}{^{ref}F}+1)}\right)T \quad (4.9)$$

4.3 RESULTS

4.3.1 *Gametogenic and ontogenic Me/Ca ratios*

In total, nine (9) specimens of *O. universa* were analyzed and found to have been labeled with an isotope spike during gametogenesis. The portion of the test labeled can be estimated by examining F, which is the mixing ratio between labeled and unlabeled calcite. Roughly 3-12% of each test was labeled. Because the labeled calcite was grown in spiked seawater, with a slightly different Me/Ca ratio than the natural seawater from which ontogenic calcite precipitated, Me/Ca ratios were converted into partition coefficients (D_{Me}) between calcite and solution, using the equation $D_{Me} = (^{ref}Me/^{48}Ca)_{calcite} / (^{ref}Me/^{48}Ca)_{seawater}$ (see Chapter 3 for more details). In order to compare gametogenic calcite and ontogenic calcite directly, partition coefficients were then converted to implied Me/Ca ratios, where the shell is implied to have grown in seawater with a Me/Ca ratio equal to natural seawater.

The following Me/Ca ratios were obtained for these samples: Li/Ca, Ba/Ca, Sr/Ca, and Mg/Ca. Mg/Ca ratios showed an apparent difference between ontogenic and gametogenic calcite, with mean gametogenic Mg/Ca (14.5 ±1.90 mmol/mol) being 75% higher than mean ontogenic

Mg/Ca from the same test (8.38 ±0.41 mmol/mol) (Figure 4.1). This difference is significant at the 99% level of confidence (see Appendix D). Sr/Ca ratios of gametogenic and ontogenic calcite appeared equal within error, with mean gametogenic Sr/Ca being 1.45 ± 0.18 mmol/mol and mean ontogenic Sr/Ca from the same test being 1.41 ± 0.10 mmol/mol.

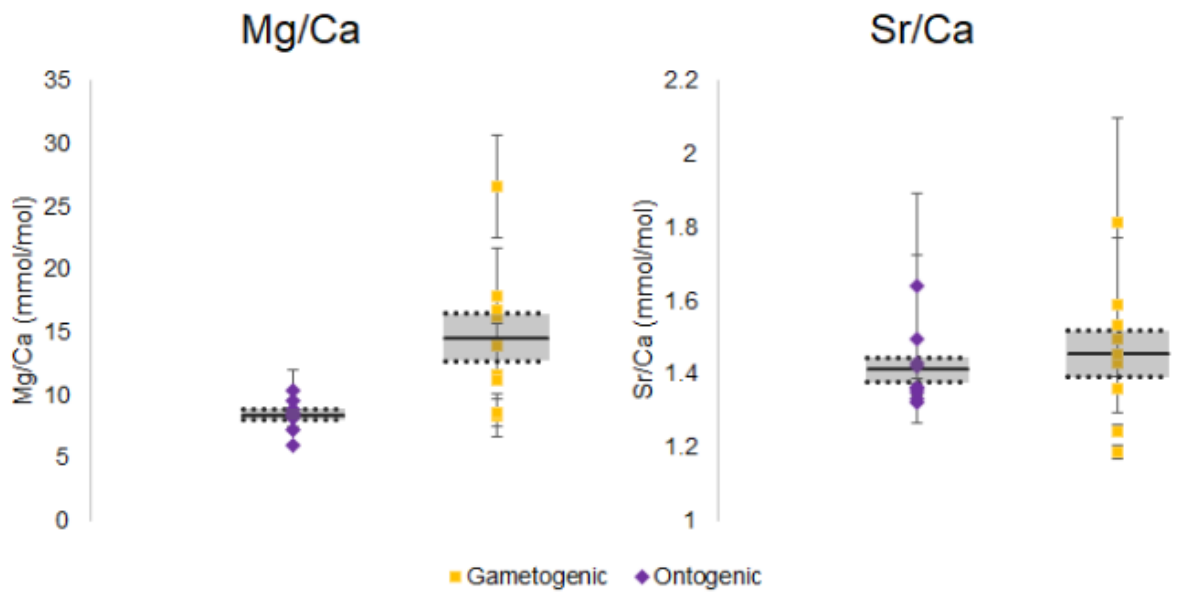

Figure 4.1. Mg/Ca (left) and Sr/Ca (right) ratios of gametogenic and ontogenic calcite from the foraminifera analyzed in this experiment. Plotted values represent the mean gametogenic and ontogenic Me/Ca ratio of nine (9) cultured *O. universa* measurements. Solid lines refer to the means of each group. Shaded areas and dashed lines mark the standard error of the mean. Error bars reflect uncertainty in each individual measurement, as calculated using the procedure outlined in Gagnon et al., (2012).

The mean Li/Ca ratios of gametogenic calcite were found to be 17.7 ±7.38 μmol/mol, compared to a mean Li/Ca of 12.0 ±0.94 for ontogenic calcite. However, the large error associated with the gametogenic calcite measurements suggest that this method may be unreliable for estimating the Li/Ca ratio of gametogenic calcite, likely due to the small fraction of labeled calcite in each test (3-12% labeled, compared to 8-35% labeled in Chapter 3). Ba/Ca measurements showed similar issues, likely exacerbated by the small amounts of Ba in

foraminiferal calcite (see Appendix D). For the remainder of this study, we focus on Sr/Ca and Mg/Ca.

4.3.2 *Correlations between Sr/Ca and Mg/Ca ratios*

There appears to be a positive correlation between Sr/Ca and Mg/Ca in both gametogenic calcite and unlabeled ontogenic calcite (Figure 4.2). In gametogenic calcite, this relationship has an R^2 value of 0.429. In ontogenic calcite, which contains an average of both calcite grown in culture and calcite precipitated in the wild, the positive correlation between Sr/Ca and Mg/Ca has an R^2 value of 0.516. Although a correlation is observed for both groups, the slopes of each line are different. The positive correlation between Sr/Ca and Mg/Ca in gametogenic calcite has a similar slope and R^2 value as the correlation between Sr/Ca and Mg/Ca observed during night calcification (Chapter 3, Figure 4.3).

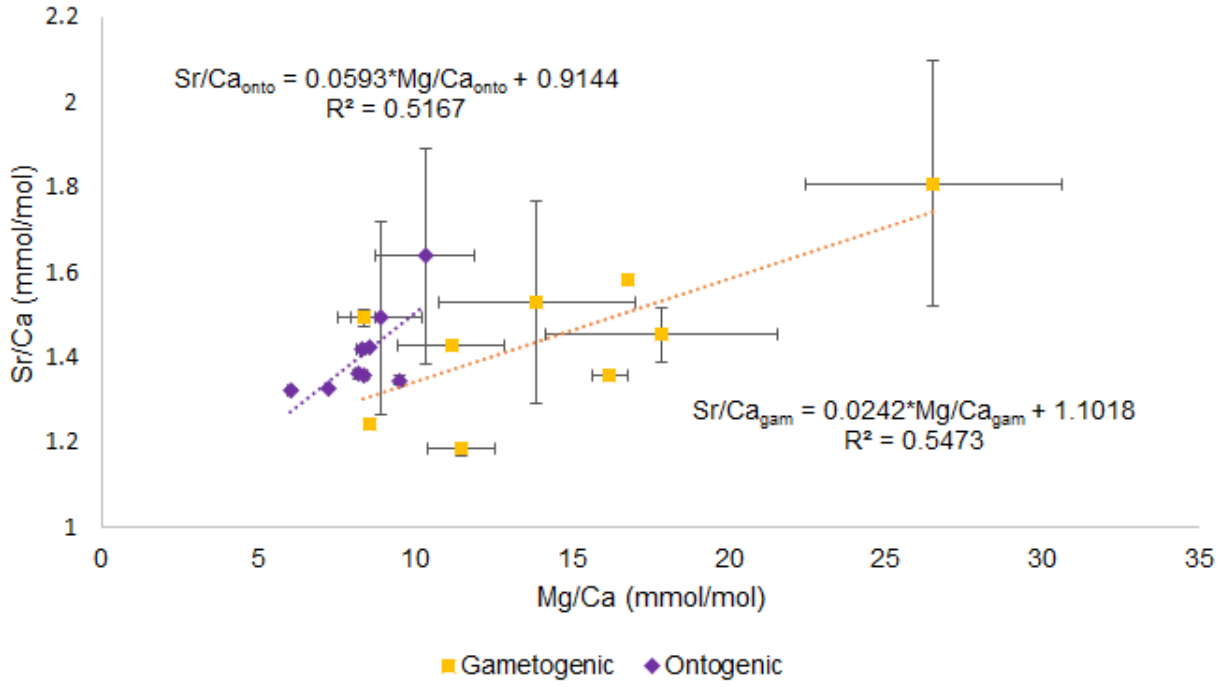

Figure 4.2. Mg/Ca and Sr/Ca ratios plotted against each other for ontogenic calcite (violet diamonds) and gametogenic calcite (yellow squares). Error bars correspond to analytical error for both Mg/Ca and Sr/Ca ratios.

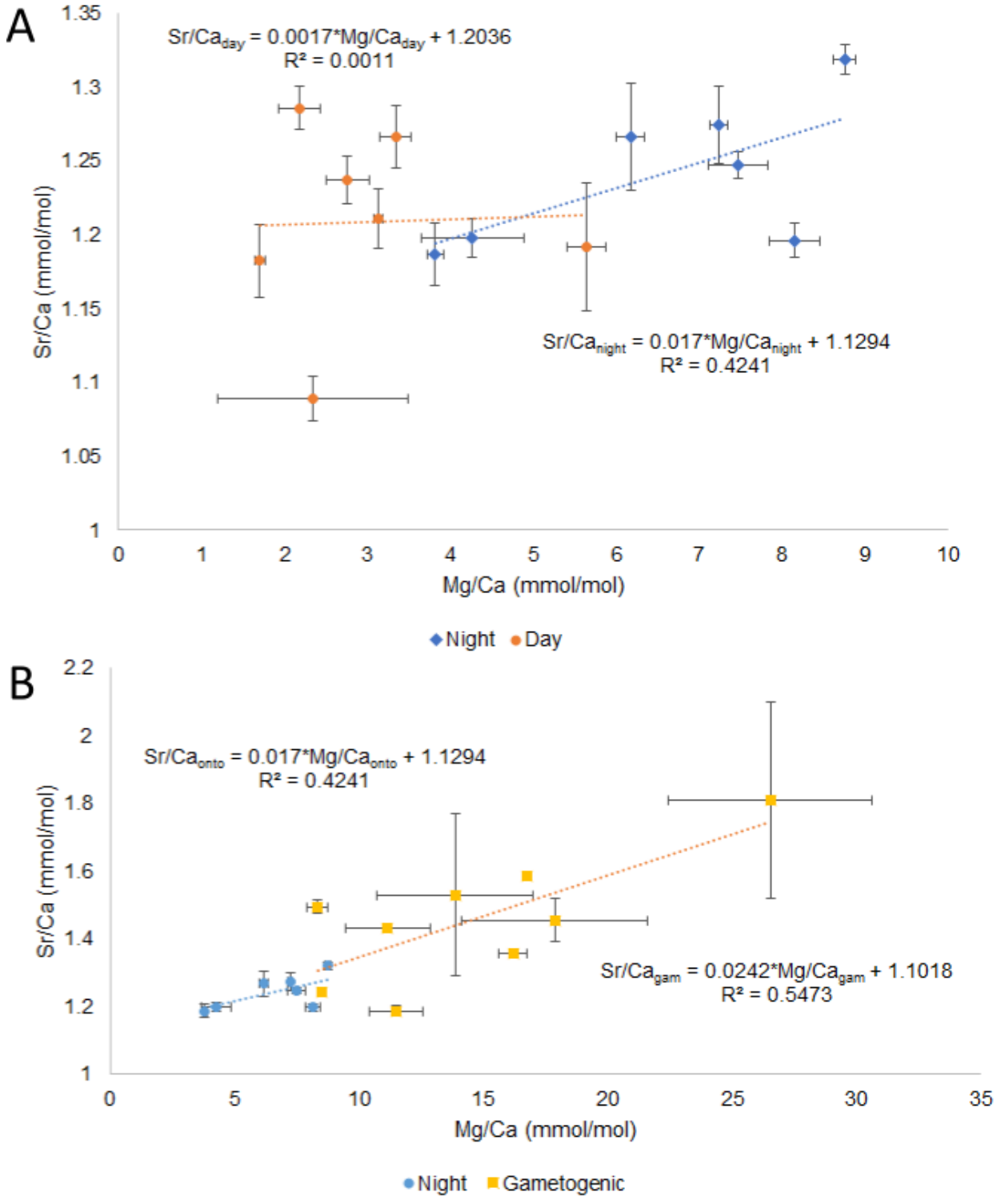

Figure 4.3. A) Mg/Ca and Sr/Ca ratios of day-grown and night-grown calcite. Data from Chapter 3. B) Mg/Ca and Sr/Ca of night calcite (A) compared to gametogenic calcite. Error bars correspond to analytical error for both Mg/Ca and Sr/Ca ratios.

4.4 DISCUSSION

4.4.1 *Variations between gametogenic and ontogenic Mg/Ca ratios*

SEM images from the surface of three out of the nine specimens examined in this experiment were obtained using a TFS Apreo-S with Lovac Scanning Electron Microscope. These images were then compared to helium ion microscope images of *O. universa* samples that had been collected prior to gametogenesis, and so would not have any gametogenic calcification, as well as to images of gametogenic calcification in *T. sacculifer* from Bé (1980) and SEM images from the surface of foraminifera that were placed in labeled seawater at the onset of gametogenesis but did not take up an isotope spike label. These images, which are reported in the Appendix D, reveal a wide range of variation in the exterior of the shells. While those specimens that were placed in labeled seawater but did not record an isotope label did appear to better resemble the specimen collected before gametogenesis than the specimens included in the ICP-MS analysis, we believe that this wide range of variation makes it difficult to determine conclusively whether gametogenic calcification has occurred using microscopy alone. However, the three samples that were labeled with isotope spike and included in this analysis do appear to more closely resemble each other than those that did not take up an isotope spike label, suggesting that some degree of detectable gametogenic calcification occurred in each of these specimens.

Our method of placing foraminifera in labeled seawater during gametogenesis is similar to the method employed by Hamilton et al., (2008), which showed that precipitation during gametogenesis produces 4-20% of the shell's final mass. By using ^{48}F, the parameter that represents the ratio of labeled calcite to unlabeled calcite in each foraminifer, we calculate that 3-12% of our shells were labeled with isotope spike during gametogenesis in our experiment,

which is consistent with Hamilton et al., (2008) (see Appendix D). Thus, it is likely that we are examining a similar terminal portion of the skeleton as was labeled during that study.

The difference in Mg/Ca between gametogenic and ontogenic calcite is significant at the 99% confidence interval, with gametogenic Mg/Ca being 75% higher than ontogenic Mg/Ca. This is comparable to the observation of Nürnberg et al., (1996) in *T. sacculifer*, which showed that gametogenic calcite in that species has a 240% higher Mg/Ca than ontogenic calcite. The enrichment observed in Nürnberg et al., (1996) is much larger than that observed in the *O. universa* specimens examined in this study (75%), which may be due to differences between the two species. ToF-SIMS measurements of cultured *O. universa* (Chapter 2) also show a high Mg/Ca layer at the end of the organism's life, which can sometimes be seen growing on the exterior of the shell inside the pore in cases where pores were imaged (see Appendix D). This observation of high Mg inside pores is consistent with the observation by Bé, (1980) that gametogenesis can 'fill' pores in late stages, assuming that gametogenic calcite is high in Mg/Ca. However, it should also be noted that this observation contradicts the statement of Sadekov et al., (2005) that gametogenic calcite is composed of low Mg/Ca calcite in *O. universa*. The presence of gametogenic calcite in that reference was confirmed by examining scanning electron microscope (SEM) images of *O. universa* specimens and identifying those with a crust that appeared morphologically similar to the gametogenic calcite observed in *T. sacculifer* (Bé, 1980).

If gametogenic Mg/Ca is truly higher than ontogenic calcite in *O. universa*, this has potential implications for the Mg/Ca paleothermometer, as high Mg/Ca may result in overestimates of calcification temperature. The Mg/Ca ratio of gametogenic calcite also appears more variable than that of ontogenic calcite, with gametogenic Mg/Ca ratios ranging from 8-25

mmol/mol, and ontogenic Mg/Ca remaining relatively consistent around 7-10 mmol/mol. If we calculate calcification temperature using the relationship between Mg/Ca and T established for *O. universa* (Lea et al., 1999), the calculated T value from ontogenic calcite alone is roughly 21.3 ±0.60°C, close to the culture temperature of 20°C. The slight discrepancy between the calculated T and the culture T may be explained by these samples not having been entirely grown in culture, but incorporating some mixture of cultured and wild shell growth. In contrast, performing the same calculation using gametogenic calcite alone results in a calcification T of 27.3 ±1.40°C, unrealistically high given both culture and environmental conditions.

We can use the percentage of labeled calcite to combine gametogenic and ontogenic calcite into a single Mg/Ca value for the entire shell, such that $(Mg/Ca)_{foram} = (Mg/Ca)_{gam} * X_{gam} + (Mg/Ca)_{onto} * (1- X_{gam})$, where $(Mg/Ca)_{gam}$ refers to the Mg/Ca ratio of ontogenic calcite, $(Mg/Ca)_{onto}$ refers to the Mg/Ca ratio of ontogenic calcite, and X_{gam} refers to the fraction of the shell composed of gametogenic calcification. Using this approach, we find that using this combined value to calculate temperature results in a mean calcification T of 21.8 ±0.61°C, which represents only a 2.3% increase from the temperature calculated using ontogenic calcite alone. This increase is on the same order as the uncertainty due to individual variability, which may suggest that the added bias due to gametogenic calcite is not as significant a concern as other factors which may bias Mg/Ca more, such as Mg/Ca banding.

The impact of gametogenic calcite on whole test Mg/Ca ratios depends heavily on X_{gam}, the fraction of the test that is composed of gametogenic calcite. At the lowest levels of gametogenic calcification measured in this study (~3%), the average Mg/Ca of gametogenic calcite would have to be ~63 mmol/mol in order to raise calculated temperatures by 5%. This ratio represents a six-fold increase in Mg/Ca between gametogenic and ontogenic calcite, which

has not been observed even in *T. sacculifer*. However, at the highest level of gametogenic calcification measured in this study (~12%), gametogenic Mg/Ca would only have to increase to ~22 mmol/mol in order to raise calculated temperatures by 5%. This is within the range of Mg/Ca ratios observed for gametogenic calcite in this study and represents a 165% increase in Mg/Ca ratios, which has been observed in *T. sacculifer*. Raising X_{day} to the highest value observed in Hamilton et al., (2008), 17%, we find that the Mg/Ca of gametogenic calcite only needs to increase to 18 mmol/mol to impact calculated temperatures by 5%. Thus, it is still possible that gametogenic calcite may bias Mg/Ca ratios, within the range of the observed contributions of gametogenic calcite to shell weight. This approach can also be used to estimate the impact of gametogenic calcite on Me/Ca ratios other than Mg/Ca, provided that the three parameters defined above—$(Me/Ca)_{gam}$, $(Me/Ca)_{onto}$, and X_{gam}—are known.

The Sr/Ca of gametogenic calcite does not appear to be appreciably different from the Sr/Ca of the remainder of the shell, although it should be noted that both Sr/Ca values are slightly higher than the Sr/Ca ratios observed earlier in ontogeny, reported in Chapter 3. The consistency of Sr/Ca ratios between gametogenic and ontogenic calcite suggests that gametogenic calcification is not a concern for geochemical proxies based on Sr/Ca.

4.4.2 *Alternate explanations for observed Me/Ca ratios*

The observed increase in Mg/Ca during gametogenesis may be related to the timing of calcification. With one notable exception (#136, Table 9.1), foraminifera that underwent gametogenesis in this experiment tended to do so during night periods. Because it has previously been observed that Mg/Ca in *O. universa* is high during the night (Eggins et al., 2004; Spero et al., 2015), it is possible that this observed Mg increase may be due to night calcification. In order to test whether this may be true, we compared the Mg/Ca values observed for gametogenic

calcite in this experiment to the Mg/Ca of night bands observed using ToF-SIMS, from the data published in Chapter 2. Gametogenic Mg/Ca was compared with the second-to-the-last Mg band visible in those ToF-SIMS images. This was done to ensure that the high Mg signal was compared to a true Mg night band, and not simply the band at the edge of the shell, which may also be resulting from gametogenic calcification.

The Mg/Ca bands observed using ToF-SIMS span a wide range of Mg/Ca ratios, however, the range of Mg/Ca ratios for the penultimate bands of 45 *O. universa* samples was 3-25 mmol/mol. This encompasses the range of gametogenic Mg/Ca observed in this study (8-25 mmol/mol), suggesting that the amplitude of the increase in Mg is comparable to that of diurnal banding. Although we have not measured the thickness of the foraminifera tests used in the gametogenic calcite experiment, we can estimate the width of these bands by assuming that the shell is 20μm thick and utilizing the percentage of labeled calcite calculated earlier in this work. From that, we estimate that this area of covered by this region is roughly 0.66-2.16μm thick, a thickness also comparable to the thickness of high Mg bands. This supports the idea that this observed increase is due to night calcification.

The relationships between Sr/Ca and Mg/Ca also appear to be consistent between gametogenic calcification and night calcification. When Sr/Ca and Mg/Ca are plotted against each other (Figure 4.3A), there appears to be a slight positive correlation between Sr/Ca and Mg/Ca during the night. Comparing the Sr/Ca and Mg/Ca ratios of night calcite and gametogenic calcite on the same scale (Figure 4.3B) reveals that the two plot on the same relationship, with gametogenic calcite showing higher Mg/Ca and Sr/Ca ratios than night calcite. This may be because the gametogenic calcite data are taken from the end of the organism's life, whereas the night calcite measurements were taken from the first few days after sphere formation, however,

the fact that they appear to follow the same relationship lends further support to the idea that this increase in Sr/Ca and Mg/Ca is due to night calcification. In this case, the difference in the slope of the relationship between Mg and Sr in ontogenic calcite and gametogenic calcite (Figure 4.2) may be because ontogenic calcite Me/Ca values are averages of both day and night calcification, while gametogenic calcite is most similar to night calcification alone.

This may suggest that there is no fundamental change in the mechanism controlling the Me/Ca ratios of gametogenic calcite in *O. universa*, and that any observed changes may be explained by the same process that affects Mg/Ca heterogeneity in the rest of the test. If true, this would mean that the same methods already employed by those using Mg/Ca geochemical proxies to reduce the impact of individual variability would also reduce any variability due to gametogenic calcification, and that constraining the mechanism of diurnal Mg/Ca heterogeneity remains an important next step in order to further correct for individual variability. It should be noted, however, that one foraminifer used in this study (#136) underwent gametogenesis during the day. If gametogenic calcification were truly only due to night calcification, one would expect the labeled portion of that foraminifer to have lower Mg/Ca than ontogenic calcite, due to the relatively low Mg/Ca recorded during the daytime. However, the Mg/Ca ratio observed in the labeled calcite in that specimen is 18.53 ±0.57 mmol/mol, compared to an ontogenic Mg/Ca ratio of 8.20 ±0.09 mmol/mol. This suggests that gametogenic calcification cannot be explained solely by night calcification, however, the chemical composition of gametogenic calcification and night calcification later in ontogeny may still be similar, and may still be contributing similarly to individual variability. The observation that Mg/Ca and Sr/Ca of gametogenic calcite plot on the same mineralogical line as night calcification, inorganic calcite, and various other biogenic

calcites (Chapter 3), suggest that the Mg/Ca ratios of gametogenic calcification are set by the same processes which set the Mg and Sr content of inorganic calcite.

Regardless of whether the chemical composition of gametogenic calcite is unique, the observation that Mg/Ca and Sr/Ca both increase towards the end of the organism's life is interesting. Foraminiferal Na/Ca has also been observed to increase in *O. universa* as the organism ages, and ToF-SIMS mapping of Mg banding in *O. universa* also shows an increase in Mg/Ca towards the end of the organism's life (Chapter 2). This age effect may indicate that something causes *O. universa* to incorporate more trace metals later in its life than early on in ontogeny. Within the framework developed in Chapter 3, this implies movement up the mineralogical line, for unknown mechanistic reasons. The calcite grown during gametogenesis also appears to have a larger range of Mg/Ca values than the remainder of the shell calcite, which may suggest that the observed individual variability between specimens increases with specimen age. This may have implications for Me/Ca proxies in foraminifera, if specimens of various ages and sizes are combined to measure temperature. Understanding what causes this pattern will be useful in order to reduce individual variability and improve paleoclimate reconstructions.

It is possible that the increase in Me/Ca with ontogeny may be due to kinetic effects. Data from our previous study (Chapter 2) appears to show that as the organism ages, the thickness of night Mg bands also increases. In order to determine the effect of age on foraminiferal growth rates, we examine growth rates at two different time periods—growth rates averaged over the first two days of terminal test formation, and growth rates over the last two days of test formation. Because *O. universa* has previously been shown to have a different growth rate between day and night (Chapter 3), we also examine day and night growth rates separately.

Performing this test, we observe that overall growth rates increase slightly over the course of the organism's life. The first two days of test formation have an overall growth rate of 0.14 ±0.06 μm/hr, while the final two days of test formation have an average growth rate of 0.16 ±0.06 μm/hr. Interestingly, this change seems to be driven more by an increase in night calcification than an increase in calcification during the day. Day growth rates do not appear significantly different within error between the first two days of test formation and the last two days of test formation, however night growth rates increase from 0.11 ±0.04 μm/hr during the first two days of test formation to 0.13 ±0.04 μm/hr during the last two days of test formation. This is reflected in calculations of X_{day}, the fraction of the foraminifer test precipitated during the day, which decreases from 0.62 ±0.081 to 0.58 ±0.085. This implies a greater contribution of night calcite to the overall Me/Ca ratio of the test with ontogeny, which may result in higher Mg/Ca ratios overall, as Mg/Ca is much higher during the night.

However, this does not explain why the Mg/Ca ratios of night bands continue to increase with age. It has previously been proposed that foraminifera actively remove Mg from the calcification space, in order to reduce the impact of Mg on calcification (Nürnberg et al., 1996; Bentov and Erez, 2006; Evans et al., 2018). If the efficiency of this process decreases as the organism ages, this would result in a higher Mg/Ca concentration. An increase in calcification rate as the organism ages may also result in a decreased ability to remove Mg from the calcifying space, assuming that the efficiency of this removal process does not also increase to compensate for increasing calcification rate. A decrease in Mg removal would serve to move Me/Ca ratios along the mineralogical line described in Chapter 3 and would explain this observed increase.

While we do observe that gametogenic calcite is shifted further along the mineralogical line from night calcite measured earlier in ontogeny, we also observe that both gametogenic

calcite and night calcification are shifted above the mineralogical line. Average night calcification has a Sr/Ca ratio 9 ±3% higher than predicted based on corresponding Mg/Ca ratios and the mineralogical line. It is possible that some of this shift may be due to kinetic effects and Rayleigh processes, which would act to raise Me/Ca ratios. Gametogenic Sr/Ca ratios are shifted on average, 14 ±9% higher than predicted based on the mineralogical line, which may indicate a stronger contribution of Rayleigh processes and kinetic effects than night calcification. This is reasonable if, for example, gametogenic calcification occurs at a faster calcification rate than night calcite.

Sr/Ca in inorganic calcite has been observed to increase as precipitation rate increases (J. Tang et al., 2008a; DePaolo, 2011). Our previous study has observed that while Sr/Ca does not appear to change between day and night due to growth rates, kinetic effects due to changes in precipitation rate may still shift Me/Ca ratios away from the mineralogical line (Chapter 3). The change in growth rates observed as the organism ages would result in a 3% increase in Sr/Ca based on the relationship between Sr/Ca and growth rate in inorganic calcite. This increase is sufficient to explain the observation that gametogenic calcite appears to be shifted above the mineralogical line more than night calcification. However, we note that our estimates of growth rate were based on diurnal Mg/Ca bands, which have consistent timing in cultured foraminifera, while the timing of gametogenic calcite is still unconstrained. Also, we note that the variability in gametogenic Me/Ca ratios is large, and this shift above the mineralogical line may not be significantly different than the shift observed for night calcification within error. These make it difficult to say for certain whether the magnitude of the kinetic effect should indeed be higher for gametogenic calcification, or whether our observations truly reflect this change. However, this highlights the potential use of the mineralogical line and the extent to which foraminiferal Me/Ca

ratios may be shifted away from it to determine the impact of kinetic effects, Rayleigh fractionation, and other environmental factors in setting the overall Me/Ca ratios of calcite. The relationship between Me/Ca ratios in foraminiferal calcite and the mineralogical line can be used to place constraints on these effects, providing us with a framework to answer questions about biomineralization based on geochemical information.

4.5 CONCLUSIONS

The layer of calcite precipitated in cultured specimens of in *O. universa* during gametogenesis appears to be high in both Mg/Ca and Sr/Ca compared to the remainder of the test. This should result in an increase in calculated temperature using the Mg/Ca sea surface temperature proxy. However, this may be due to diurnal heterogeneity in Mg/Ca and Sr/Ca, rather than gametogenic calcification. The amplitude and width of the high Mg/Ca area examined in this experiment are comparable to the amplitudes and widths of high Mg night bands observed using ToF-SIMS (Chapter 2).

Mg/Ca and Sr/Ca from the outermost layer of the test also appear to have the same positive relationship with each other as observed in night calcification (Figure 4.2), which is also consistent with the Mg/Ca and Sr/Ca ratios of inorganic calcite and other biogenic calcite specimens (Chapter 3). This suggests that night calcification and gametogenic calcification are chemically similar, and are responding to the same processes that also set the Mg/Ca and Sr/Ca of inorganic calcite. However, the Mg/Ca and Sr/Ca ratios of the outer layer of the test are higher than those observed earlier in the organism's life, and are also shifted slightly above the mineralogical line. An increase in Me/Ca ratios with ontogeny has also been observed for Na/Ca using ToF-SIMS (Chapter 2). Increasing calcification rates as the organism ages may be

contributing to these observed increases in Me/Ca ratios, along with an increase in calcification rate during gametogenic calcification. Examining the position of gametogenic Mg/Ca and Sr/Ca ratios relative to the mineralogical line allows us to estimate the potential impact of this yet unconstrained kinetic effect.

Chapter 5. CONCLUSIONS

A high Na and high Mg band similar to the POS associated band that initiates primary sphere formation in *O. universa* was observed in *O. bilobata,* suggesting that this morphotype lays down a new POS over the terminal sphere when it creates this new chamber. This indicates that *O. universa* follows the bilamellar growth model described by Reiss et al. (1957), with an organic sheet laid down over all existing calcite at the formation of each chamber and shows that chamber formation in foraminifera may affect intrashell Me/Ca ratios. However, it is unclear whether the co-location of Na and Mg bands relates to organic sheets in all species. A survey of Na banding in *G. bulloides* and *N. dutertrei* may indicate the presence of species-specific patterns for Na banding. Li observed using NanoSIMS appears to be high in spines (Chapter 3) and in the inner lamella of *O. universa*, suggesting that Li may also be affected by the presence of organic matrices, however, no link between Li/Ca and the POS has yet been observed using this method.

Outside of the POS, Na is also observed to exhibit systematic heterogeneity, which appears as regularly spaced thick and lower magnitude Na bands that are found throughout the test. This form of Na banding is typically inversely related to Mg banding for at least the first few days of sphere formation in *O. universa,* suggesting elevated Na occurs during the daytime. While a $Mg^{2+}/2\ Na^{+}$ exchange mechanism can explain the timing and magnitude of this inverse pattern, such a mechanism cannot explain why the relationship between Mg and Na often diverges later in the test thickening process. To explain this shift in timing, additional or alternative mechanisms should be present.

Other elements and proxies besides Na also appear to display banding on a diurnal scale, when measured using the multi-isotope spike method described in Gagnon et al., (2012) (Chapter

3). In particular, Sr/Ca appears to show a slight difference between day and night, with higher Sr/Ca during the night. This result is inconsistent with the observation that Sr/Ca increases with growth rate in inorganic calcite (Tang et al., 2008a), as growth rates are high during the day and low at night. However, the Sr/Ca ratios of day and night calcite are still consistent with the inorganic curve, suggesting that kinetics may still play a role in setting the overall Sr/Ca of the shell.

Mg/Ca and Sr/Ca are observed to be positively correlated during the night, in a manner that is consistent with both gametogenic calcite and other inorganic and biogenic calcites. This suggests that the correlation between Mg/Ca and Sr/Ca is an inherent mineralogical property of calcite, and thus, some mechanism must be shifting Me/Ca ratios away from this mineralogical line during the day. The correlation between Mg/Ca and Li/Ca during the day is consistent with Rayleigh distillation of the internal [Ca] pool, thus, it is possible that as the foraminifer calcifies more during the day, the internal [Ca] pool becomes depleted, driving Me/Ca ratios away from the mineralogical line. Kinetic effects likely also act to drive Me/Ca ratios away from the mineralogical line and may be contributing to this effect.

Gametogenic calcite (Chapter 4) appears to be high in Mg/Ca compared to ontogenic calcite. This may result in an increase in calculated temperature using the Mg/Ca sea surface temperature proxy. However, this appears chemically similar to night calcification in Mg/Ca, regardless of the timing of gametogenic calcification. The amplitude and width of the high Mg/Ca area examined in this experiment are comparable to the amplitudes and widths of high Mg night bands observed using ToF-SIMS (Chapter 2), and high Sr/Ca night bands observed using the multi-isotope spike method (Chapter 3). Thus, gametogenic calcite may share similar mechanisms of precipitation as night calcification, and may not be a significant concern for

Mg/Ca reconstructions in this species. The Mg/Ca and Sr/Ca ratios of the outer layer of the test are also observed to be higher and more variable than Mg/Ca and Sr/Ca ratios from earlier in ontogeny. This pattern has also been observed for Na/Ca using ToF-SIMS (Chapter 2), suggesting that Me/Ca ratios tend to increase with age, and that this increase with age moves calcite composition along the mineralogical line.

Overall, the results of this dissertation show that the Me/Ca ratios of planktic foraminifera, and by extension, geochemical proxies that rely on these Me/Ca ratios, are affected by the growth processes of these organisms. It is possible that the necessity of species-specific calibration curves during the application of the Mg/Ca proxy may stem from each species having a different test morphology and method of calcification, which affects proxy incorporation. For example, the planktic foraminifera *O. universa* and *G. bulloides* have slightly different distributions of Mg/Ca and Sr/Ca ratios around the mineralogical line (Figure 3.19), with *G. bulloides* Me/Ca ratios being shifted slightly higher above the mineralogical line than *O. universa* Me/Ca ratios. This may indicate a higher influence of kinetic effects on the Me/Ca ratios of *G. bulloides*, potentially suggesting faster calcification rates. The variability in *G. bulloides* samples with regards to pH is also small, which may indicate either a smaller kinetic response with regards to pH, or a greater ability for this species to regulate the pH of its calcifying space. If the latter, this may suggest that *G. bulloides* is more resilient to ocean acidification, and possibly to other environmental perturbations.

One of the goals of this dissertation was to examine the link between intrashell heterogeneity and individual variability. Previous examinations of Mg/Ca variability in *O. universa* under different pH conditions have shown that the observed increase in Mg/Ca as pH decreases is reflected in the high Mg night bands, with the amplitude of high Mg night bands

increasing as pH decreases (Spero et al., 2015). This observation highlights the importance of considering intrashell heterogeneity, and the internal processes which govern calcification at the microscale, when considering foraminiferal proxies. Being able to examine, through the analysis of banding, the contribution of pH to night Mg/Ca ratios will likely reduce the impact of individual variability on foraminiferal samples, as it may become possible to avoid the use of samples that were exposed to varying pH levels or to pick samples from time periods with less heterogeneity. The observation that temperature acts to move the Me/Ca ratios of *O. universa* and *G. bulloides* along the mineralogical line, while pH tends to shift these ratios off the mineralogical line, may allow us to correct for the pH effect on the Mg/Ca temperature proxy in future paleoclimate analyses.

Diurnal heterogeneity is also important to consider for emerging proxies, such as those based on Li/Ca and Na/Ca. If other species of foraminifera are also expressing diurnal heterogeneity, and if this variability is of concern for analysis, it may be possible to limit these effects by focusing on species with less diurnal variability. For example, it may be possible that foraminifera without photosynthetic symbionts exhibit less variability, because the chemistry of the microenvironment may be more constant, resulting in a smaller difference in Me/Ca ratios between day and night. Observing that diurnal variability still exists in these species, however, would also be important, as it would suggest that these species are somehow able to distinguish between day and night without photosynthetic symbionts, suggesting that foraminifera may have some internal clock or circadian rhythm that allows them to regulate their activities on a diurnal cycle. The use of the multi-isotope spike method to examine heterogeneity in more species of foraminifera will be necessary in order to determine whether this is plausible.

The observation that Me/Ca ratios increase with age may contribute to the observation that Mg/Ca ratios are affected by individual size. The effect of ontogeny on Me/Ca ratios is not constant for each individual, however, Me/Ca ratios appear to become more variable as the age of the foraminifer increases (Figure 4.2). Thus, variability may be higher in larger size fractions, and smaller size fractions may have smaller contributions to individual variability. If the observation that gametogenic calcite is chemically indistinguishable from night calcite holds for other species of foraminifera, the presence or absence of gametogenic calcite may not be a concern for paleoceanographers, however, this will need to be confirmed in other species in which a high-Mg/Ca gametogenic layer has been reported.

Overall, this dissertation highlights the various ways by which different growth processes contribute to test Me/Ca. One important result from this dissertation is that there is likely not one single mechanism to explain all of Me/Ca banding in foraminifera, however, Me/Ca banding is likely linked to processes which can shift calcite composition along the mineralogical line. By examining which relationships exist between different sets of elements and proxies, we can continue to constrain the mechanism for Me/Ca heterogeneity, as well as improve on existing paleoproxies. As sample size requirements decrease and as more geochemical proxies continue to be developed, assessing the impact of Me/Ca banding on variability becomes more and more important. Multi-proxy analysis such as the type described in this dissertation can be used to quantify the impact of heterogeneity on internal variability in paleoclimate proxies.

Foraminifera utilize diverse life cycles, morphologies, habitats and methods of shell formation. Some species have photosynthetic symbionts, while some do not, some form gametogenic or crust calcite, while some do not. Even among the perforate foraminifera discussed in this dissertation, there are many unique morphologies and patterns of chamber

formation. Each of these differences may contribute in some way to individual variability. It may be tempting to disregard the use of proxies which appear to be highly impacted by species-specific vital effects or by banding, however, the systematic, regular pattern of intrashell heterogeneity may be in itself a source of information about processes that occur on diurnal scales. The examination of this banding and the causes of it may ultimately help reduce the impact of individual variability on paleoclimate proxies, to the benefit of the field as a whole.

BIBLIOGRAPHY

Allen K. A., Hönisch B., Eggins S. M., Haynes L. L., Rosenthal Y. and Yu J. (2016) Trace element proxies for surface ocean conditions: A synthesis of culture calibrations with planktic foraminifera. *Geochim. Cosmochim. Acta*. Available at: http://linkinghub.elsevier.com/retrieve/pii/S0016703716304525.

Allen K. A., Hönisch B., Eggins S. M., Yu J., Spero H. J. and Elderfield H. (2011) Controls on boron incorporation in cultured tests of the planktic foraminifer Orbulina universa. *Earth Planet. Sci. Lett.* **309**, 291–301. Available at: http://linkinghub.elsevier.com/retrieve/pii/S0012821X11004250.

Anand P. and Elderfield H. (2005) Variability of Mg/Ca and Sr/Ca between and within the planktonic foraminifers Globigerina bulloides and Globorotalia truncatulinoides. *Geochemistry, Geophys. Geosystems* **6**.

Barker S., Greaves M. and Elderfield H. (2003) A study of cleaning procedures used for foraminiferal Mg/Ca paleothermometry. *Geochemistry, Geophys. Geosystems* **4**.

Bé A. W. H. (1980) Gametogenic calcification in a spinose planktonic foraminifer, Globigerinoides sacculifer (Brady). *Mar. Micropaleontol.* **5**, 283–310.

Bé A. W. H., Harrison S. M., Lott L. and Be A. W. H. (2006) Orbulina universa d'Orbigny in the Indian Ocean. *Micropaleontology*.

Bé A. W. H., Harrison S. M., Lott L. and Harrison S. M. (1973) Orbulina universa d ' Orbigny in the Indian Ocean. **19**, 150–192.

Bé A. W. and Lott L. (1964) Shell Growth and Structure of Planktonic Foraminifera. *Science* **145**, 823–4. Available at: http://www.sciencemag.org/content/145/3634/823.abstract.

Bender M. L., Lorens R. B. and Williams D. F. (1975) Sodium, magnesium and strontium in the test of planktonic foraminifera. *Micropaleontology* **21**, 448–459.

Bentov S., Brownlee C. and Erez J. (2009) The role of seawater endocytosis in the biomineralization process in calcareous foraminifera. *Proc. Natl. Acad. Sci. U. S. A.* **106**, 21500–21504.

Bentov S. and Erez J. (2006) Impact of biomineralization processes on the Mg content of foraminiferal shells: A biological perspective. *Geochemistry Geophys. Geosystems* **7**, Q01P08 2005GC001015.

Bentov S. and Erez J. (2005) Novel observations on biomineralization processes in foraminifera and implications for Mg/Ca ratio in the shells. *Geology* **33**, 841–844.

Bijma J., Spero H. J. and Lea D. W. (1999) Reassessing Foraminiferal Stable Isotope Geochemistry : Impact of the Oceanic Carbonate System (Experimental Results). *Use proxies Paleoceanogr. examples from South Atl.*, 489–512.

Bolton A. and Marr J. P. (2013) Trace element variability in crust-bearing and non crust-bearing Neogloboquadrina incompta, P-D intergrade and Globoconella inflata from the Southwest Pacific Ocean: Potential paleoceanographic implications. *Mar. Micropaleontol.* **100**, 21–33.

Boyle E. A. (1995) Limits on benthic foraminiferal chemical analyses as precise measures of environmental properties. *J. Foraminifer. Res.* **25**, 4–13.

Branson O., Bonnin E. A., Perea D. E., Spero H. J., Zhu Z., Winters M., Hönisch B., Russell A. D., Fehrenbacher J. S. and Gagnon A. C. (2016) Nanometer-Scale Chemistry of a Calcite Biomineralization Template: Implications for Skeletal Composition and Nucleation. *Proc. Natl. Acad. Sci. U. S. A.* **113**.

Branson O., Redfern S. A. T., Tyliszczak T., Sadekov A., Langer G., Kimoto K. and Elderfield

H. (2013) The coordination of Mg in foraminiferal calcite. *Earth Planet. Sci. Lett.* **383**, 134–141.

Brown S. J. and Elderfield H. (1996) Variations in Mg/Ca and Sr/Ca ratios of planktonic foraminifera caused by postdepositional dissolution: Evidence of shallow Mg-dependent dissolution. *Paleoceanography* **11**, 543–551.

Bryan S. P. and Marchitto T. M. (2008) Mg/Ca-temperature proxy in benthic foraminifera: New calibrations from the Florida Straits and a hypothesis regarding Mg/Li. *Paleoceanography* **23**.

Burton E. A. and Walter L. M. (1987) Relative precipitation rates of aragonite and Mg calcite from seawater: temperature or carbonate ion control? *Geology*.

Caron D. A., Faber W. W. and Be A. W. H. (1987) Growth of the Spinose Planktonic Foraminifer Orbulina universa in Laboratory Culture and the Effect of Temperature on Life Processes. *J. Mar. Biol. Assoc. United Kingdom* **67**, 343–358.

Caron D. A., Roger Anderson O., Lindsey J. L., Faber W. W. and Lin Lim E. E. (1990) Effects of gametogenesis on test structure and dissolution of some spinose planktonic foraminifera and implications for test preservation. *Mar. Micropaleontol.* **16**, 93–116.

Davis C. V., Fehrenbacher J. S., Hill T. M., Russell A. D. and Spero H. J. (2017) Relationships Between Temperature, pH, and Crusting on Mg/Ca Ratios in Laboratory-Grown Neogloboquadrina Foraminifera. *Paleoceanography* **32**, 1137–1152.

Delaney M. L., Bé A. and Boyle E. A. (1985) Li, Sr, Mg, and Na in foraminiferal calcite shells from laboratory culture, sediment traps, and sediment cores. *Geochim. Cosmochim. Acta* **49**, 1327–1341. Available at: http://www.sciencedirect.com/science/article/pii/0016703785902844.

DePaolo D. J. (2004) Calcium Isotopic Variations Produced by Biological, Kinetic, Radiogenic and Nucleosynthetic Processes. *Rev. Mineral. Geochemistry* **55**, 255–288. Available at: http://rimg.geoscienceworld.org/cgi/doi/10.2138/gsrmg.55.1.255.

DePaolo D. J. (2011) Surface kinetic model for isotopic and trace element fractionation during precipitation of calcite from aqueous solutions. *Geochim. Cosmochim. Acta* **75**, 1039–1056.

Doss W., Marchitto T. M., Eagle R., Rashid H. and Tripati A. (2018) Deconvolving the saturation state and temperature controls on benthic foraminiferal Li/Ca, based on downcore paired B/Ca measurements and coretop compilation. *Geochim. Cosmochim. Acta* **236**, 297–314.

Duckworth D. L. (1977) Magnesium Concentration in the Tests of the Planktonic Foraminifer Globorotalia truncatulinoides. *J. Foraminifer. Res.* **7**, 304–312.

Eggins S. M., Sadekov A. and De Deckker P. (2004) Modulation and daily banding of Mg/Ca in Orbulina universa tests by symbiont photosynthesis and respiration: A complication for seawater thermometry? *Earth Planet. Sci. Lett.* **225**, 411–419.

Elderfield H., Bertram C. J. and Erez J. (1996) Biomineralization model for the incorporation of trace elements into foraminiferal calcium carbonate. *Earth Planet. Sci. Lett.* **142**, 409–423.

Erez J. (2003) The source of ions for biomineralization in foraminifera and their implications for paleoceanographic proxies (Review). *Rev. Mineral. geochemistry* **54**, 115. Available at: http://rimg.geoscienceworld.org/cgi/content/full/54/1/115?ijkey=08ecc7e72affc62b13fb2b1119ac817cb2f292ee&keytype2=tf_ipsecsha.

Evans D., Erez J., Oron S. and Müller W. (2015) Mg/Ca-temperature and seawater-test chemistry relationships in the shallow-dwelling large benthic foraminifera Operculina ammonoides. *Geochim. Cosmochim. Acta*.

Evans D., Müller W. and Erez J. (2018) Assessing foraminifera biomineralisation models through trace element data of cultures under variable seawater chemistry. *Geochim. Cosmochim. Acta* **236**, 198–217.

Fehrenbacher J. S., Russell A. D., Davis C. V., Gagnon A. C., Spero H. J., Cliff J. B., Zhu Z. and Martin P. (2017) Link between light-triggered Mg-banding and chamber formation in the planktic foraminifera Neogloboquadrina dutertrei. *Nat. Commun.* **8**, 15441. Available at: http://www.nature.com/doifinder/10.1038/ncomms15441.

Füger A., Konrad F., Leis A., Dietzel M. and Mavromatis V. (2019) Effect of growth rate and pH on lithium incorporation in calcite. *Geochim. Cosmochim. Acta* **248**, 14–24.

Gabitov R. I., Gagnon A. C., Guan Y., Eiler J. M. and Adkins J. F. (2013) Accurate Mg/Ca, Sr/Ca, and Ba/Ca ratio measurements in carbonates by SIMS and NanoSIMS and an assessment of heterogeneity in common calcium carbonate standards. *Chem. Geol.* **356**, 94–108.

Gabitov R. I., Sadekov A. and Leinweber A. (2014) Crystal growth rate effect on Mg/Ca and Sr/Ca partitioning between calcite and fluid: An in situ approach. *Chem. Geol.* **367**, 70–82.

Gagnon A. C., Adkins J. F., Erez J., Eiler J. M. and Guan Y. (2013) Sr/Ca sensitivity to aragonite saturation state in cultured subsamples from a single colony of coral: Mechanism of biomineralization during ocean acidification. *Geochim. Cosmochim. Acta* **105**, 240–254.

Gagnon A. C., DePaolo D. J. and Adkins J. F. (2012) Precise overgrowth composition during biomineral culture and inorganic precipitation. *Chem. Geol.* **330**–**331**, 188–196.

Geerken E., de Nooijer L. J., Roepert A., Polerecky L., King H. E. and Reichart G. J. (2019) Element banding and organic linings within chamber walls of two benthic foraminifera. *Sci. Rep.*

Hamilton C. P., Spero H. J., Bijma J. and Lea D. W. (2008) Geochemical investigation of gametogenic calcite addition in the planktonic foraminifera Orbulina universa. *Mar. Micropaleontol.* **68**, 256–267.

Hathorne E. C., Alard O., James R. H. and Rogers N. W. (2003) Determination of intratest variability of trace elements in foraminifera by laser ablation inductively coupled plasma-mass spectrometry. *Geochemistry, Geophys. Geosystems* **4**, n/a-n/a. Available at: http://doi.wiley.com/10.1029/2003GC000539.

Hathorne E. C., James R. H. and Lampitt R. S. (2009) Environmental versus biomineralization controls on the intratest variation in the trace element composition of the planktonic foraminifera G. inflata and G. scitula. *Paleoceanography* **24**.

Hauzer H., Evans D., Müller W., Rosenthal Y. and Erez J. (2018) Calibration of Na partitioning in the calcitic foraminifer Operculina ammonoides under variable Ca concentration: Toward reconstructing past seawater composition. *Earth Planet. Sci. Lett.* **497**, 80–91.

Holland K., Eggins S. M., Hönisch B., Haynes L. L. and Branson O. (2017) Calcification rate and shell chemistry response of the planktic foraminifer Orbulina universa to changes in microenvironment seawater carbonate chemistry. *Earth Planet. Sci. Lett.* **464**, 124–134.

Hönisch B., Allen K. A., Lea D. W., Spero H. J., Eggins S. M., Arbuszewski J., deMenocal P., Rosenthal Y., Russell A. D. and Elderfield H. (2013) The influence of salinity on Mg/Ca in planktic foraminifers – Evidence from cultures, core-top sediments and complementary δ18O. *Geochim. Cosmochim. Acta* **121**, 196–213. Available at: http://linkinghub.elsevier.com/retrieve/pii/S0016703713004080.

Hönisch B., Allen K. A., Russell A. D., Eggins S. M., Bijma J., Spero H. J., Lea D. W. and Yu J. (2011) Planktic foraminifers as recorders of seawater Ba/Ca. *Mar. Micropaleontol.* **79**, 52–

57.
Hori M., Shirai K., Kimoto K., Kurasawa A., Takagi H., Ishida A., Takahata N. and Sano Y. (2018) Chamber formation and trace element distribution in the calcite walls of laboratory cultured planktonic foraminifera (Globigerina bulloides and Globigerinoides ruber). *Mar. Micropaleontol.* **140**, 46–55.
Huang K. F., You C. F., Liu Y. H., Wang R. M., Lin P. Y. and Chung C. H. (2010) Low-memory, small sample size, accurate and high-precision determinations of lithium isotopic ratios in natural materials by MC-ICP-MS. *J. Anal. At. Spectrom.* **25**, 1019–1024.
Huber B. T., Bijma J. and Spero H. J. (1996) Blue-water SCUBA collection of planktonic foraminifera. *Methods Tech. Underw. Res. Proc. Am. Acad. Underw. Sci.*, 127–132.
IPCC (2013) *IPCC Fifth Assessment Report (AR5) - The physical science basis*.,
Jonkers L., Buse B., Brummer G. J. A. and Hall I. R. (2016) Chamber formation leads to Mg/Ca banding in the planktonic foraminifer Neogloboquadrina pachyderma. *Earth Planet. Sci. Lett.* **451**, 177–184.
Katz A. (1973) The interaction of magnesium with calcite during crystal growth at 25–90°C and one atmosphere. *Geochim. Cosmochim. Acta* **37**, 1563–1586.
Katz M. E., Cramer B. S., Franzese a., Honisch B., Miller K. G., Rosenthal Y. and Wright J. D. (2010) Traditional and Emerging Geochemical Proxies in Foraminifera. *J. Foraminifer. Res.* **40**, 165–192.
Kisakürek B., Eisenhauer A., Böhm F., Hathorne E. C. and Erez J. (2011) Controls on calcium isotope fractionation in cultured planktic foraminifera, Globigerinoides ruber and Globigerinella siphonifera. *Geochim. Cosmochim. Acta* **75**, 427–443.
Krabbenhöft A., Fietzke J., Eisenhauer A., Liebetrau V., Böhm F. and Vollstaedt H. (2009) Determination of radiogenic and stable strontium isotope ratios (87Sr/86Sr; δ88/86Sr) by thermal ionization mass spectrometry applying an87Sr/84Sr double spike. In *Journal of Analytical Atomic Spectrometry* pp. 1267–1271.
Kunioka D., Shirai K., Takahata N., Sano Y., Toyofuku T. and Ujiie Y. (2006) Microdistribution of Mg/Ca, Sr/Ca, and Ba/Ca ratios in *Pulleniatina obliquiloculata* test by using a NanoSIMS: Implication for the vital effect mechanism. *Geochemistry, Geophys. Geosystems* **7**, n/a-n/a. Available at: http://doi.wiley.com/10.1029/2006GC001280.
Lammers L. N. and Mitnick E. H. (2019) Magnesian calcite solid solution thermodynamics inferred from authigenic deep-sea carbonate. *Geochim. Cosmochim. Acta*.
Lea D. W. and Boyle E. A. (1991) Barium in planktonic foraminifera. *Geochim. Cosmochim. Acta* **55**, 3321–3331.
Lea D. W., Martin P. A., Chan D. A. and Spero H. J. (2009) Calcium uptake and calcification rate in the planktonic foraminifer Orbulina universa. *J. Foraminifer. Res.*
Lea D. W., Mashiotta T. a. and Spero H. J. (1999) Controls on magnesium and strontium uptake in planktonic foraminifera determined by live culturing. *Geochim. Cosmochim. Acta* **63**, 2369–2379.
Lea D. W. and Spero H. J. (1992) Experimental determination of barium uptake in shells of the planktonic foraminifera Orbulina universa at 22°C. *Geochim. Cosmochim. Acta* **56**, 2673–2680.
Lear C. H. and Rosenthal Y. (2006) Benthic foraminiferal Li/Ca: Insights into Cenozoic seawater carbonate saturation state. *Geology* **34**, 985–988.
Limpert E. and Stahel W. A. (2011) Problems with using the normal distribution - and ways to improve quality and efficiency of data analysis. *PLoS One* **6**.

Lorens R. B. (1981) Sr, Cd, Mn and Co distribution coefficients in calcite as a function of calcite precipitation rate. *Geochim. Cosmochim. Acta* **45**, 553–561.
Mavromatis V., Gautier Q., Bosc O. and Schott J. (2013) Kinetics of Mg partition and Mg stable isotope fractionation during its incorporation in calcite. *Geochim. Cosmochim. Acta*.
Mavromatis V., Goetschl K. E., Grengg C., Konrad F., Purgstaller B. and Dietzel M. (2018) Barium partitioning in calcite and aragonite as a function of growth rate. *Geochim. Cosmochim. Acta*.
Mezger E. M., de Nooijer L. J., Boer W., Brummer G. J. A. and Reichart G. J. (2016) Salinity controls on Na incorporation in Red Sea planktonic foraminifera. *Paleoceanography* **31**, 1562–1582.
Morse J. W. and Bender M. L. (1990) Partition coefficients in calcite: Examination of factors influencing the validity of experimental results and their application to natural systems. *Chem. Geol.* **82**, 265–277.
Morse J. W., Wang Q. and Tsio M. Y. (1997) Influences of temperature and Mg:Ca ratio on CaCO3precipitates from seawater. *Geology*.
Mucci A. (1987) Influence of temperature on the composition of magnesian calcite overgrowths precipitated from seawater. *Geochim. Cosmochim. Acta*.
Mucci A. and Morse J. W. (1983) The incorporation of Mg2+ and Sr2+ into calcite overgrowths: influences of growth rate and solution composition. *Geochim. Cosmochim. Acta* **47**, 217–233. Available at: http://www.sciencedirect.com/science/article/pii/0016703783901357.
Nehrke G., Keul N., Langer G., De Nooijer L. J., Bijma J. and Meibom A. (2013) A new model for biomineralization and trace-element signatures of Foraminifera tests. *Biogeosciences* **10**, 6759–6767.
Nielsen L. C., DePaolo D. J. and De Yoreo J. J. (2012) Self-consistent ion-by-ion growth model for kinetic isotopic fractionation during calcite precipitation. *Geochim. Cosmochim. Acta*.
de Nooijer L. J., Spero H. J., Erez J., Bijma J. and Reichart G. J. (2014) Biomineralization in perforate Foraminifera. *Earth-Science Rev.* **135**, 48–58. Available at: http://www.sciencedirect.com/science/article/pii/S0012825214000610.
Nürnberg D., Bijma J. and Hemleben C. (1996) Assessing the reliability of magnesium in foraminiferal calcite as a proxy for water mass temperatures. *Geochim. Cosmochim. Acta* **60**, 803–814.
Ogliore R. C., Huss G. R. and Nagashima K. (2011) Ratio estimation in SIMS analysis. *Nucl. Instruments Methods Phys. Res. Sect. B Beam Interact. with Mater. Atoms* **269**, 1910–1918.
Oomori T., Kaneshima H., Maezato Y. and Kitano Y. (1987) Distribution coefficient of Mg2+ ions between calcite and solution at 10-50°C. *Mar. Chem.*
Paris G., Fehrenbacher J. S., Sessions A. L., Spero H. J. and Adkins J. F. (2014) Experimental Determination of Carbonate Associated Sulfate δ34S in Planktonic Foraminifera Shells. *Geochemistry, Geophys. Geosystems*, n/a-n/a. Available at: http://dx.doi.org/10.1002/2014GC005295.
Reiss Z. (1957) The Bilamellidea, nov. superfam., and remarks on Cretaceous Globorotaliids. *Contrib. from Cushman Found. Foraminifer. Res.* **8**, 127–145.
Robbins L. L. (1988) Environmental significance of morphologic variability in open-ocean versus ocean-margin assemblages of Orbulina universa. *J. Foraminifer. Res.* **18**, 326–333. Available at: http://jfr.geoscienceworld.org/cgi/content/abstract/18/4/326%5Cnhttp://jfr.geoscienceworld.org/cgi/doi/10.2113/gsjfr.18.4.326.

Roberts J., Kaczmarek K., Langer G., Skinner L. C., Bijma J., Bradbury H., Turchyn A. V., Lamy F. and Misra S. (2018) Lithium isotopic composition of benthic foraminifera: A new proxy for paleo-pH reconstruction. *Geochim. Cosmochim. Acta* **236**, 336–350.

Rollion-Bard C. and Erez J. (2010) Intra-shell boron isotope ratios in the symbiont-bearing benthic foraminiferan Amphistegina lobifera: Implications for δ11B vital effects and paleo-pH reconstructions. *Geochim. Cosmochim. Acta* **74**, 1530–1536. Available at: http://linkinghub.elsevier.com/retrieve/pii/S0016703709007169.

Rollion-Bard C., Erez J. and Zilberman T. (2008) Intra-shell oxygen isotope ratios in the benthic foraminifera genus Amphistegina and the influence of seawater carbonate chemistry and temperature on this ratio. *Geochim. Cosmochim. Acta* **72**, 6006–6014.

Rosenthal Y., Boyle E. A. and Slowey N. (1997) Temperature control on the incorporation of magnesium, strontium, fluorine, and cadmium into benthic foraminiferal shells from Little Bahama Bank: Prospects for thermocline paleoceanography. *Geochim. Cosmochim. Acta* **61**, 3633–3643.

Russell A. D., Hönisch B., Spero H. J. and Lea D. W. (2004) Effects of seawater carbonate ion concentration and temperature on shell U, Mg, and Sr in cultured planktonic foraminifera. *Geochim. Cosmochim. Acta* **68**, 4347–4361.

Russell W. A., Papanastassiou D. A. and Tombrello T. A. (1978) Ca isotope fractionation on the Earth and other solar system materials. *Geochim. Cosmochim. Acta* **42**, 1075–1090.

Sadekov A., Eggins S. M., De Deckker P. and Kroon D. (2008) Uncertainties in seawater thermometry deriving from intratest and intertest Mg/Ca variability in Globigerinoides ruber. *Paleoceanography* **23**, 1–12.

Sadekov A., Eggins S. M., De Deckker P., Ninnemann U., Kuhnt W. and Bassinot F. (2009) Surface and subsurface seawater temperature reconstruction using Mg/Ca microanalysis of planktonic foraminifera *Globigerinoides ruber* , *Globigerinoides sacculifer* , and *Pulleniatina obliquiloculata*. *Paleoceanography* **24**, n/a-n/a. Available at: http://doi.wiley.com/10.1029/2008PA001664.

Sadekov A. Y., Eggins S. M. and De Deckker P. (2005) Characterization of Mg/Ca distributions in planktonic foraminifera species by electron microprobe mapping. *Geochemistry, Geophys. Geosystems* **6**.

Senoner M., Wirth T., Unger W., Osterle W., Kaiander I., Sellin R. L. and Bimberg D. (2004) BAM-L002?a new type of certified reference material for length calibration and testing of lateral resolution in the nanometre range. *Surf. Interface Anal.* **36**, 1423–1426. Available at: http://doi.wiley.com/10.1002/sia.1936.

Spero H. J. (1988) Ultrastructural examination of chamber morphogenesis and biomineralization in the planktonic foraminifer Orbulina universa. *Mar. Biol.* **99**, 9–20.

Spero H. J., Eggins S. M., Russell A. D., Vetter L., Kilburn M. R. and Hönisch B. (2015) Timing and mechanism for intratest Mg/Ca variability in a living planktic foraminifer. *Earth Planet. Sci. Lett.* **409**, 32–42. Available at: http://www.sciencedirect.com/science/article/pii/S0012821X14006578.

Stephenson a E., DeYoreo J. J., Wu L., Wu K. J., Hoyer J. and Dove P. M. (2008) Peptides enhance magnesium signature in calcite: insights into origins of vital effects. *Science* **322**, 724–727.

Tang J., Köhler S. J. and Dietzel M. (2008a) Sr2+/Ca2+ and 44Ca/40Ca fractionation during inorganic calcite formation: I. Sr incorporation. *Tang, J., Köhler, S.J., Dietzel, M., 2008. Sr2+/Ca2+ 44Ca/40Ca fractionation Dur. Inorg. calcite Form. I. Sr Inc. Geochim.*

Cosmochim. Acta 72, 3718–3732. doi10.1016/j.gca.2008.05.031Geochimica Cosmochim. Acta **72**, 3718–3732.

Tang J., Dietzel M., Bohm F., Kohler S. J. and Eisenhauer A. (2008b) Sr2+/Ca2+ and Ca-44/Ca-40 fractionation during inorganic calcite formation: II. Ca isotopes. *Geochim. Cosmochim. Acta* **72**, 3733–3745.

Tesoriero A. J. and Pankow J. F. (1996) Solid solution partitioning of Sr2+, Ba2+, and Cd2+ to calcite. *Geochim. Cosmochim. Acta* **60**, 1053–1063.

Vetter L., Kozdon R., Mora C. I., Eggins S. M., Valley J. W., Hönisch B. and Spero H. J. (2013) Micron-scale intrashell oxygen isotope variation in cultured planktic foraminifers. *Geochim. Cosmochim. Acta* **107**, 267–278.

Vigier N., Rollion-Bard C., Levenson Y. and Erez J. (2015) Lithium isotopes in foraminifera shells as a novel proxy for the ocean dissolved inorganic carbon (DIC). *Comptes Rendus Geosci.* **347**, 43–51. Available at: http://linkinghub.elsevier.com/retrieve/pii/S1631071314001540.

Wasylenki L. E., Dove P. M., Wilson D. S. and De Yoreo J. J. (2005) Nanoscale effects of strontium on calcite growth: An in situ AFM study in the absence of vital effects. *Geochim. Cosmochim. Acta*.

Wasylenki L. E., Dove P. M. and De Yoreo J. J. (2005) Effects of temperature and transport conditions on calcite growth in the presence of Mg2+: Implications for paleothermometry. *Geochim. Cosmochim. Acta*.

Wit J. C., de Nooijer L. J., Wolthers M. and Reichart G. J. (2013) A novel salinity proxy based on Na incorporation into foraminiferal calcite. *Biogeosciences* **10**, 6375–6387. Available at: http://www.biogeosciences.net/10/6375/2013/.

Wombacher F., Eisenhauer A., Böhm F., Gussone N., Regenberg M., Dullo W. C. and Rüggeberg A. (2011) Magnesium stable isotope fractionation in marine biogenic calcite and aragonite. *Geochim. Cosmochim. Acta* **75**, 5797–5818.

APPENDIX A: SUPPLEMENTAL INFORMATION FROM CHAPTER 2

6.1 METHODS

6.1.1 *Foraminiferal Culturing*

Each *O. universa* and *O. bilobata* specimen used during this study was cultured under constant seawater conditions. These conditions covered a range of temperature (18°C, 20°C, and 22°C), pH (7.90 to 8.59) and salinity (30 to 36.6) (Table 6.1). The *G. bulloides* specimen and *N. dutertrei* specimen were cultured at ambient conditions (T = 22°C, salinity = 33.4, and pH =8.06). More details about the culturing of the *N. dutertrei* specimen can be found in (Fehrenbacher et al., 2017).

pH (NBS scale) was altered by adding HCl or NaOH until seawater reached a target pH. For high salinity experiments, salinity was raised by evaporating seawater underneath a heat lamp. For low salinity experiments, salinity was lowered by the addition of deionized water. Alkalinity was determined using a Metrohm open-cell auto-titrator. Titrations were conducted using 0.01N HCl. Dickson CRM standards were used to check for accuracy.

Table 6.1. Culturing conditions for *O. universa* and *O. bilobata* experiments.

Experiment Name	**Year**	**Specimen**	**T (°C)** (±0.3)	**Salinity** (±0.1)	**pH@25°C** (±0.02)	**Total Alkalinity (µeq/kg)** (*±8 †±5)	**Banding Pattern**
AG-01	2013	001	22	33.4	8.06	2249*	S
AG-01	2013	032	22	33.4	8.06	2249*	S
AG-01b	2013	002	22	36.5	7.95	2293*	I
AG-01b	2013	022	22	36.5	7.95	2293*	S
AG-02	2013	226	18	33.4	8.06	2249*	I
AG-02	2013	248	18	33.4	8.06	2249*	S
AG-02	2013	315	18	33.4	8.06	2249*	O
AG-02	2013	316	18	33.4	8.06	2249*	I

AG-04	2013	263 (bilob)	18	33.7	8.56	2621*	S
AG-05	2013	342 (bilob)	18	35.9	8.07	2279*	O
AG-06	2013	510	22	33.4	8.59	2603*	O
AG-06	2013	541	22	33.4	8.59	2603*	O
AG-06	2013	543	22	33.4	8.59	2603*	O
AG-06	2013	547	22	33.4	8.59	2603*	I
AG-07	2013	516	22	33.2	7.90	2142*	I
AG-07	2013	518	22	33.2	7.90	2142*	I
AG-07	2013	555	22	33.2	7.90	2142*	S
AG-07	2013	557	22	33.2	7.90	2142*	I
AG-08	2013	633	22	33.2	8.10	2231*	I
AG-09	2013	549 (bilob)	22	30.0	8.21	2091*	O
AG-09	2013	603	22	30.0	8.21	2091*	I
AG-09	2013	642	22	30.0	8.21	2091*	I
AG-09	2013	644	22	30.0	8.21	2091*	S
AG-09	2013	645	22	30.0	8.21	2091*	O
AG-10	2013	675	22	36.3	8.01	2281*	O
AG-10	2013	680	22	36.3	8.01	2281*	O
AG-12	2013	863	22	33.2	8.06	2238*	O
AG-12	2013	864	22	33.2	8.06	2238*	O
AG-12	2013	865	22	33.2	8.06	2238*	I
AG-12	2013	866 (bilob)	22	33.2	8.06	2238*	O
AG-13	2013	810	20	33.4	8.06	2238*	O
AG-13	2013	811	20	33.4	8.06	2238*	I
AG-13	2013	859	20	33.4	8.06	2238*	I
AG-14	2013	910	22	36.6	8.06	2317*	O
AG-14	2013	913	22	36.6	8.06	2317*	S
AG-14	2013	915	22	36.6	8.06	2317*	S
EB-01	2014	046	22	33.4	8.07	2233†	I
EB-01	2014	048	22	33.4	8.07	2233†	O
EB-01	2014	049	22	33.4	8.07	2233†	O
EB-02	2014	004	22	33.4	8.30	2327†	O
EB-02	2014	012	22	33.4	8.30	2327†	O
EB-03	2014	070	22	33.4	8.20	2248†	I
EB-03	2014	074	22	33.4	8.20	2248†	O
EB-03	2014	078	22	33.4	8.20	2248†	O
EB-04	2014	122	22	33.4	8.40	2409†	O
EB-04	2014	138	22	33.4	8.40	2409†	O
EB-14	2014	475	22	33.4	8.55	2326†	I
EB-14	2014	477	22	33.4	8.55	2326†	I

EB-14	2014	478	22	33.4	8.55	2326†	S

6.1.2 *Sample cleaning*

The revised cleaning method outlined in the main text was used for this study because preliminary cleaning experiments using multiple heated H_2O_2 steps showed signs of dissolution as monitored through mass loss of individual tests. The results for those preliminary experiments are displayed in Figure 6.1 below.

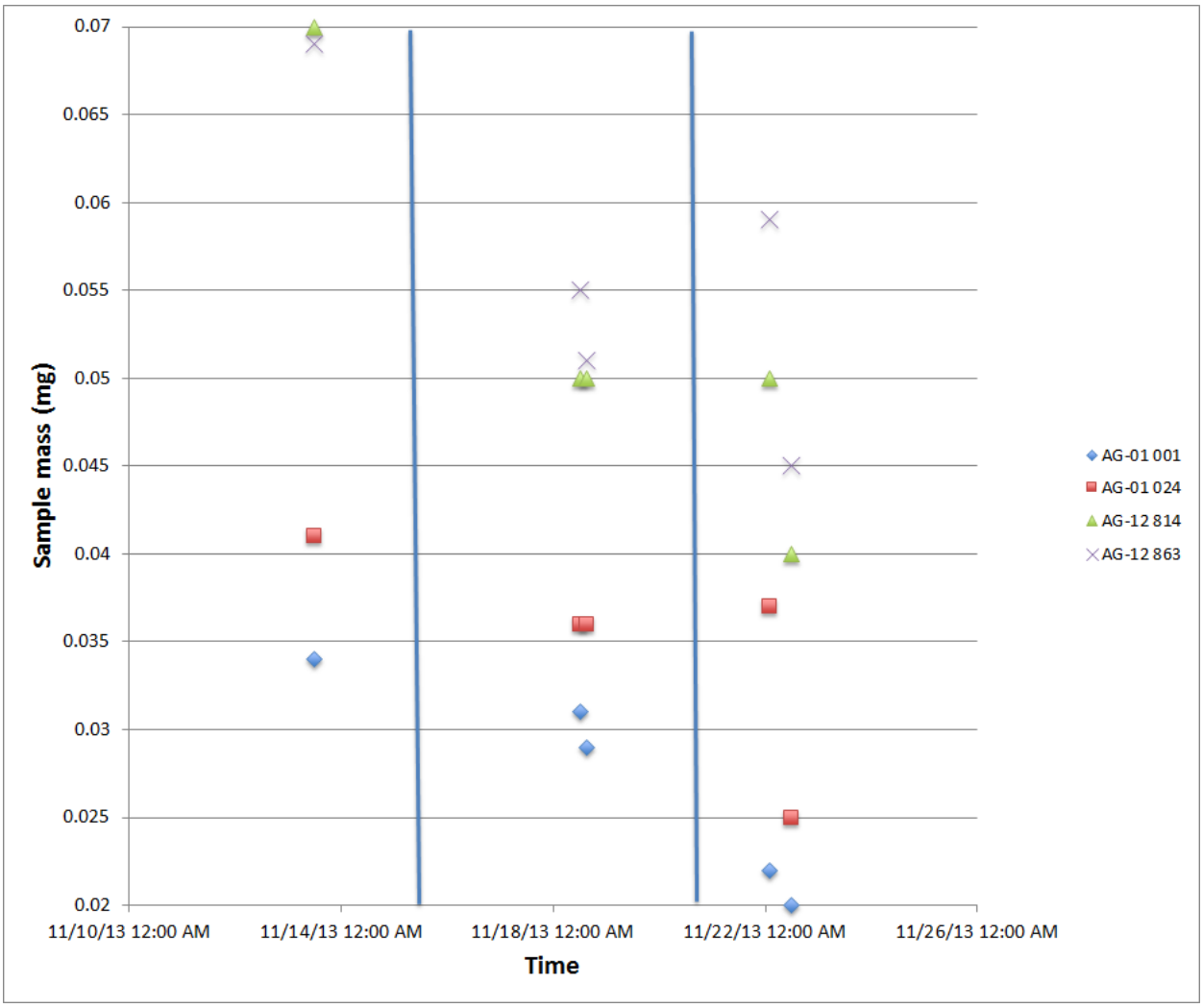

Figure 6.1. Mass of individual samples is monitored through time. The vertical blue lines indicate high-temperature cleaning steps.

6.1.3 *ToF-SIMS analysis*

The Ca, Mg, and Na intensity images obtained from ToF-SIMS analysis were examined prior to image processing to test whether the Mg/Ca and Na/Ca bands observed in this study are true features and not caused by variations or cracks in the calcite. Foraminifera samples were compared to calcite standards, which are observed to be relatively homogeneous in Ca, Mg, and Na. Ca in foraminiferal samples was relatively homogeneous with typical counts of approximately 4000 per pixel, suggesting that the bands observed in the Mg and Na intensity images are true features and not an artifact of measurement. These results are summarized in Figure 6.2.

Figure 6.3 shows the process by which individual peaks were selected. The relevant portion of the mass range sampled is shown in the figure. Ion peaks are identified by their masses, with Na+ (red) at approximately 23 (22.8674 in this image), Mg+ (green) at ~24 (23.8533), and Ca+ (blue) at ~40 (39.7495). Because Ca+ is the largest peak in each foraminifera sample, it is often used for purposes of mass calibration. Since a time of flight instrument was used for analysis, all peaks within the mass range specified (0-78 amu) were collected and can be examined during data processing if required.

Because the masses observed in ToF-SIMS are not true masses but the mass/charge (m/z) ratio, it is possible that certain doubly charged masses or isotopes (e.g. $^{46}Ca^{2+}$) may interfere with the Na+ peak at 23 amu. However, the existence of a high Na/Ca concentration at the POM region has also been observed using Atom Probe Tomography (APT), as reported in the study by Branson et al., 2016. In addition, the natural abundance of 46Ca is low enough that it is unlikely that this isotope alone could result in the Na peak observed in planktonic foraminifera.

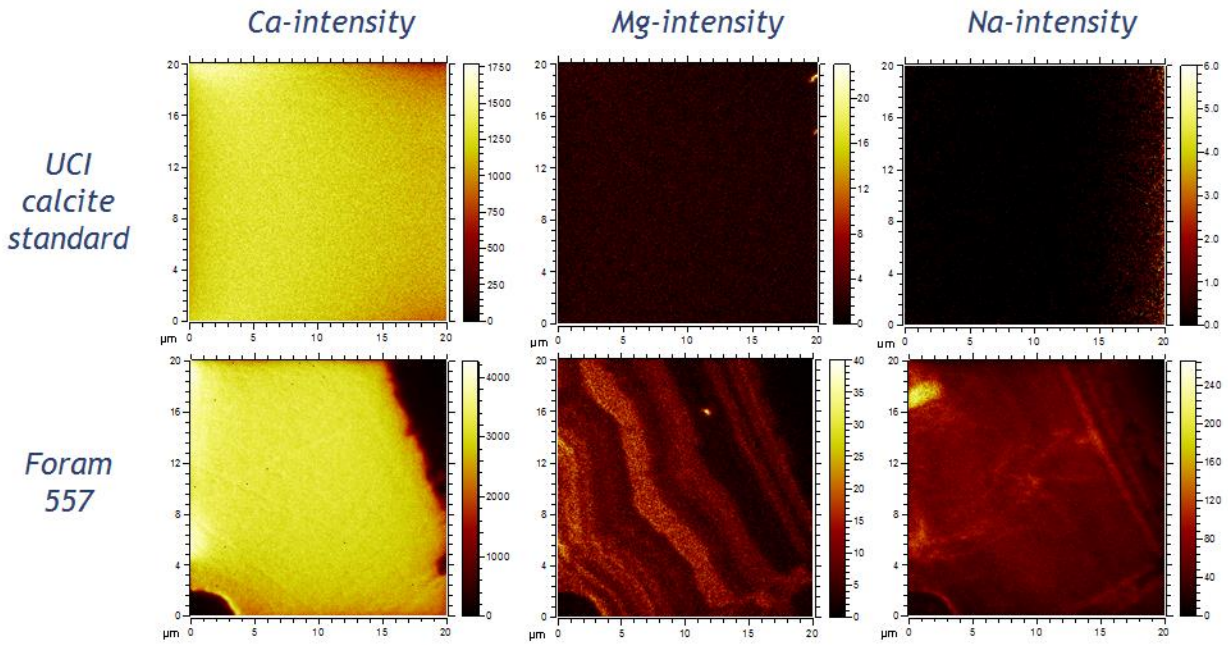

Figure 6.2. A comparison between the Ca, Mg, and Na intensity ToF-SIMS images from a homogeneous calcite standard (top row) and those from a foraminifer sample (bottom row).

During analysis, the beam intensity profiles (Figure 6.4) were monitored in order to ensure that the beam was running at steady state. Beam intensity profiles over the course of several different runs are pictured, including samples of normal and abnormal beams. In most cases, the beam reached steady state at some point before the halfway point of the measurement (Scan 1600), so only the latter half of scans are considered from each sample. Typical and atypical beam profiles are pictured in Figure 6.4.

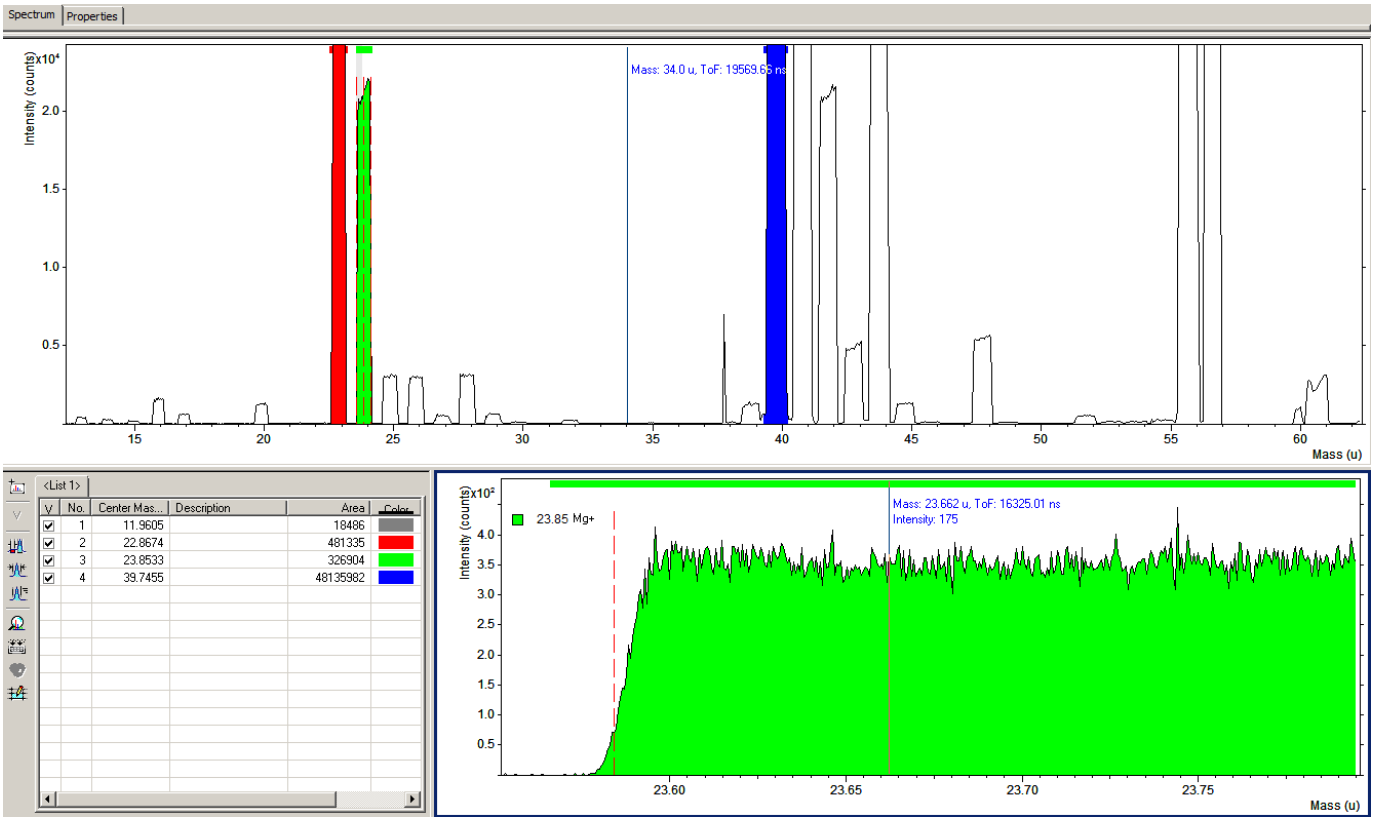

Figure 6.3. A screenshot of the process by which individual peaks are selected. The relevant portion of the mass range sampled is shown in the picture above.

In addition, beam stability over time was measured by running the same calcite standard several times over the course of an experimental day and examining the Mg/Ca ratios of that standard (Figure 6.5). It was found that in the case of minor beam instability such as that depicted in Profile B, comparing data drawn from the same scan numbers is more important than taking data from smooth areas of the beam profile. In the case of major instability such as that observed in Profile C, the entire measurement was excluded from consideration.

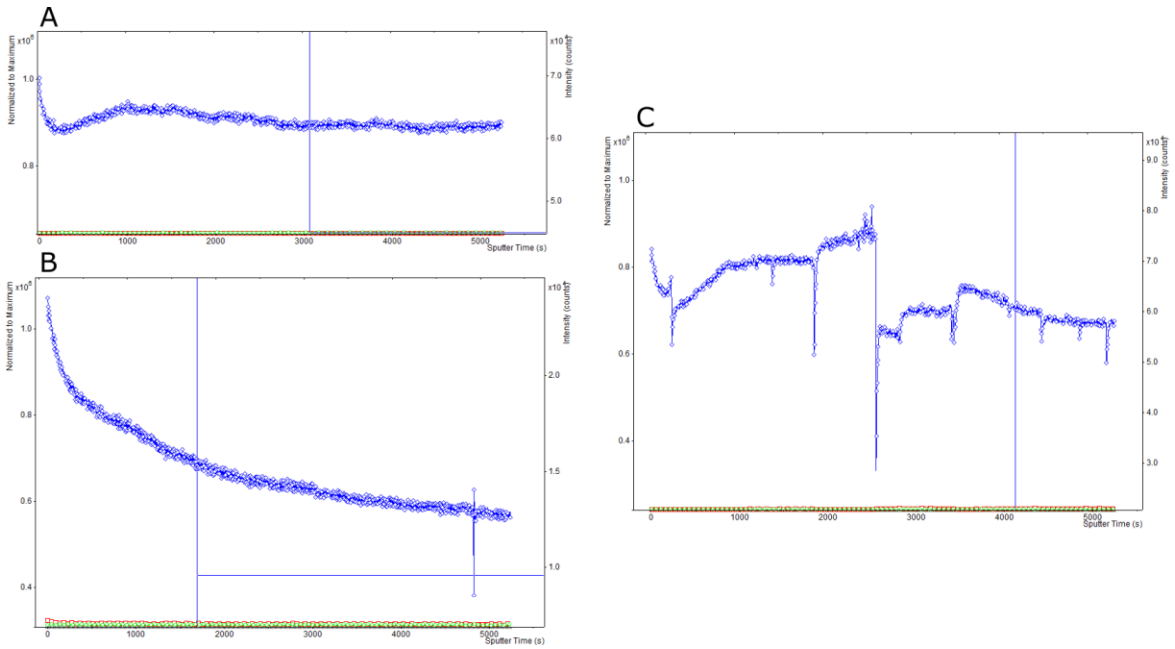

Figure 6.4. Sample beam intensity profiles over the course of several different runs. Pictured is Ca-intensity, with analysis time on the x-axis and counts per second (cps) on the right. A typical beam profile is A, where counts drop before stabilizing towards the end of the measurement. B and C are atypical and suggest instability in the source during those runs. Profile B corresponds to the first BC measurement in Figure 6.4, where Scans 200-1800 were taken to avoid the observed instability.

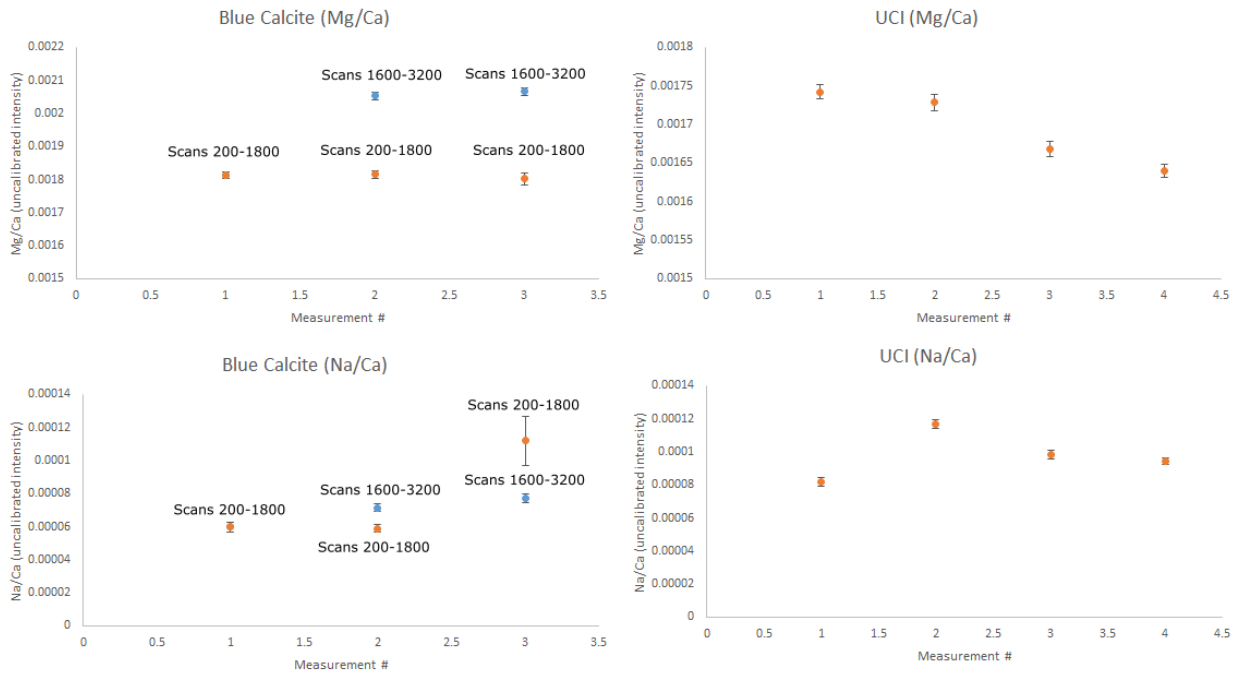

Figure 6.5. Stability/time measurements of BC (left) and UCI (right). In BC measurements, a distinction is made between Mg/Ca and Na/Ca ratios obtained from Scans 1600-3200 (blue circles) and Scans 200-1800 (orange circles). The first BC measurement corresponds to Profile B in Figure 6.3. In the case of Mg/Ca, it appears more important to obtain measurements from the same scan numbers in the case of minor beam instability.

6.1.4 *Data processing and shift correction*

The spatial resolution of the instrument was calculated using the method outlined in Senoner et al., 2004 (Figure 6.6). A profile 40 pixels wide was examined over a crack in a standard image, where the intensity of Ca dipped over a relatively straight edge. The amount of change over the edge was calculated and the number of pixels between 88% intensity and 12% intensity were counted. In this case, that number was 4 pixels. Given that one side of the image is 20µm in length and contains 256 pixels, the amount of area covered by a single pixel is 78nm/px. 4 pixels translates to a spatial resolution of 312 nm.

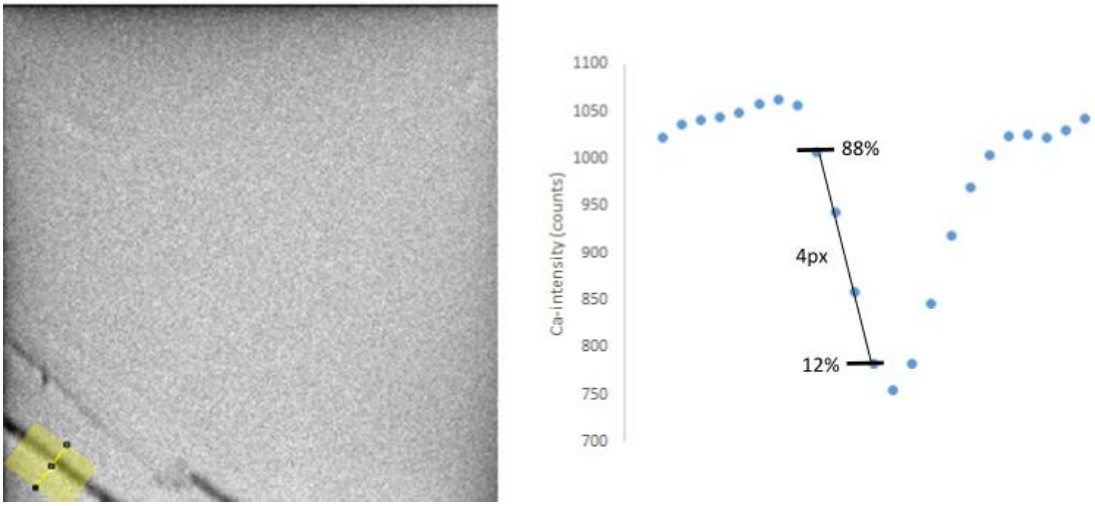

Figure 6.6. An illustration of the process by which the spatial resolution of the instrument was calculated.

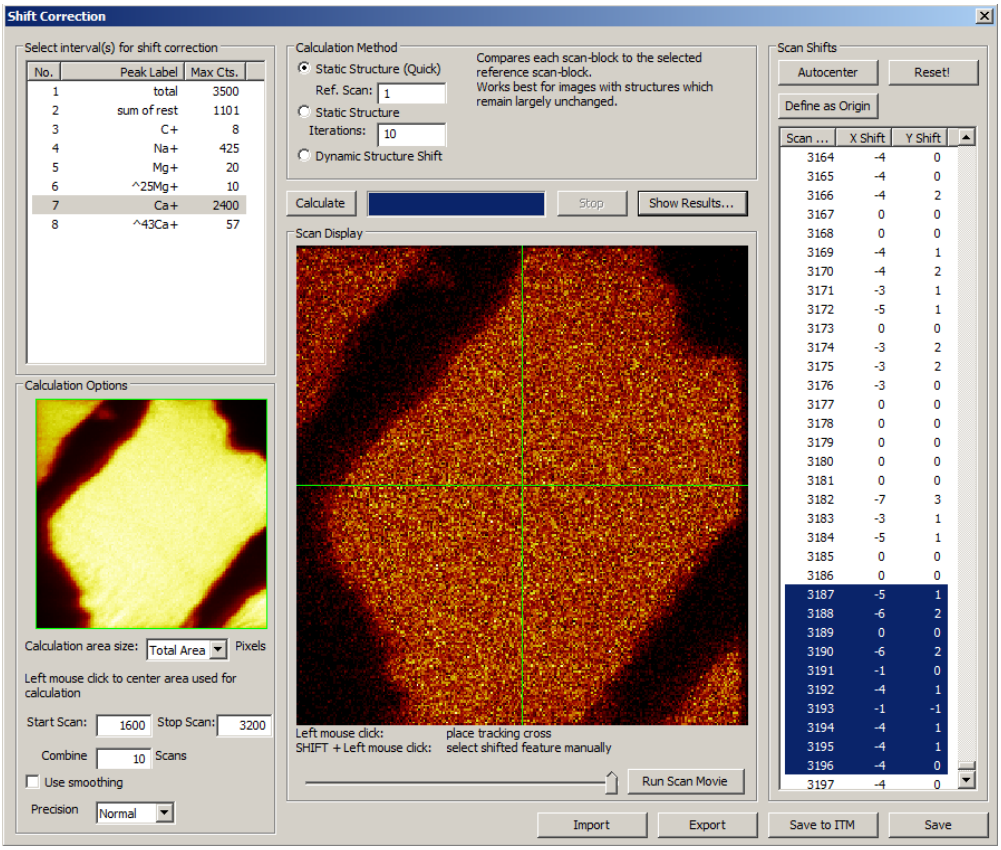

Figure 6.7. A screenshot showing the shift correction process.

The shift correction process is shown in Figure 6.7. The Ca intensity image is used for shift correction because of the high number of Ca counts. Ten scans were summed together and compared to the succeeding 10 scans, with the software taking note of any translational shift in the image. At the end of the comparison, an image corrected for translational shift was reconstructed. Shift correction was performed on a case-by-case basis using the ToF-SIMS software. A comparison between two different shift correction cases, one where the original image was shifted and one where the original image was not shifted, is shown in Figure 6.8.

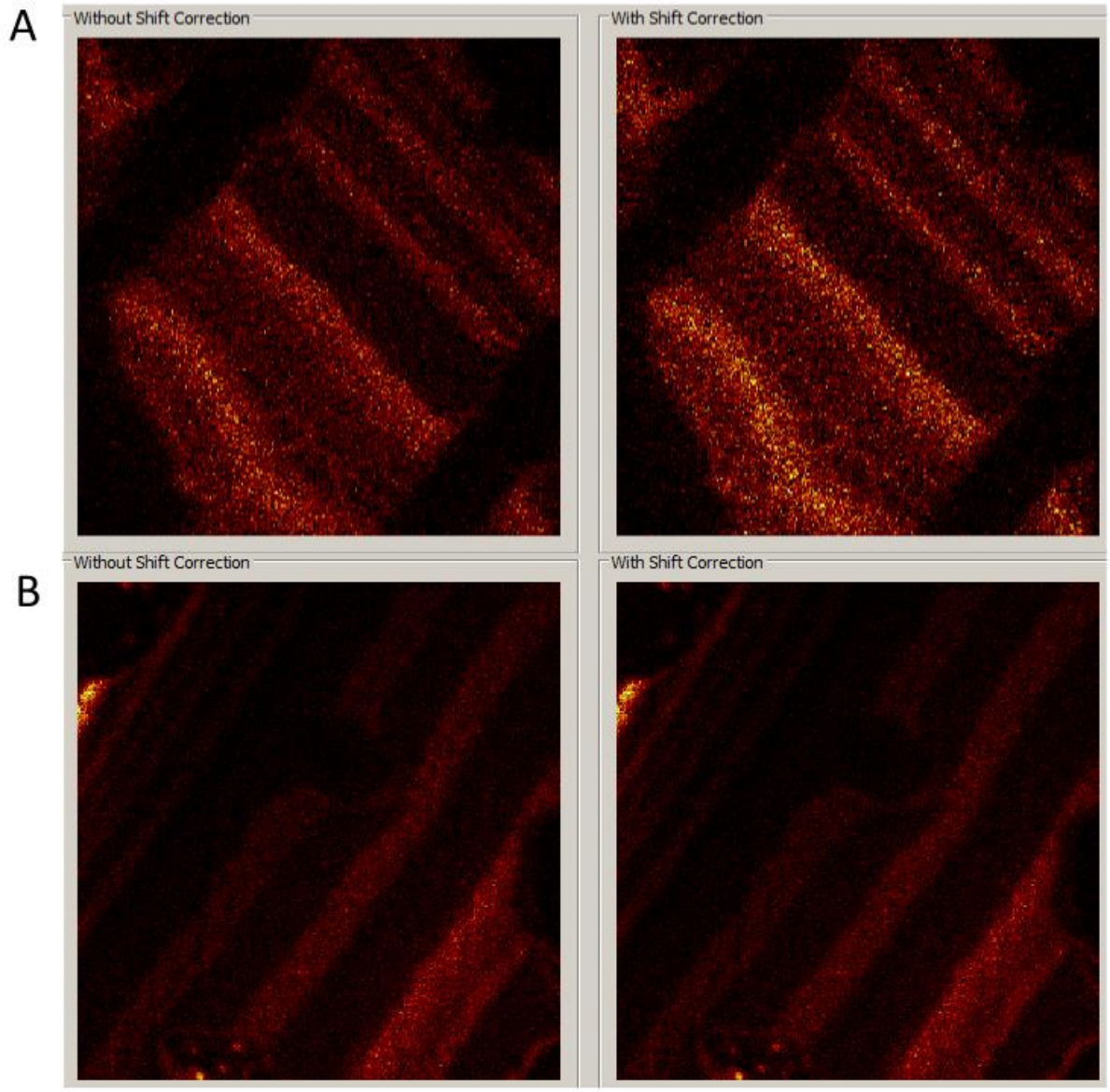

Figure 6.8. A comparison between two different shift correction cases. In Case A, which experienced a greater spatial shift during measurement, the Mg banding in the corrected image (right) is sharper and cleaner than in the uncorrected image (left). In this case, shift correction was applied. In Case B, the corrected image was not observably different from the uncorrected image, suggesting a reduced amount of spatial shift. In this case, shift correction was not necessary.

6.1.4.1 Creating Mg/Ca and Na/Ca profiles

Mg/Ca and Na/Ca profiles were created using a custom MATLAB script that traces the contour of each Mg/Ca band. The script works as illustrated in the images below:

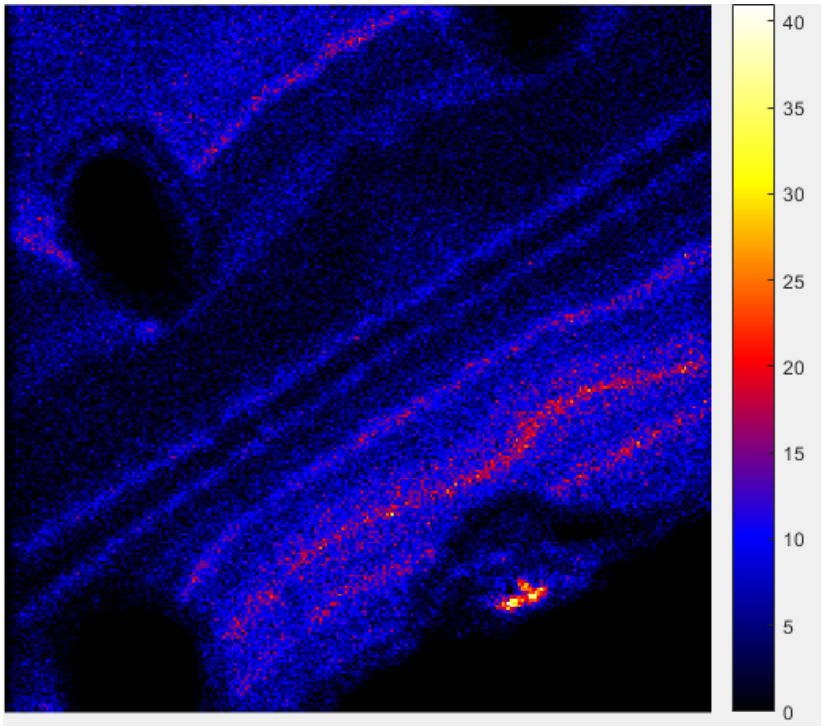

First, Na, Mg, and Ca intensity images are processed into MATLAB. The images are visually inspected for high Mg or Na locations that occur outside the foraminifer test. These high Mg or high Na spots tend to be due to edge effects, and occasionally obscure real signal.

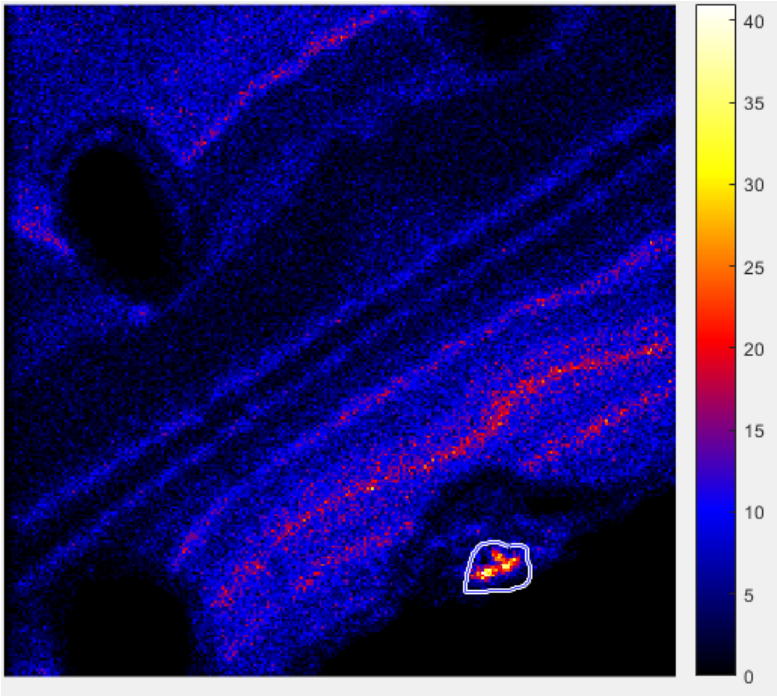

Abnormally high Mg or high Na locations are flagged by manually tracing a circle around the location, identifying the location as a region of interest.

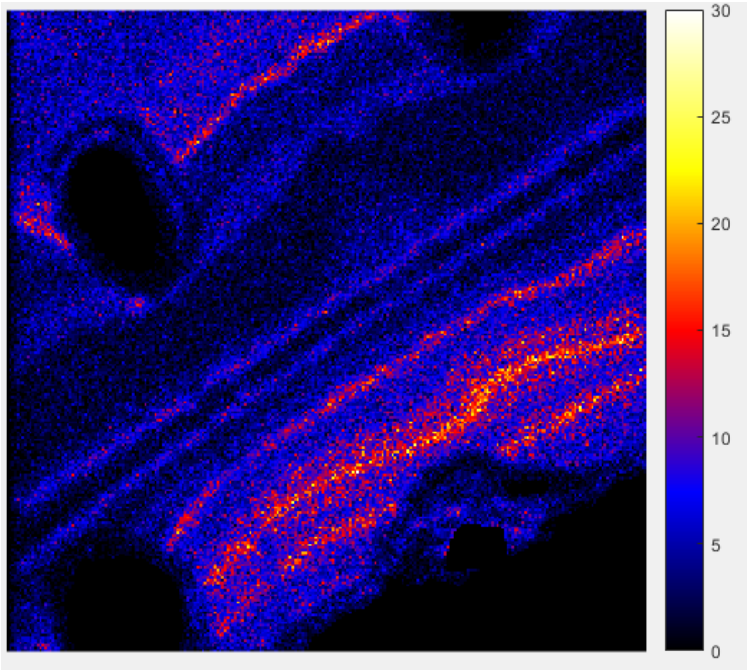

Identified regions of interest are then removed by the MATLAB script, improving contrast and reducing the effect of these regions on the final profile.

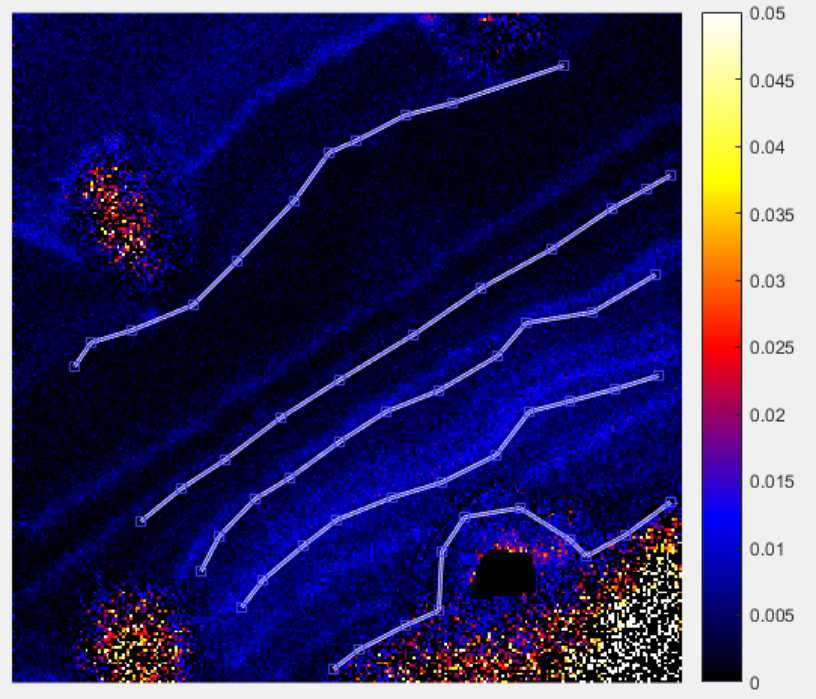

The edges of the foraminifer and the edges of each Mg/Ca band are then traced using contour lines. Mg/Ca banding is used for this step because Mg/Ca bands are easier to identify and are visible in more samples than Na/Ca bands. The number of manually-drawn contour lines and the number of joints in each line is customizable and varies from specimen to specimen.

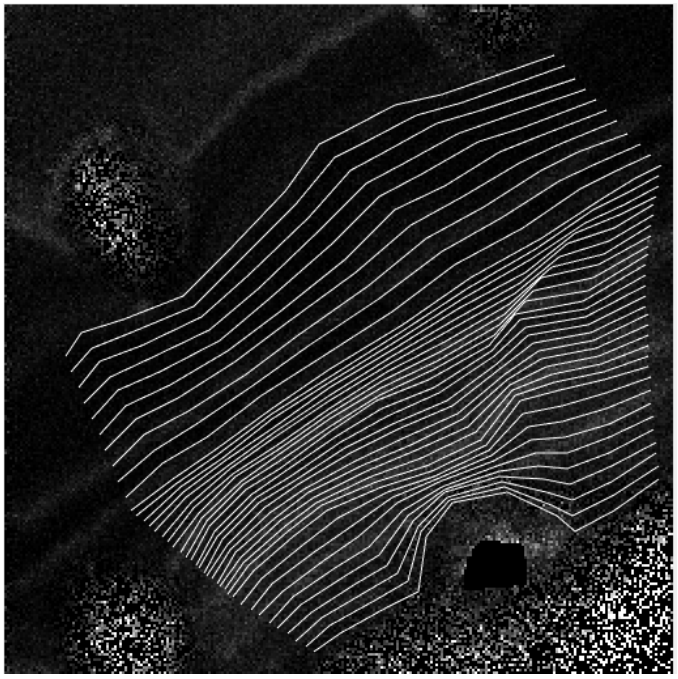

Once the contour lines are drawn, the script fills the gaps between the lines. Profiles are generated by summing the integer number of pixels between each contour line. The Mg/Ca and Na/Ca profile generated from this specimen is shown below.

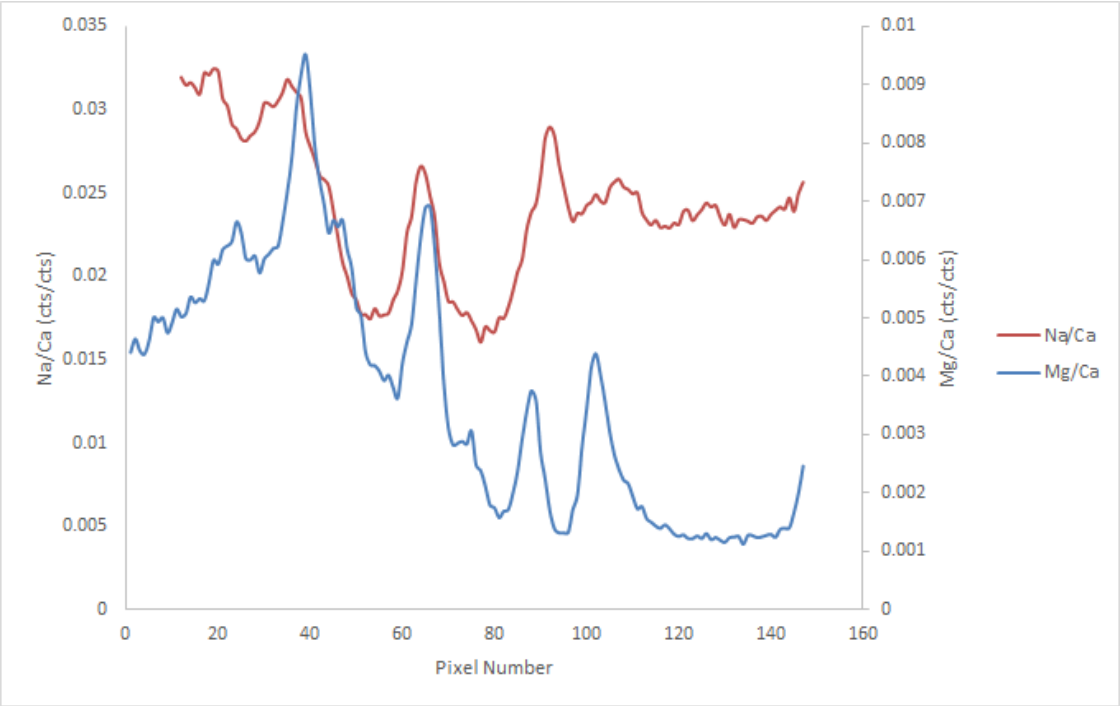

6.1.5 *Standardization*

6.1.5.1 ^{43}Ca isotope labeling

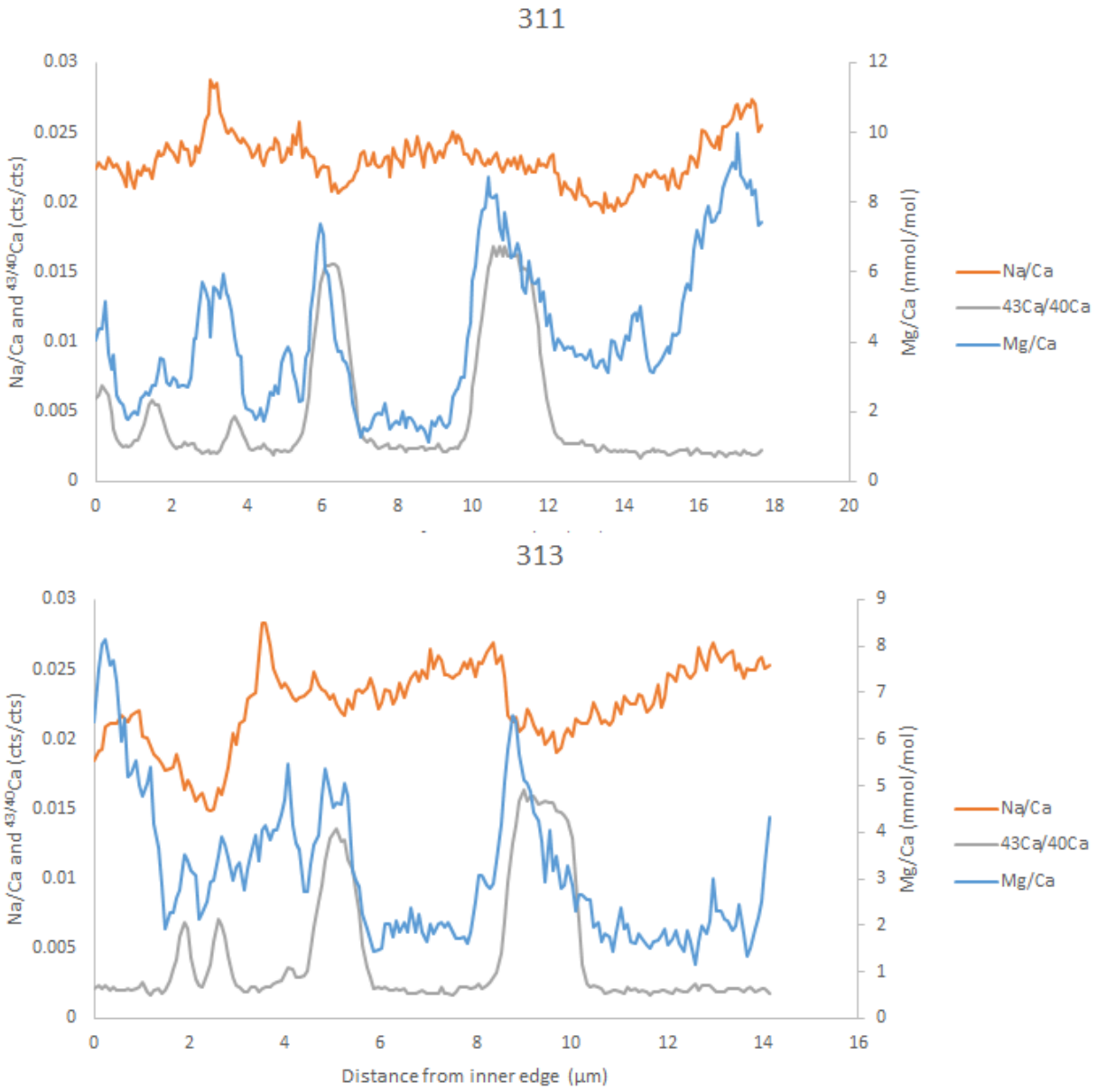

Figure 6.9. Mg/Ca and Na/Ca banding in Foraminifera 311 and 313, which were grown in culture media labeled with ^{43}Ca for two-night periods. Na/Ca and $^{43/40}$Ca are reported in uncalibrated counts/counts. Mg/Ca is reported in mmol/mol.

6.1.5.2 Consistency standard

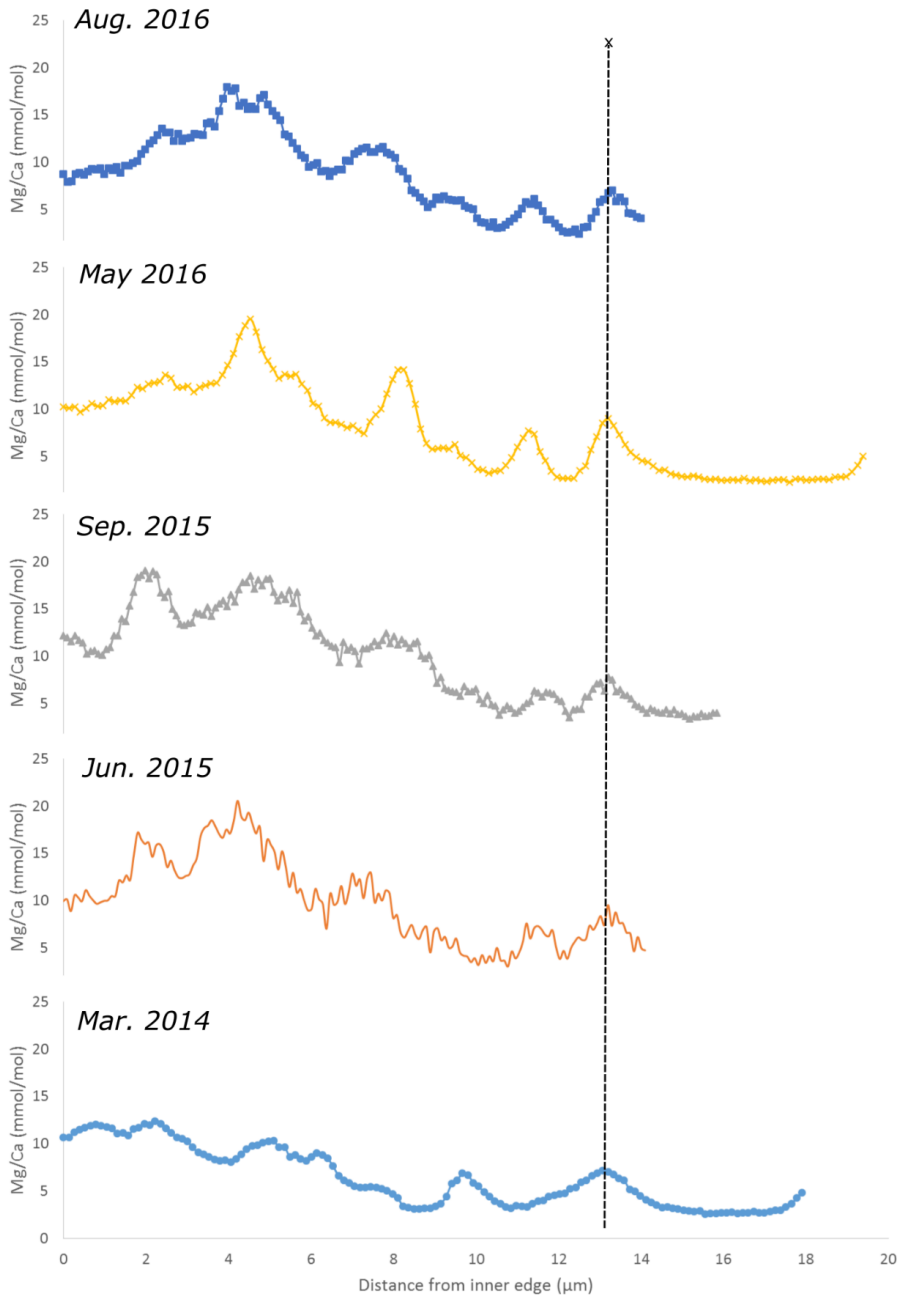

Figure 6.10. Foram 510, the consistency standard, was examined five times over the course of two years of analyses. The banding pattern of the consistency standard is reproducible between analyses in Mg/Ca. Because this foraminifer was polished between measurements, each successive measurement was taken at a slightly more oblique angle, shifting the x-axis from previous measurements. In the figure above, all Mg/Ca bands are adjusted to a single length scale using the last Mg band (dotted line) in order to observe reproducibility in the pattern of Mg/Ca banding.

6.1.5.3 Calcite standards

The stability of calcite standards over time was measured by taking multiple measurements of the same calcite standard over the length of an experimental day. A summary plot of these measurements can be found in Figure 6.5. In brief, when measurements are compared using the same scan numbers, the drift in Mg/Ca of Blue Calcite is less than 1%. In the same standard, the drift in Na/Ca is more variable. In the first two measurements of Na/Ca in Blue Calcite, Na/Ca was fairly constant, varying only by 2%, however, between the second and third measurements, Na/Ca varied in Blue Calcite by 85%. In UCI, the drift in Mg/Ca is less than 5%. The drift in Na/Ca for measurements taken over the course of the same day is approximately 15%. However, because UCI has a Na/Ca ratio too low to be detected by the method used to measure the Na/Ca ratio of standards in Branson et al., 2016, UCI is not used as a standard for Na/Ca.

A suite of calcite standards (Gabitov et al., 2013) was examined in order to determine whether the choice of standard affected the final, calibrated Mg/Ca ratio. Mg/Ca concentrations in the standards ranged from 0.07 mmol/mol (CAL) to 45.3 mmol/mol (LAS-20). Figure 6.11 below shows that the measured intensity of Mg/Ca standards is linearly correlated with their Mg/Ca concentration, over four orders of magnitude. This suggests that the choice of standard does not matter for Mg/Ca calibrations, as even standards with drastically different Mg/Ca ratios from foraminifera would still yield accurate calibrations.

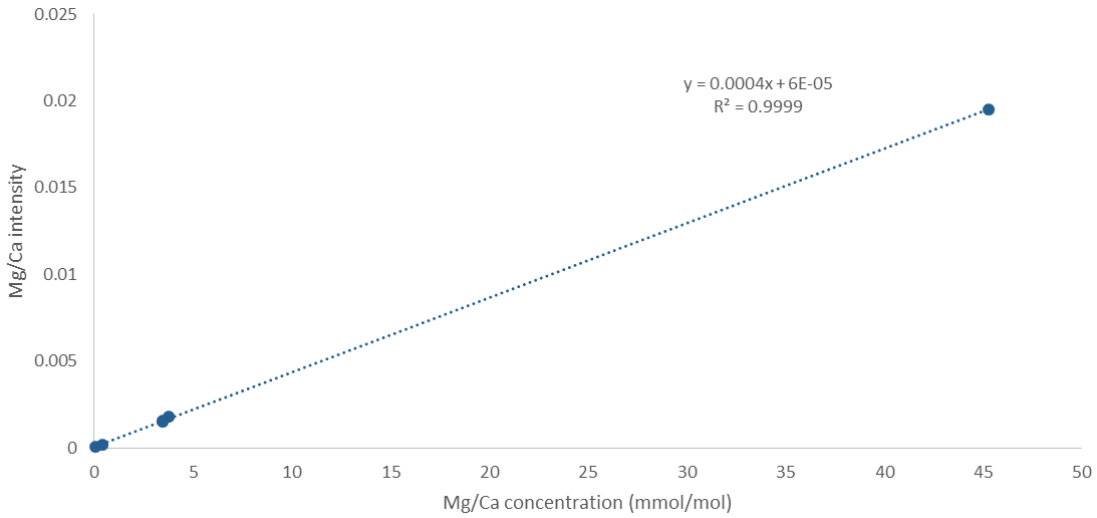

Figure 6.11. The Mg/Ca intensities (cts/cts) of calcite standards obtained using ToF-SIMS are compared against the calibrated Mg/Ca concentrations of the standard. The relationship is highly linear, with an R2 value close to 1. This implies that the choice of standard does not affect the quality of the final Mg/Ca ratio.

6.2 Other Results

6.2.1 *Na/Ca banding at various culture conditions*

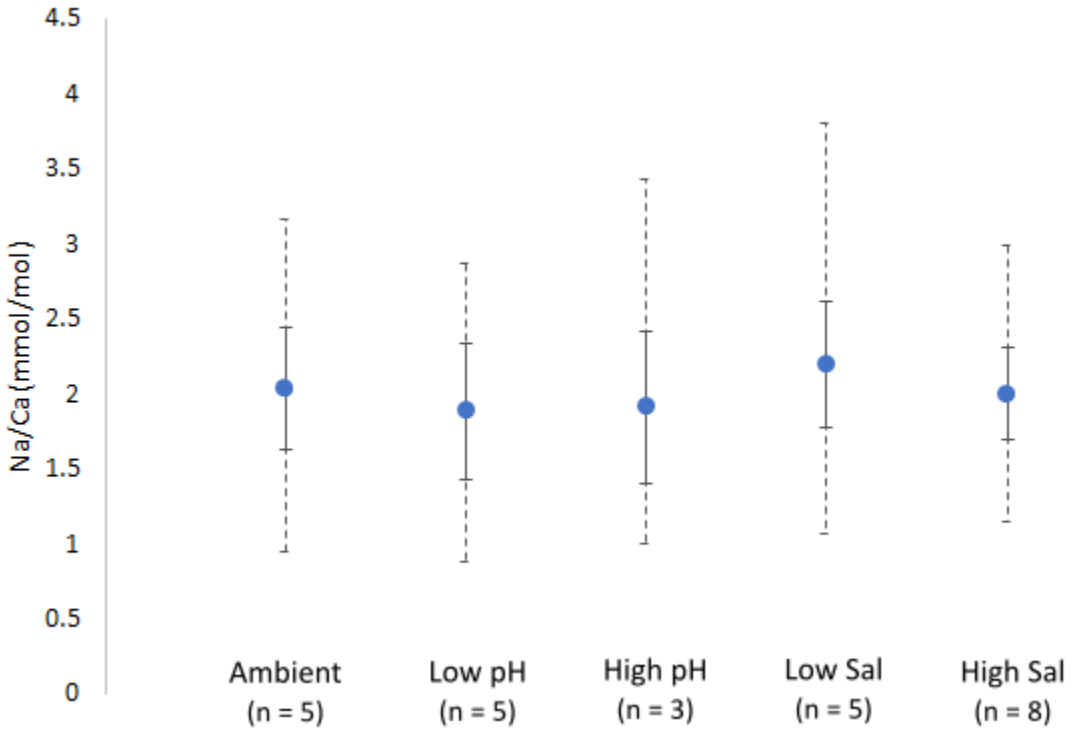

Figure 6.12. Specimens cultured under different salinity and pH conditions appear to have similar Na banding patterns and ratios. Mean Na/Ca ratios (mmol/mol) from the following experimental treatments: ambient (salinity = 33.4, pH = 8.06), low pH (salinity = 33.2, pH = 7.90), high pH (salinity = 33.4, pH = 8.59), low salinity (salinity = 30.0, pH = 8.21), and high salinity (salinity = 36.3, pH = 8.01) are reported. All samples were cultured at 22ºC (Table 6.1). Solid error bars represent 1 standard deviation from the mean (1σ). Dashed bars denote the full range of Na banding across all specimens in each experimental treatment.

6.2.2 *Bilobata post-analysis images*

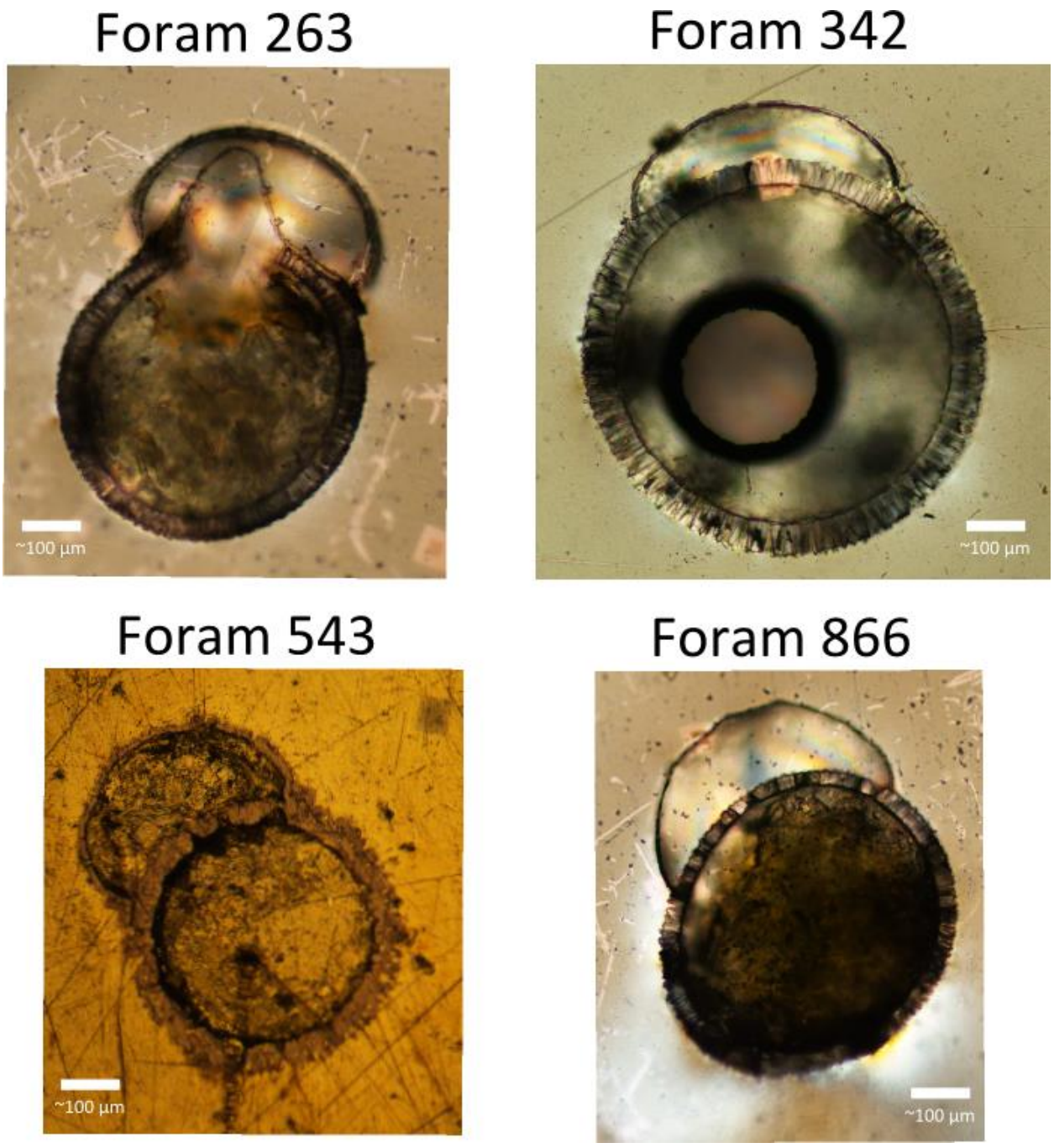

Figure 6.13. Images of *bilobata* samples post analysis. Data from Foram 342 were used to create the *bilobata* images in the main text. Data from the remaining three samples are displayed in the appendix.

6.2.3 *Additional bilobata samples*

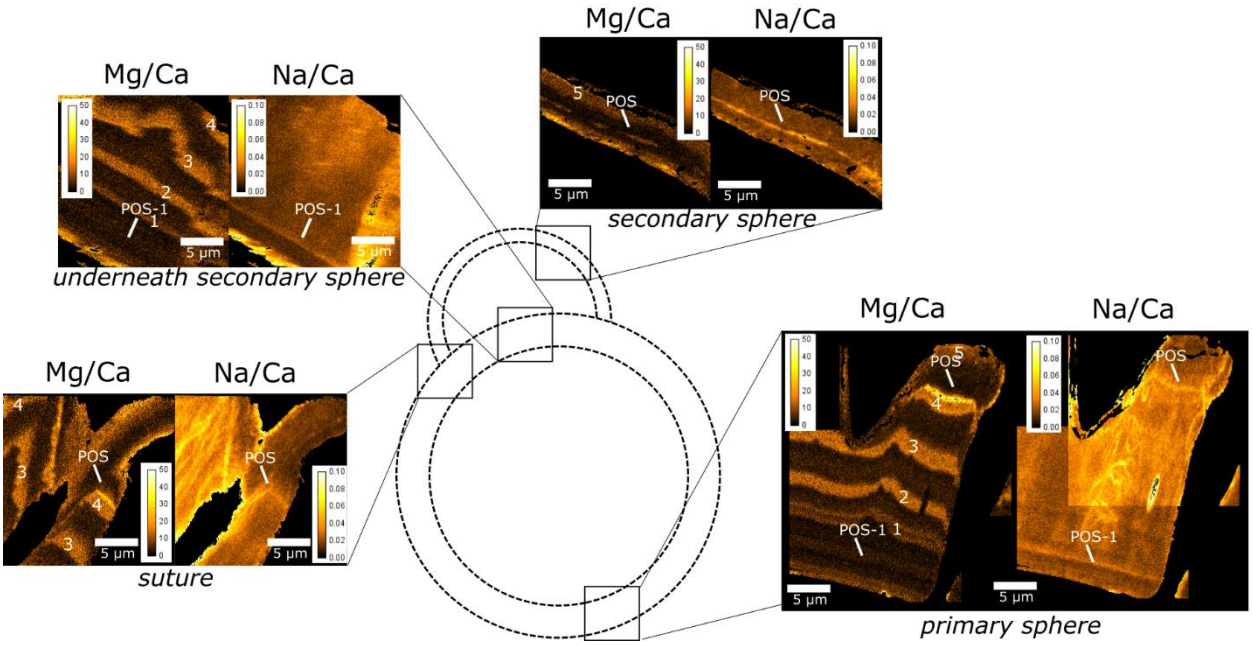

Figure 6.14. Foram 866, the third *bilobata* analyzed, has similar patterns to the specimen in Figure 2.3. Mg/Ca and Na/Ca values are provided in mmol/mol, and the locations from which the images were taken are indicated on the schematic. Suspected locations for the POS and POS-1 are labeled. Mg/Ca bands are numbered for reference.

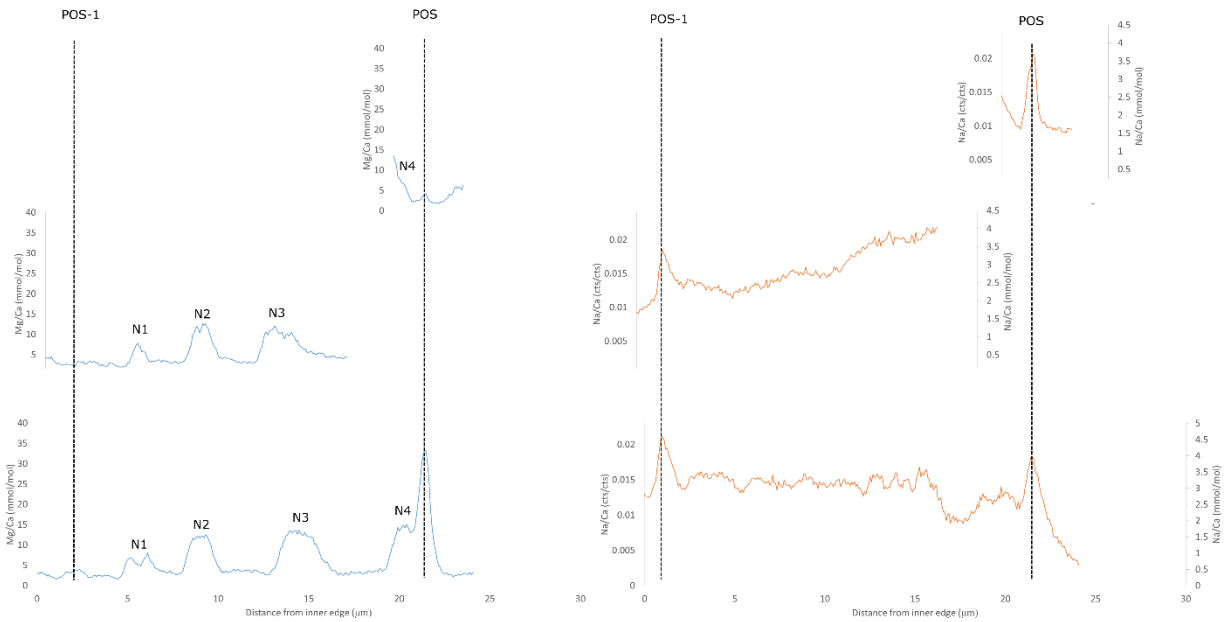

Figure 6.15. A summary of Mg/Ca and Na/Ca profiles from Foram 866. Profiles are arranged with the secondary sphere profiles at the top, the area beneath the secondary sphere as the middle profile, and the primary sphere at the bottom. Locations for the POS and POS-1 are labeled, along with Mg/Ca night bands. Note that due to oblique polishing and sectioning, the alignment of Mg/Ca bands may not be exact throughout the figure.

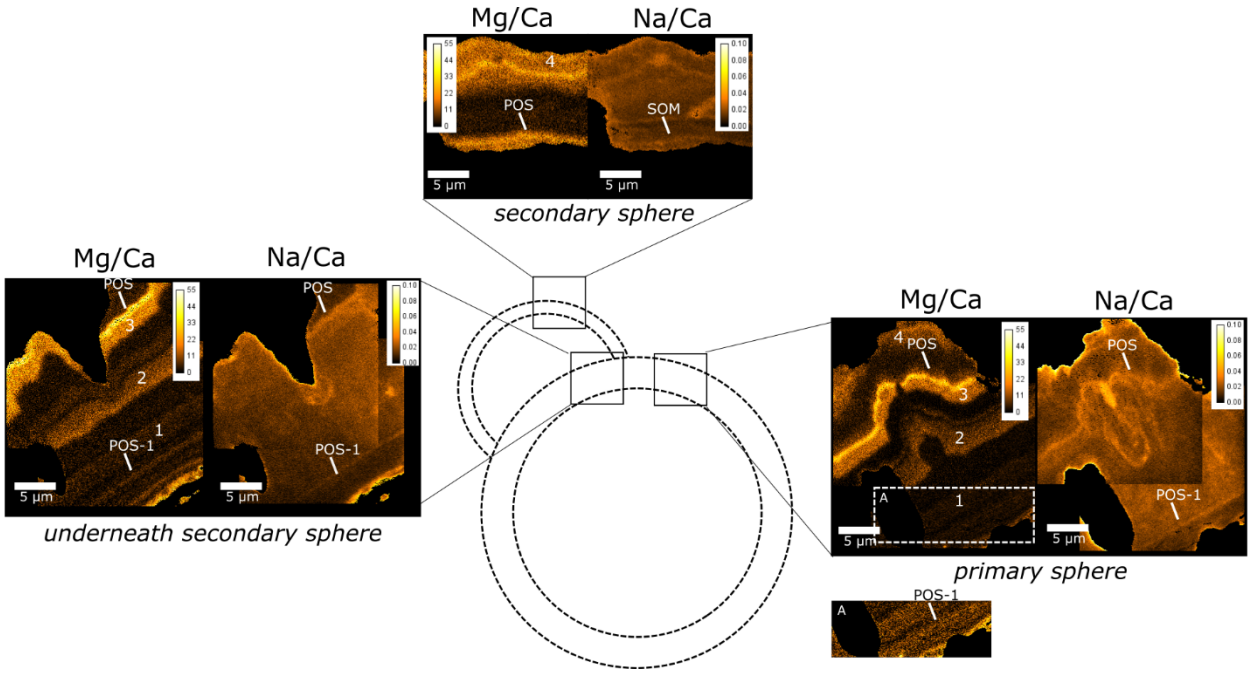

Figure 6.16. Foram 263, the second *bilobata* analyzed, has similar patterns to the specimen in Figure 2.3. Mg/Ca and Na/Ca values are provided in mmol/mol, and the locations from which the images were taken are indicated on the schematic. Suspected locations for the POS and POS-1 are labeled. The POS-1 portion of the primary sphere is inset, and the bands are numbered.

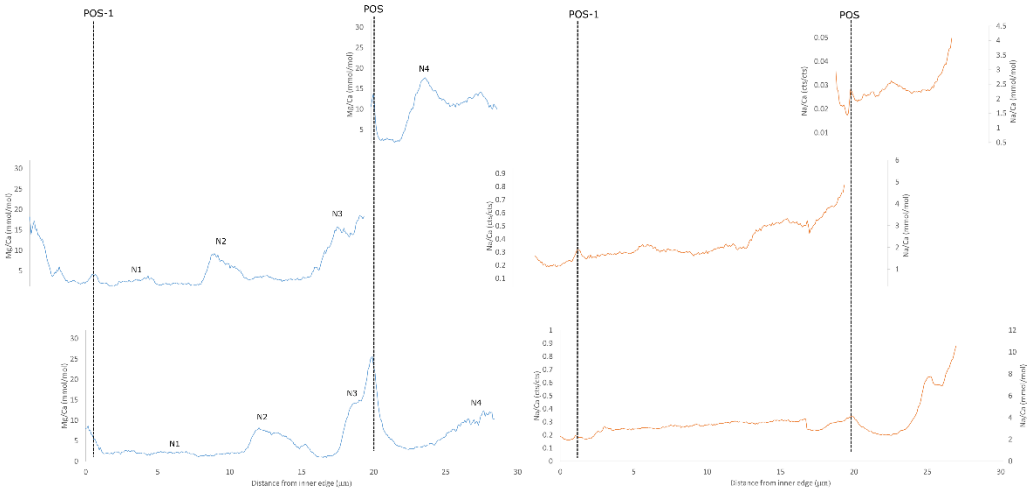

Figure 6.17. A summary of Mg/Ca and Na/Ca profiles from Foram 263. Profiles are arranged with the secondary sphere profiles at the top, the area beneath the secondary sphere as the middle profile, and the primary sphere at the bottom. Locations for the POS and POS-1 are labeled, along with Mg/Ca night bands. Note that due to oblique polishing and sectioning, the alignment of Mg/Ca bands may not be exact throughout the figure.

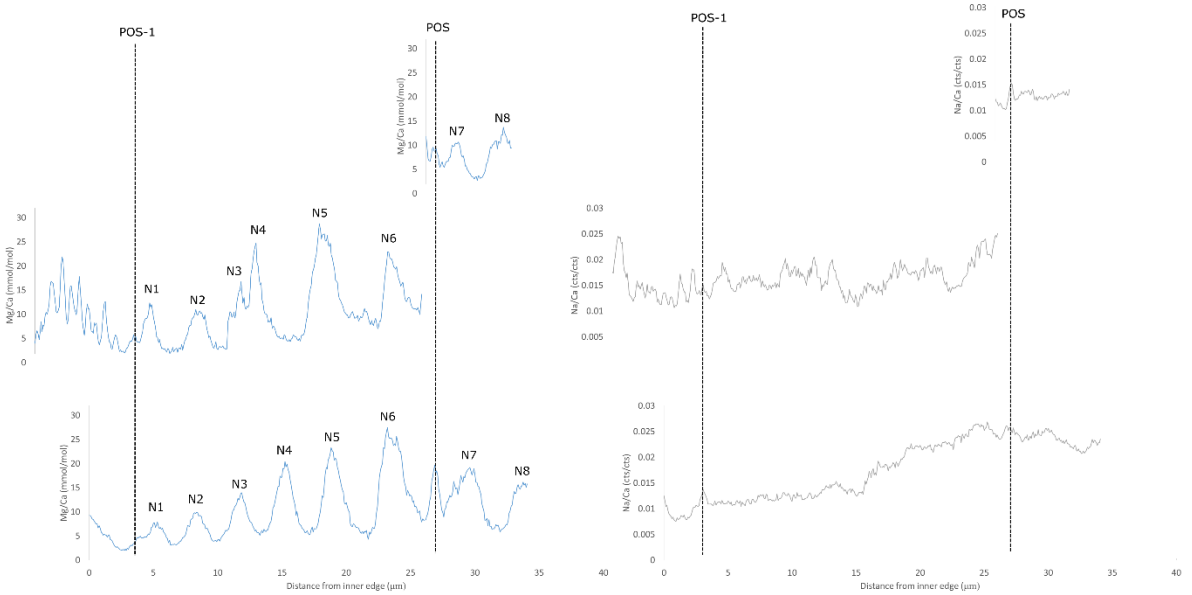

Figure 6.18. A summary of Mg/Ca and Na/Ca profiles from Foram 342, the *bilobata* imaged in Figure 2.3. Profiles are arranged with the secondary sphere profiles at the top, the area beneath the secondary sphere as the middle profile, and the primary sphere at the bottom. Locations for the POS and POS-1 are labeled, along with Mg/Ca night bands. Note that due to oblique polishing and sectioning, the alignment of Mg/Ca bands may not be exact throughout the figure.

6.2.4 *Abnormal growth patterns in bilobata*

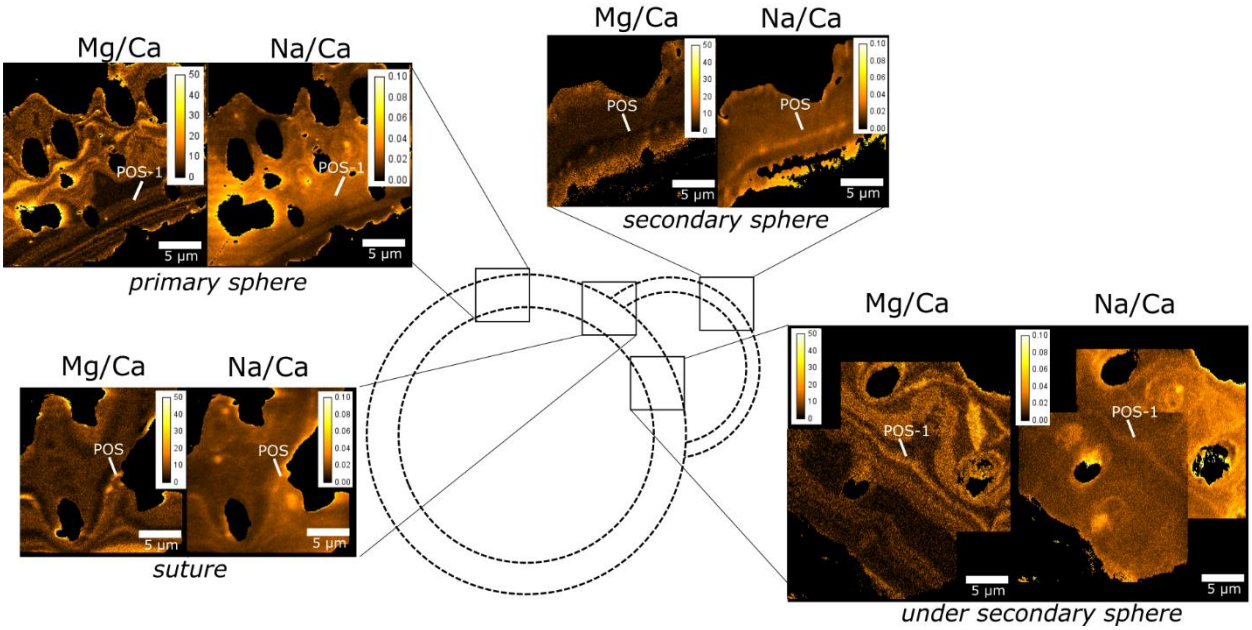

Figure 6.19. Mg/Ca images of Foram 543, arranged spatially. Potential locations for POS and POS-1 are labeled where available. The banding in this specimen is less straightforward than the banding of the *bilobata* presented in the main text, however, despite the unique growth pattern exhibited by this individual, the point at which calcification begins on both the primary and secondary sphere is still visible. Here it appears that this individual formed its secondary chamber and underwent gametogenesis in the span of one day, as suggested by the single low Mg band that makes up the secondary sphere on both sides of the POS. The same low Mg band is visible on the outer edge of the primary sphere, except where the primary sphere is under the secondary sphere. This is consistent with the growth pattern that would be expected for *bilobata*. Because of the atypical banding pattern exhibited by this individual, the POS is difficult to resolve in the primary sphere.

6.2.5 G. bulloides *Mg/Ca and Na/Ca profiles*

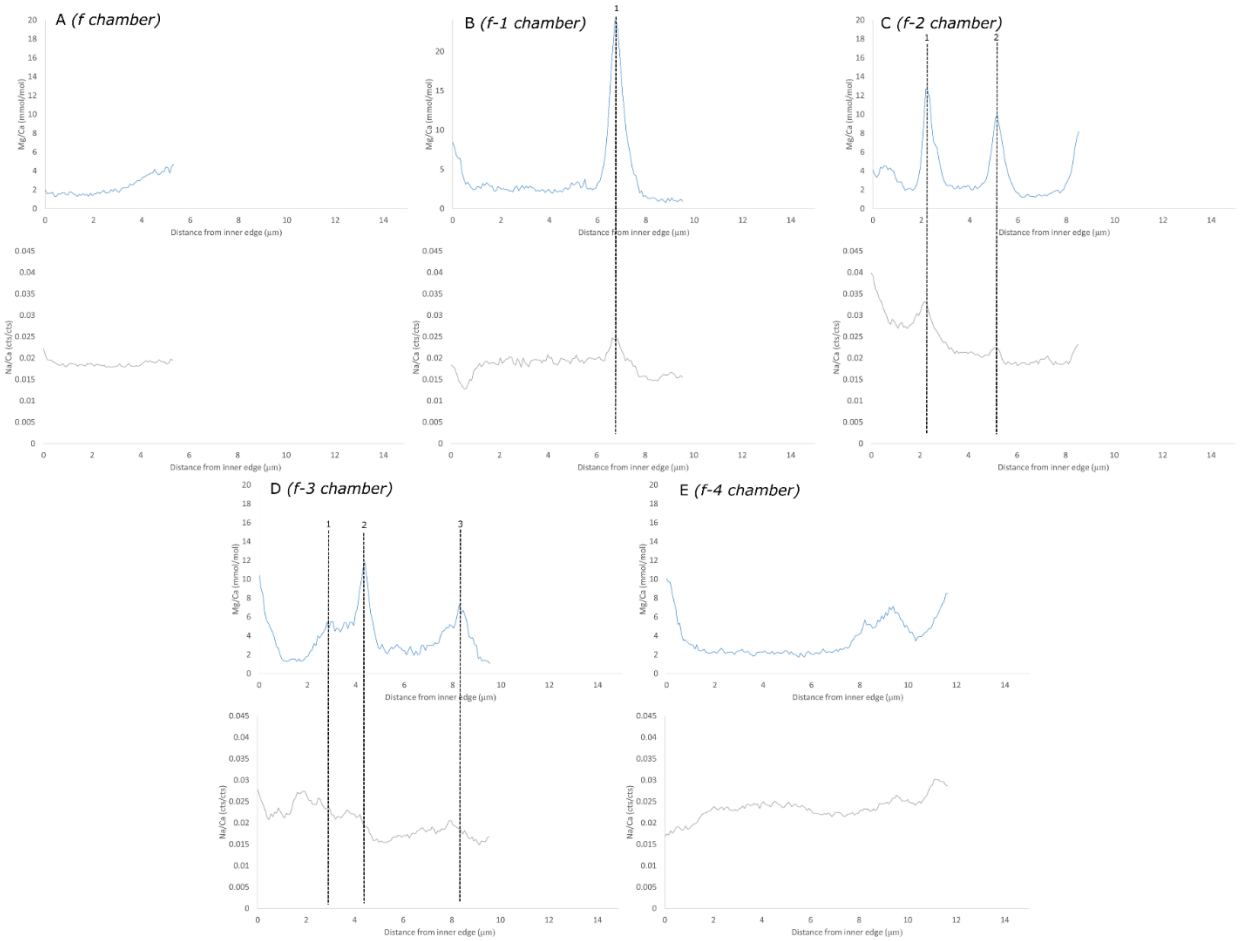

Figure 6.20. Mg/Ca and Na/Ca profiles of the *G. bulloides* specimen discussed in the main text (Fig. 2.3), separated by chamber. The *f-4* chamber was facing upwards at the time of polishing, and thus was polished at a very oblique angle, making it difficult to resolve banding. In the final whorl (*f, f-1,* and *f-2),* which are the best polished chambers of this specimen, the number of high Mg/Ca bands appears to increase with the age of the chamber. The final chamber, *f,* has no Mg/Ca bands visible, *f-1* has one visible Mg/Ca band, and *f-2* has two visible Mg/Ca bands. All Mg/Ca bands are labeled.

6.2.6 N. dutertrei *Mg/Ca and Na/Ca profiles*

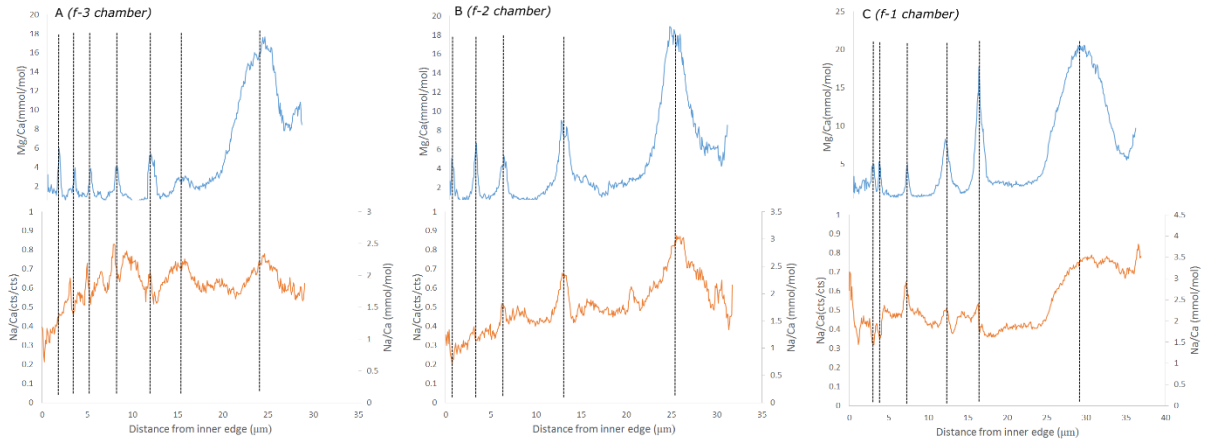

Figure 6.21. Mg/Ca and Na/Ca profiles of the *N. dutertrei* specimen 152A discussed in the main text (Fig. 2.6), separated by chamber. Mg/Ca bands are indicated by dotted lines. The number of Mg/Ca bands does not seem to vary from chamber to chamber in a regular pattern. In addition, while every Mg/Ca band corresponds to a high Na/Ca band, not all Na/Ca bands in *N. dutertrei* seem to correspond to Mg/Ca bands. A NanoSIMS image of this specimen was previously published in Fehrenbacher et al., 2017 (152A).

APPENDIX B: TOF-SIMS DATA FROM O. UNIVERSA SPECIMENS

7.1 AMBIENT (SALINITY = 33 PPT, $[CO_3]^{2-}$ = 170MMOL/KGSW, T = 22°C)

001:

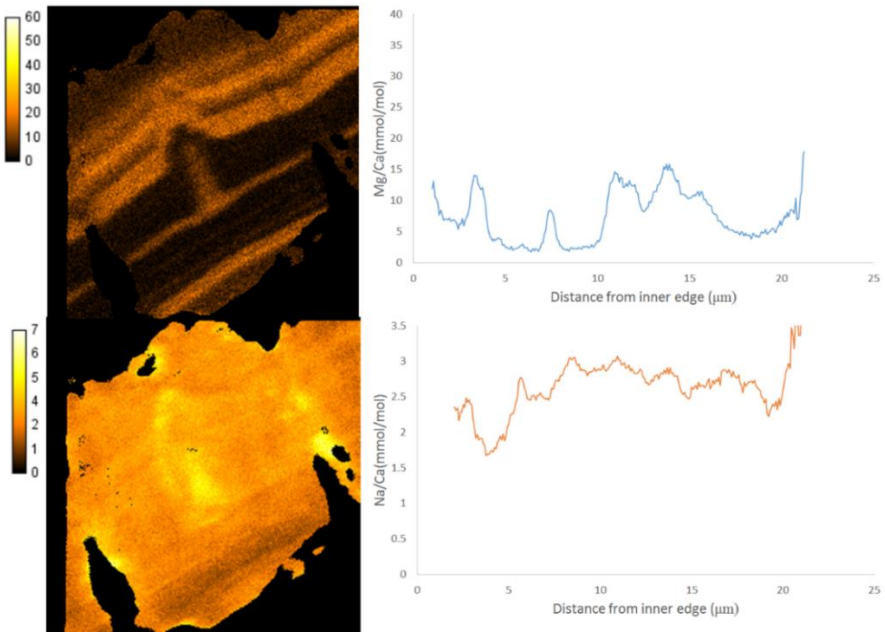

032:

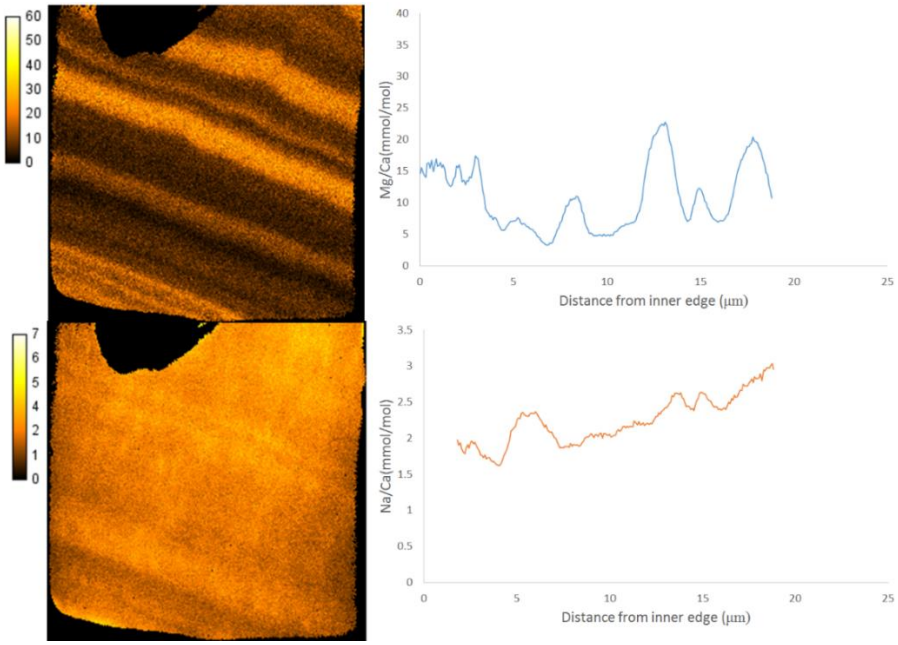

046:

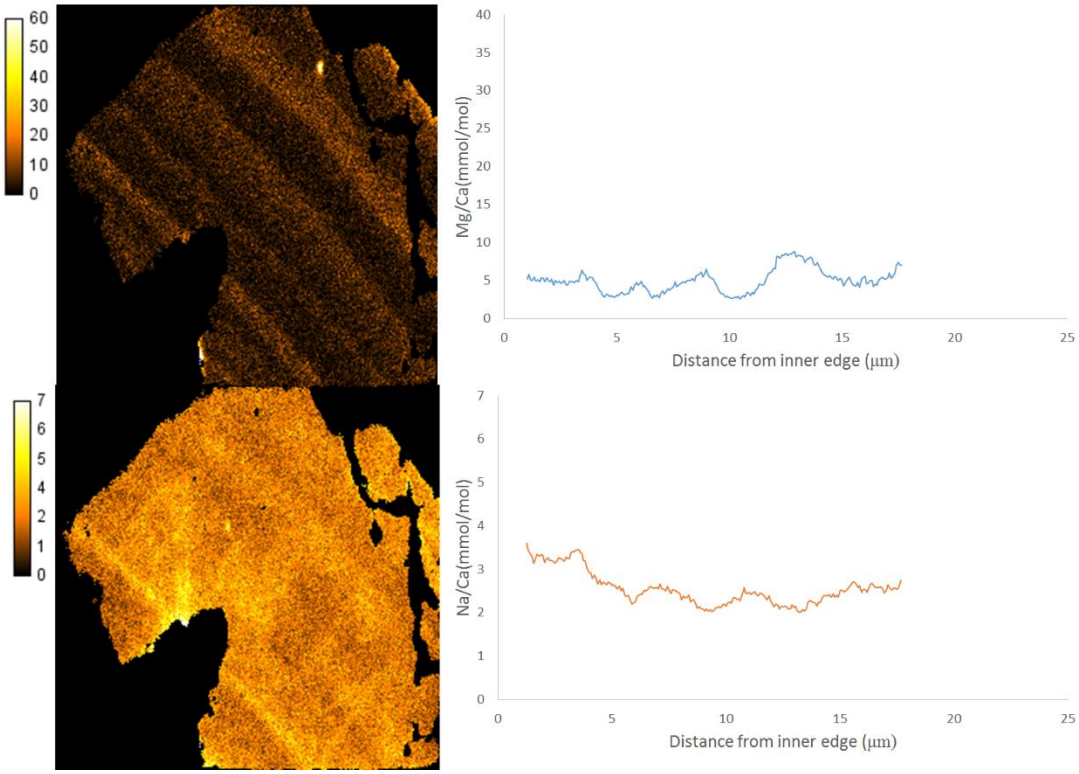
60
50
40
30
20
10
0
Mg/Ca(mmol/mol)
40
35
30
25
20
15
10
5
0
0
5
10
15
20
25
Distance from inner edge (μm)
7
6
5
4
2
1
0
Na/Ca(mmol/mol)
7
6
5
4
3
2
1
0
0
5
10
15
20
25
Distance from inner edge (μm)

048:

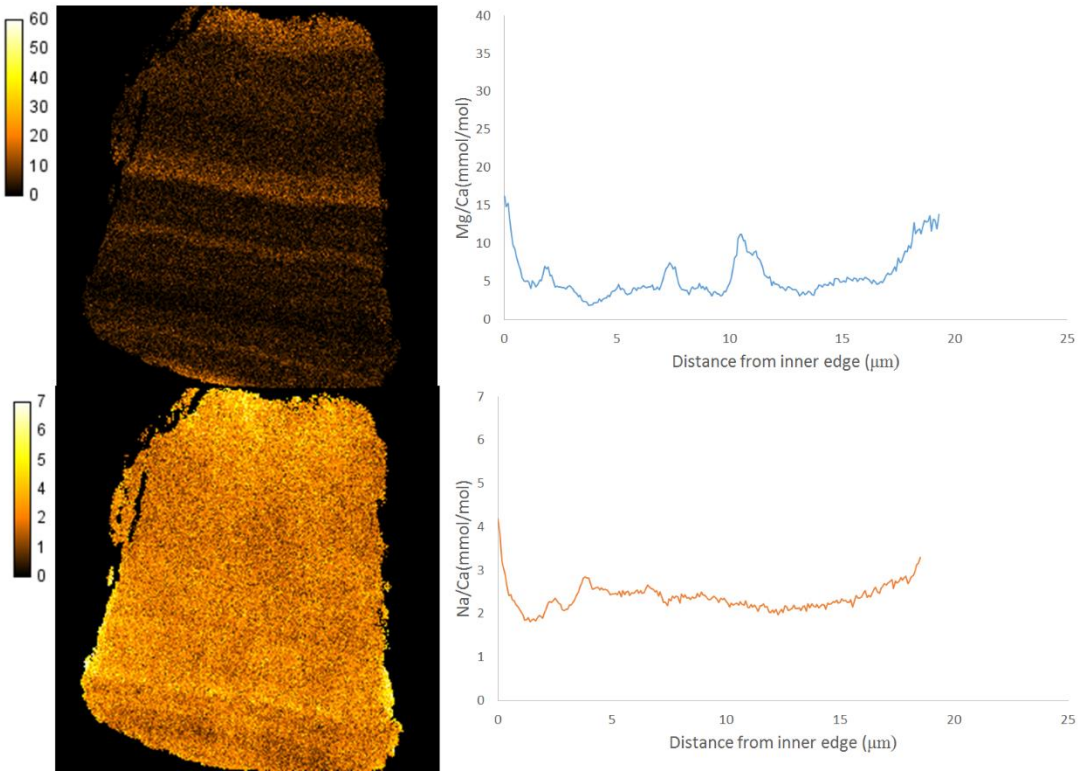
60
50
40
30
20
10
0
Mg/Ca(mmol/mol)
40
35
30
25
20
15
10
5
0
0
5
10
15
20
25
Distance from inner edge (μm)
7
6
5
4
2
1
0
Na/Ca(mmol/mol)
7
6
5
4
3
2
1
0
0
5
10
15
20
25
Distance from inner edge (μm)

049:

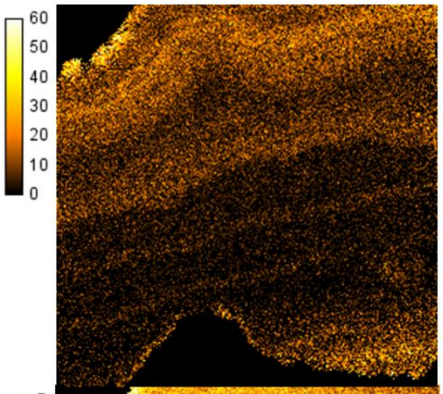
60
50
40
30
20
10
0

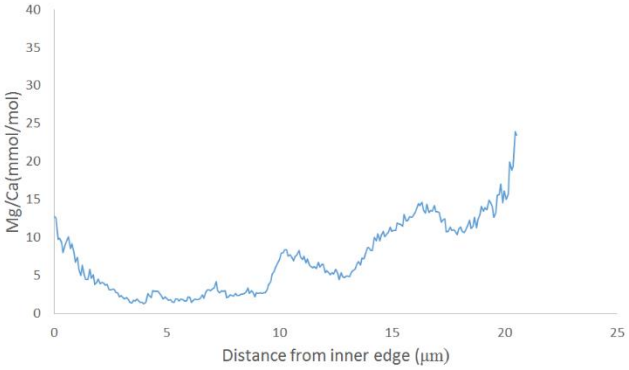
Mg/Ca(mmol/mol)
Distance from inner edge (μm)

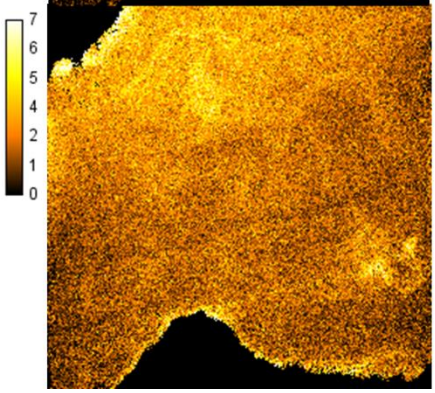
7
6
5
4
2
1
0

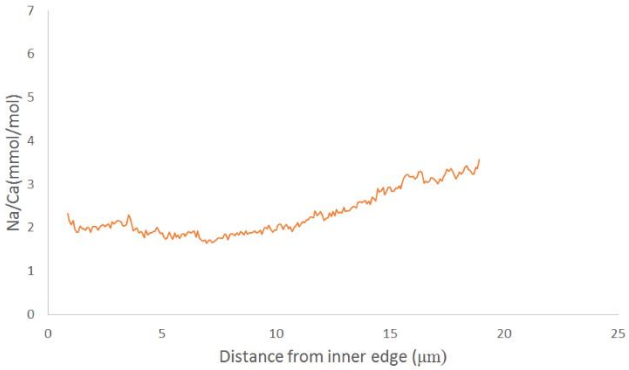
Na/Ca(mmol/mol)
Distance from inner edge (μm)

633:

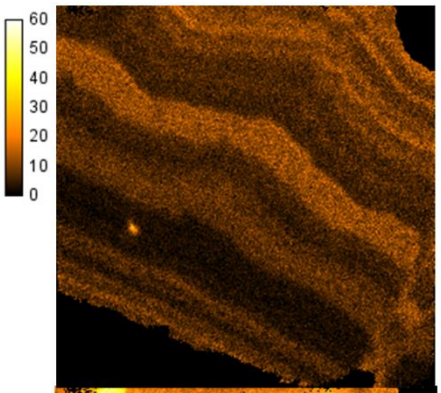
60
50
40
30
20
10
0

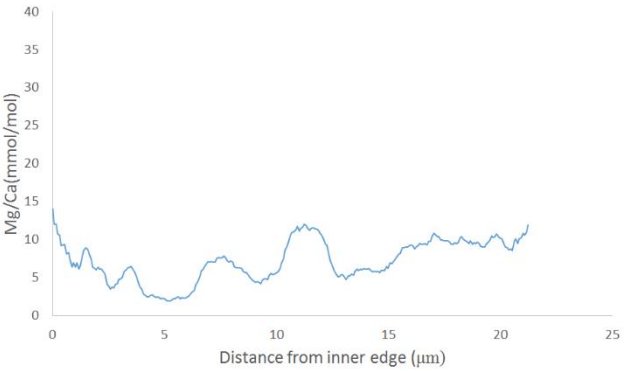
Mg/Ca(mmol/mol)
Distance from inner edge (μm)

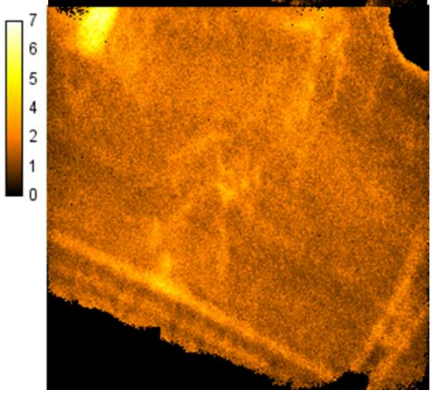
7
6
5
4
2
1
0

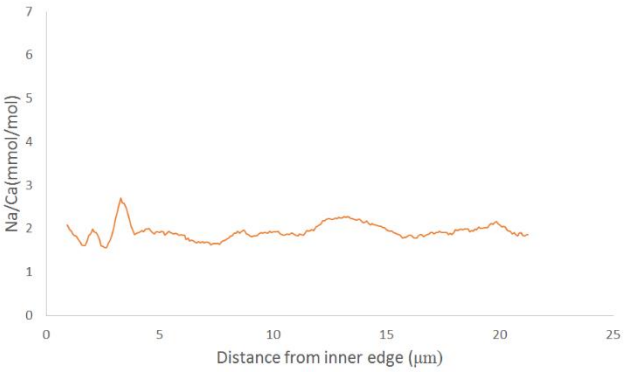
Na/Ca(mmol/mol)
Distance from inner edge (μm)

863_1:

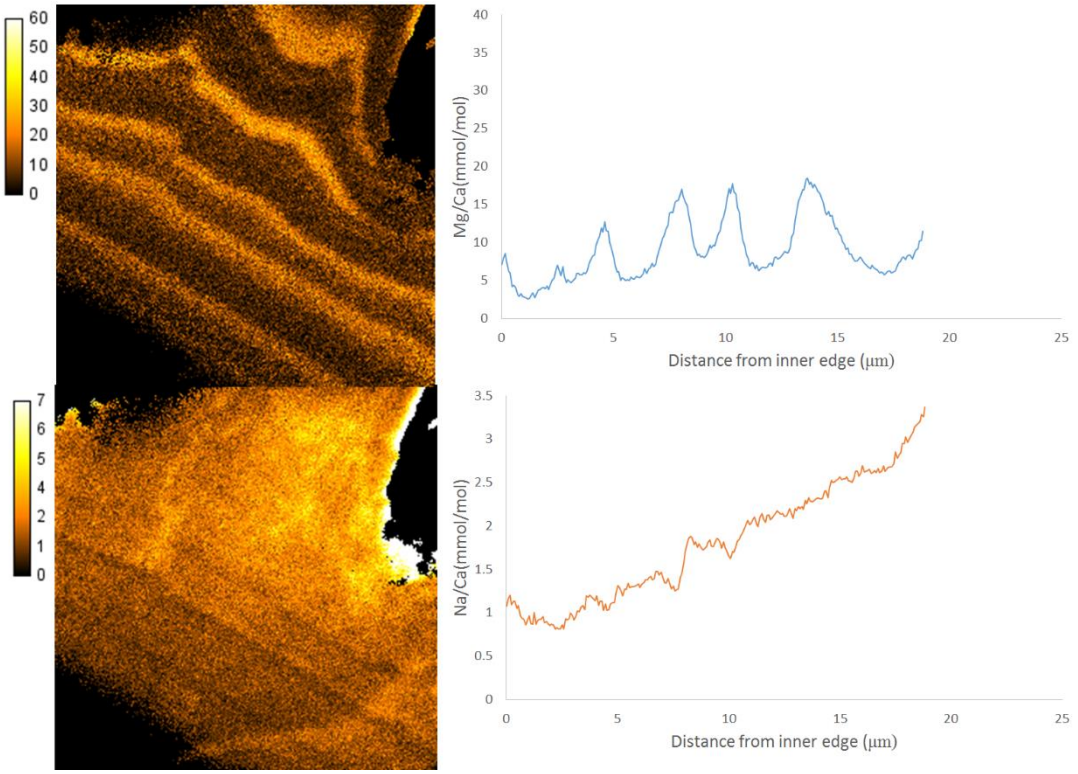
60
50
40
30
20
10
0
7
6
5
4
2
1
0
Mg/Ca(mmol/mol)
Distance from inner edge (µm)
Na/Ca(mmol/mol)
Distance from inner edge (µm)

863_2:

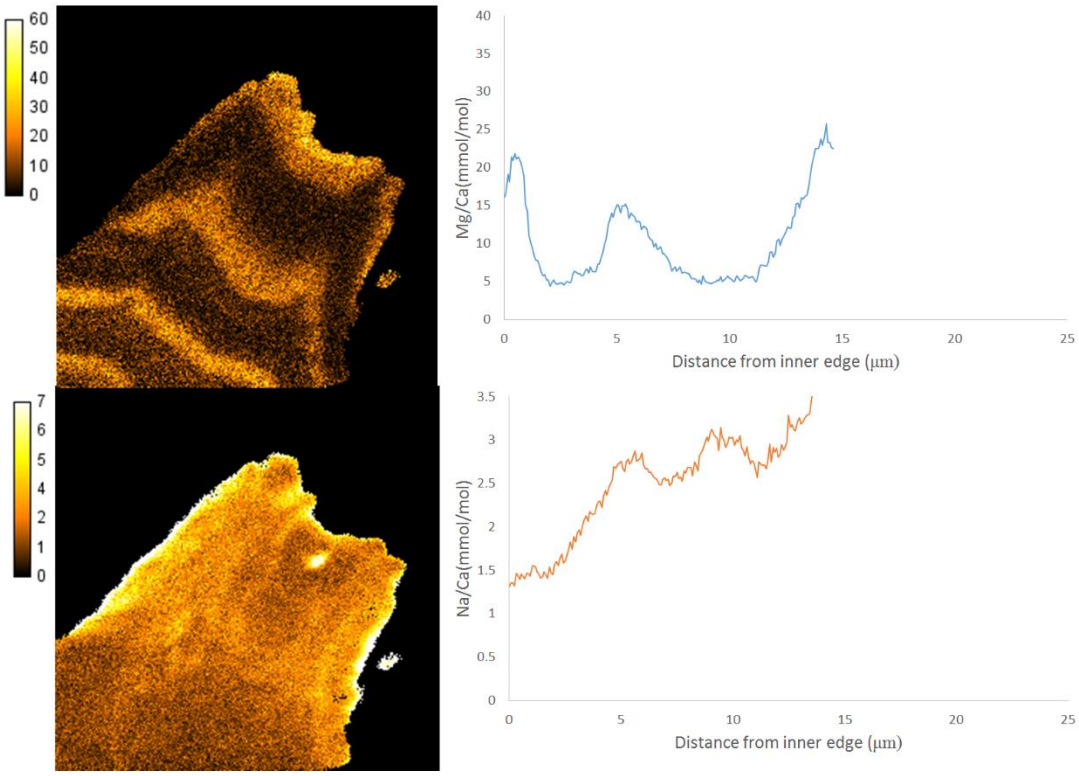
60
50
40
30
20
10
0
7
6
5
4
2
1
0
Mg/Ca(mmol/mol)
Distance from inner edge (µm)
Na/Ca(mmol/mol)
Distance from inner edge (µm)

864:

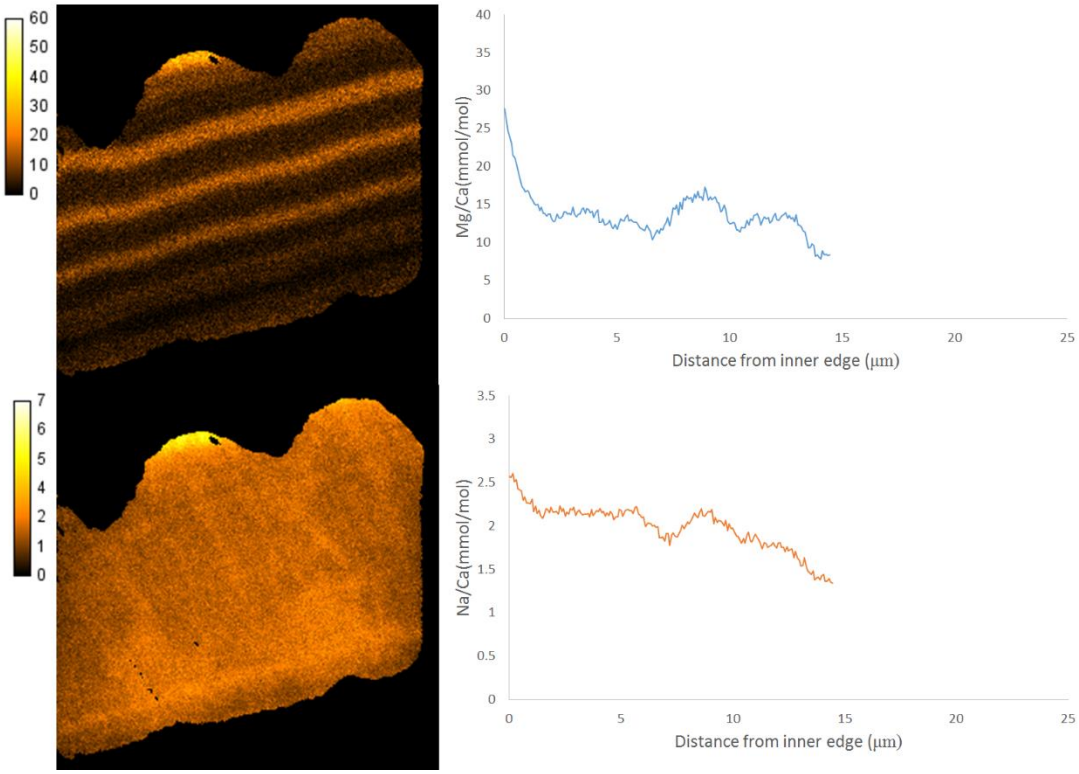
60
50
40
30
20
10
0
7
6
5
4
2
1
0
Mg/Ca(mmol/mol)
Distance from inner edge (μm)
Na/Ca(mmol/mol)
Distance from inner edge (μm)

865:

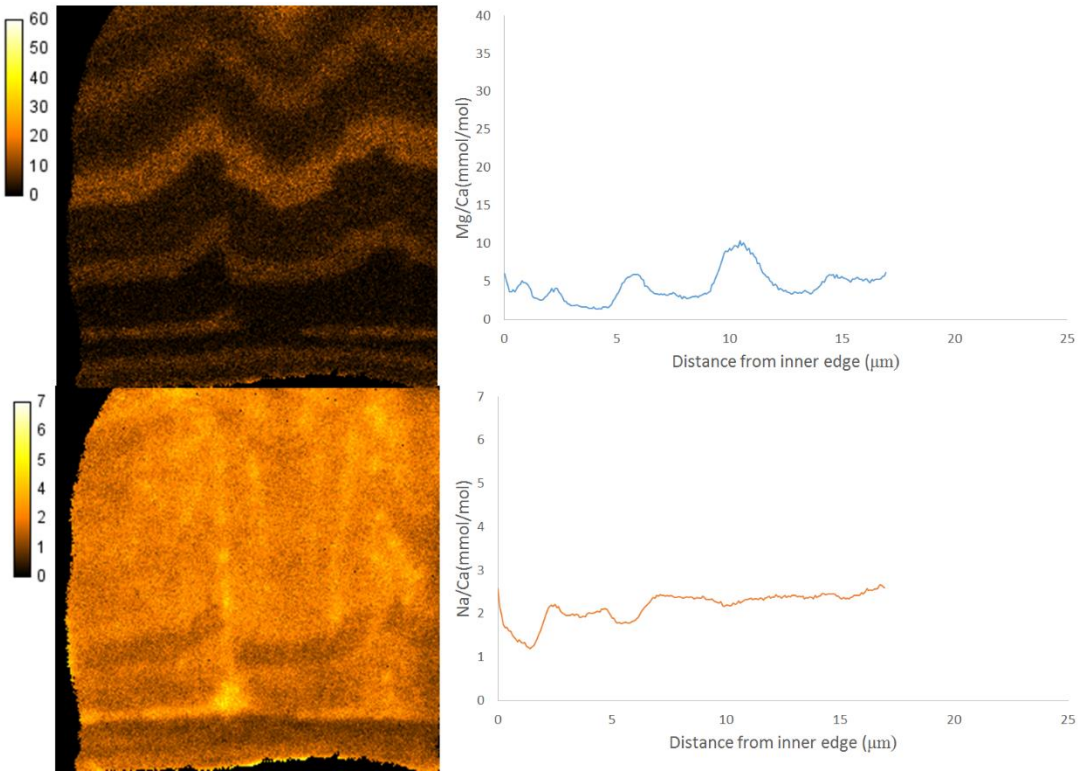
60
50
40
30
20
10
0
7
6
5
4
2
1
0
Mg/Ca(mmol/mol)
Distance from inner edge (μm)
Na/Ca(mmol/mol)
Distance from inner edge (μm)

7.2 Low $[CO_3]^{2-}$ ($[CO_3]^{2-}$ = 90mmol/kgSW)

516:

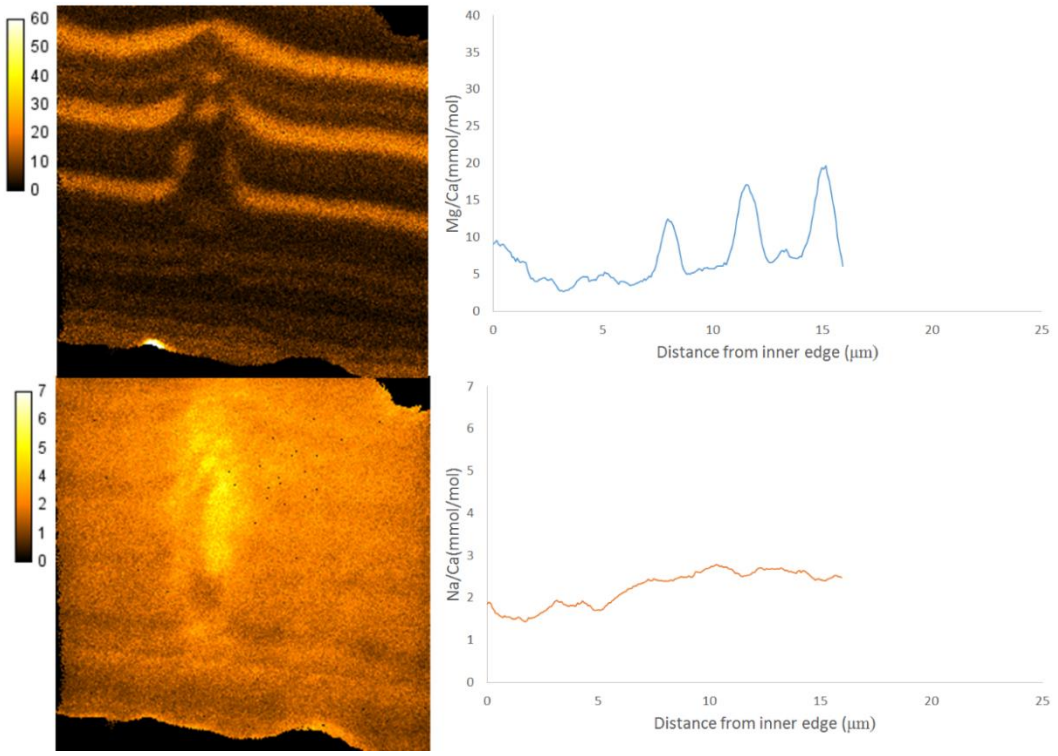

518:

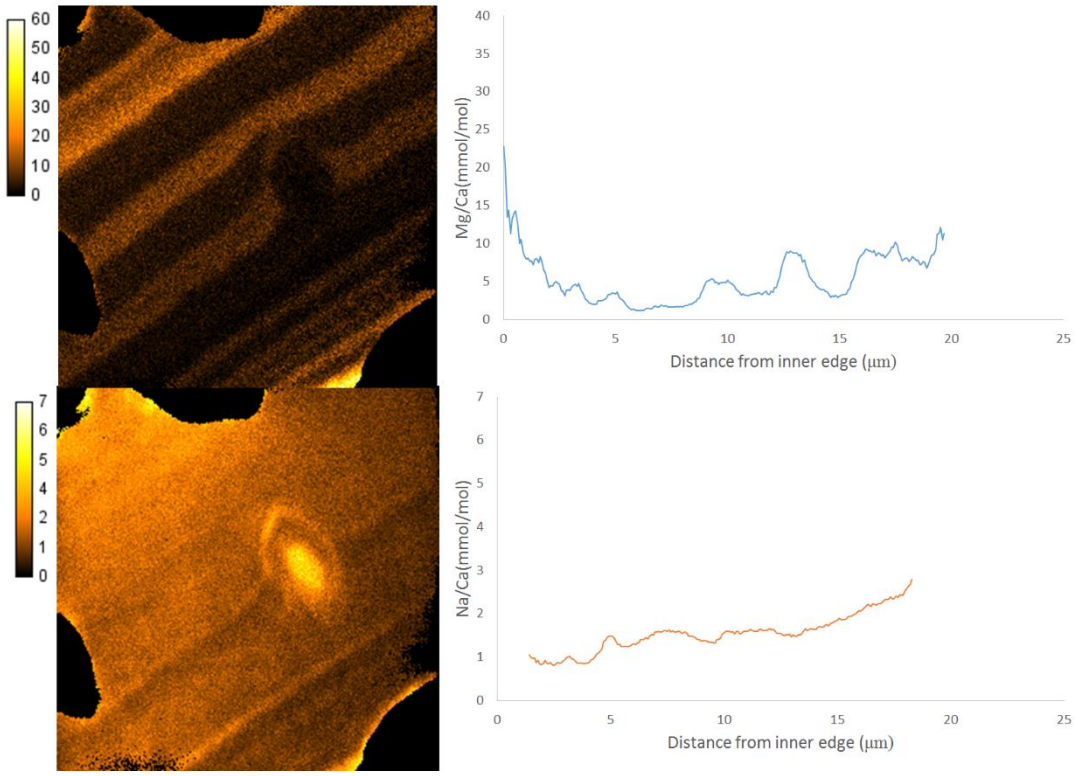

522_1:

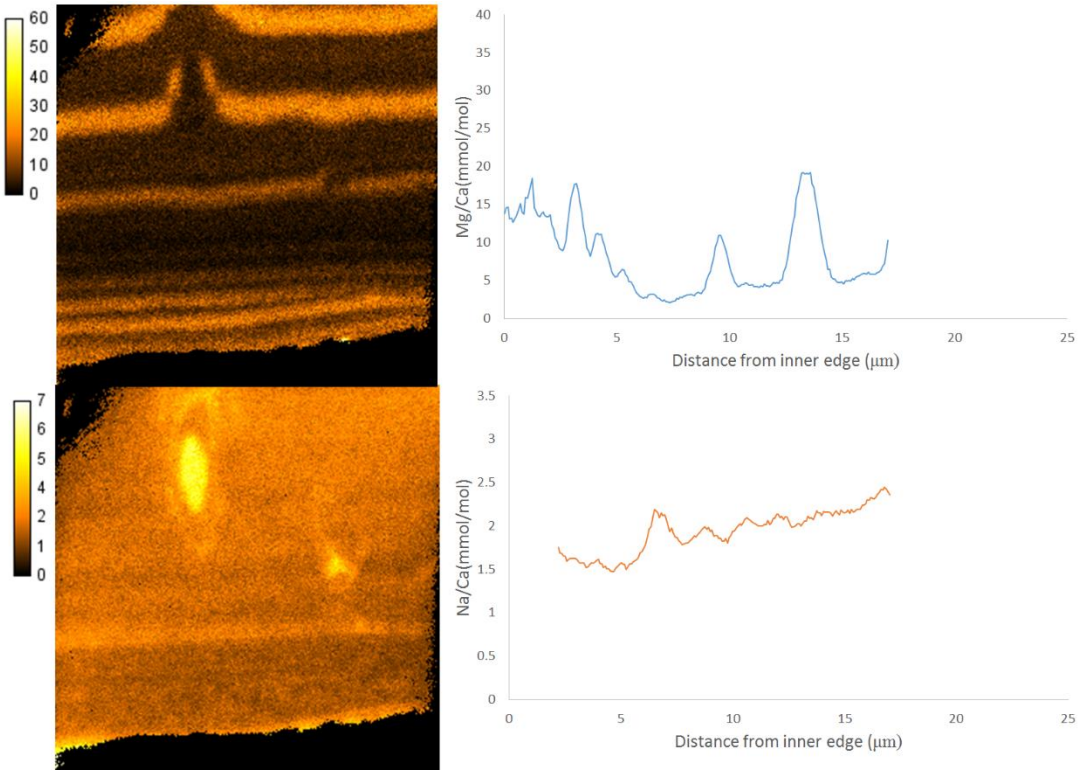
60
50
40
30
20
10
0
7
6
5
4
2
1
0
Mg/Ca(mmol/mol)
Distance from inner edge (μm)
Na/Ca(mmol/mol)
Distance from inner edge (μm)

522_2:

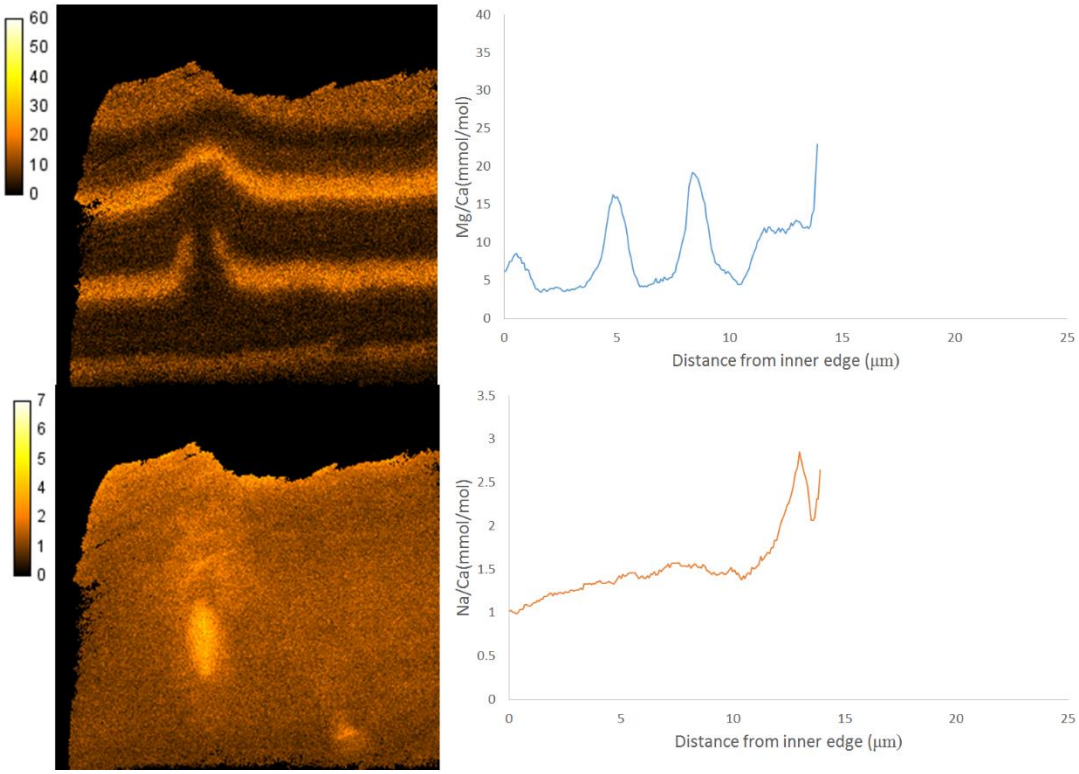
60
50
40
30
20
10
0
7
6
5
4
2
1
0
Mg/Ca(mmol/mol)
Distance from inner edge (μm)
Na/Ca(mmol/mol)
Distance from inner edge (μm)

555_1:

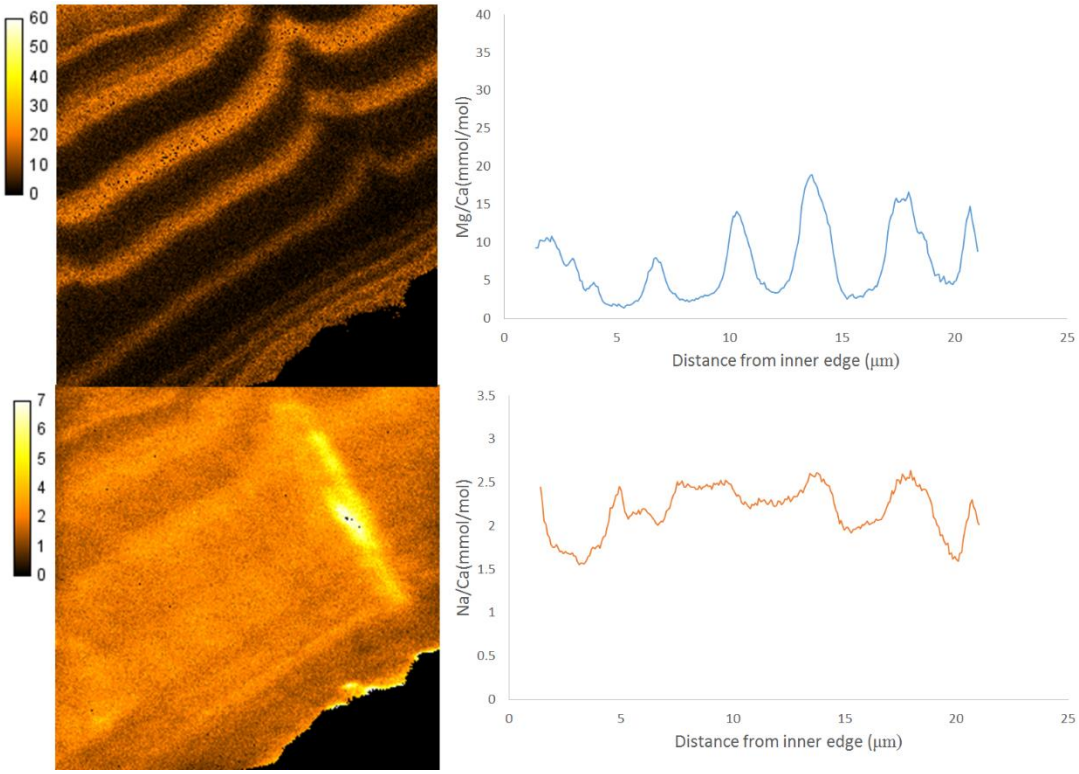
60
50
40
30
20
10
0
Mg/Ca(mmol/mol)
Distance from inner edge (μm)
7
6
5
4
2
1
0
Na/Ca(mmol/mol)
Distance from inner edge (μm)

555_2:

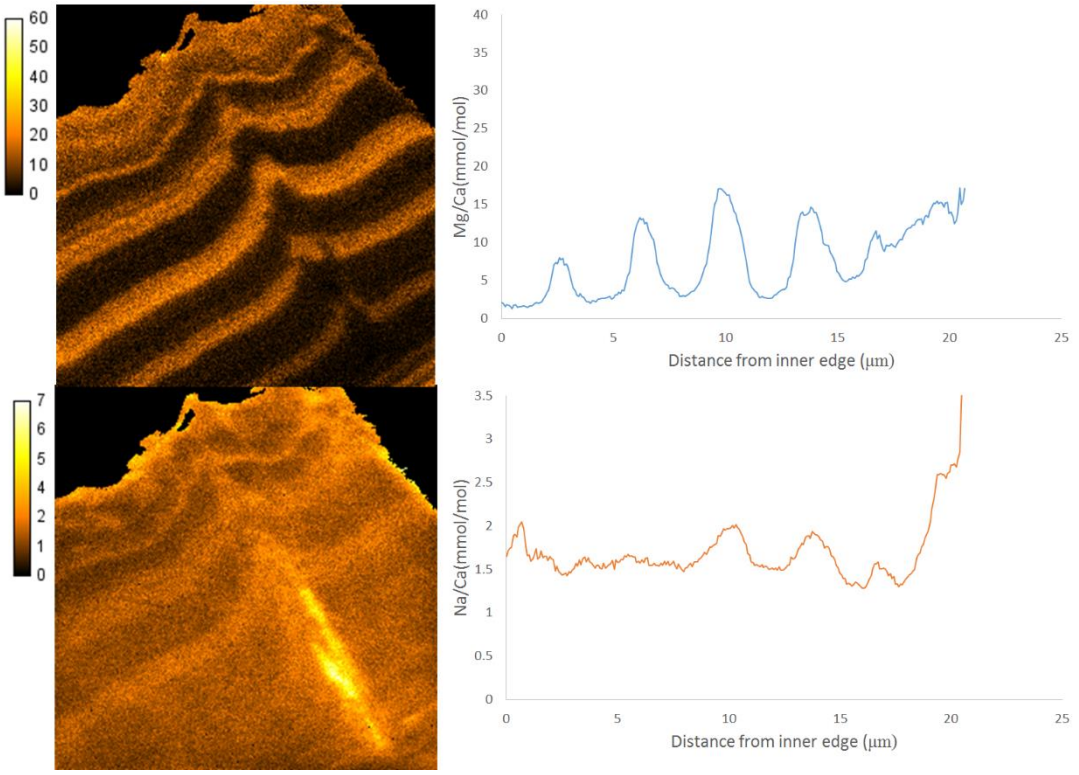
60
50
40
30
20
10
0
Mg/Ca(mmol/mol)
Distance from inner edge (μm)
7
6
5
4
2
1
0
Na/Ca(mmol/mol)
Distance from inner edge (μm)

557:

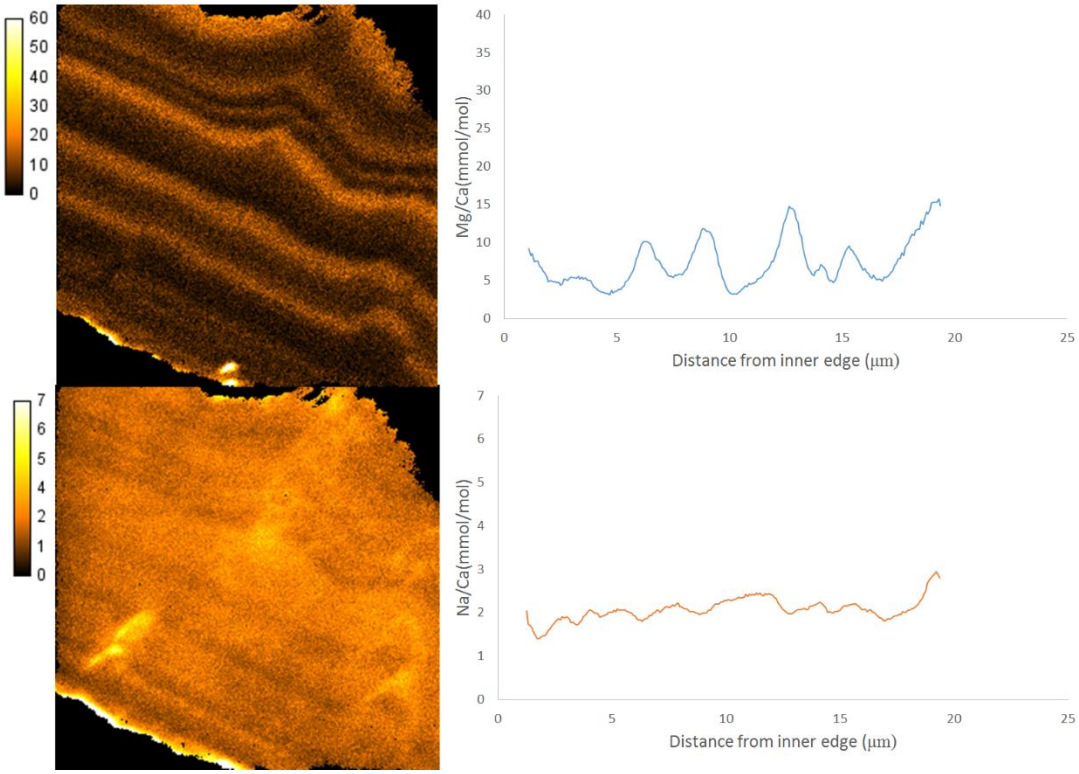
60
50
40
30
20
10
0
40
35
30
25
20
15
10
5
0
Mg/Ca(mmol/mol)
0
5
10
15
20
25
Distance from inner edge (μm)
7
6
5
4
2
1
0
7
6
5
4
3
2
1
0
Na/Ca(mmol/mol)
0
5
10
15
20
25
Distance from inner edge (μm)

7.3 $[CO_3]^{2-}$ = 200MMOL/KGSW

(Note that Na/Ca mmol/mol measurements are approximate)

070_1:

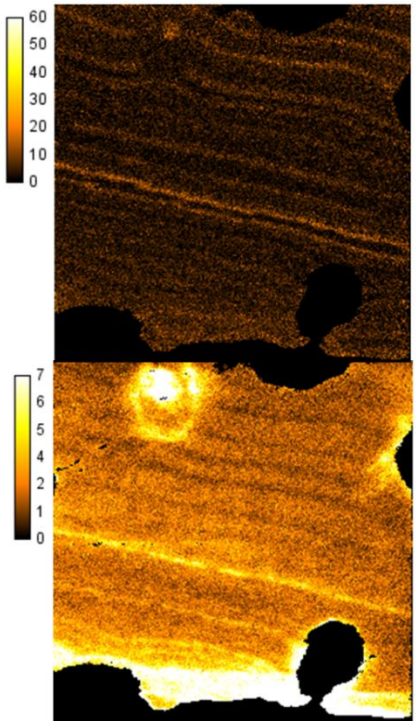

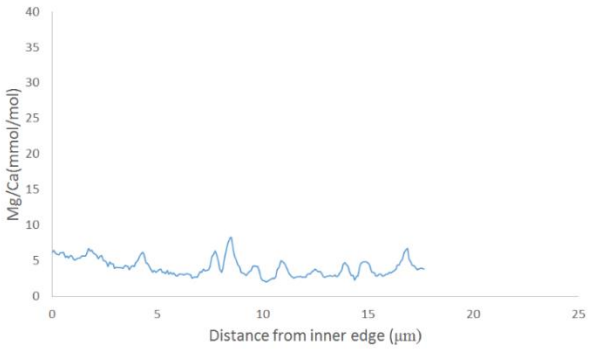

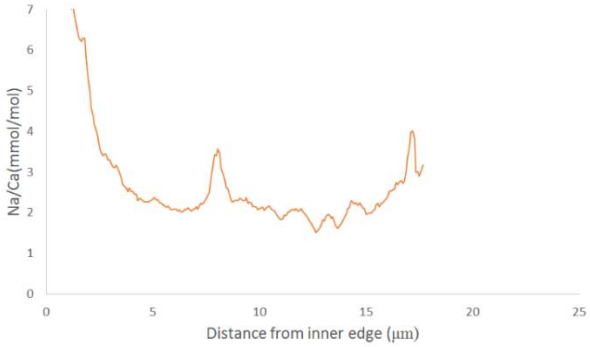

070_2:

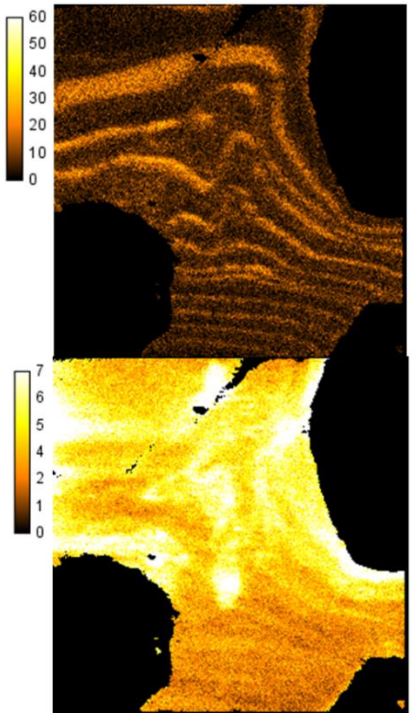

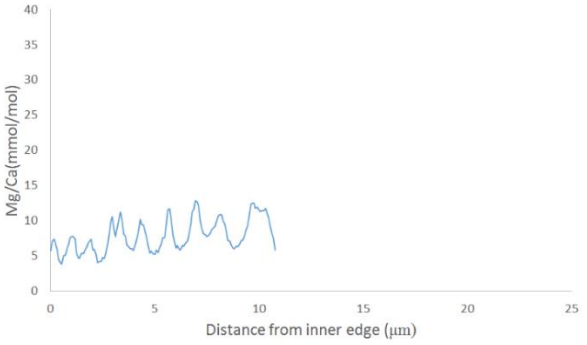

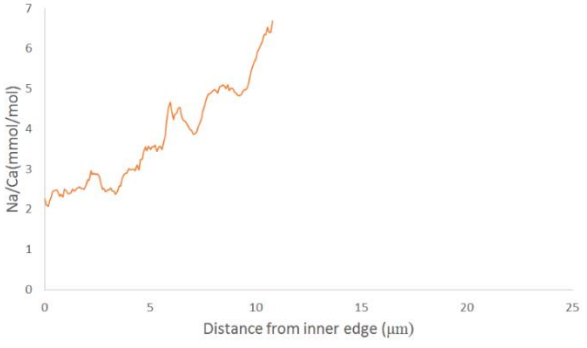

070_3:

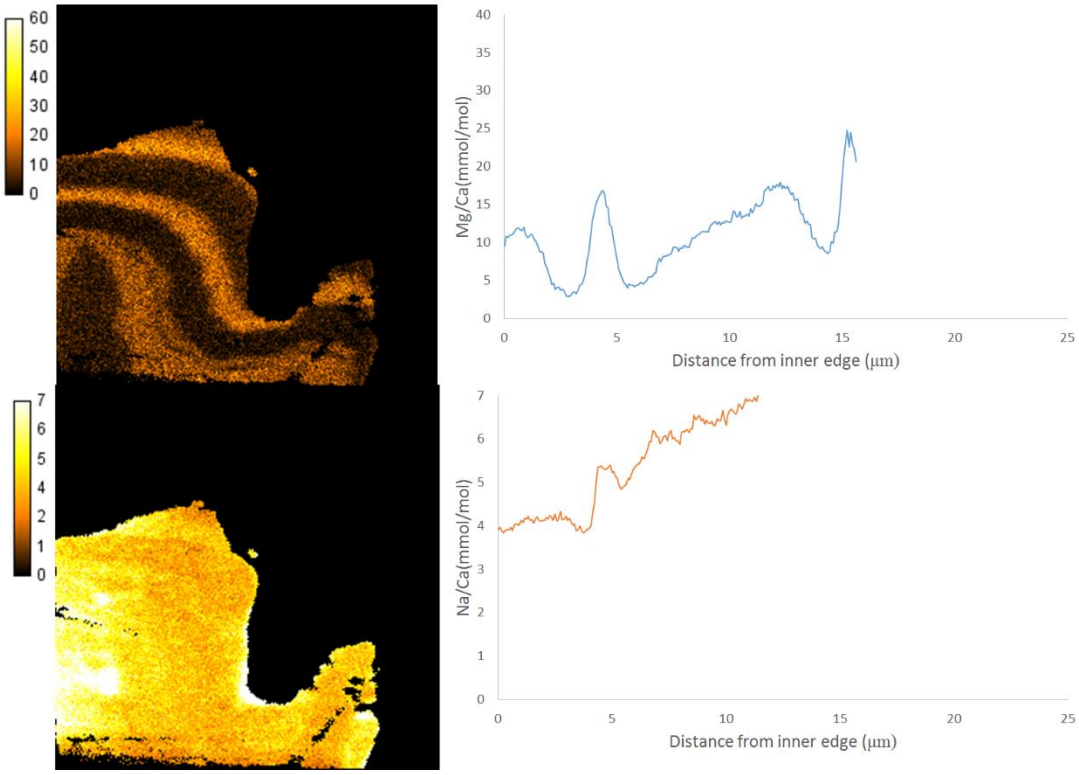
60
50
40
30
20
10
0
7
6
5
4
2
1
0
Mg/Ca(mmol/mol)
Distance from inner edge (μm)
Na/Ca(mmol/mol)
Distance from inner edge (μm)

074_1:

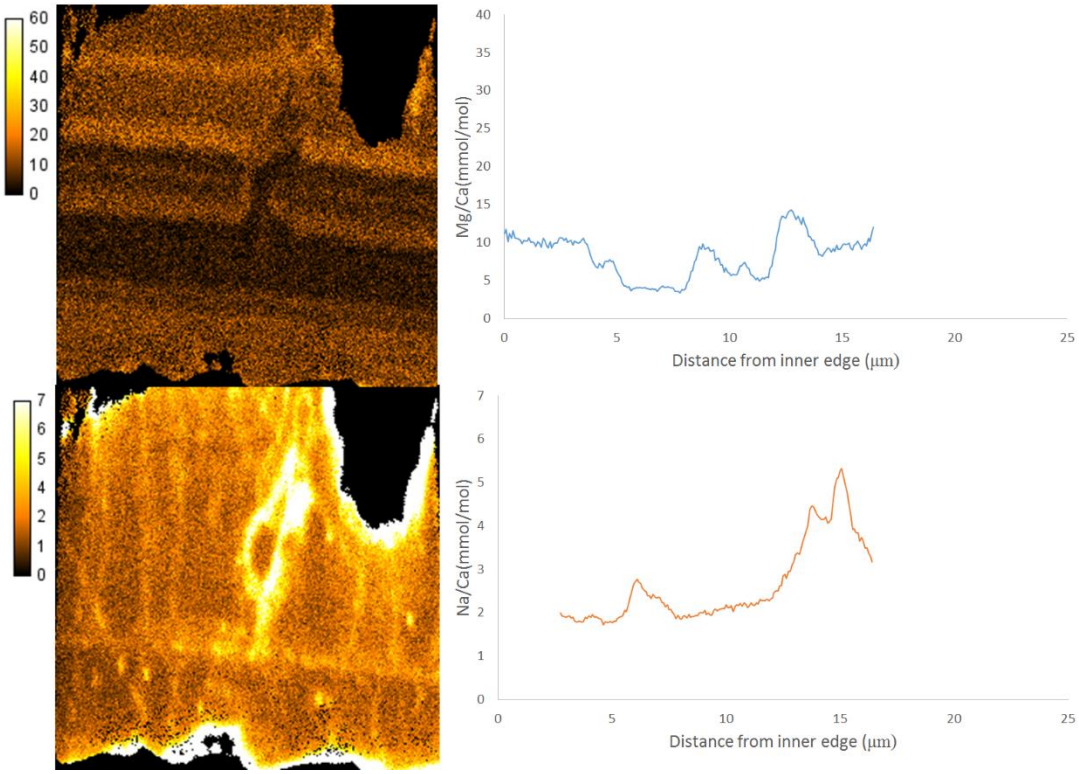
60
50
40
30
20
10
0
7
6
5
4
2
1
0
Mg/Ca(mmol/mol)
Distance from inner edge (μm)
Na/Ca(mmol/mol)
Distance from inner edge (μm)

074_2:

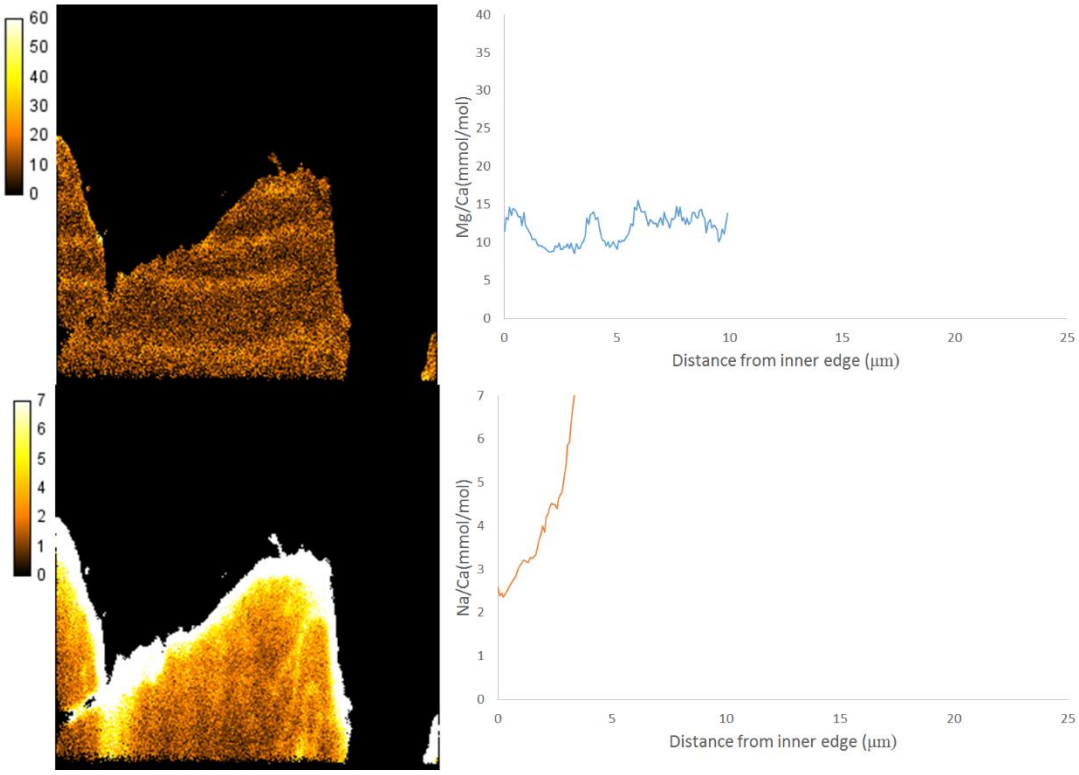
60
50
40
30
20
10
0
7
6
5
4
2
1
0
Mg/Ca(mmol/mol)
Distance from inner edge (μm)
Na/Ca(mmol/mol)
Distance from inner edge (μm)

078:

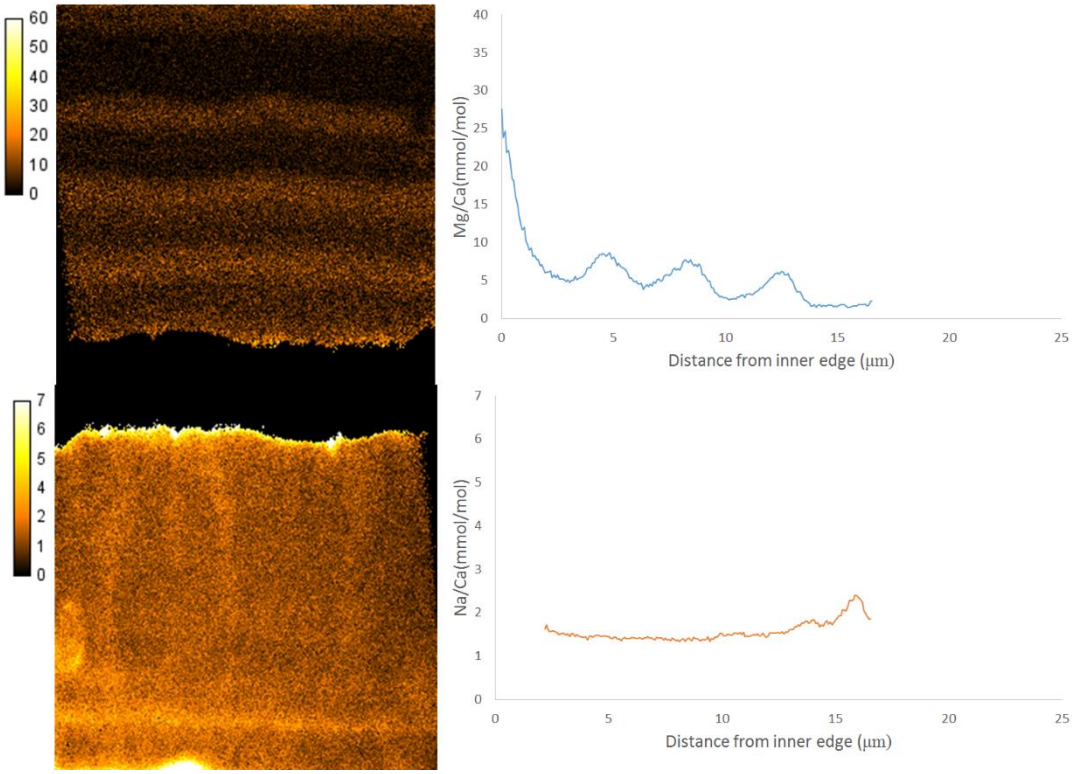
60
50
40
30
20
10
0
7
6
5
4
2
1
0
Mg/Ca(mmol/mol)
Distance from inner edge (μm)
Na/Ca(mmol/mol)
Distance from inner edge (μm)

7.4 $[CO_3]^{2-}$ = 250MMOL/KGSW

(Note that Na/Ca mmol/mol measurements are approximate)

004:

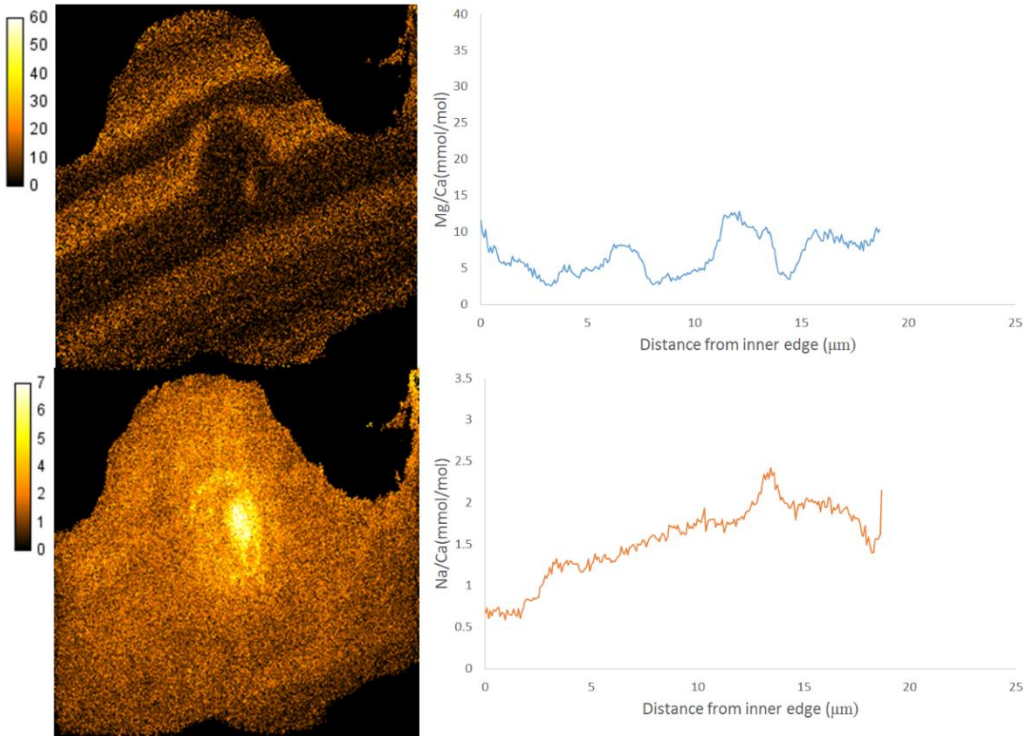

012:

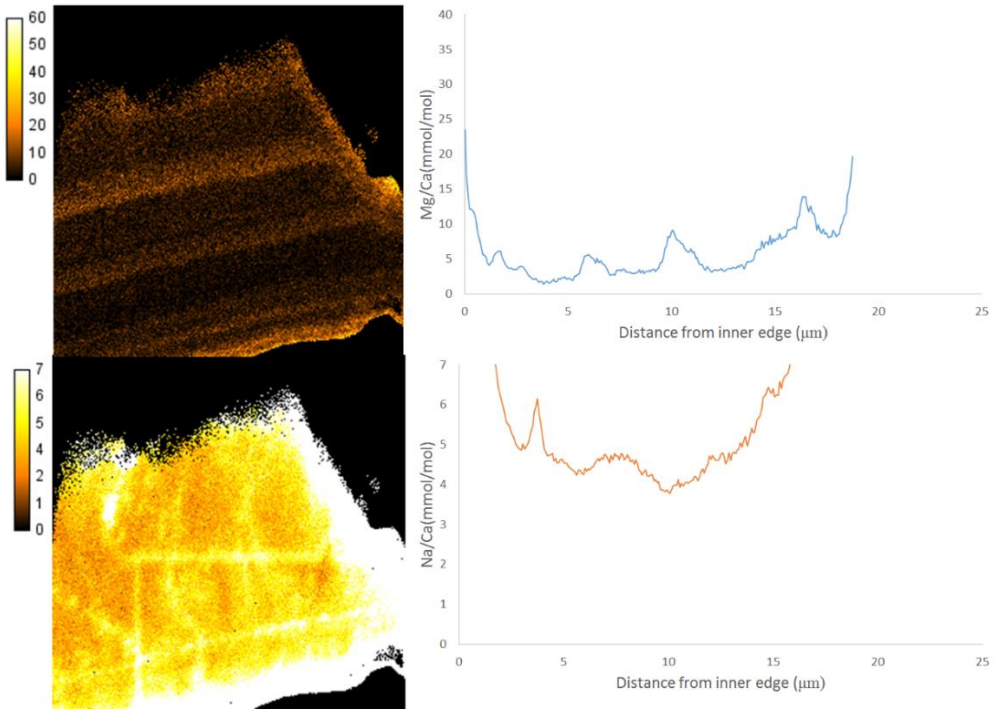

7.5 $[CO_3]^{2-}$ = 300MMOL/KGSW

(Note that Na/Ca mmol/mol measurements are approximate)

122_1:

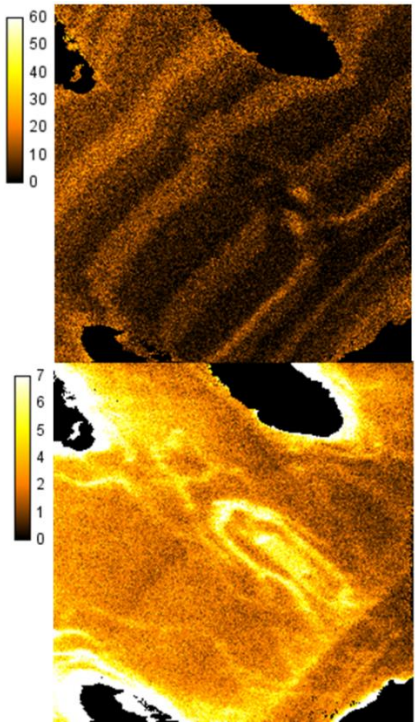

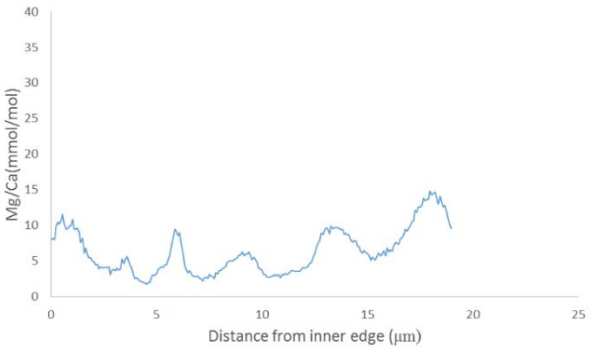

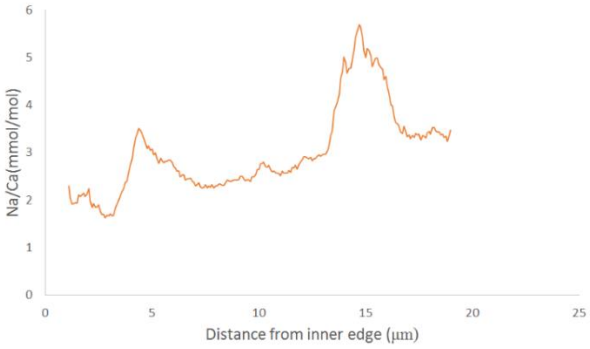

122_2:

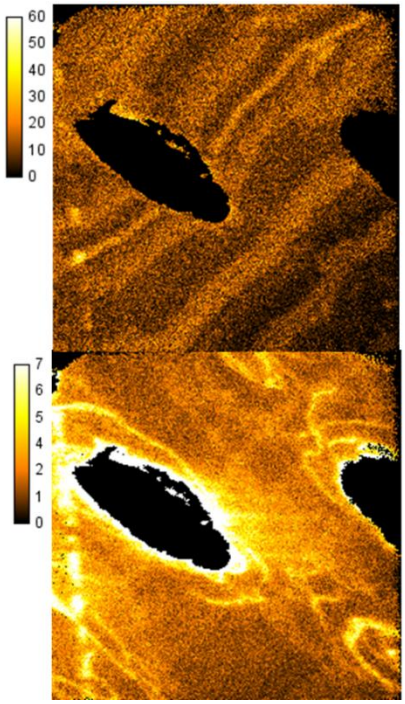

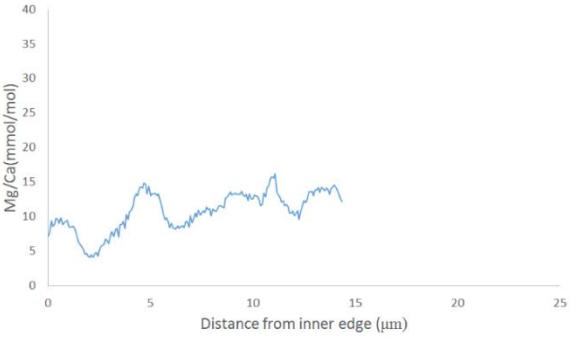

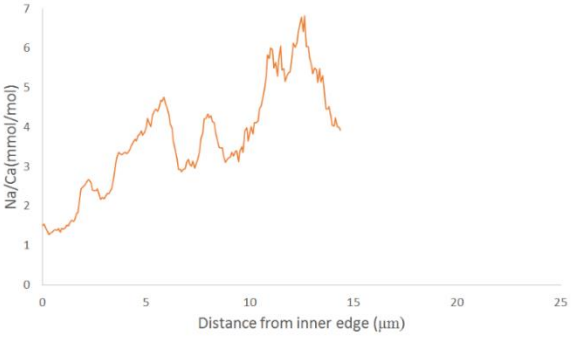

122_3:

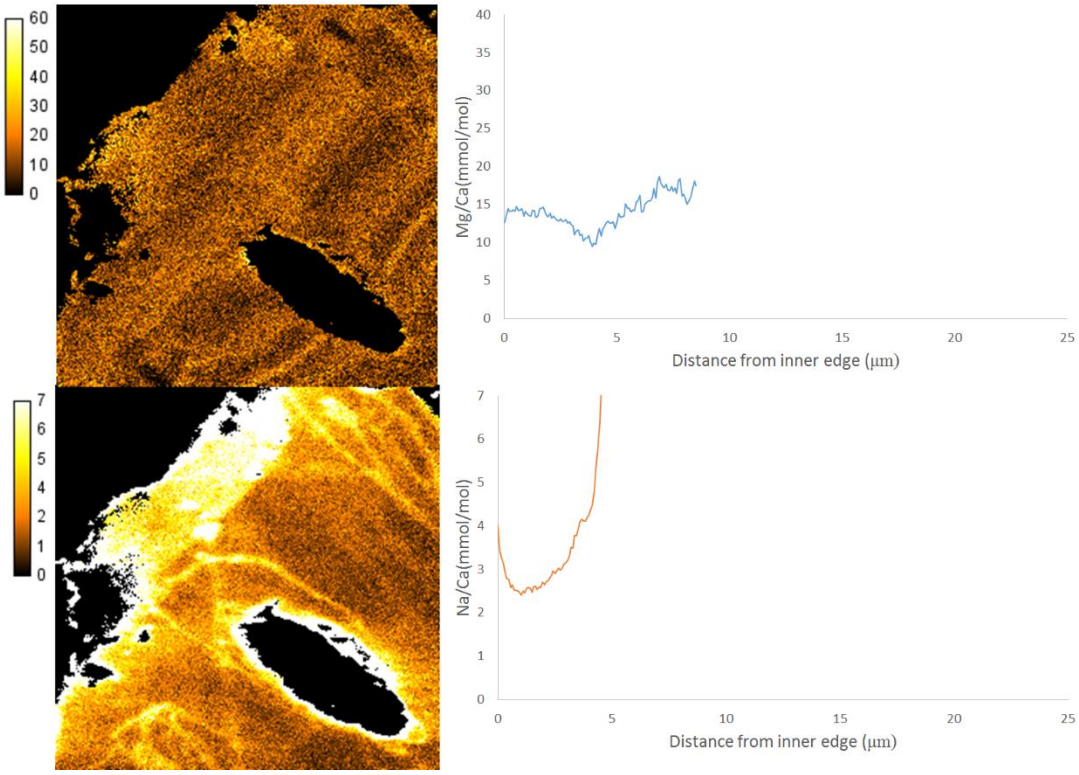
60
50
40
30
20
10
0
7
6
5
4
2
1
0
Mg/Ca(mmol/mol)
Na/Ca(mmol/mol)
Distance from inner edge (μm)
Distance from inner edge (μm)

138:

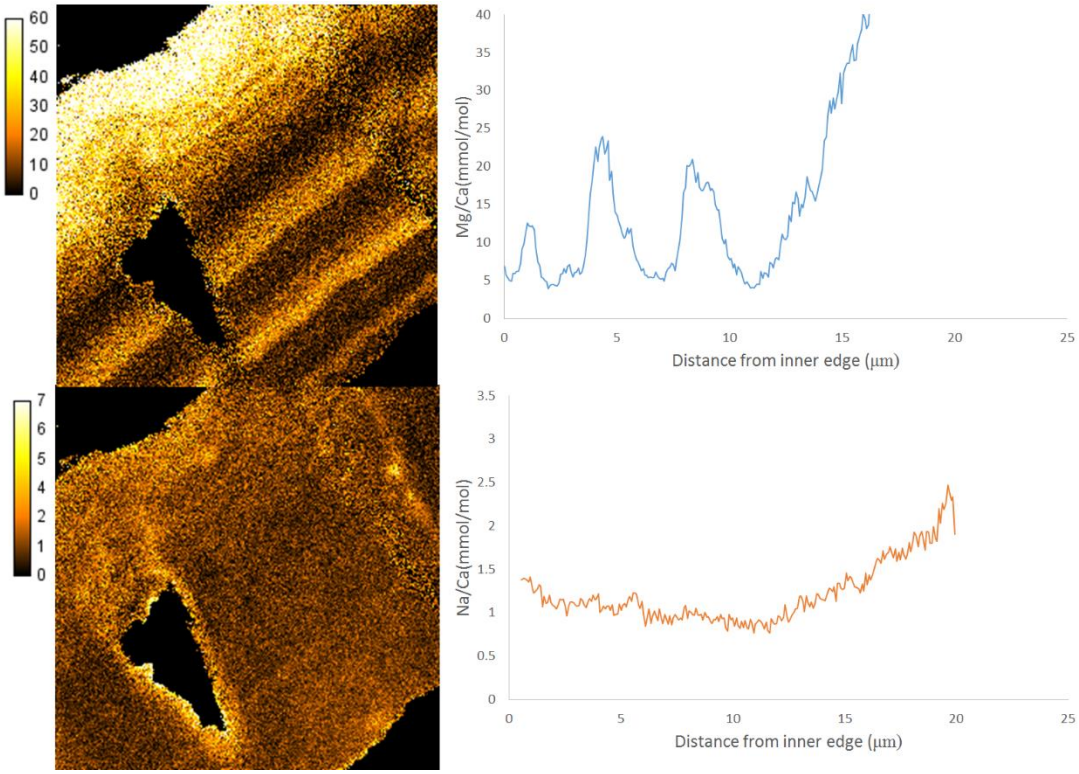
60
50
40
30
20
10
0
7
6
5
4
2
1
0
Mg/Ca(mmol/mol)
Na/Ca(mmol/mol)
Distance from inner edge (μm)
Distance from inner edge (μm)

7.6 HIGH $[CO_3]^{2-}$ ($[CO_3]^{2-}$ = 350MMOL/KGSW)

510_1:

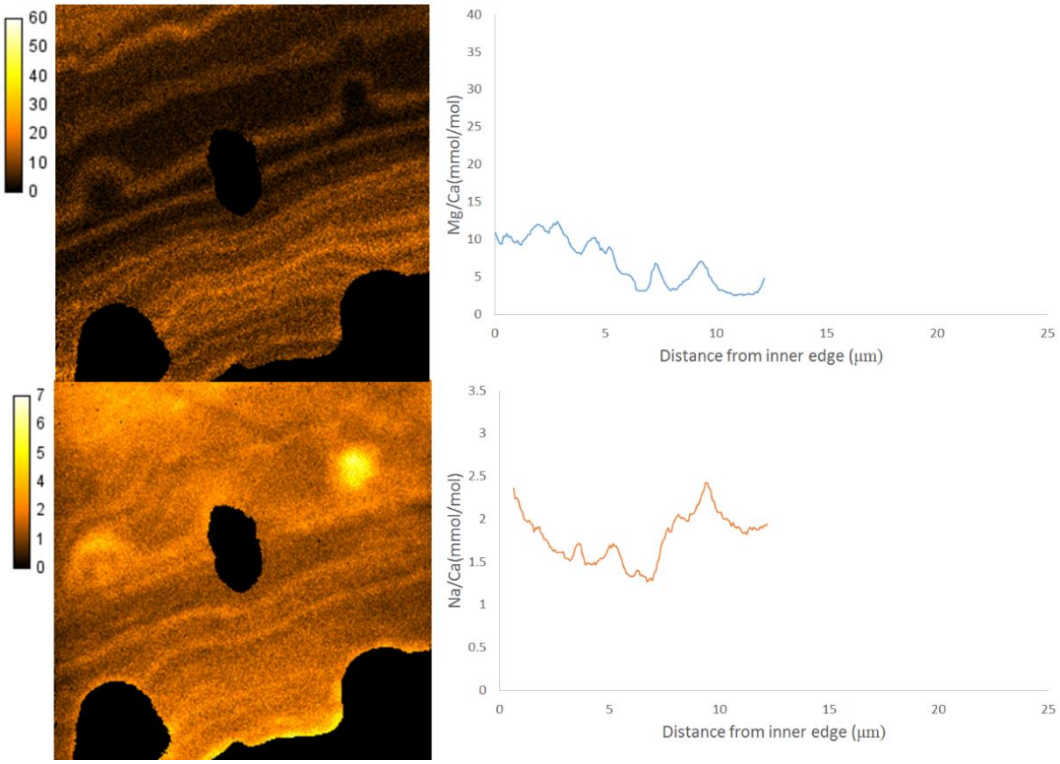

510_2:

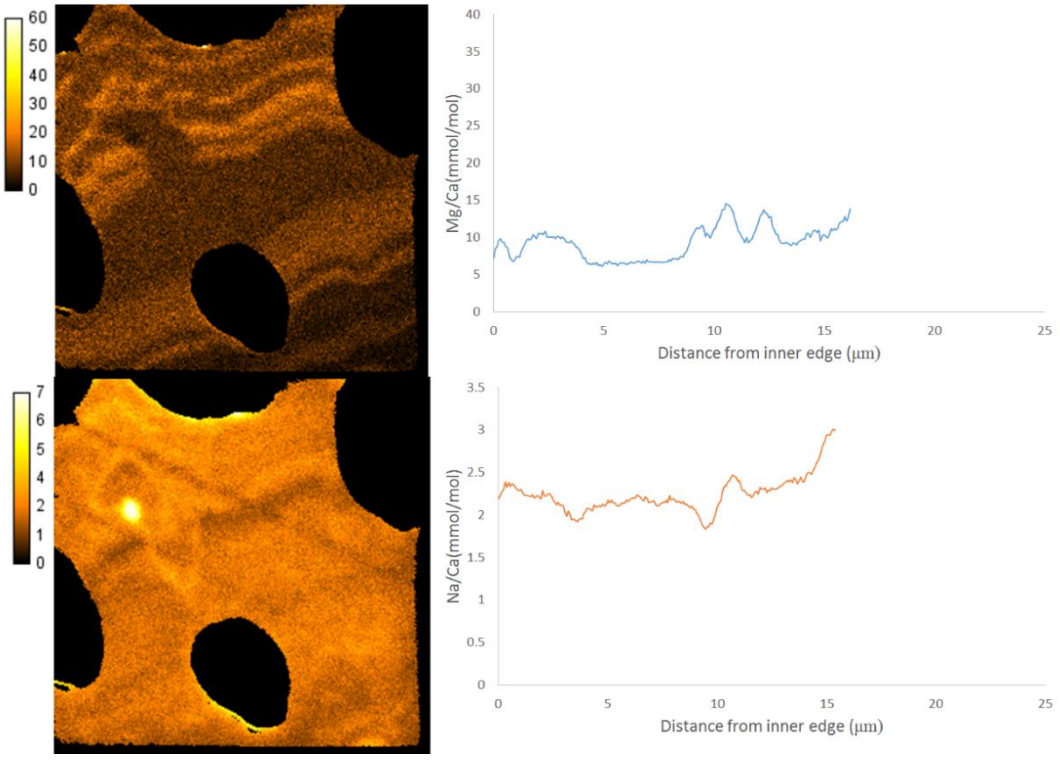

543_1:

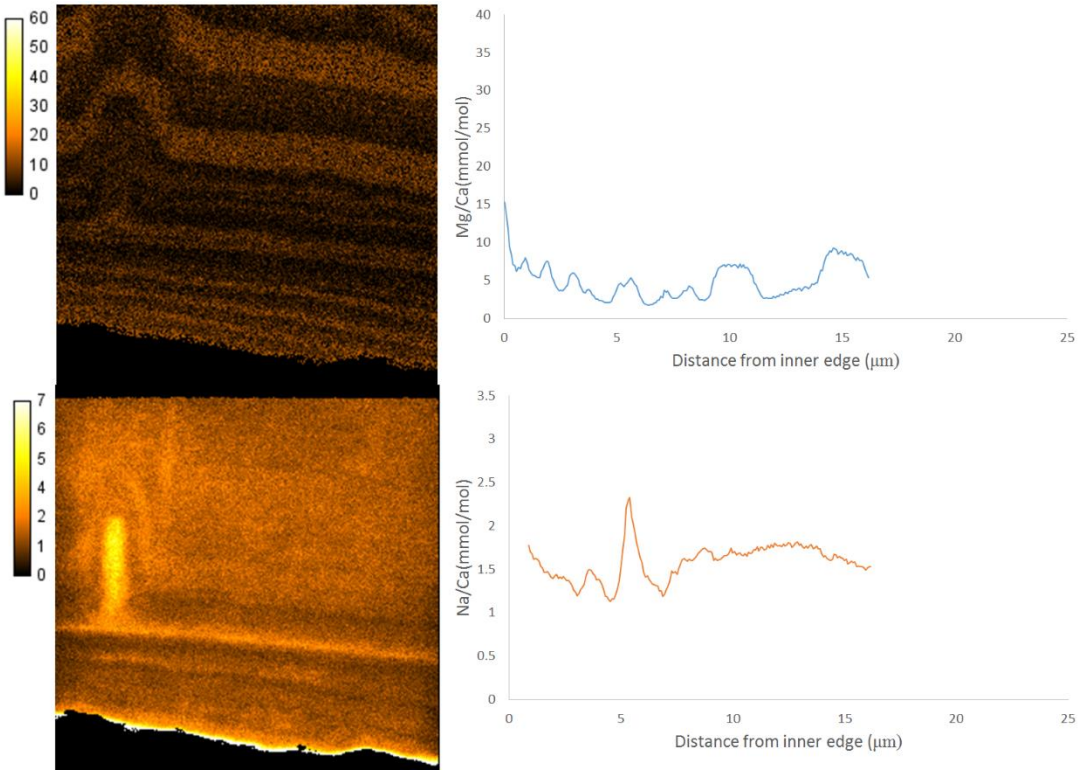
60
50
40
30
20
10
0
7
6
5
4
2
1
0
Mg/Ca(mmol/mol)
Distance from inner edge (μm)
Na/Ca(mmol/mol)
Distance from inner edge (μm)

543_2:

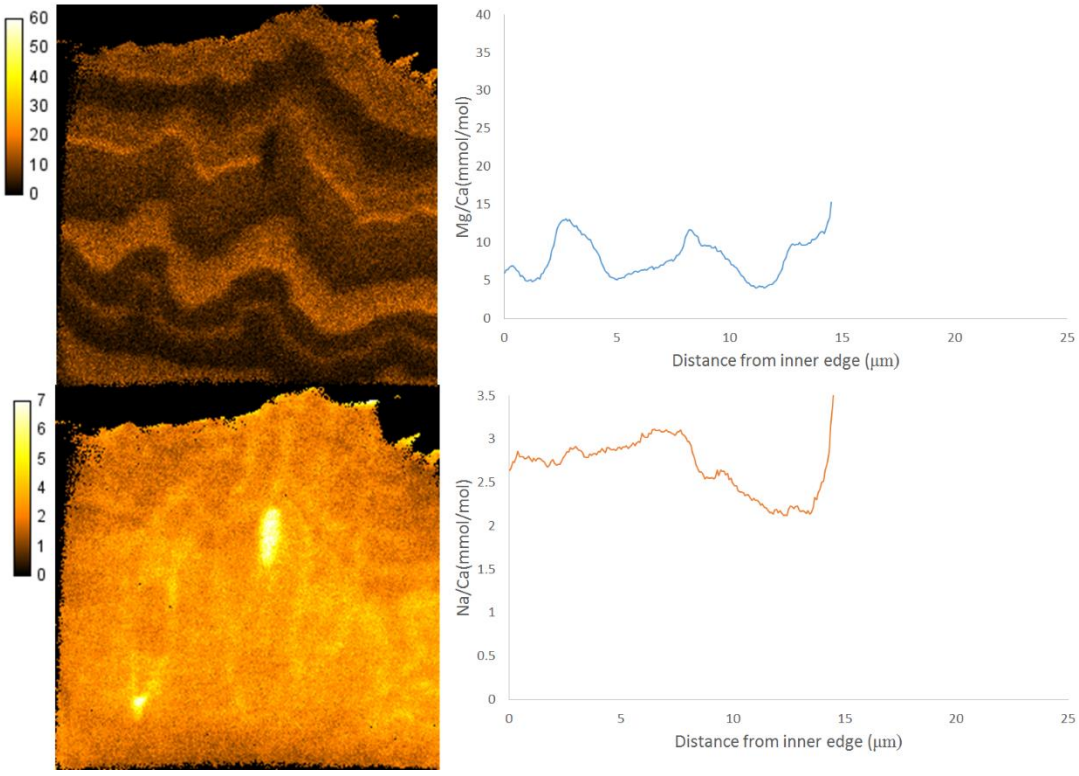
60
50
40
30
20
10
0
7
6
5
4
2
1
0
Mg/Ca(mmol/mol)
Distance from inner edge (μm)
Na/Ca(mmol/mol)
Distance from inner edge (μm)

547_1:

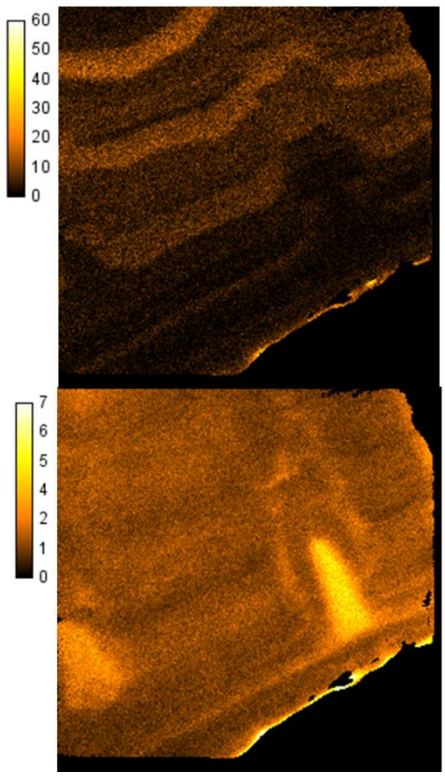
60
50
40
30
20
10
0
7
6
5
4
2
1
0

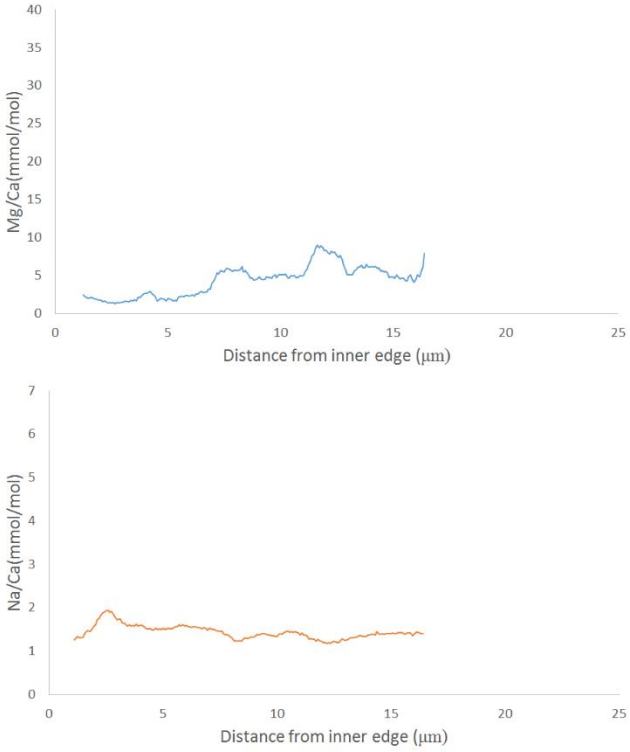
Mg/Ca(mmol/mol)
Distance from inner edge (µm)
Na/Ca(mmol/mol)
Distance from inner edge (µm)

547_2:

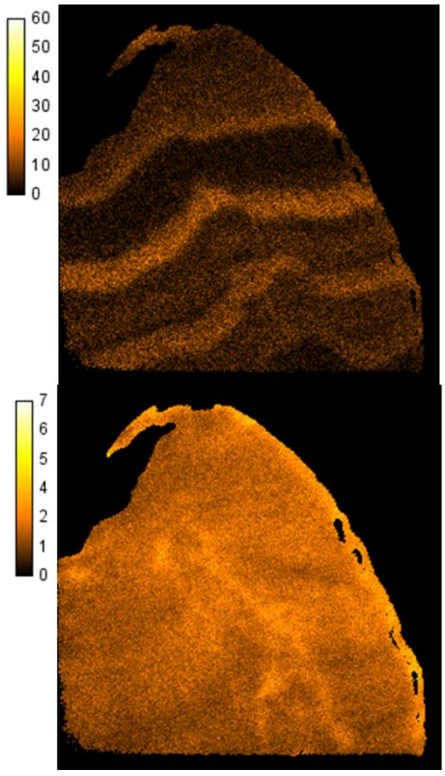
60
50
40
30
20
10
0
7
6
5
4
2
1
0

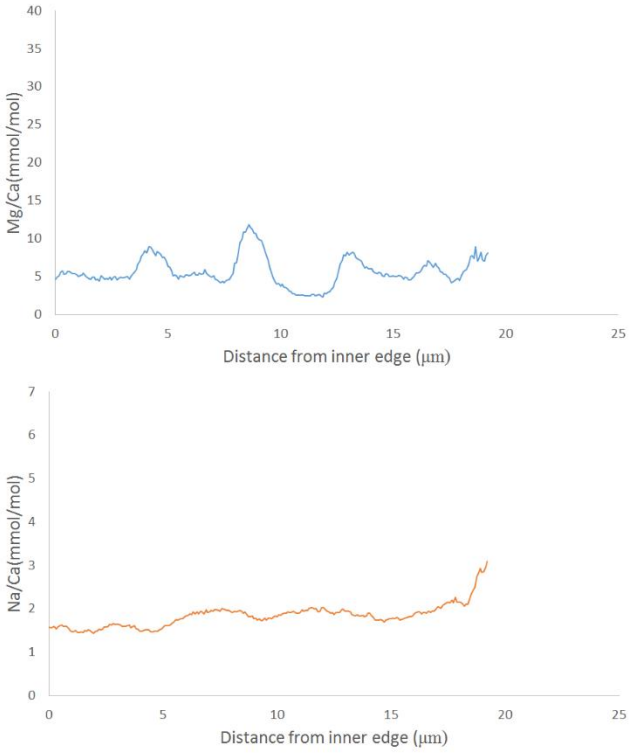
Mg/Ca(mmol/mol)
Distance from inner edge (µm)
Na/Ca(mmol/mol)
Distance from inner edge (µm)

7.7 $[CO_3]^{2-}$ = 400MMOL/KGSW

475_1:

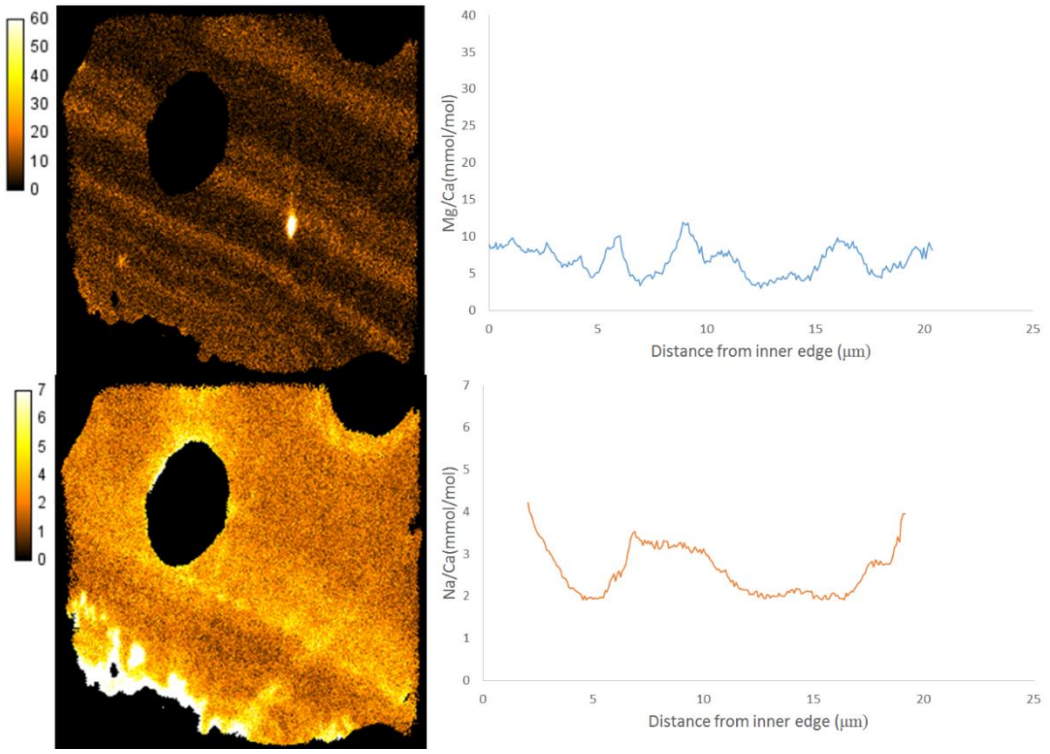

475_2:

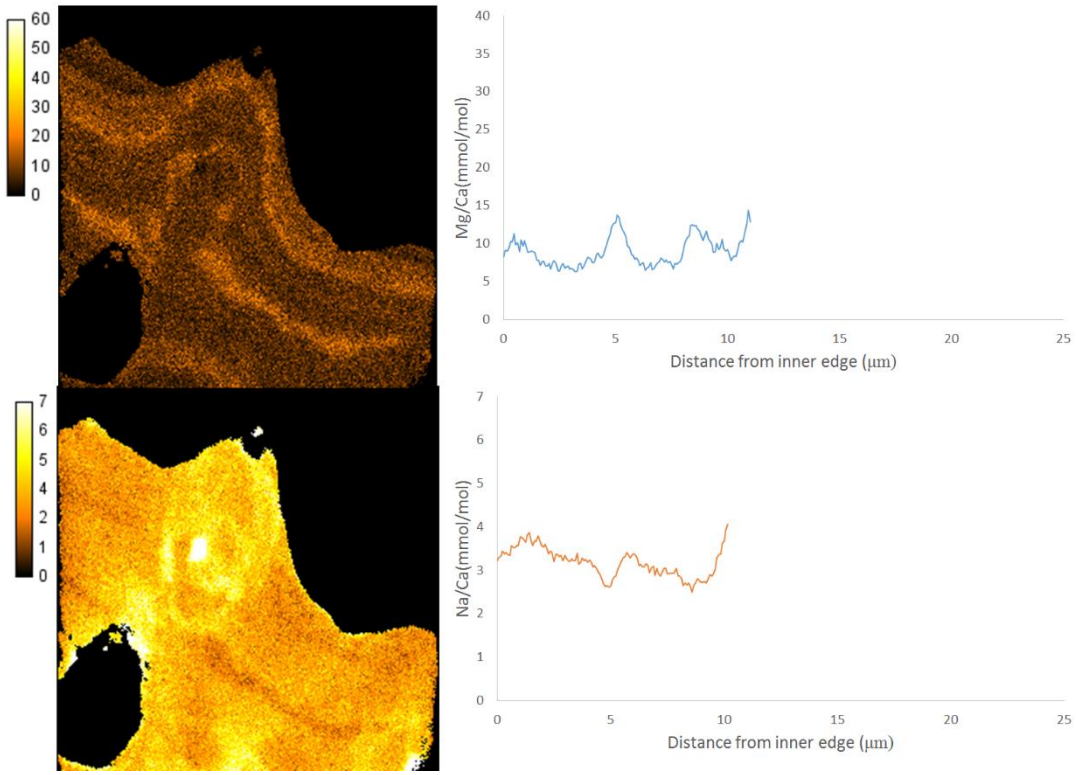

477_1 (Note different color scale):

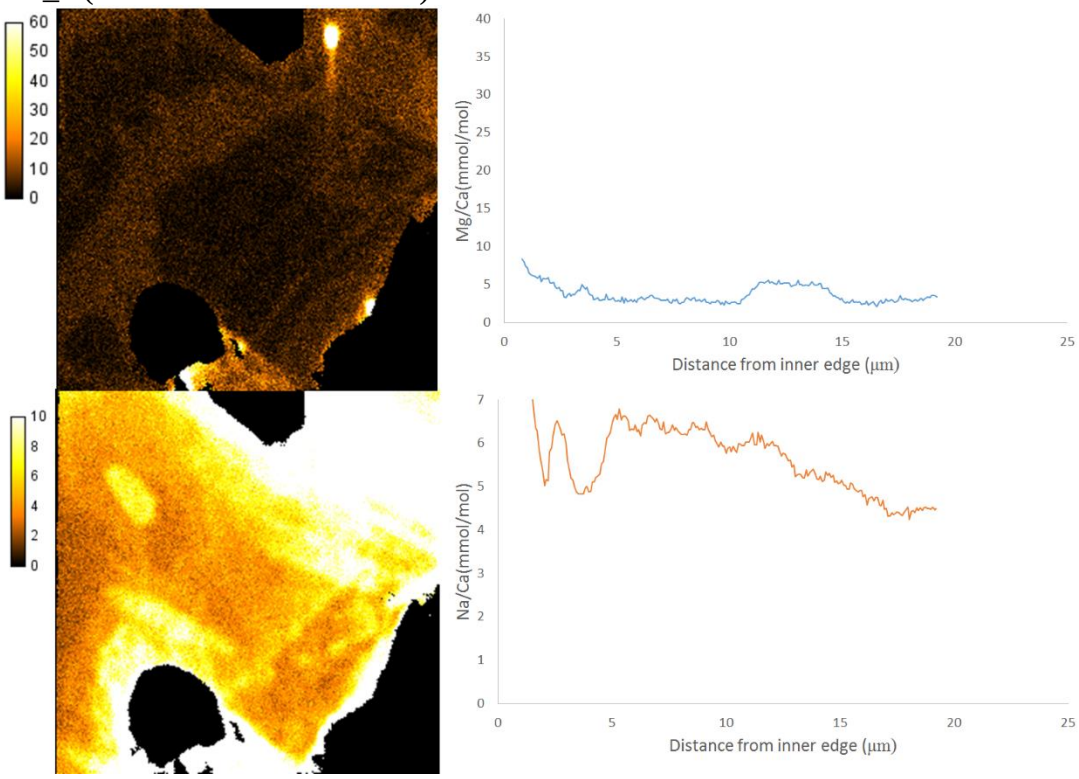

477_2 (Note different color scale):

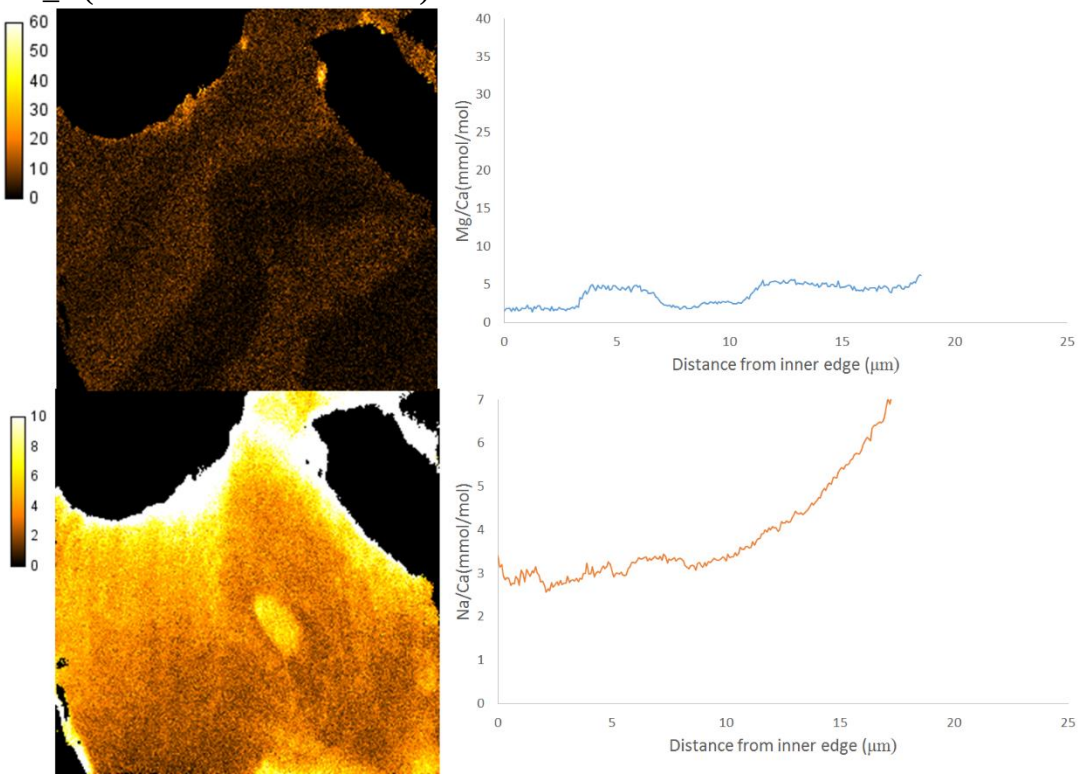

478_1:

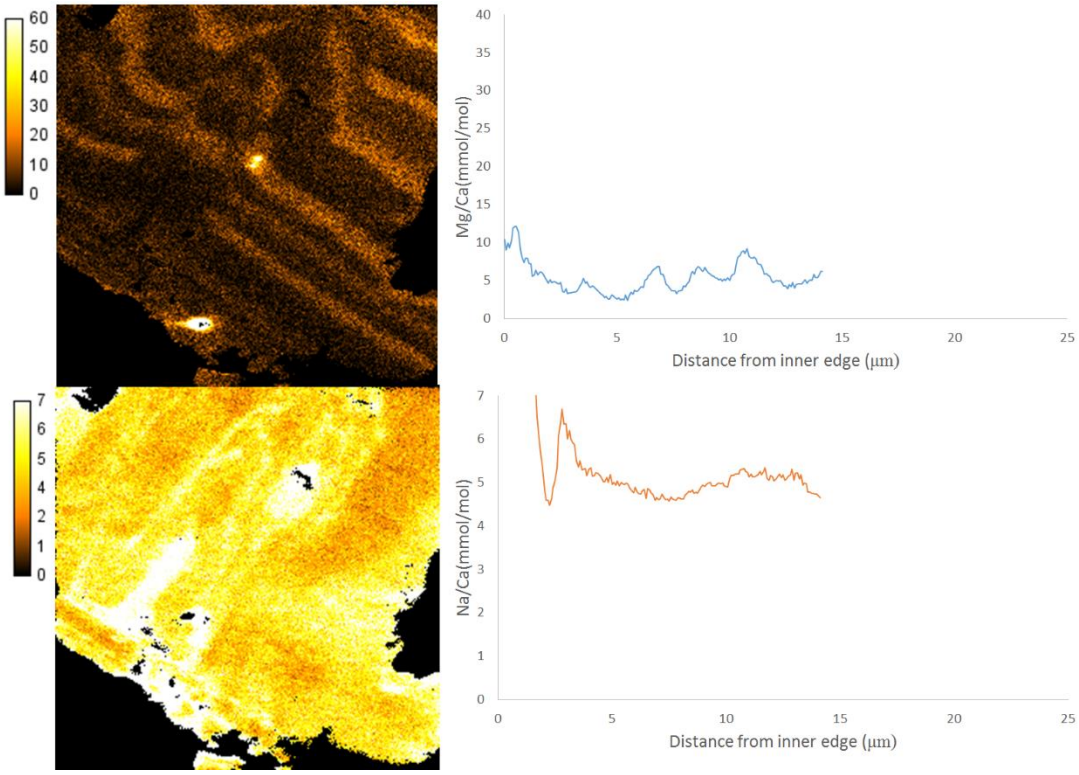
60
50
40
30
20
10
0
7
6
5
4
2
1
0
Mg/Ca(mmol/mol)
Distance from inner edge (μm)
Na/Ca(mmol/mol)
Distance from inner edge (μm)

478_2:

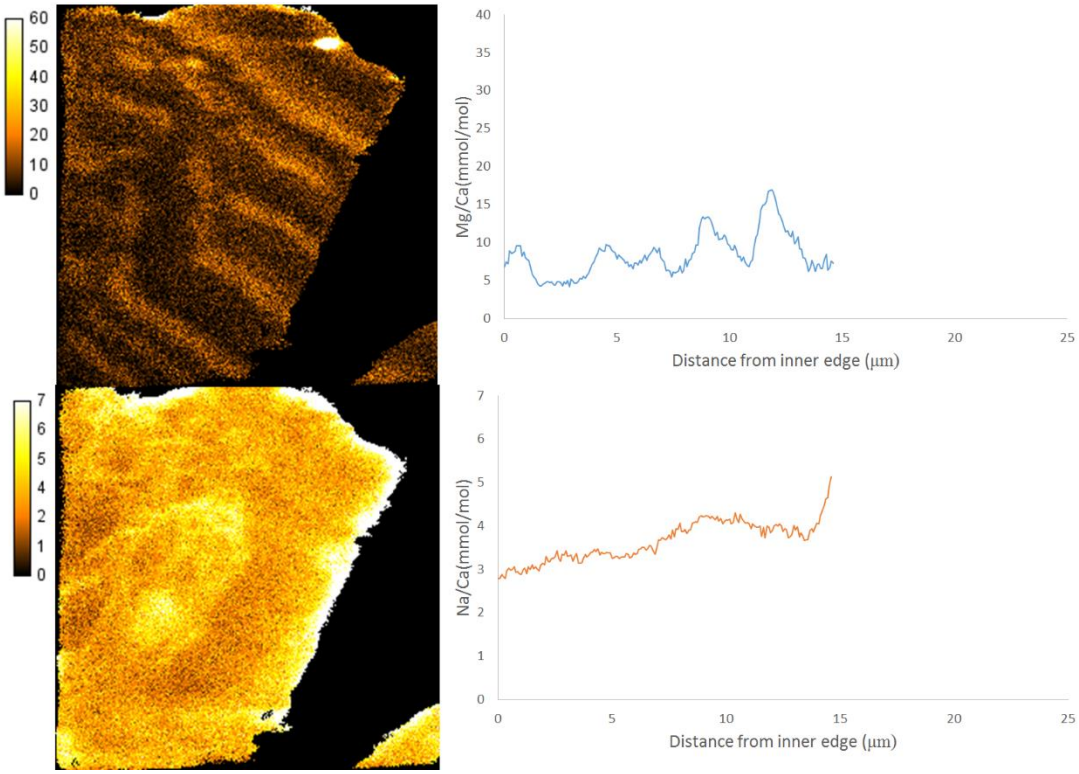
60
50
40
30
20
10
0
7
6
5
4
2
1
0
Mg/Ca(mmol/mol)
Distance from inner edge (μm)
Na/Ca(mmol/mol)
Distance from inner edge (μm)

7.8 Low Salinity (Salinity = 30 ppt)

549:

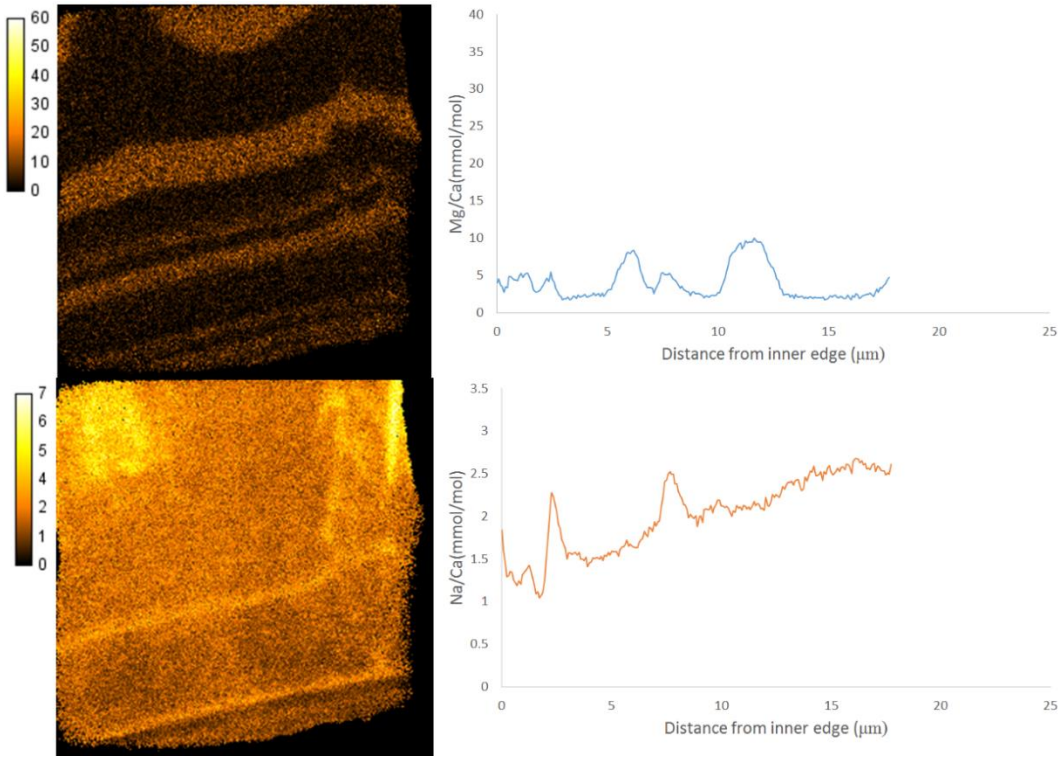

603:

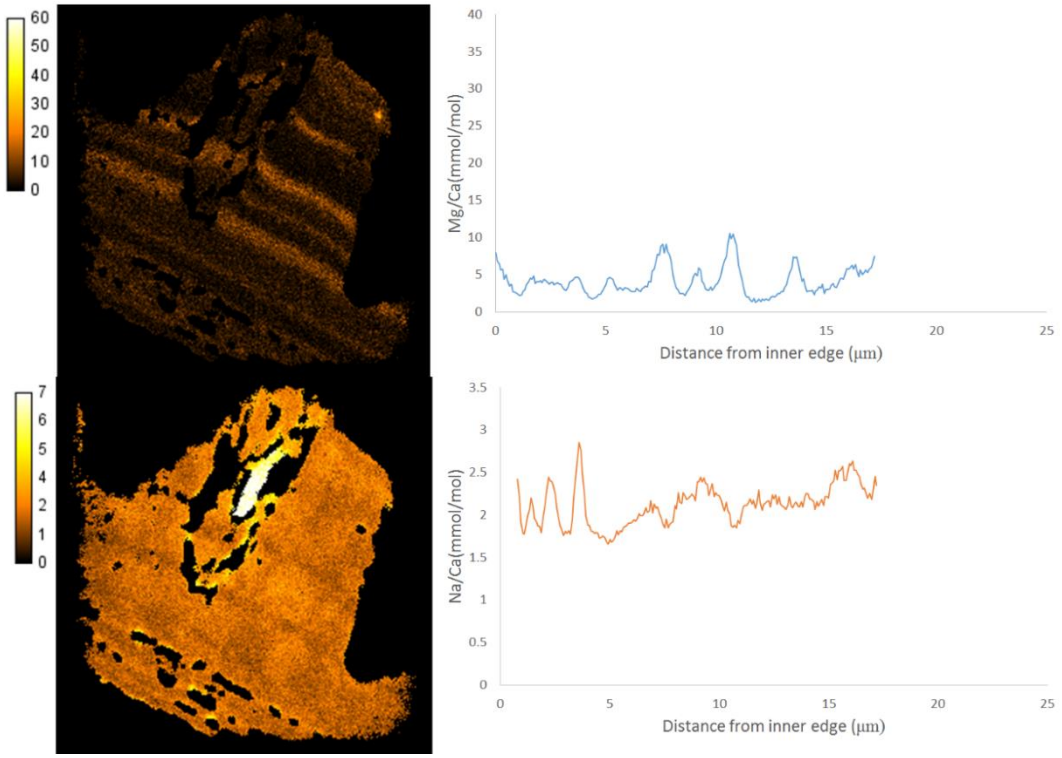

642:

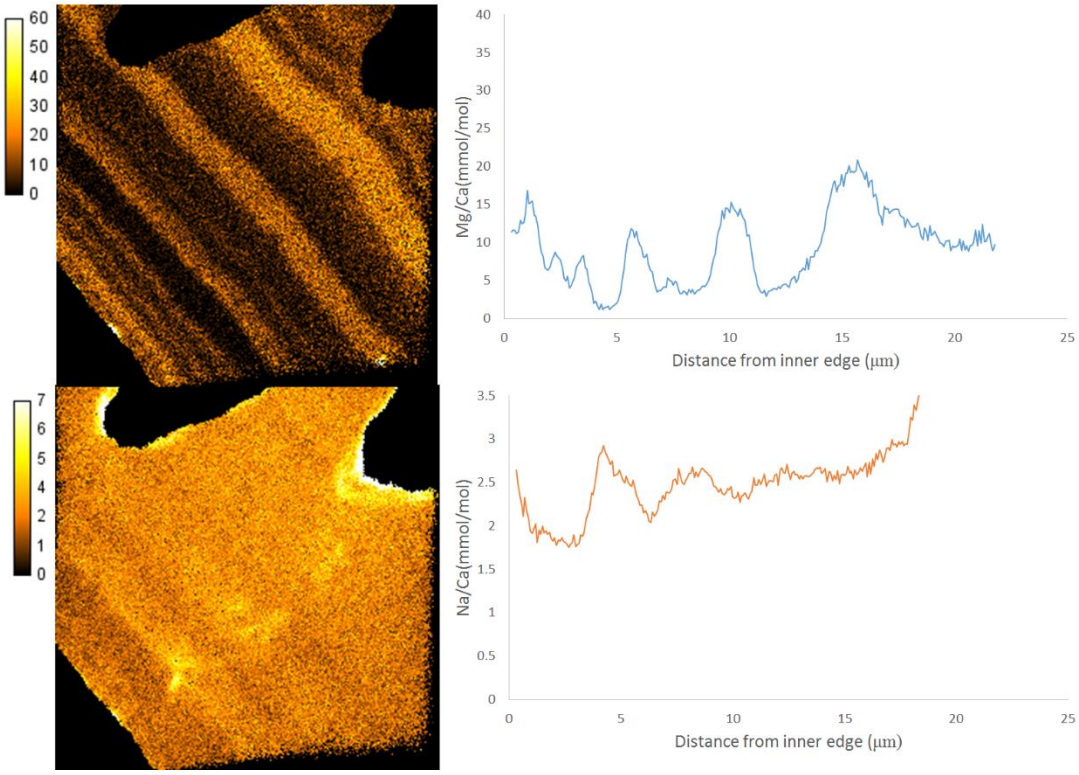
60
50
40
30
20
10
0
7
6
5
4
2
1
0
Mg/Ca(mmol/mol)
Distance from inner edge (μm)
Na/Ca(mmol/mol)
Distance from inner edge (μm)

644_1:

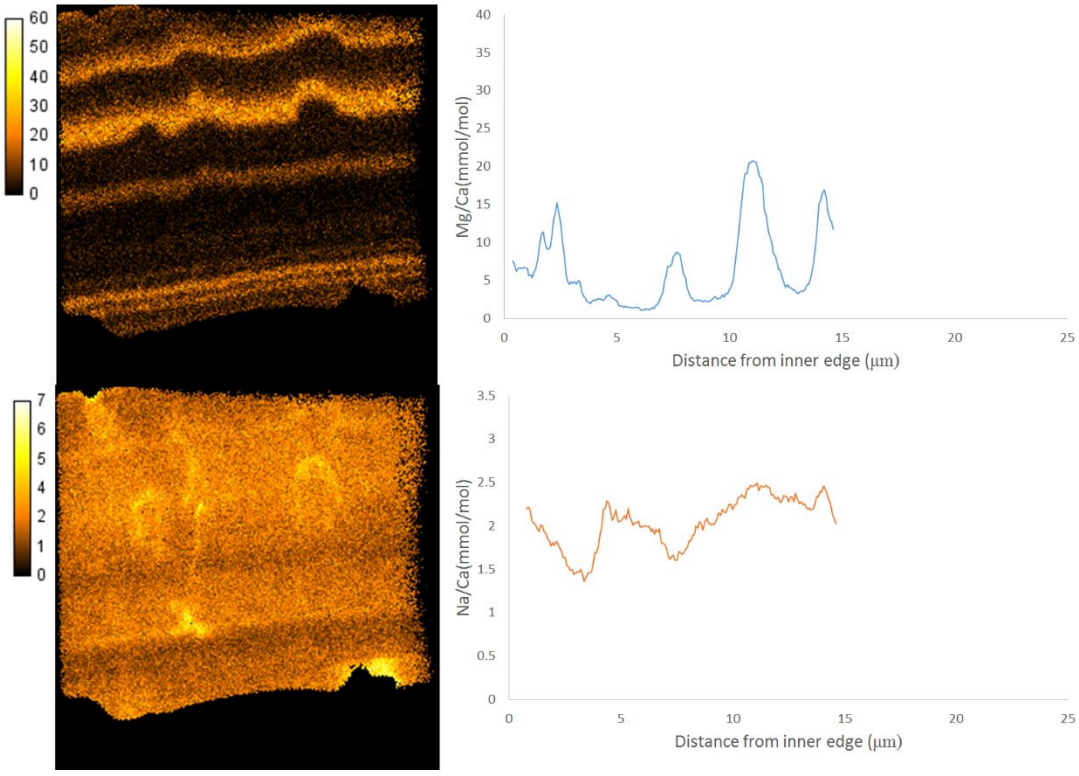
60
50
40
30
20
10
0
7
6
5
4
2
1
0
Mg/Ca(mmol/mol)
Distance from inner edge (μm)
Na/Ca(mmol/mol)
Distance from inner edge (μm)

644_2:

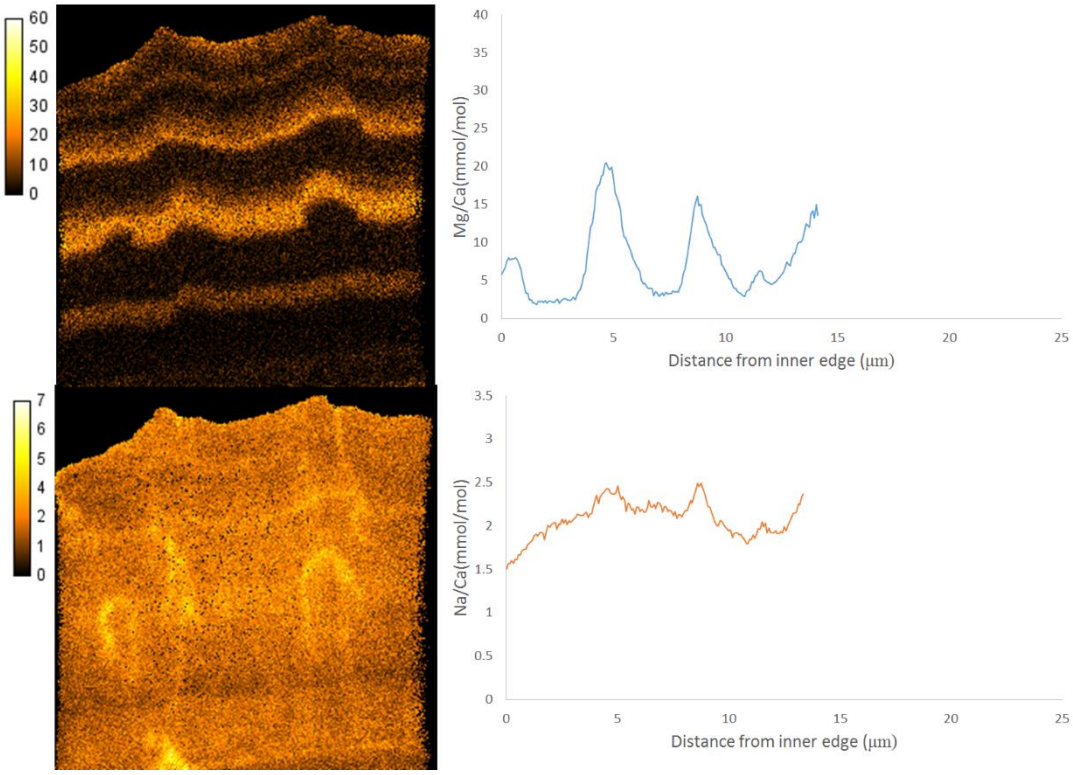
60
50
40
30
20
10
0
7
6
5
4
2
1
0
Mg/Ca(mmol/mol)
Distance from inner edge (μm)
Na/Ca(mmol/mol)
Distance from inner edge (μm)

645:

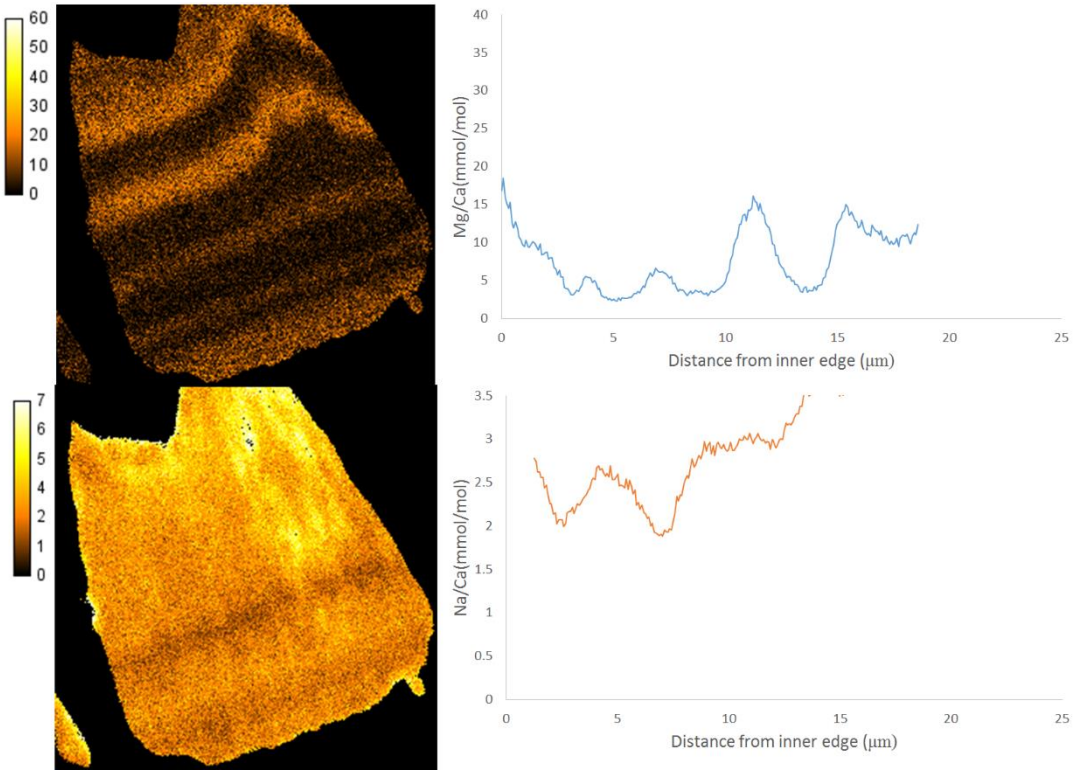
60
50
40
30
20
10
0
7
6
5
4
2
1
0
Mg/Ca(mmol/mol)
Distance from inner edge (μm)
Na/Ca(mmol/mol)
Distance from inner edge (μm)

7.9 HIGH SALINITY (SALINITY = 35 PPT)

002:

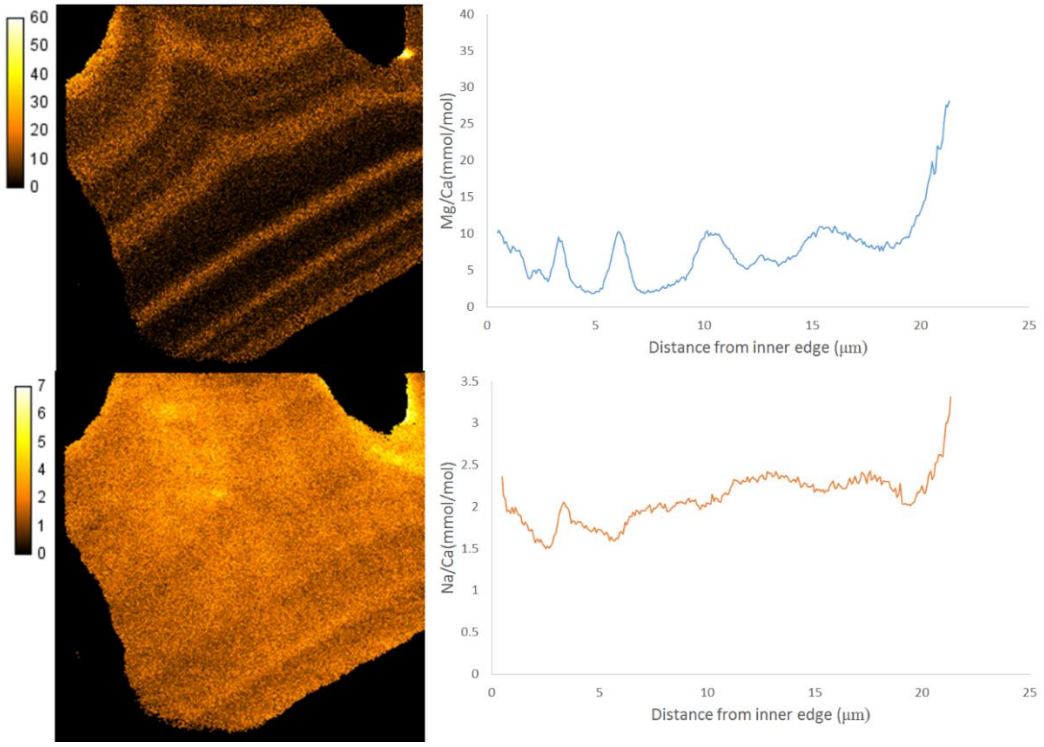

022:

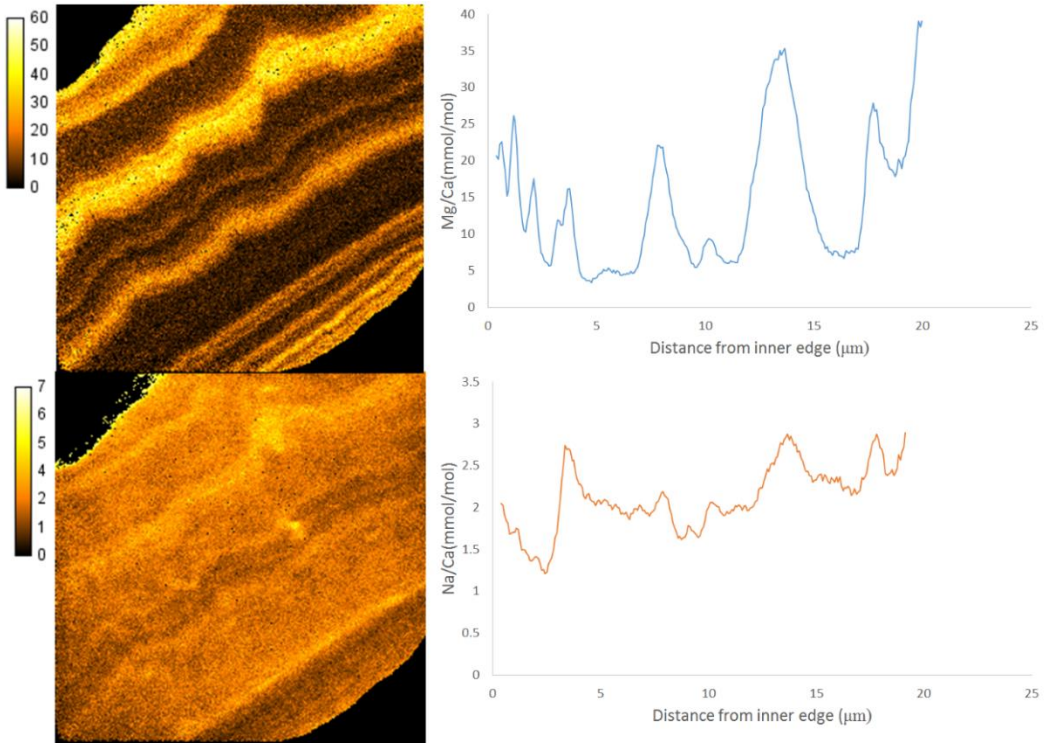

675:

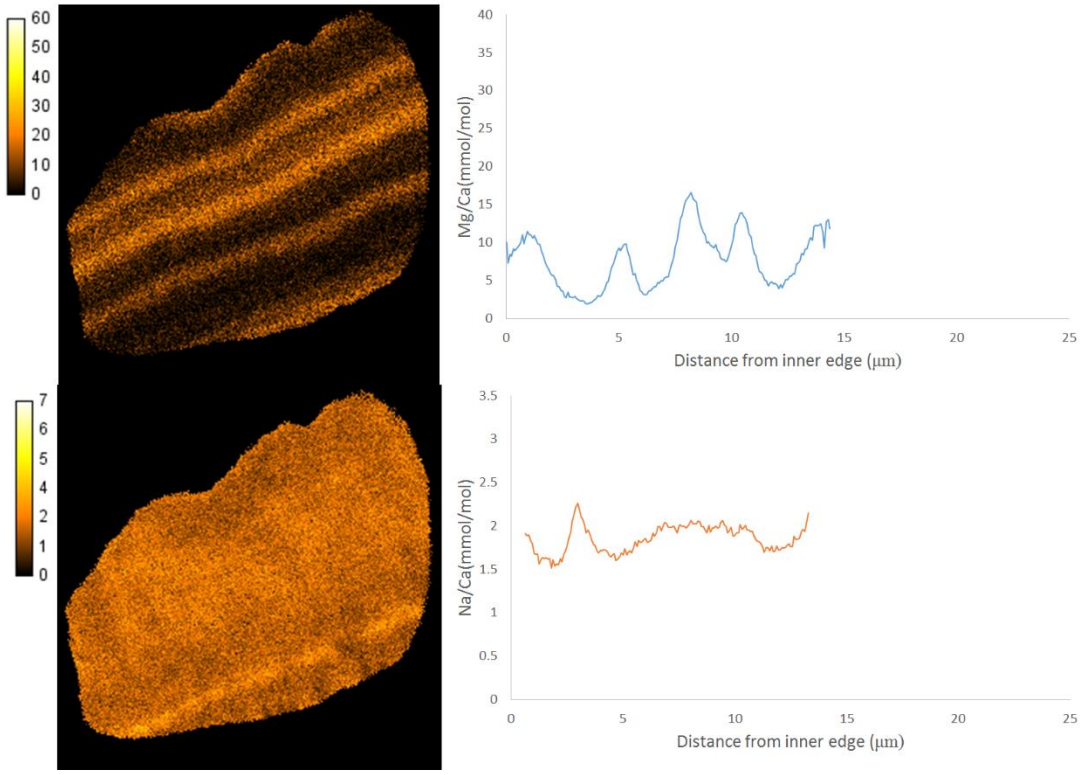
60
50
40
30
20
10
0
7
6
5
4
2
1
0
Mg/Ca(mmol/mol)
Distance from inner edge (μm)
Na/Ca(mmol/mol)
Distance from inner edge (μm)

680:

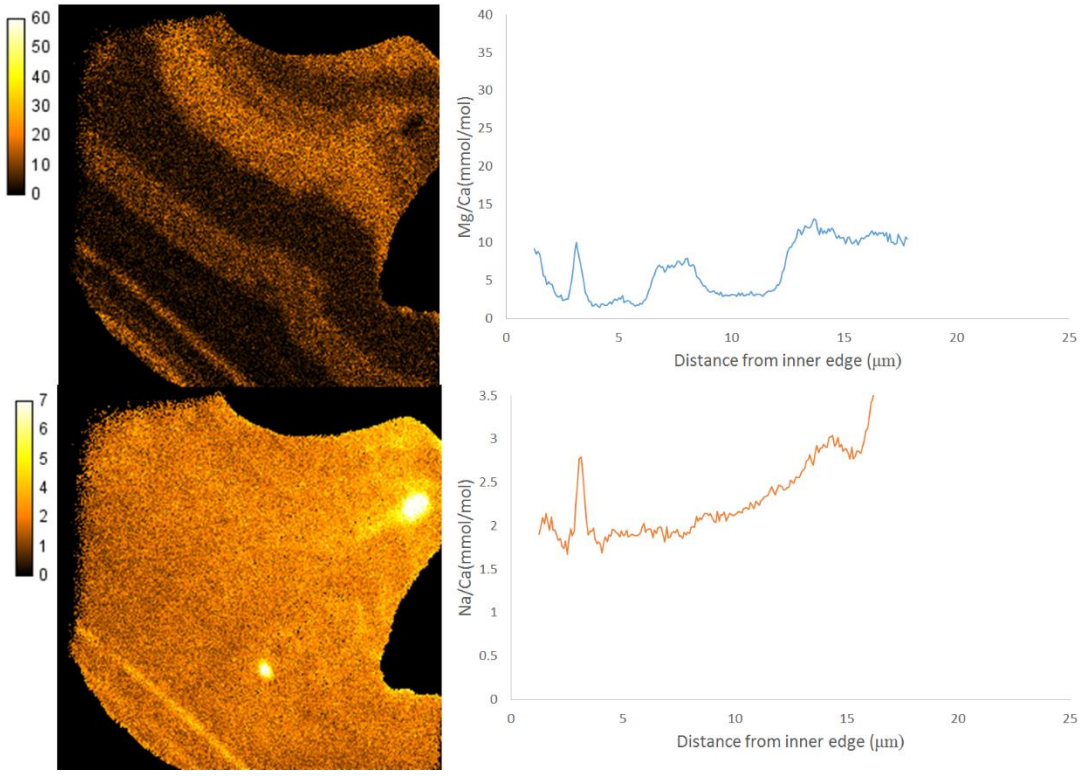
60
50
40
30
20
10
0
7
6
5
4
2
1
0
Mg/Ca(mmol/mol)
Distance from inner edge (μm)
Na/Ca(mmol/mol)
Distance from inner edge (μm)

910:

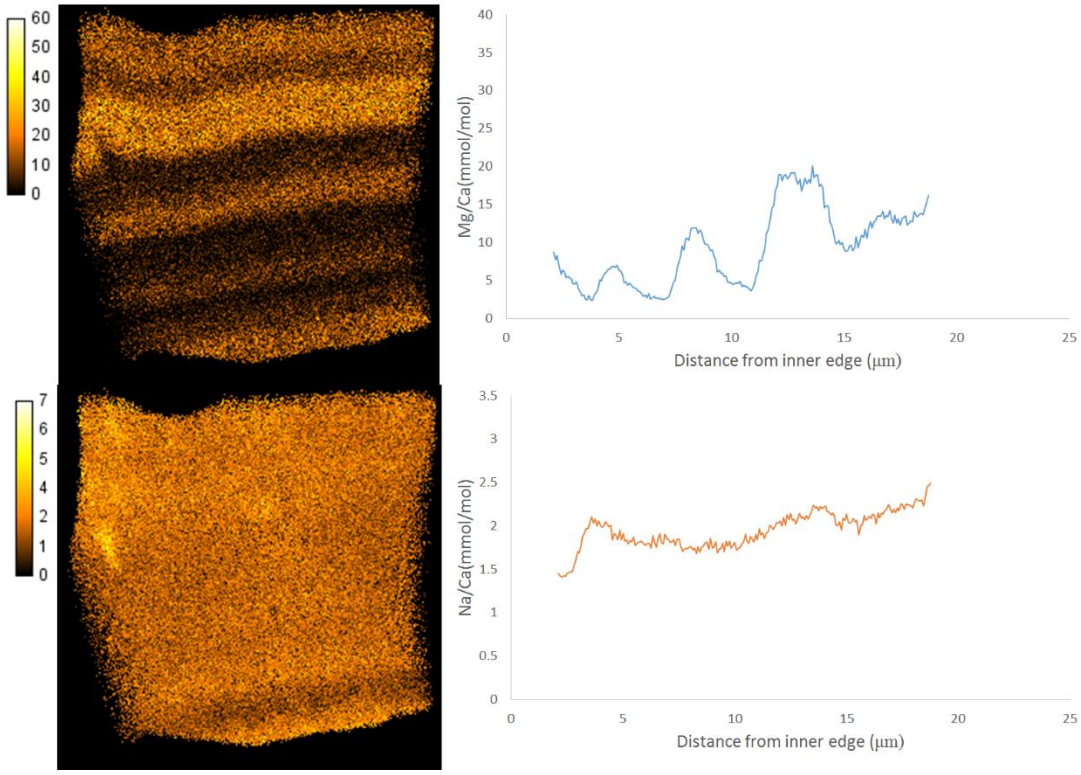
60
50
40
30
20
10
0
7
6
5
4
2
1
0
Mg/Ca(mmol/mol)
Distance from inner edge (μm)
Na/Ca(mmol/mol)
Distance from inner edge (μm)

913:

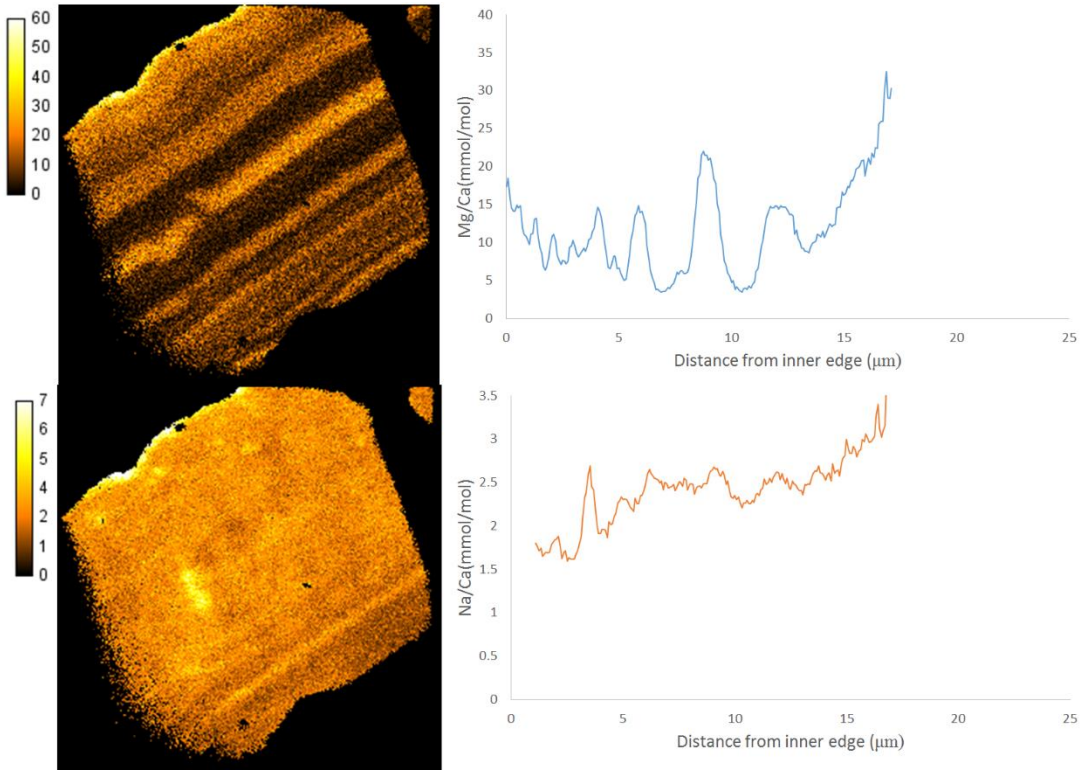
60
50
40
30
20
10
0
7
6
5
4
2
1
0
Mg/Ca(mmol/mol)
Distance from inner edge (μm)
Na/Ca(mmol/mol)
Distance from inner edge (μm)

915:

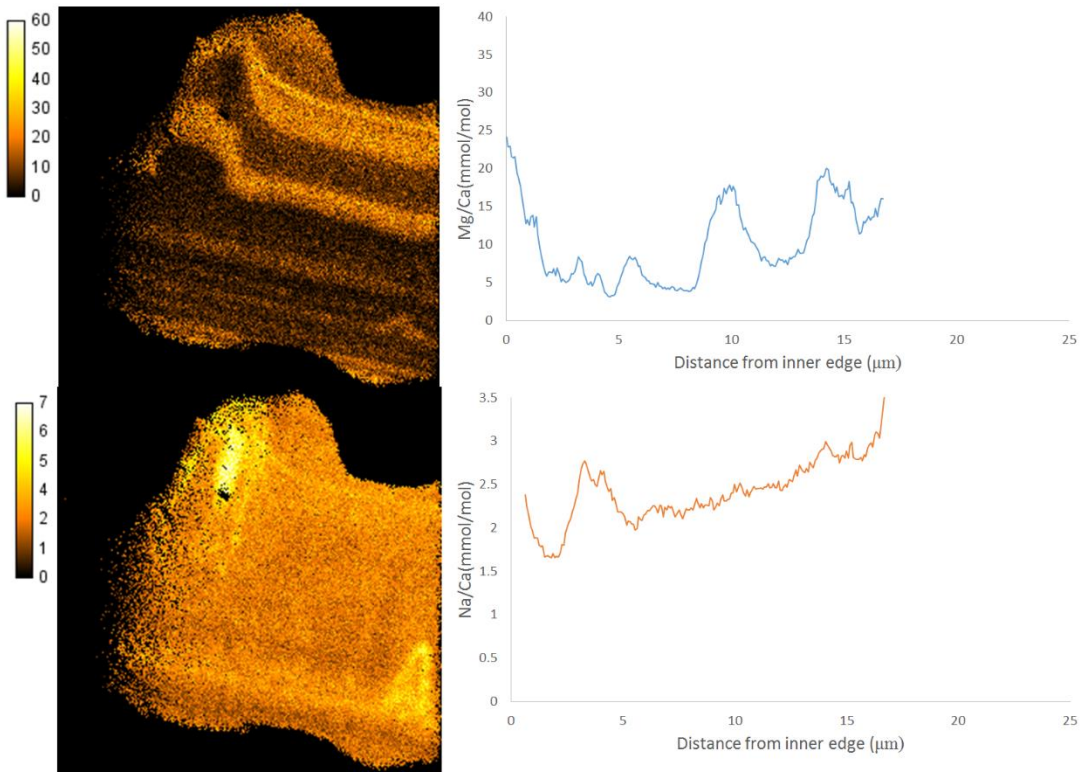
60
50
40
30
20
10
0
7
6
5
4
2
1
0
Mg/Ca(mmol/mol)
40
35
30
25
20
15
10
5
0
0
5
10
15
20
25
Distance from inner edge (μm)
Na/Ca(mmol/mol)
3.5
3
2.5
2
1.5
1
0.5
0
0
5
10
15
20
25
Distance from inner edge (μm)

7.10 Low Temperature (T = 18°C)

226:

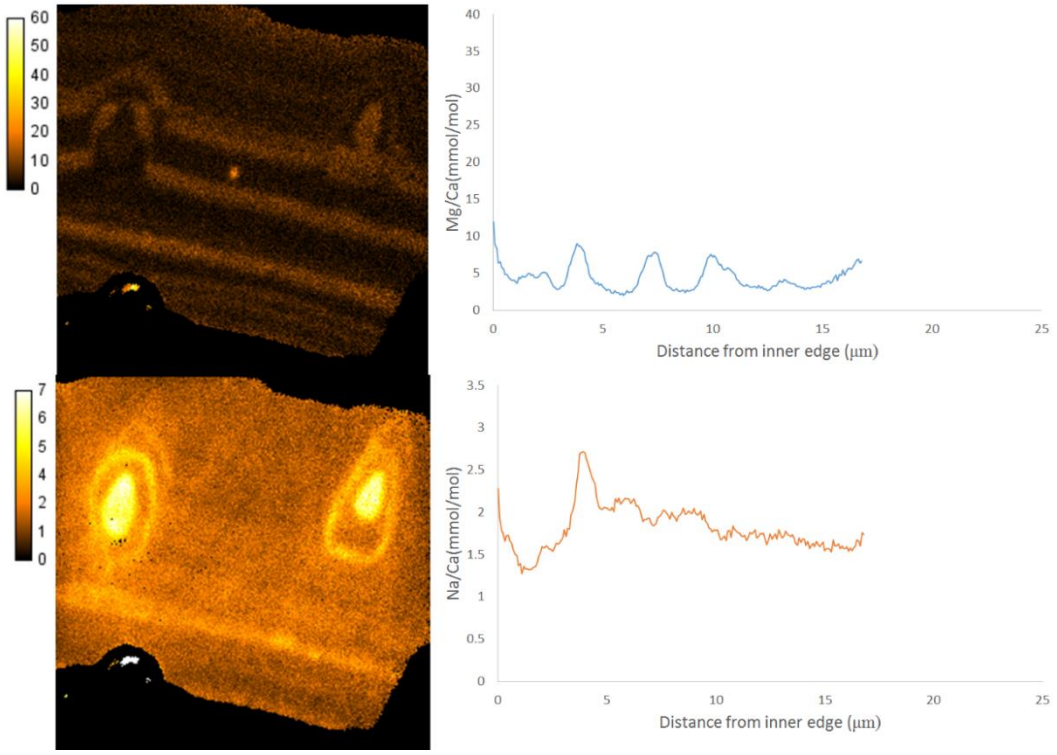

248:

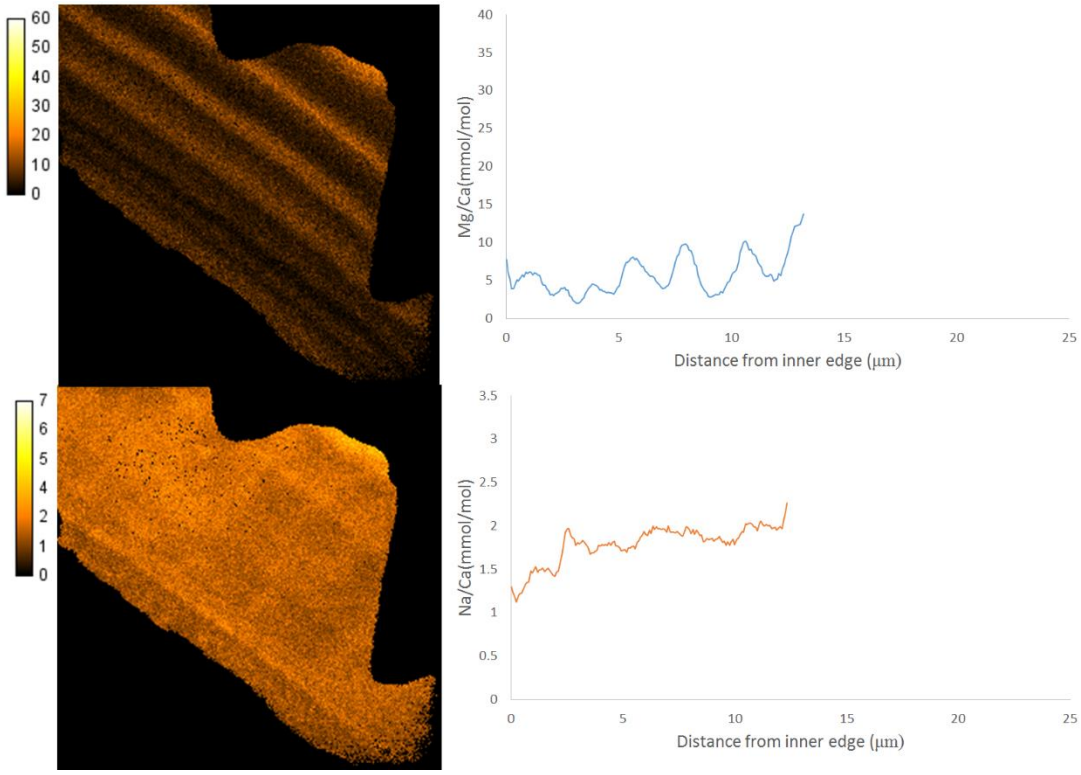

315:

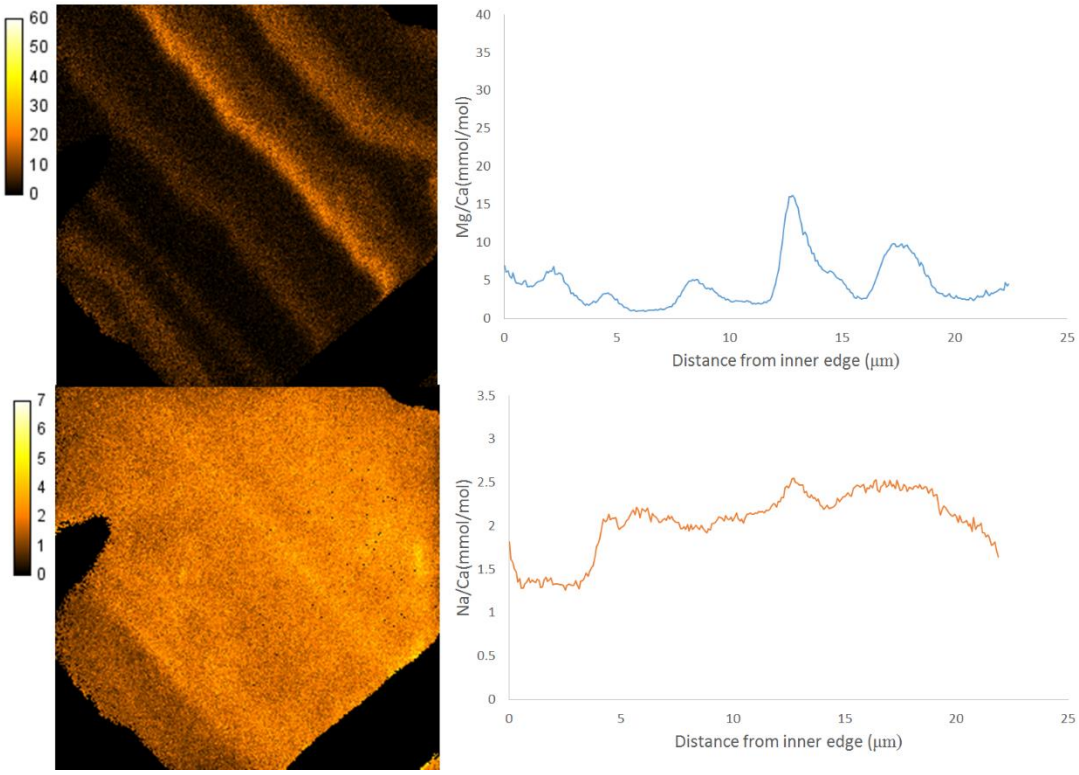
60
50
40
30
20
10
0
7
6
5
4
2
1
0
Mg/Ca(mmol/mol)
Distance from inner edge (μm)
Na/Ca(mmol/mol)
Distance from inner edge (μm)

316:

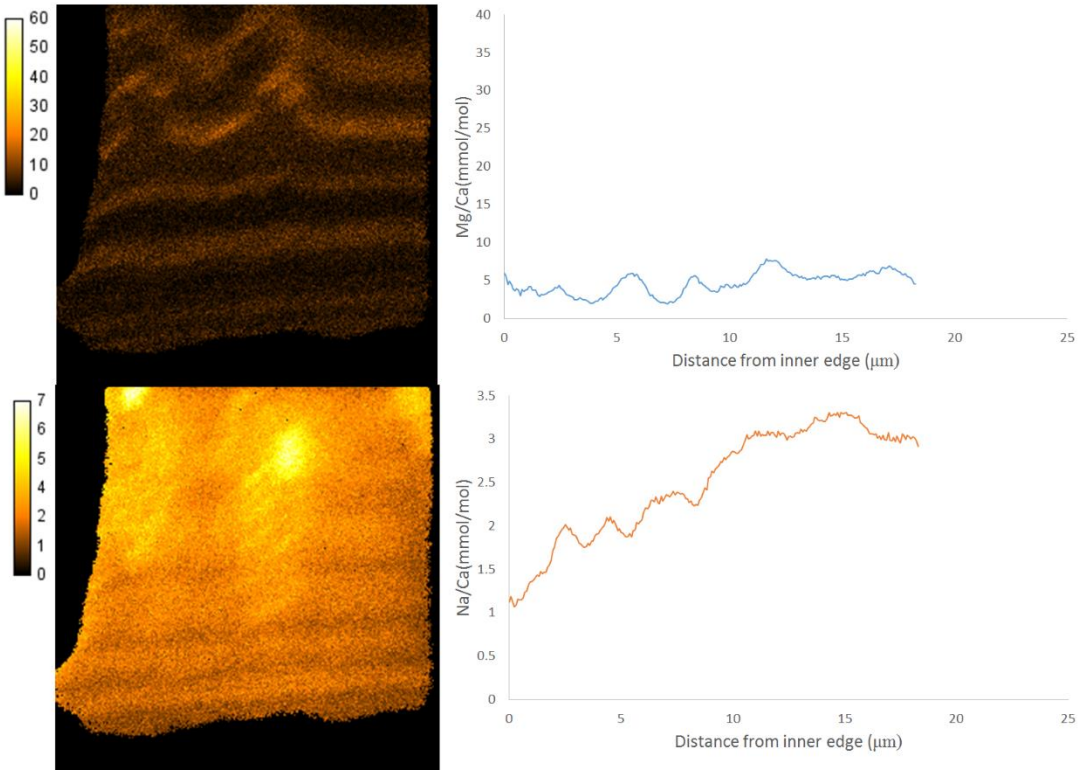
60
50
40
30
20
10
0
7
6
5
4
2
1
0
Mg/Ca(mmol/mol)
Distance from inner edge (μm)
Na/Ca(mmol/mol)
Distance from inner edge (μm)

7.11 T = 20°C

810:

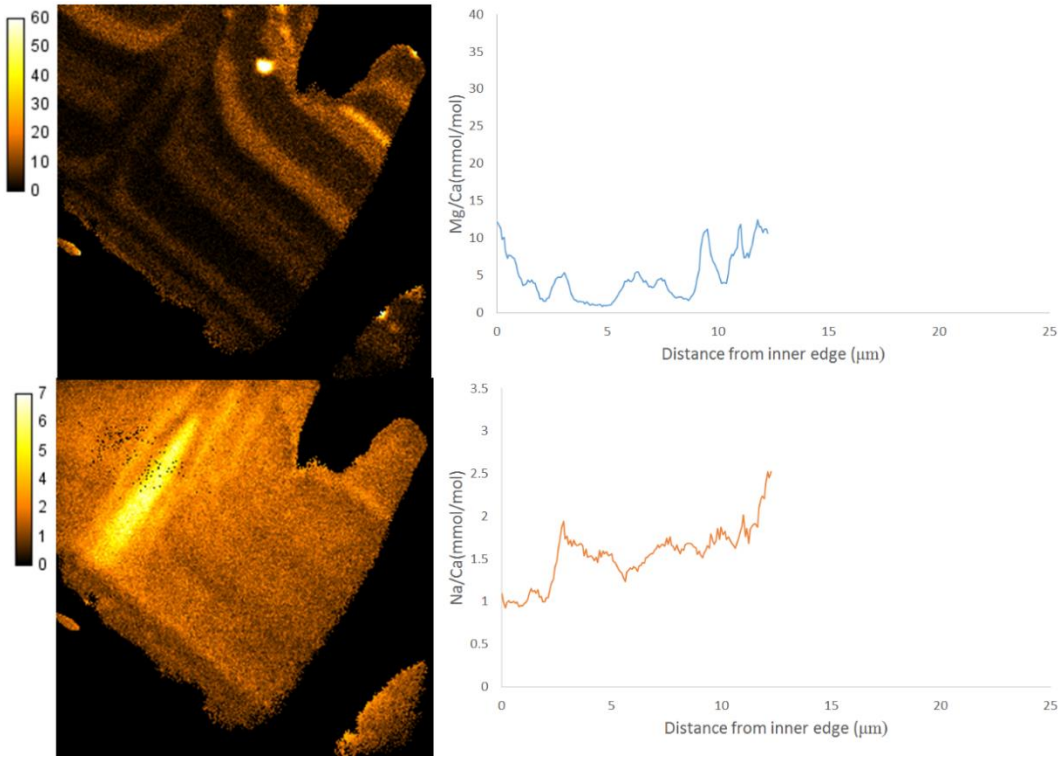

811:

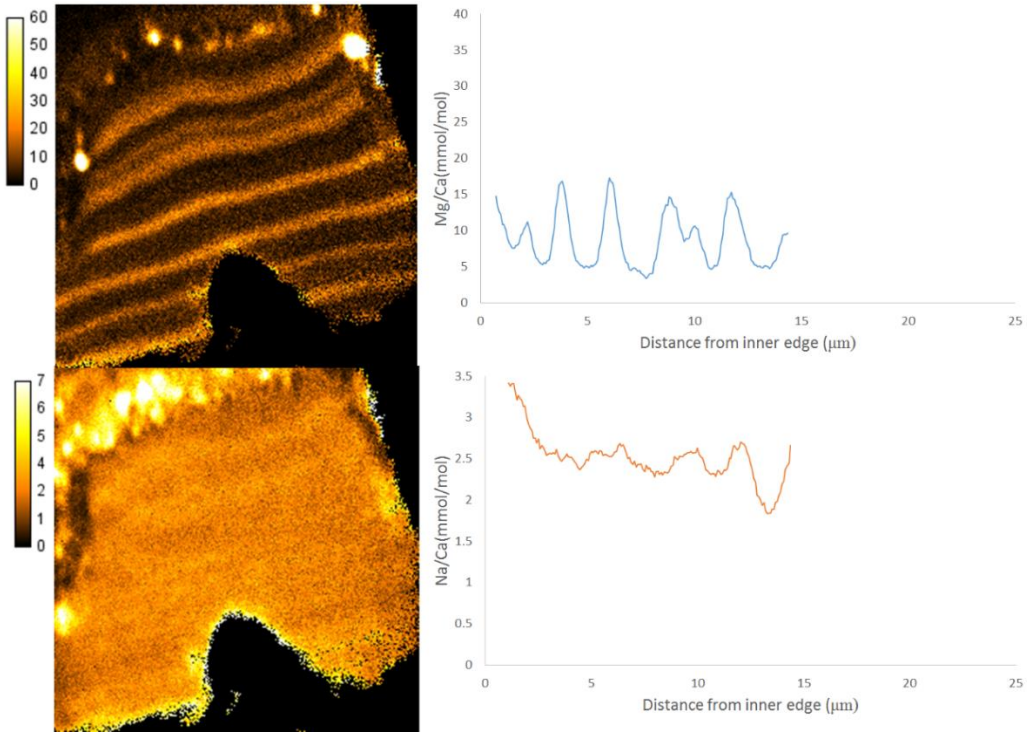

859:

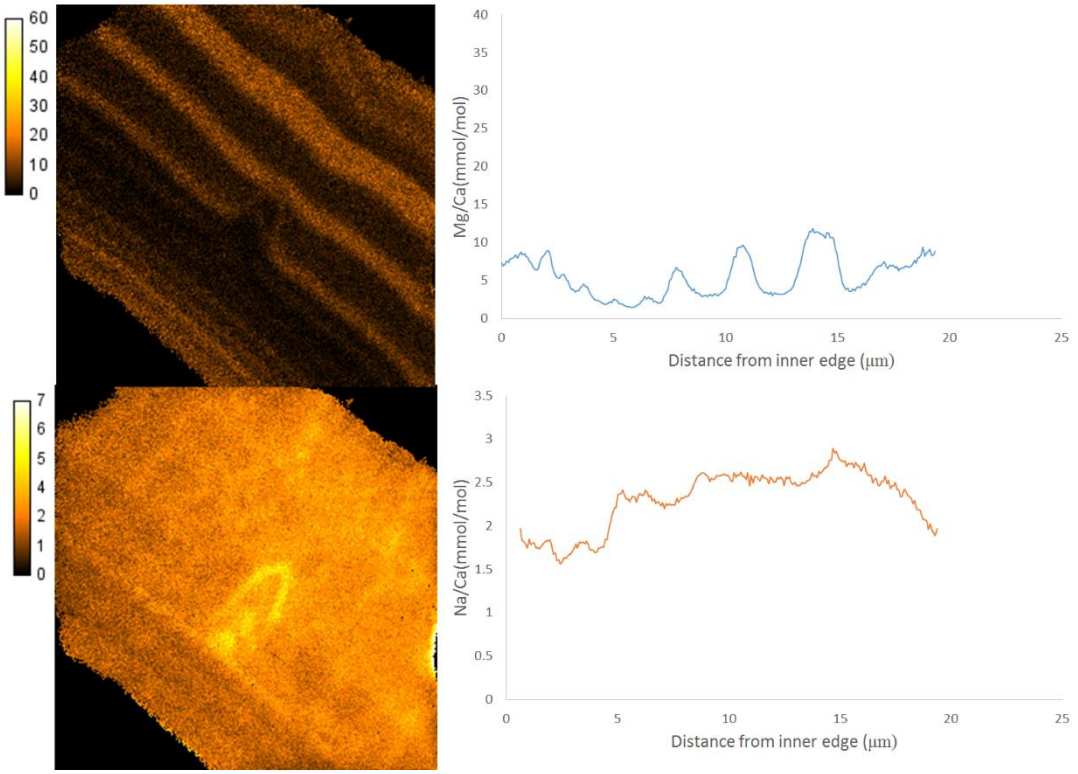

862 (Note different color scale):

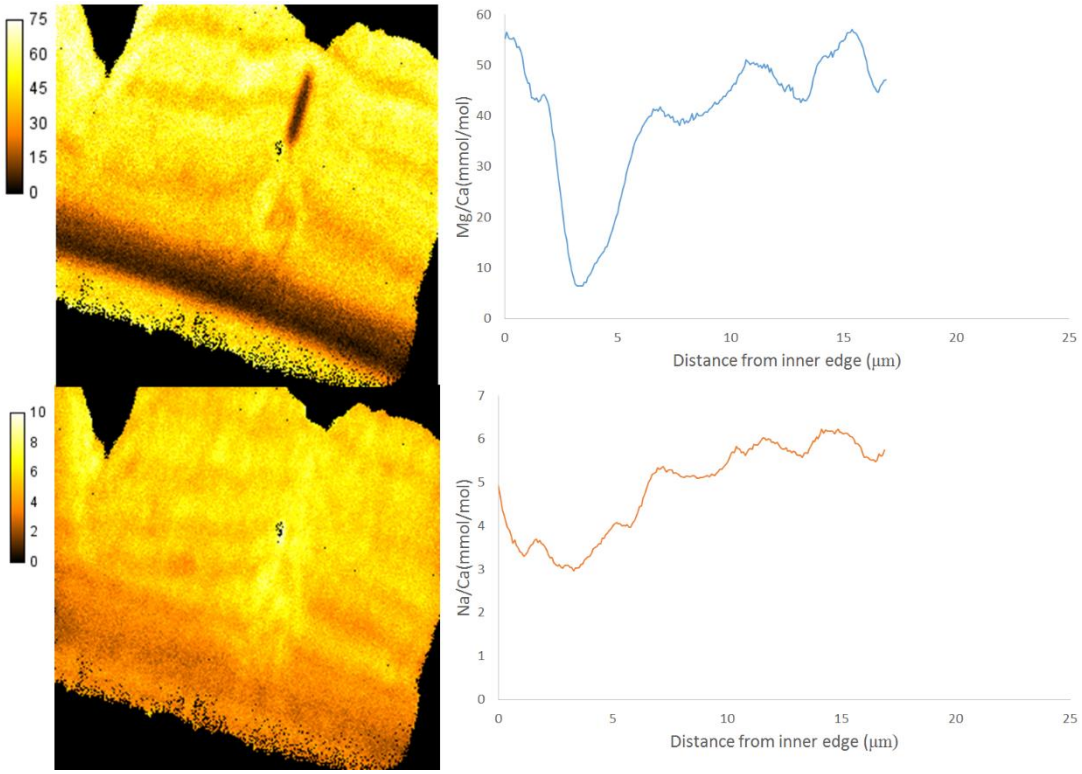

APPENDIX C: SUPPLEMENTAL INFORMATION FROM CHAPTER 3

8.1 METHODS

8.1.1 *ICP-MS Analysis Settings*

In order to avoid multiple magnet hops within a single method, a separate method was used for each element of interest. The parameters of each method are summarized in Table 8.1. All measurements were taken in low resolution (Figure 8.1), except for Mg, which was measured in medium resolution (Figure 8.2) to distinguish between the ^{24}Mg peak and the NaH^{+} peak, both of which can be found at mass 24. Ca was also measured in medium resolution when seawater samples were measured, because of a significant interference at mass 48 from the $^{32}S^{16}O$ peak in seawater. An interference due to ^{87}Rb also exists at mass 87, however, ^{85}Rb was collected to correct for that (assuming an $^{85}Rb/^{87}Rb$ ratio equal to natural abundance).

Table 8.1. Analysis parameters for each element of interest.

Element	Resolution	# cycles	Mode	Measurements Taken
Li	LR	4000	Counting	^{6}Li, ^{7}Li
Mg	MR	150	Counting	$^{48}Ca^{++}$, ^{24}Mg, NaH^{+}, ^{25}Mg, ^{26}Mg
Ca	LR	400	Analog	^{43}Ca, $^{87}Sr^{++}$, ^{48}Ca
Ca (SW)	MR	500	Both	^{43}Ca, $^{87}Sr^{++}$, ^{48}Ca, $^{32}S^{16}O$
Sr	LR	400	Analog	^{81}Kr, ^{82}Kr, ^{83}Kr, ^{84}Sr, ^{85}Rb, ^{86}Sr, ^{87}Sr
Ba	LR	1000	Both	^{131}Xe, ^{132}Xe, ^{135}Ba, ^{137}Ba, ^{138}Ba

The number of cycles measured differs for each element because of the different concentrations of each element in foraminiferal calcite, and the number of counts each isotope produces at the indicated resolution. Four thousand (4000) cycles are measured for Li because of the low concentration of Li in foraminiferal calcite, and the low counts associated with Li measurements. While Ba has a lower concentration in foraminifera than Li, Ba ionizes better and

thus has more counts than Li, allowing for only 1000 cycles to be taken. Ca and Sr are abundant in foraminiferal calcite, however, 400 cycles are taken in order to improve internal error due to counting statistics. Because of the decrease in sensitivity in medium resolution, 150 cycles of Mg are taken. Internal error in Mg would be improved by taking more cycles, however, because each cycle in MR takes significantly longer than LR cycles, the amount of cycles able to be measured for Mg are dependent on the length of the injection. Ca in seawater was measured for 500 cycles, in order to ensure that a measurement is being taken for the full length of the injection time (~15 minutes).

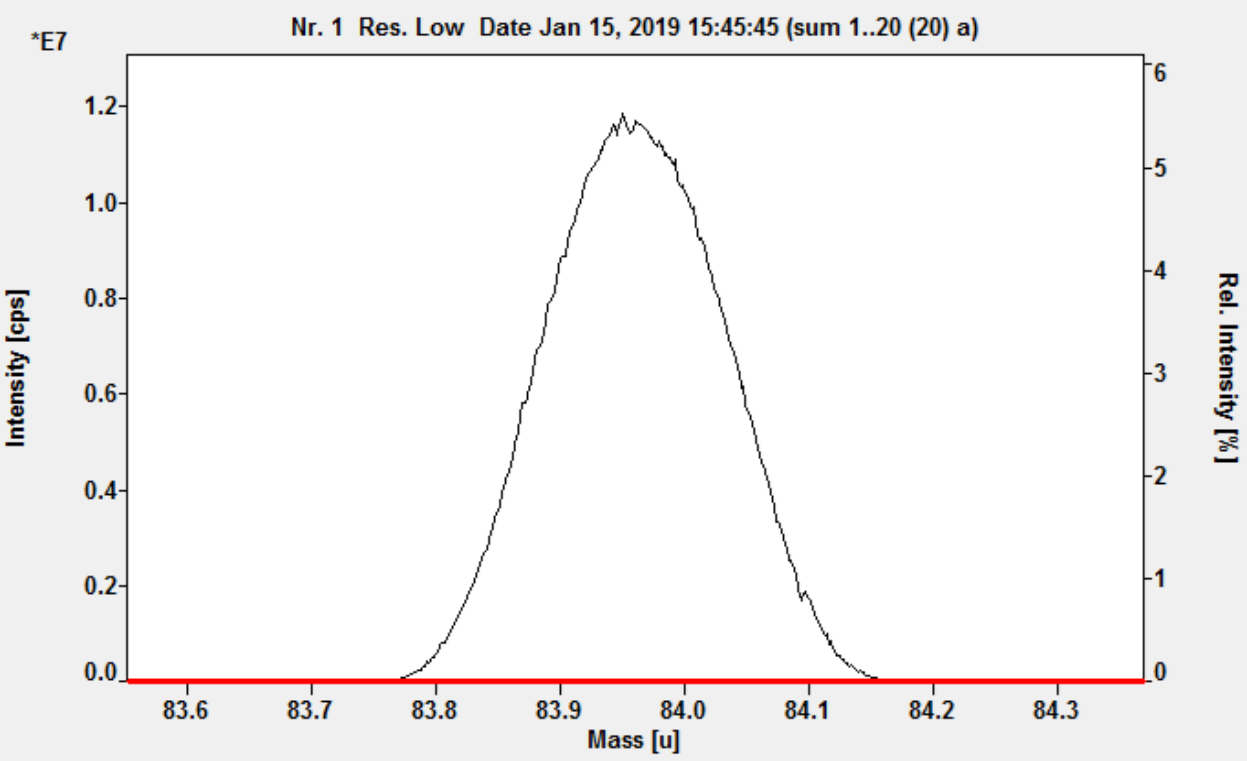

Figure 8.1. A sample low resolution peak (^{84}Sr). Measurements were taken from 10% of the flat-topped portion of the peak.

The double charged $^{87}Sr^{++}$ was measured to correct for interferences in ^{43}Ca from the $^{86}Sr^{++}$ double charged peak. This correction was applied by comparing the number of counts of

$^{87}Sr^{++}$ to the number of counts of ^{87}Sr to calculate the double charge formation rate, and then applying that rate to ^{86}Sr to determine the contribution of $^{86}Sr^{++}$ to the ^{43}Ca peak. ^{81}Kr, ^{82}Kr, and ^{83}Kr were measured to correct for interferences from ^{84}Kr in the ^{84}Sr peak. This was done by assuming a natural abundance distribution between the stable Kr isotopes, determining how much ^{84}Kr should be present from the counts of the other three isotopes. This amount was then subtracted from the ^{84}Sr peak.

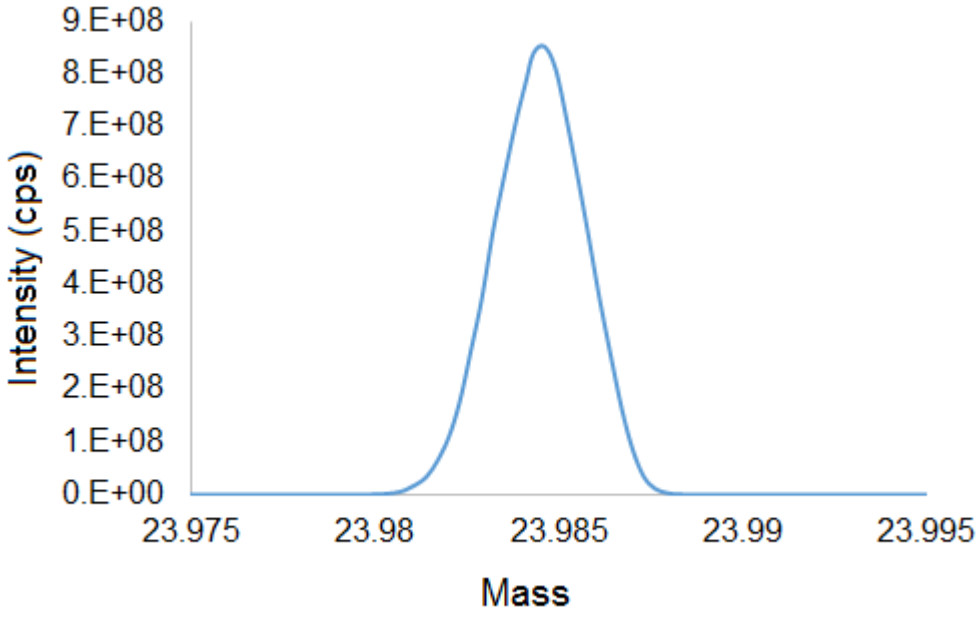

Figure 8.2. A sample medium resolution peak (^{24}Mg). Measurements were taken across the entire area of the peak.

8.1.2 *ICP-MS Sample Sequences*

8.1.2.1 Isotope Dilution Spike (xx) Calibration

A sample Element sequence from calibration of the isotope dilution (xx) spike is shown in Table 8.2 below. HPS refers to High Purity Standards for the element of interest, diluted down to a concentration that resembles sample concentration. XX refers to an aliquot of the xx-spike

solution, in this case, 30µL of xx-spike for 1mL of 2% HNO_3. IMF refers to an IMF-standard created by combining the xx-spike with dissolved coral (*Balanophyllia elegans*) samples.

Runs 4-16 are used to calibrate the isotope ratio of XX, HPS, and IMF by comparing them to an isotopic standard (STD) which differs for each element of interest. In practice, the order in which each analyte is run is randomized. RID1, RID2, and RID3 are reverse isotope dilution solutions created by adding 30µL of xx-spike to 1mL of HPS. If the isotope ratio of HPS and the isotope ratio of the xx-spike are known, the concentration of the enriched isotope in the spike solution can be determined (see main text).

Runs 1-3 serve to ensure that the instrument is stable before running actual samples. Blanks (2% HNO_3) are run before and after each list item. More than one calibration run is done per element, to ensure that results are consistent between runs.

Table 8.2. Sample sequence for xx-spike calibration.

Run #	Sample	Run #	Sample	Run #	Sample
1	HPS	11	XX*	21	RID1
2	HPS	12	STD	22	RID2
3	HPS	13	HPS*	23	RID3
4	STD	14	STD	24	STD
5	XX*	15	IMF*	25	HPS
6	STD	16	STD		
7	HPS*	17	RID1		
8	STD	18	RID2		
9	IMF*	19	RID3		
10	STD	20	STD		

*Randomized order

8.1.2.2 Recreated Culture Spike (x') Calibration

A sample Element sequence from calibration of the recreated culture spike (x') is shown in Table 8.3 below. HPS refers to High Purity Standards for the element of interest, XP refers to an aliquot of the x' spike solution, in this case 100µL of x'spike in 900µL of 2% HNO_3, and

RMS refers to an IMF-standard created by combining the x'spike with the dissolved foraminifera consistency standard. The ratio of x'spike to dissolved foraminifera consistency standard in RMS is 1:5 (20% enriched).

Runs 4-16 are used to calibrate the isotope ratio of XP, HPS, and RMS by comparing them to an isotopic standard. In practice, the order in which each analyte is run is randomized. RID1, RID2, and RID3 are reverse isotope dilution solutions created by adding 30µL of x' spike to 1mL of HPS for Mg, Ca, and Sr, and 100µL x'spike to 900µL HPS for Li and Ba. The reason for the different concentrations is that the concentration of Li and Ba is much lower in foraminifera than the concentration of Mg, Ca, and Sr. Thus, because the concentration of elements in the x'spike is intended to estimate actual foraminifera concentration, the more dilute solution makes it difficult to measure the x'spike for Li and Ba. In contrast, using the more concentrated solution amplifies error in Mg, Ca, and Sr, so the more concentrated solution is not used for reverse isotope dilution for these elements. Blanks (2% HNO_3) are run before and after each list item. More than one calibration run is done per element, to ensure that results are consistent between runs.

Table 8.3. Sample sequence for x' spike calibration.

Run #	Sample	Run #	Sample	Run #	Sample
1	HPS	11	XP*	21	RID1
2	HPS	12	STD	22	RID2
3	HPS	13	HPS*	23	RID3
4	STD	14	STD	24	STD
5	XP*	15	RMS*	25	HPS
6	STD	16	STD		
7	HPS*	17	RID1		
8	STD	18	RID2		
9	RMS*	19	RID3		
10	STD	20	STD		

*Randomized order

8.1.2.3 Method Test

The multi-spike method was tested by creating a set of solutions (R_m) that combined the foraminifera consistency standard and the x' spike. This test was done over a single run, in order to ensure that all isotope ratios are collected during each run. A sample Element sequence for the run to measure R_m is shown below. In this sequence, JCp refers to a dissolved solution of JCp-1, IMF refers to the IMF-standard used to calibrate the xx-spike, here used as another isotopic standard, RMS refers to the internal mass fractionation standard created using the consistency standard and the x' spike, here used as the main isotopic standard, and 10X, 25X, 50X, 65X, and 80X refer to test solutions made using a combination of the x' spike and the consistency standard (10% spike, 25% spike…respectively). CS refers to the consistency standard, which was used to represent the natural abundance end member.

Table 8.4. Sample sequence for the method test.

Run #	Sample	Run #	Sample	Run #	Sample	Run #	Sample	Run #	Sample
1	RMS	11	10XID*	21	50X*	31	JCp	41	IMF
2	RMS	12	25X*	22	JCp	32	IMF	42	RMS
3	RMS	13	JCp	23	IMF	33	RMS	43	JCp
4	JCp	14	IMF	24	RMS	34	JCp	44	CS*
5	IMF	15	RMS	25	JCp	35	65XID*	45	CS*
6	RMS	16	JCp	26	50XID*	36	80X*	46	XX*
7	JCp	17	25X*	27	50XID*	37	80X*	47	XX*
8	10X*	18	25XID*	28	65X*	38	80XID*	48	JCp
9	10X*	19	25XID*	29	65X*	39	80XID*	49	IMF
10	10XID*	20	50X*	30	65XID*	40	JCp	50	RMS

*Randomized order

10XID, 25XID, 50XID, 65XID, and 80XID refer to isotope dilution runs of the same solutions as above, with 30µL of the xx-spike added to 1mL of solution. This ratio of spike to solution is based on calculations of error amplification, and is optimal for Sr, Mg, Li, and Ca measurements. A lower spike-to-solution ratio would be optimal for Ba, however, would result in higher errors for Sr, Mg, Li, and Ca. Because Ba measurement is not the major focus of this

project, the higher spike-to-solution ratio is used. The IMF standard created using the xx-spike (IMF) is used as the primary standard for this run because it is closer in composition to the isotope dilution solutions than other standards. Samples are run in randomized order, with two replicate measurements taken per sample. Blanks (2% HNO_3) are run before and after each list item.

8.1.2.4 Day/Night Spiked Foraminifera Analysis

Day- and night-spiked foraminifera samples were analyzed using a sequence similar to that outlined in Table 8.4 above. However, because six foraminifera samples were analyzed in each run, each sample requiring two replicates of both an R_{ID} and R_m measurement, the runs were much longer than the method test run, lasting between 48 and 72 hours for each analysis. Samples of the spiked culture solution, YYH, were analyzed as part of each run. However, because seawater contains more impurities than dissolved, cultured foraminifera, to ensure that the analysis of spiked seawater did not affect the analysis of other samples, analyses of YYH were done at the end of each run, after data from all samples had been collected.

8.2 RESULTS

8.2.1 *Monte Carlo Analyses*

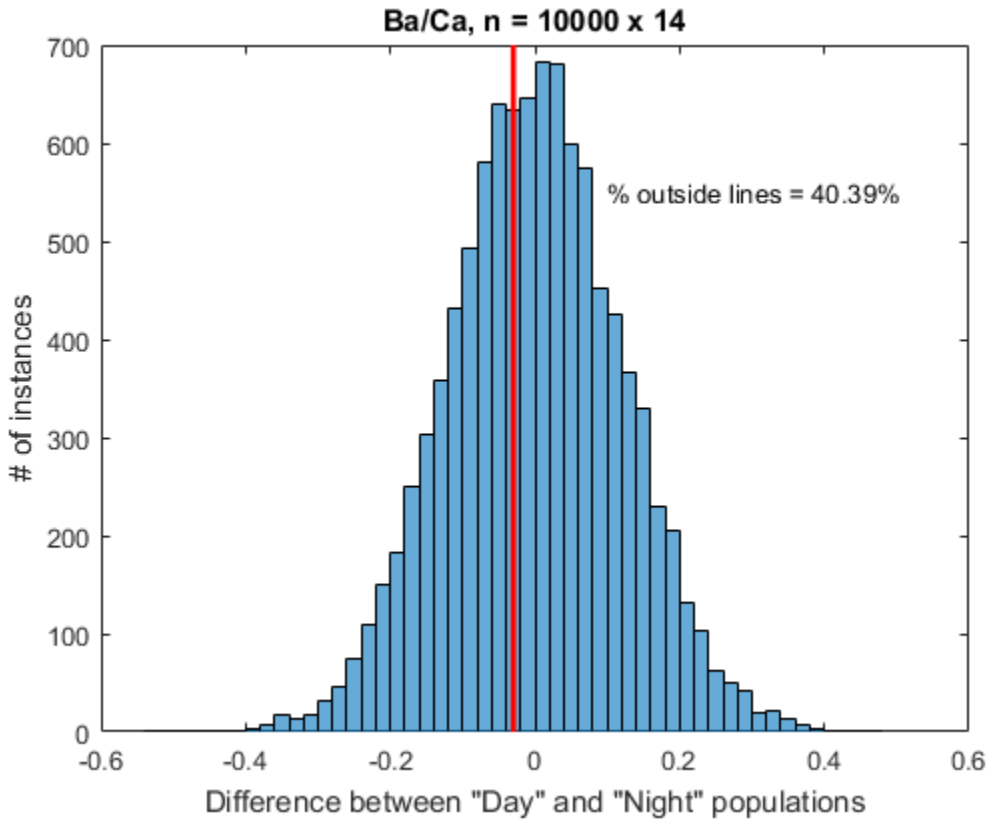

Figure 8.3. Results of Monte Carlo analysis for Ba/Ca. The number of points with a Δmean greater than the observed Δmean are 40.39%, reflecting a 40.39% possibility that the day- and night-spiked Ba/Ca ratios were drawn from the same population.

8.2.2 *Conversion to Partition Coefficients*

Me/Ca ratios are converted to partition coefficients (D_{Me}) using the following relationship:

$$D_{Me} = \frac{(^{Me}/_{Ca})_{calcite}}{(^{Me}/_{Ca})_{seawater}} \quad (7.1)$$

In the case of the foraminifera examined in this study, 'calcite' refers to the spiked portion of the calcite (x), and seawater refers to the spiked culture solution (YYH). If we assume that the ratio of the abundance of reference isotopes ($^{ref}A/^{48}A$) in the calcite is equal to the ratio of the abundance of reference isotopes in the spiked seawater—that is, that there is no fractionation between calcite and solution, or that the fractionation between calcite and solution is measurable, this equation can also be written as:

$$D_{Me} = \frac{(^{Me}/_{Ca})_x}{(^{Me}/_{Ca})_{YYH}} * \frac{(^{ref}A/_{^{48}A})_x}{(^{ref}A/_{^{48}A})_{YYH}} \tag{7.2}$$

$$D_{Me} = \frac{(^{ref}Me/_{^{48}Ca})_x}{(^{ref}Me/_{^{48}Ca})_{YYH}} \tag{7.3}$$

Thus, in order to calculate D_{Me}, two things must be measured: the ratio of the concentrations of reference isotopes in the spiked calcite, and the ratio of the concentrations of reference isotopes in YYH. The latter can be measured using the same reverse isotope dilution step as that used to measure this ratio in the isotope dilution spike (xx, see Section 3.2.7). The former is calculated as an intermediate step in the mixed spike method (Gagnon et al., 2012), as follows:

$$(^{ref}Me/_{^{48}Ca})_x = \left(\frac{\left(\frac{^{ref}n_x}{^{ref}n_x + ^{ref}n_o}\right)}{\left(\frac{^{48}n_x}{^{48}n_x + ^{48}n_o}\right)}\right) * \left(\frac{^{ref}n_x + ^{ref}n_o}{^{48}n_x + ^{48}n_o}\right) \tag{7.4}$$

where the first term equates to the mole fraction of the reference isotope in the spiked portion of the calcite and the second term equates to the total $^{ref}Me/^{48}Ca$ ratio of the mixed sample. Using the terminology established in Gagnon et al., (2012), this equates to:

$$\left({}^{ref}Me/_{48}Ca\right)_x = \left(\frac{{}^{48}F+1}{{}^{ref}F+1}\right) * T \quad (7.5)$$

The final equation for total Me/Ca ratios described in Gagnon et al., (2012) is:

$$\left(\frac{\mathrm{Me}}{\mathrm{Ca}}\right)_x = \left(\frac{{}^{48}A_x\,({}^{48}F+1)}{{}^{ref}A_x\,({}^{ref}F+1)}\right)T = \frac{{}^{48}A_x}{{}^{ref}A_x} * \left(\frac{{}^{ref}Me}{{}^{48}Ca}\right)_x \quad (7.6)$$

Thus, it is possible to calculate (^{ref}Me/^{48}Ca)$_x$ as an intermediate product of the multi-spike method.

8.2.3 *Spike Incorporation from NanoSIMS Data*

NanoSIMS profiles of ^{25}Mg/^{24}Mg, ^{24}Mg/^{40}Ca and ^{43}Ca/^{40}Ca from three different foraminifera samples are displayed in Figures 8.4 to 8.15 below. These profiles show a slight discrepancy between the incorporation of the ^{43}Ca spike and the ^{25}Mg spike into foraminiferal calcite, and a slight off-set between the location of high Mg/Ca bands and areas spiked with ^{43}Ca. However, these offsets are minor, with >75% of the band of interest being captured by the labeled calcite in each instance. The labeled calcite is the portion of the shell whose Me/Ca ratio can be calculated by the multi-spike method. Thus, the Me/Ca ratio of the labeled portion of the calcite is still dominantly set by the day or night band of interest.

8.2.3.1 Specimen # 311 (Night-Spiked)

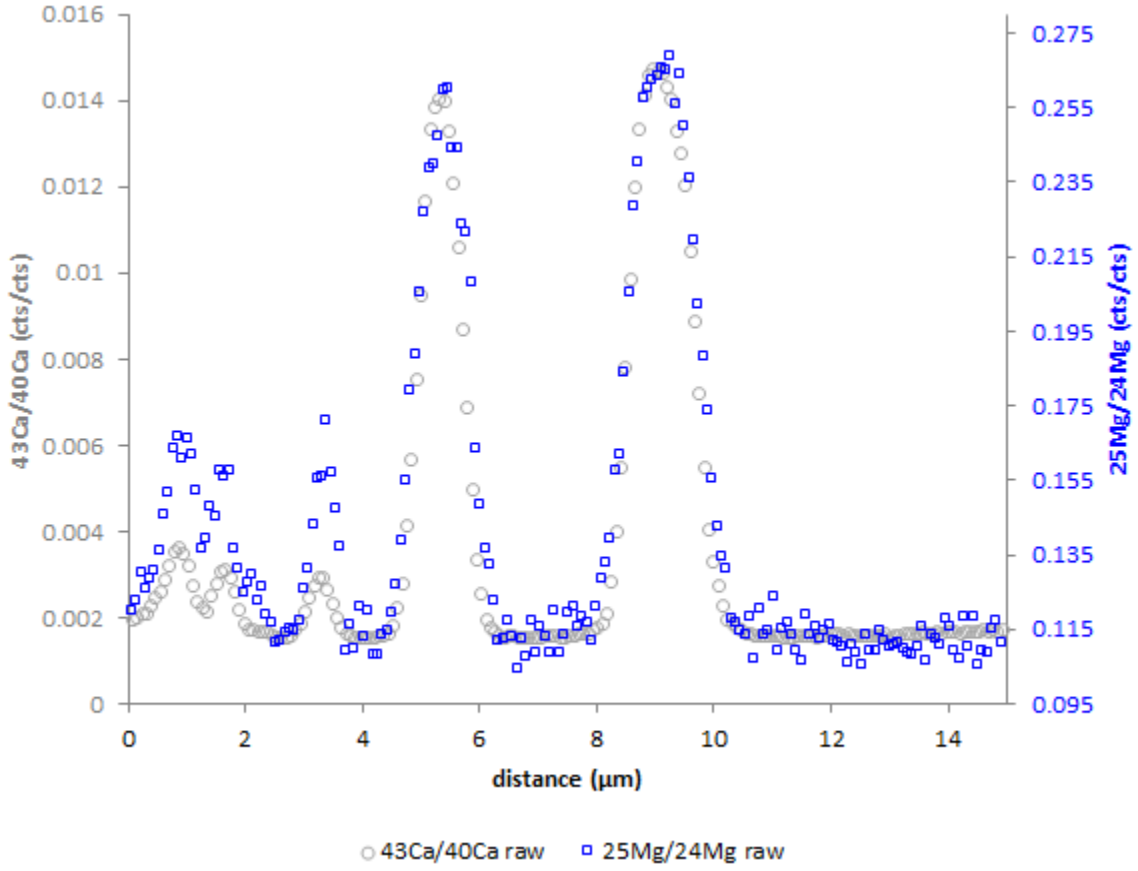

Figure 8.4. Full $^{43}Ca/^{40}Ca$ and $^{25}Mg/^{24}Mg$ from Foram 311 (Table 3.8).

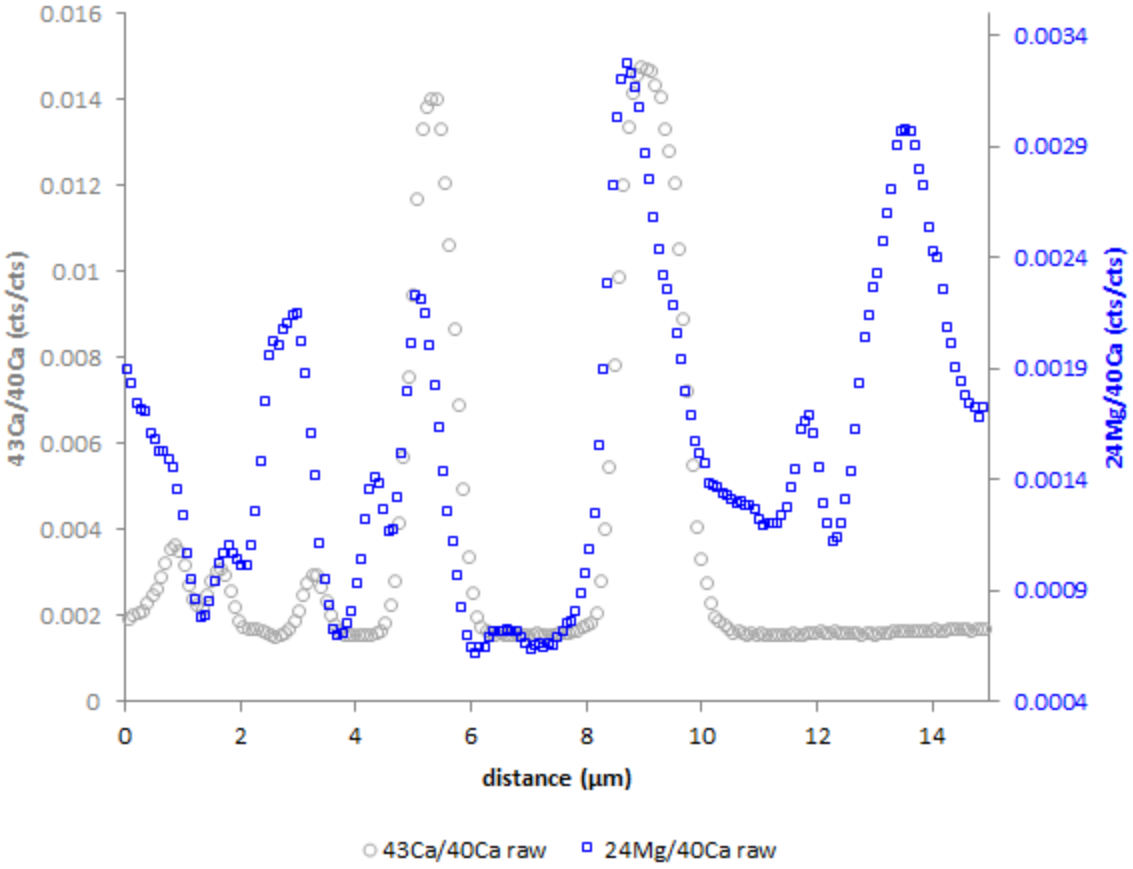

Figure 8.5. Full $^{43}Ca/^{40}Ca$ and $^{24}Mg/^{40}Mg$ from Foram 311 (Table 3.8).

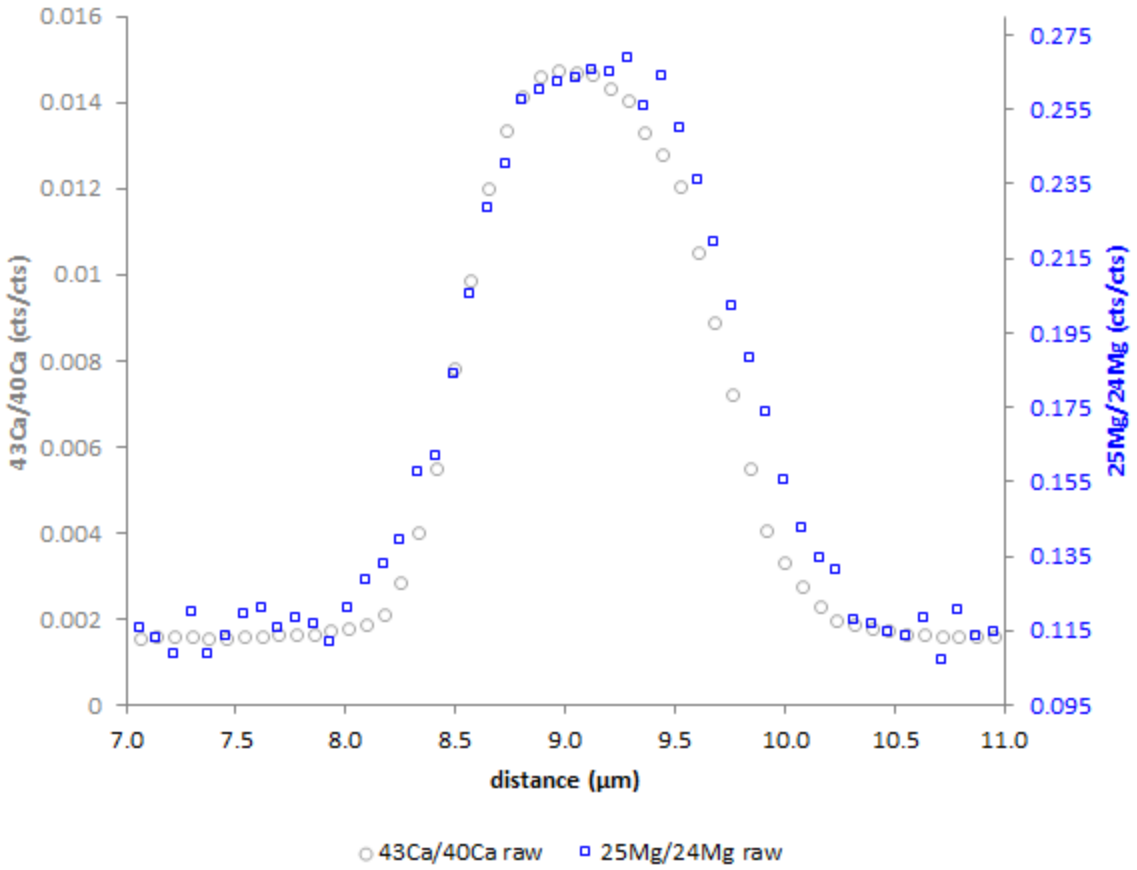

Figure 8.6. Close view of $^{43}Ca/^{40}Ca$ and $^{25}Mg/^{24}Mg$ from a single band of Foram 311 (Table 3.8).

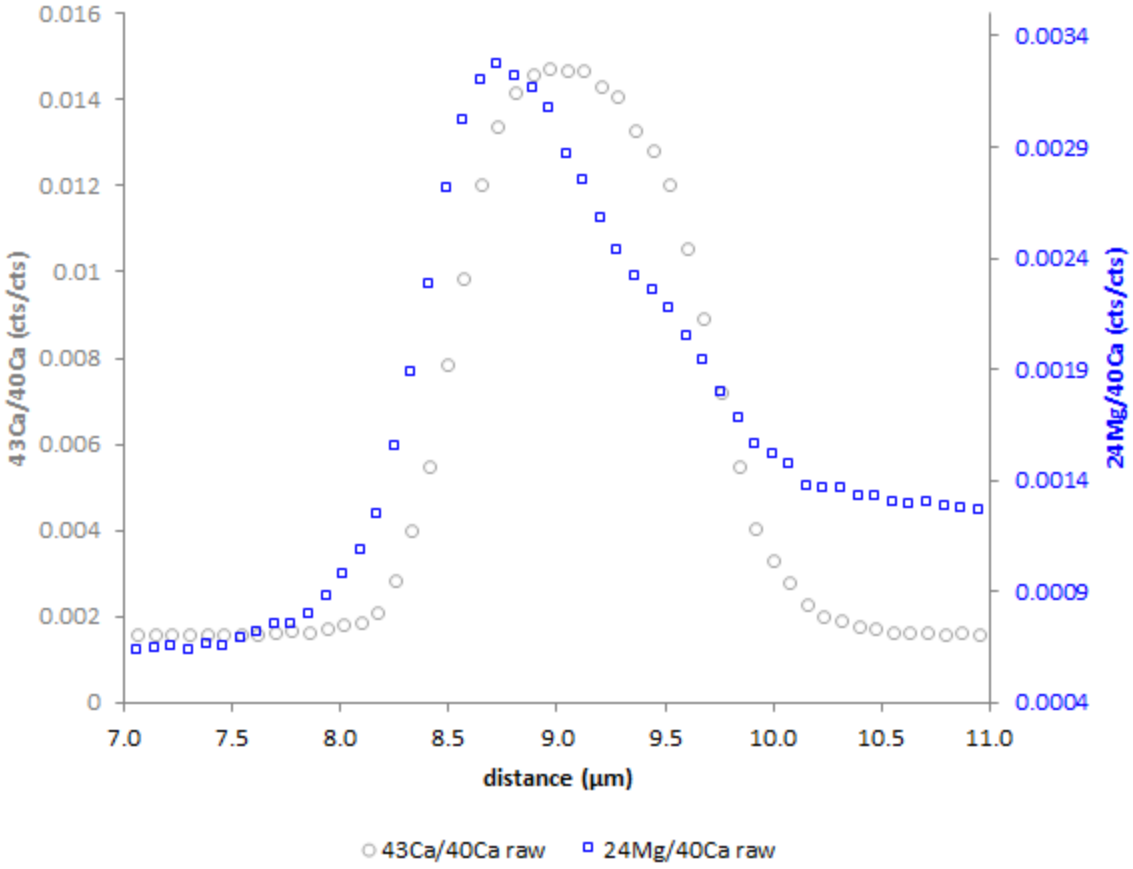

Figure 8.7. Close view of $^{43}Ca/^{40}Ca$ and $^{24}Mg/^{40}Mg$ from a single band of Foram 311 (Table 3.8).

8.2.3.2 Specimen # 313 (Night-Spiked)

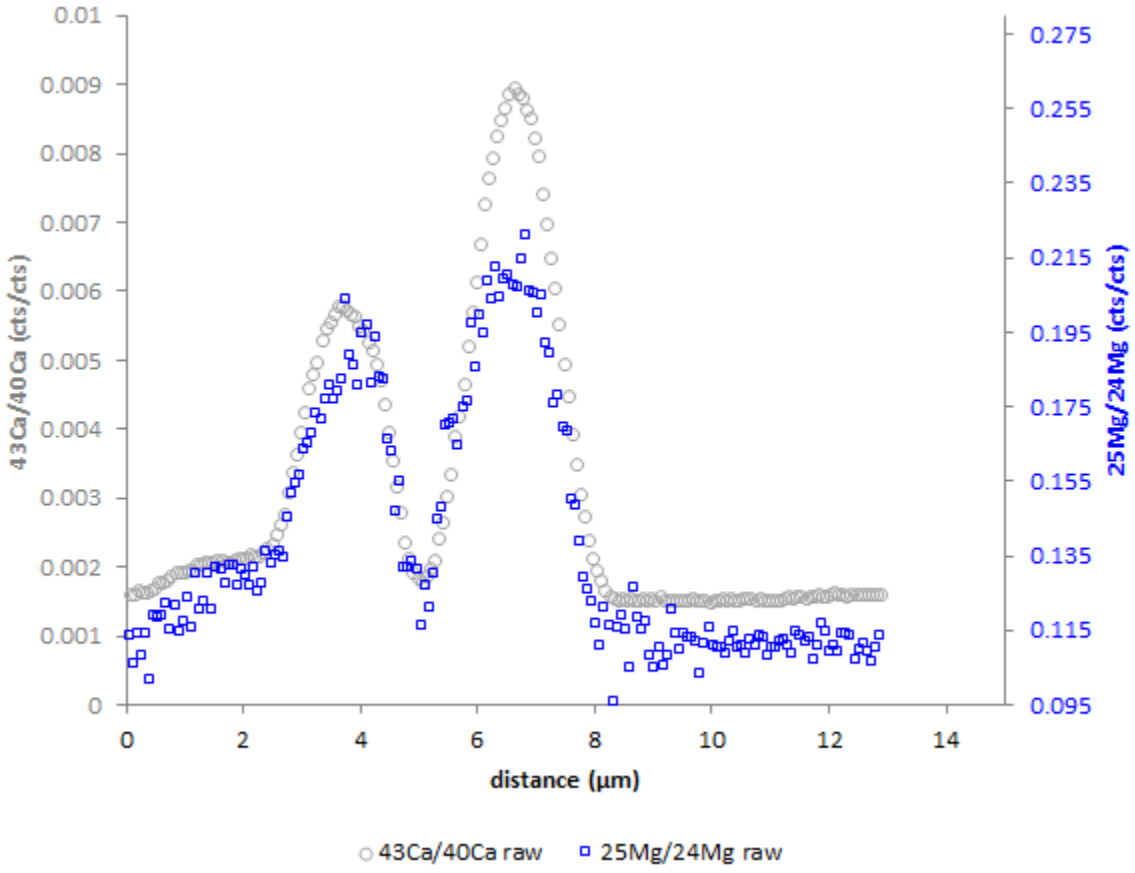

Figure 8.8. Full $^{43}Ca/^{40}Ca$ and $^{25}Mg/^{24}Mg$ from Foram 313.

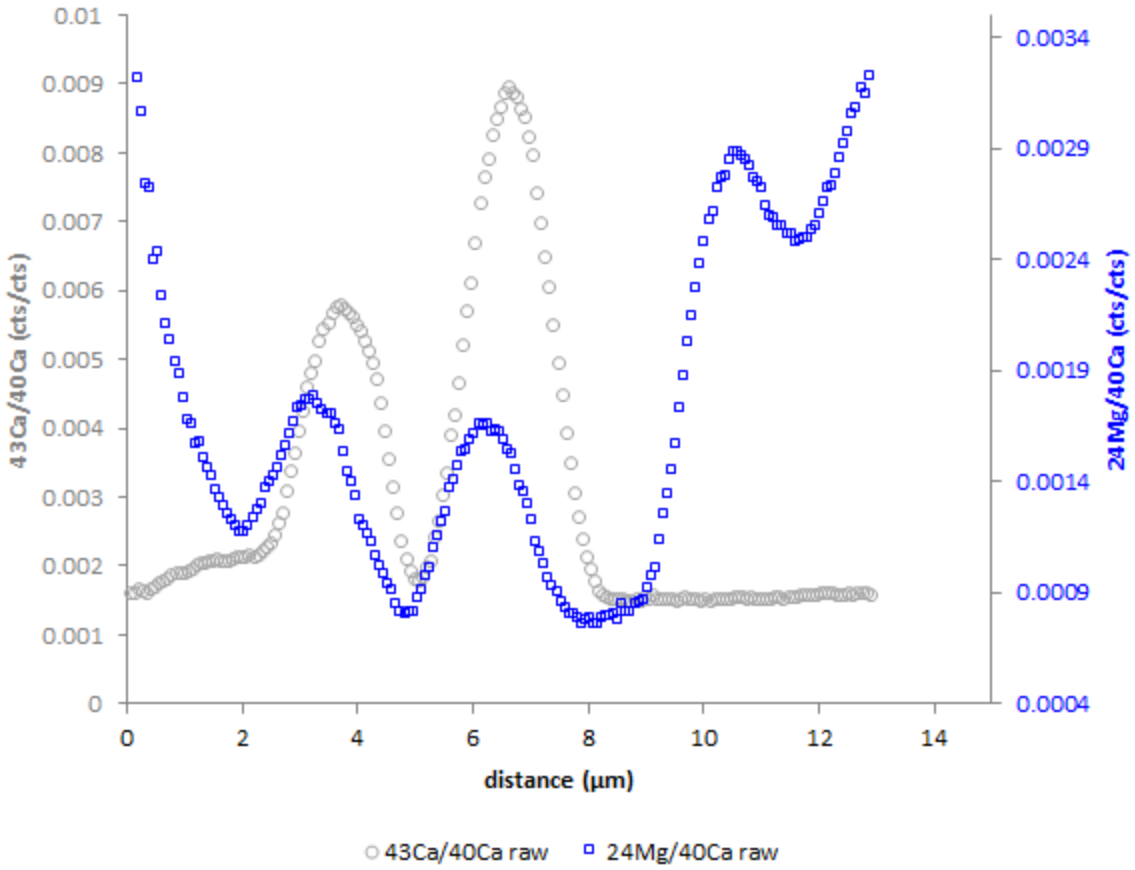

Figure 8.9. Full $^{43}Ca/^{40}Ca$ and $^{24}Mg/^{40}Mg$ from Foram 313.

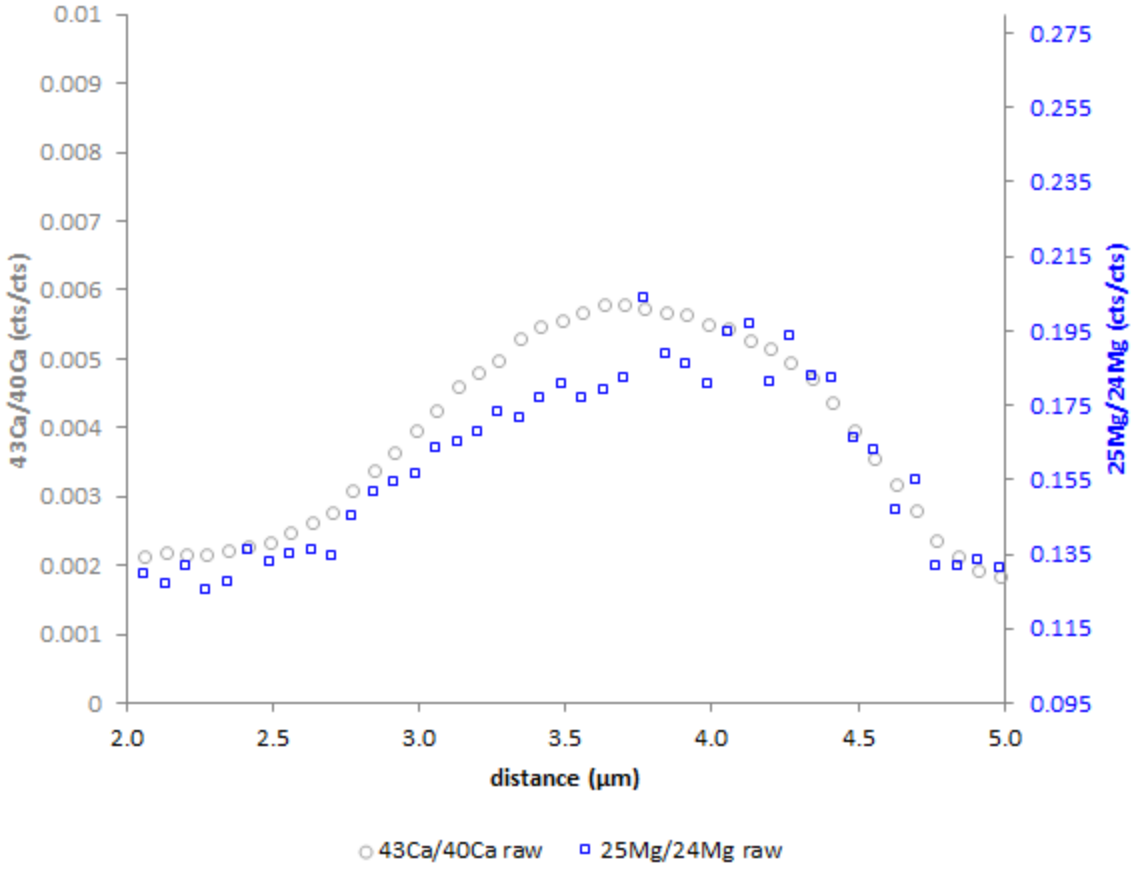

Figure 8.10. Close view of $^{43}Ca/^{40}Ca$ and $^{25}Mg/^{24}Mg$ from a single band of Foram 313.

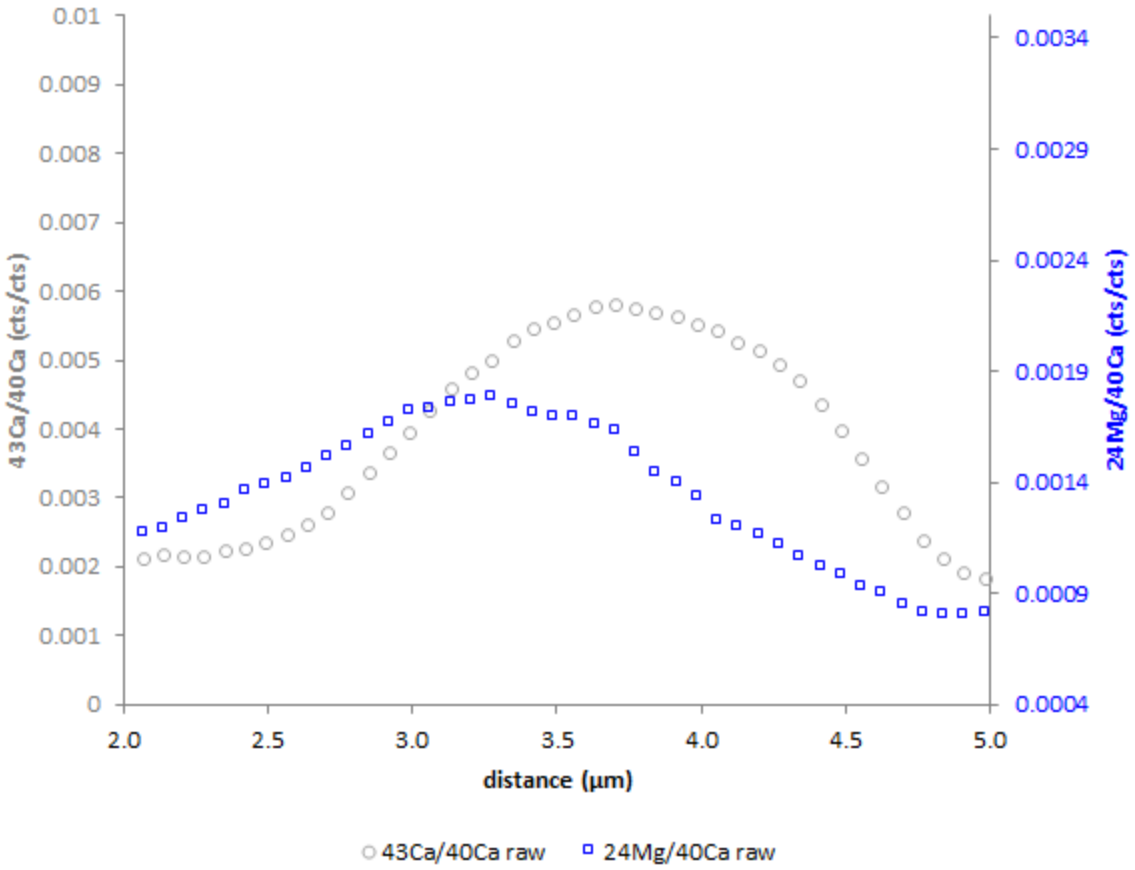

Figure 8.11. Close view of $^{43}Ca/^{40}Ca$ and $^{24}Mg/^{40}Mg$ from a single band of Foram 313.

8.2.3.3 Specimen # 423 (Day-Spiked)

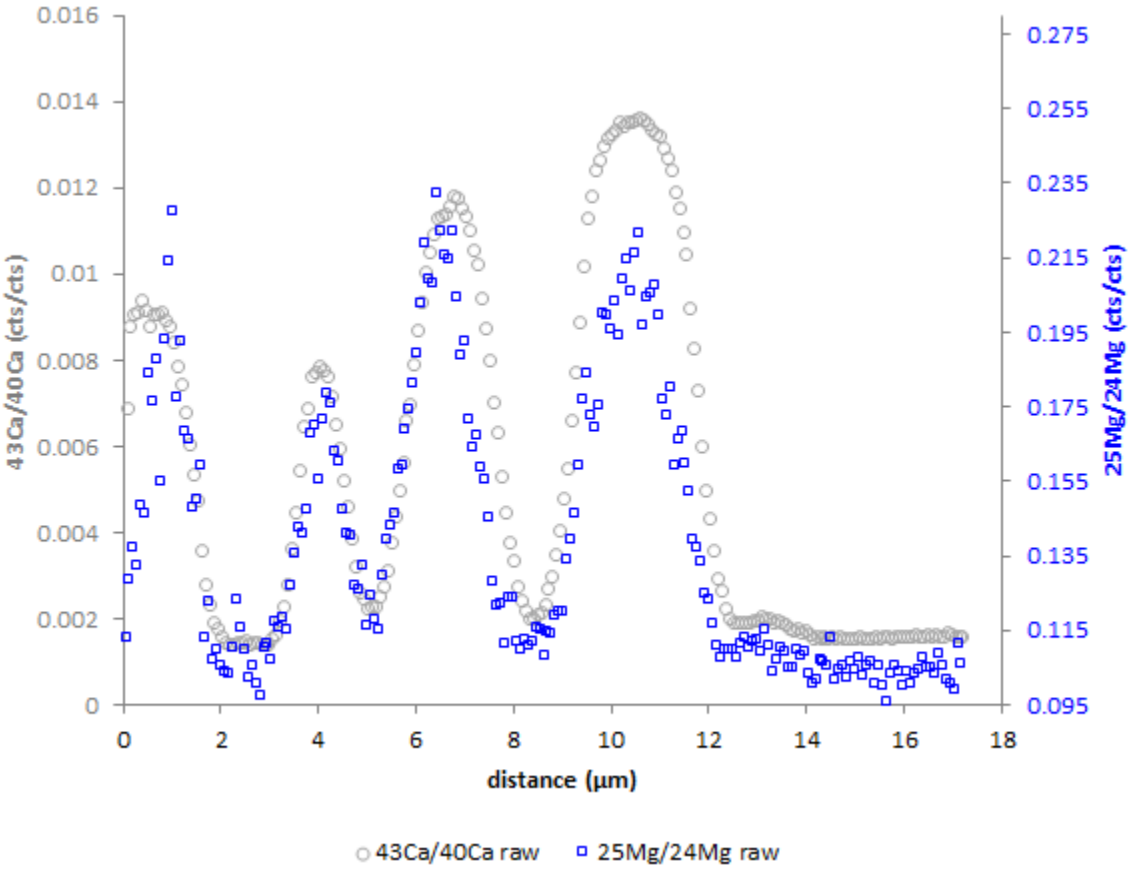

Figure 8.12. Full $^{43}Ca/^{40}Ca$ and $^{25}Mg/^{24}Mg$ from Foram 423.

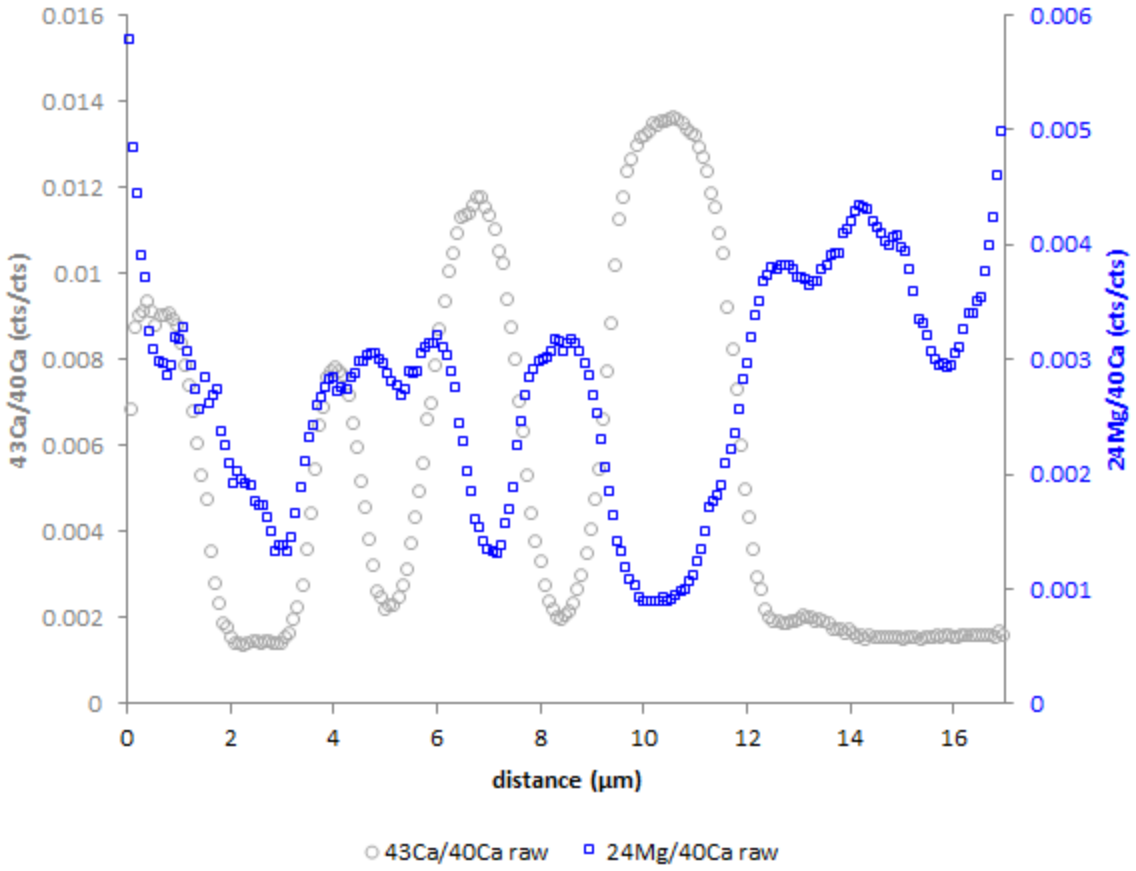

Figure 8.13. Full $^{43}Ca/^{40}Ca$ and $^{24}Mg/^{40}Mg$ from Foram 423.

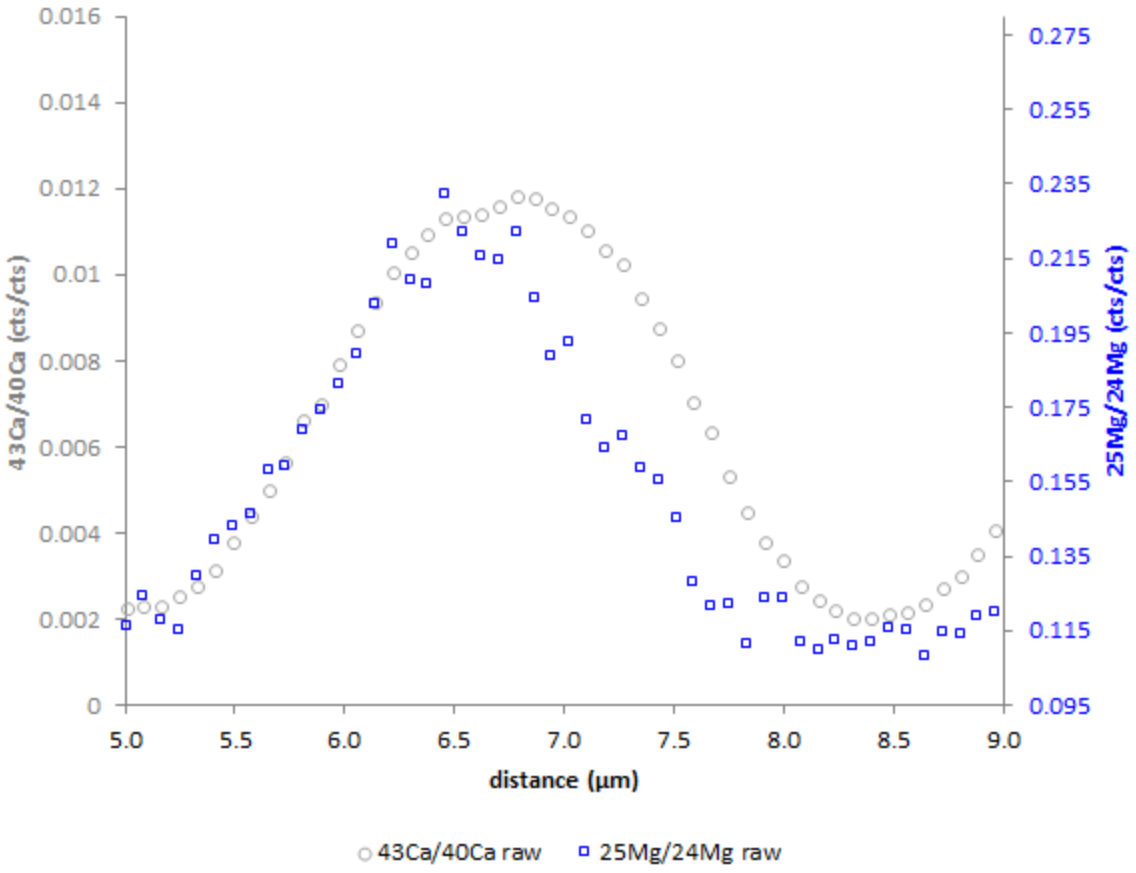

Figure 8.14. Close view of $^{43}Ca/^{40}Ca$ and $^{25}Mg/^{24}Mg$ from a single band of Foram 423.

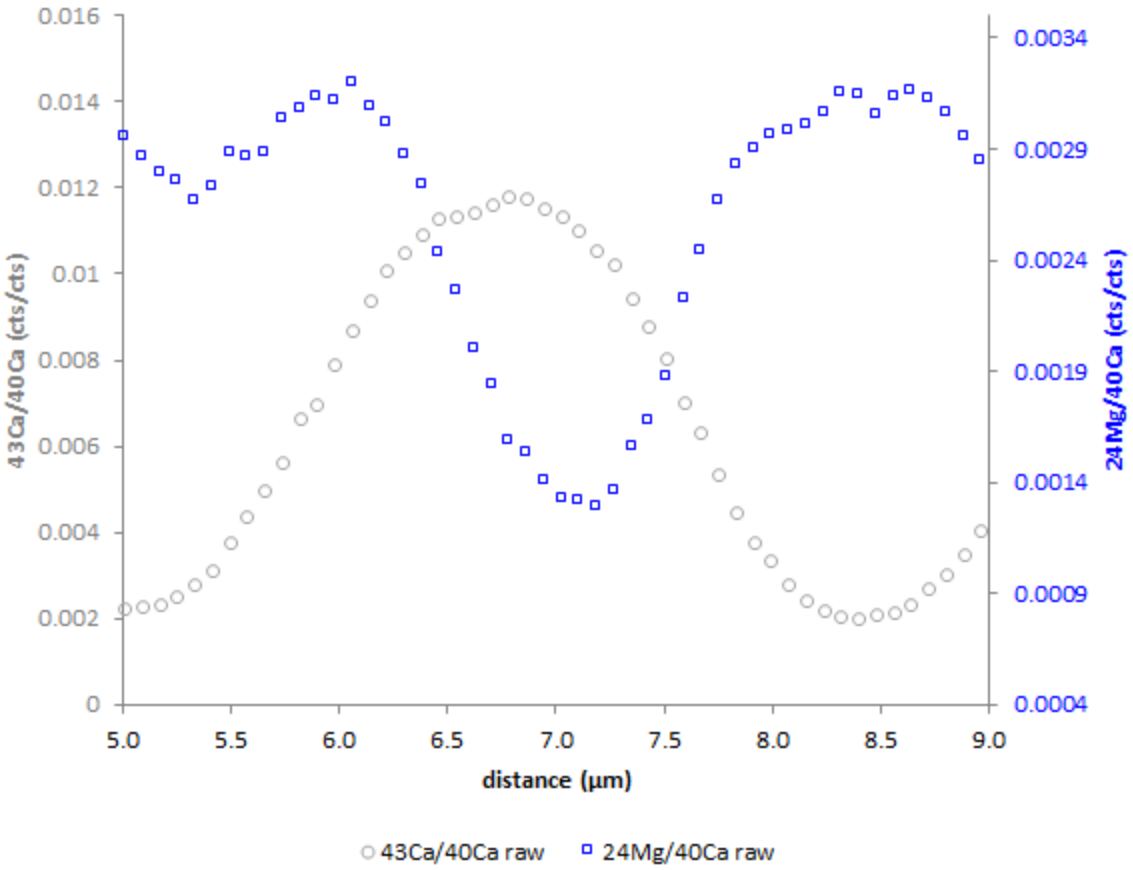

Figure 8.15. Close view of $^{43}Ca/^{40}Ca$ and $^{24}Mg/^{40}Mg$ from a single band of Foram 423.

8.2.4 *Additional Li/Ca NanoSIMS Images*

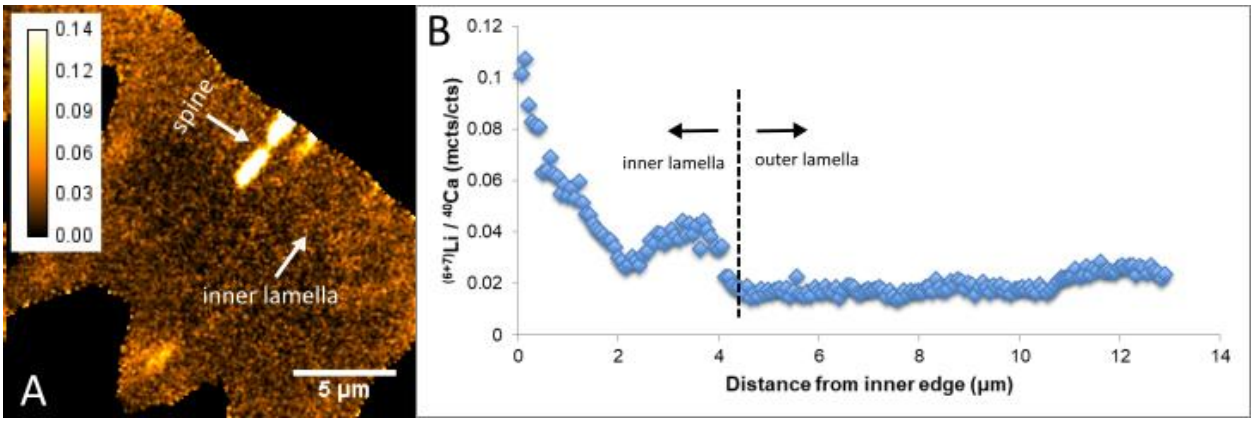

Figure 8.16. NanoSIMS Li/Ca images from Foram 313 (night-spiked) A) Intensity image of Li/Ca across the test wall of a cultured *O. universa* created from NanoSIMS data. Spine and inner lamella regions are labeled. Intensity ratios are reported in ^{7}Li cts x 10^{3} /^{40}Ca cts. B) A $^{(6+7)}$Li/^{40}Ca profile drawn across the test wall of the same foraminifer imaged in Figure 8.16A. The boundary between the inner and outer lamellae is labeled. The spine region is excluded from this profile.

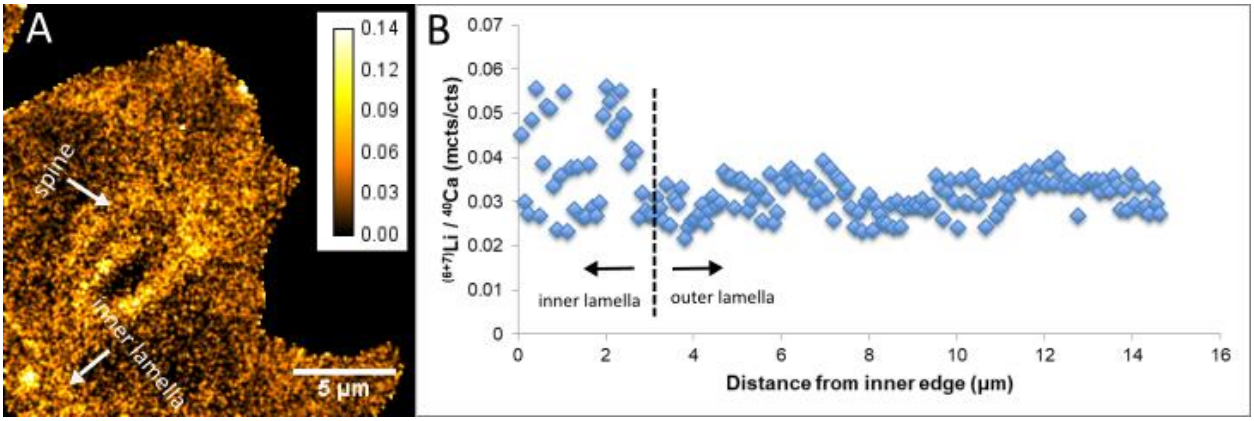

Figure 8.17. NanoSIMS Li/Ca images from Foram 423 (day-spiked) A) Intensity image of Li/Ca across the test wall of a cultured *O. universa* created from NanoSIMS data. Spine and inner lamella regions are labeled. This is the same specimen imaged in Figure 3.9B of the main text. Intensity ratios are reported in ^{7}Li cts x 10^{3} /^{40}Ca cts. B) A $^{(6+7)}$Li/^{40}Ca profile drawn across the test wall of the same foraminifer imaged in Figure 8.17A. The boundary between the inner and outer lamellae is labeled. The spine region is excluded from this profile.

8.2.5 *Response of X_{day} to pH*

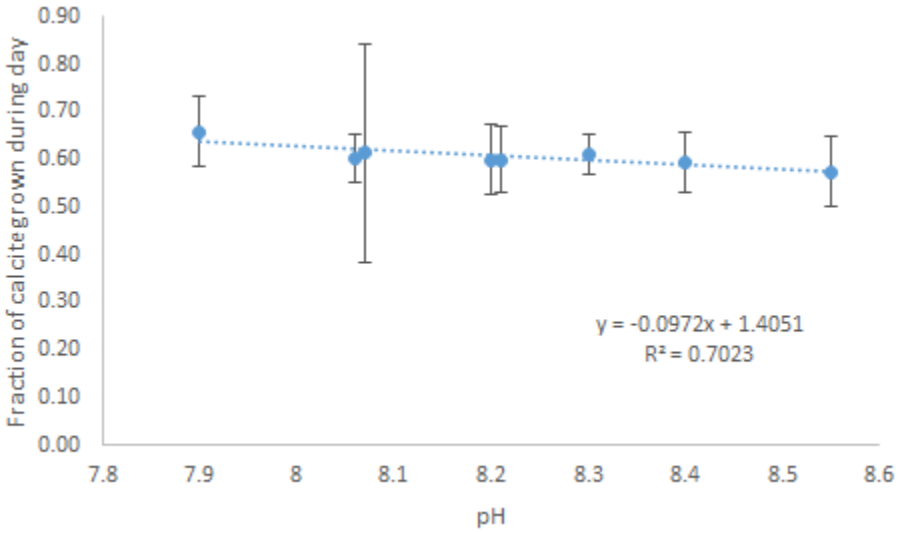

Figure 8.18. Mean X_{day} values from experimental treatments cultured at different pH values (Table 7.1).

8.2.6 *Response of X_{day} to salinity*

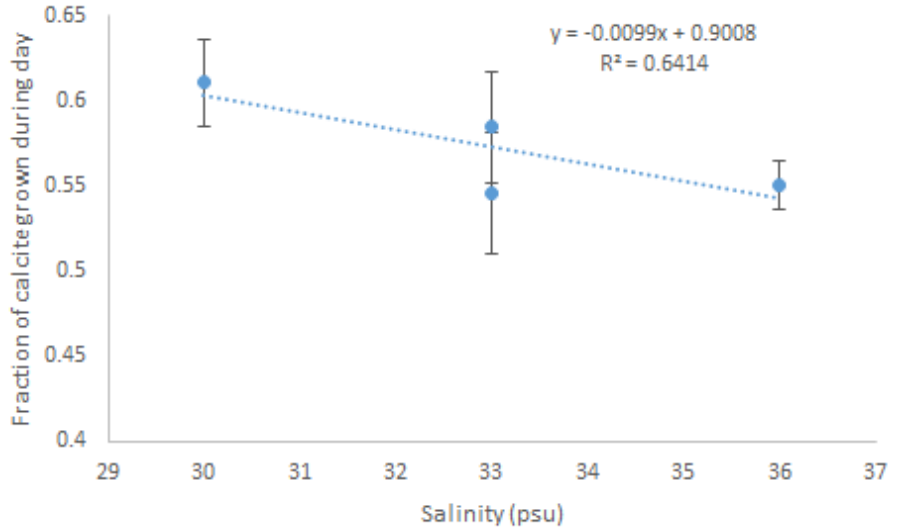

Figure 8.19. Mean X_{day} values from experimental treatments cultured at different salinities (Table 6.1).

APPENDIX D: SUPPLEMENTAL INFORMATION FROM CHAPTER 4

9.1 Ba/Ca and Li/Ca Measurements

Li/Ca and Ba/Ca results are summarized in Figures 9.1 and 9.2 below. Measurements of Li/Ca in gametogenic calcite have high variability (Fig. 9.1), which is indicative of samples with low isotope enrichment. Ba/Ca ratios (Fig. 9.2) initially appear less variable, however, Ba/Ca calculations report an unrealistically high Ba/Ca for ontogenic calcite, particularly compared to average Ba/Ca in *O. universa* which has been observed to be between 0.6 and 1.0 μmol/mol (Lea and Boyle, 1991). Because foraminiferal Ba/Ca has previously been shown to be difficult to measure accurately using this method (Chapter 3), due to low counts and low Ba enrichment in the culture spike, we interpret this high Ba/Ca to be an artifact of measurement, and likely not a true signal.

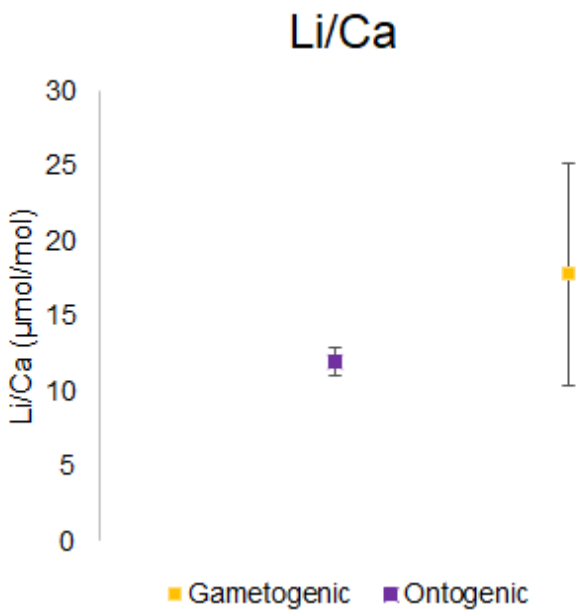

Figure 9.1. Li/Ca ratios of gametogenic and ontogenic calcite from the foraminifera analyzed in this experiment. Plotted values represent the mean gametogenic and ontogenic Li/Ca ratio of nine (9) cultured *O. universa* measurements. Solid lines refer to the means of each group. Shaded areas and dashed lines mark the standard error of the mean. Error bars reflect uncertainty in each individual measurement, as calculated using the procedure outlined in Gagnon et al., (2012).

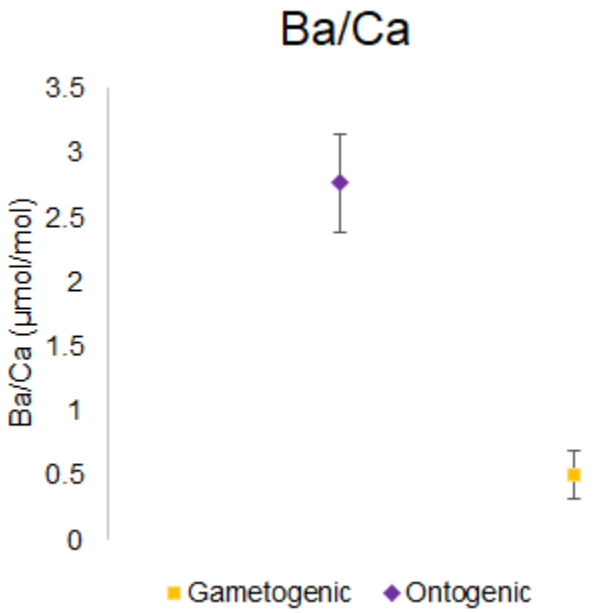

Figure 9.2. Ba/Ca ratios of gametogenic and ontogenic calcite from the foraminifera analyzed in this experiment. Plotted values represent the mean gametogenic and ontogenic Ba/Ca ratio of nine (9) cultured *O. universa* measurements. Solid lines refer to the means of each group. Shaded areas and dashed lines mark the standard error of the mean. Error bars reflect uncertainty in each individual measurement, as calculated using the procedure outlined in Gagnon et al., (2012).

9.2 Estimation of Percentage of Shell Labeled

The amount of the shell labeled is calculated using $^{43}Ca/^{48}Ca$ ratios, since Ca appears in the denominator of each Me/Ca ratio. The percentage of the shell labeled is interpreted as the fraction of ^{48}Ca in the labeled calcite, compared to the ^{48}Ca of the entire test, expressed in the following equation:

$$\%labeled = \left(\frac{^{48}n_x}{^{48}n_o + ^{48}n_x}\right) * 100\% \quad (8.1)$$

where $^{48}n_x$ refers to the number of moles of ^{48}Ca in the labeled calcite, and $^{48}n_o$ refers to the number of moles of ^{48}Ca in the unlabeled calcite.

Because F (Gagnon et al., 2012) is defined as:

$$^{48}F = \frac{^{48}n_o}{^{48}n_x} \quad (8.2)$$

the percentage of shell labeled can also be described as:

$$\%labeled = \left(\frac{1}{^{48}F+1}\right) * 100\% \quad (8.3)$$

9.3 Individual Mg/Ca and Sr/Ca Ratios

Table 9.1. Individual Mg/Ca and Sr/Ca ratios of gametogenic and ontogenic calcite. Uncertainties are derived from estimates of analytical error described in Gagnon et al., (2012).

Foram #	Gametogenic		Ontogenic		Percent Labeled
	Mg/Ca (mmol/mol)	Sr/Ca (mmol/mol)	Mg/Ca (mmol/mol)	Sr/Ca (mmol/mol)	
136	18.53 ±0.57	1.43 ±0.01	8.20 ± 0.09	1.36 ±0.01	8.2%
187	10.69 ±1.69	1.53 ±0.02	6.05 ±0.10	1.36 ±0.01	6.9%
208	9.54 ±0.41	1.25 ±0.02	8.42 ±0.07	1.35 ±0.01	8.4%
216	8.16 ±0.07	1.47 ±0.01	7.27 ±0.02	1.33 ±0.00	12.1%
270	13.14 ±1.07	1.31 ±0.01	9.53 ±0.09	1.33 ±0.00	3.3%
338	16.06 ±0.12	1.63 ±0.01	8.58 ±0.01	1.43 ±0.00	8.0%
361	17.12 ±3.71	1.49 ±0.06	8.30 ±0.13	1.42 ±0.00	4.1%
383	25.41 ±4.11	1.86 ±0.29	10.34 ±1.60	1.64 ±0.25	3.5%
391	13.29 ±3.13	1.57 ±0.24	8.91 ±1.36	1.50 ± 0.23	7.0%

9.4 Monte Carlo Analyses

An analysis was conducted using a custom MATLAB script to test whether the Me/Ca ratios obtained for gametogenic and ontogenic calcite (Table 9.1) could have come from the same population. For each Me/Ca ratio, a population of 14 random samples was generated with a mean equal to the mean of all measured foraminiferal samples, and a standard deviation equal to the standard deviation of all measured samples. A log-normal distribution was used to produce this population, to avoid negative Me/Ca ratios (Limpert and Stahel, 2011). From this population, seven samples were randomly assigned to be gametogenic calcite, and seven were randomly assigned to be ontogenic. The mean of all 'gametogenic' samples was then collected

and compared to the mean of all 'ontogenic' samples. The difference between them (Δmean) was connected, such that Δmean = $mean_{gam}$ – $mean_{onto}$. This process was repeated 10,000 times, and a histogram of all Δmeans plotted.

The observed Δmean from measurements was then plotted on each histogram as a red line, and the number of observations outside of that line (farther from zero) was counted. The percentage of those observations relative to the whole population represents the possibility that a random set of samples could produce a difference in means equal to the difference observed in our measurements. Histograms from this set of analyses are displayed in Figures 9.3 and 9.4 below.

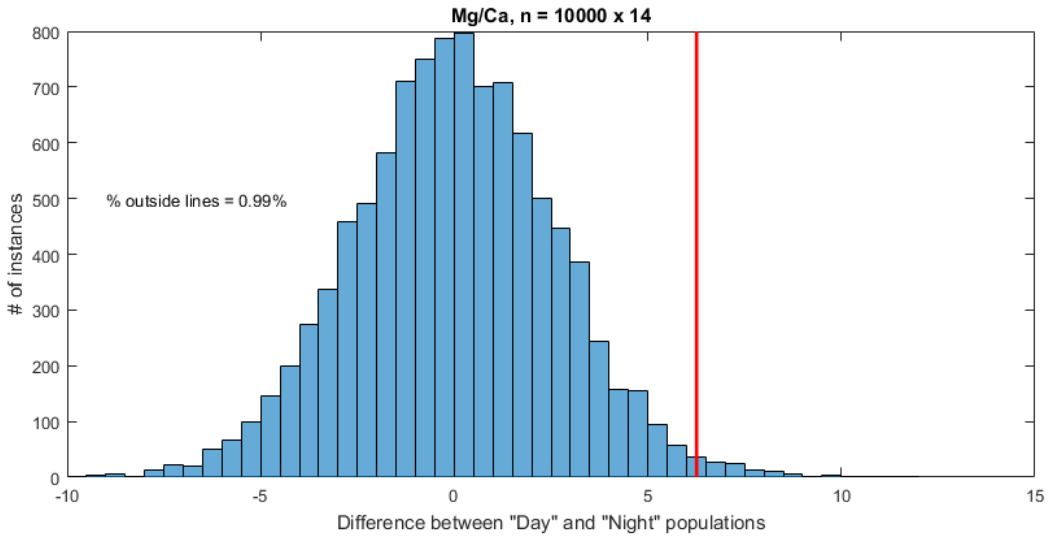

Figure 9.3. Results of Monte Carlo analysis for Mg/Ca. Less than 1% of points (0.99%) had a Δmean greater than the observed Δmean, reflecting a 0.99% possibility that the gametogenic and ontogenic Mg/Ca ratios were drawn from the same population.

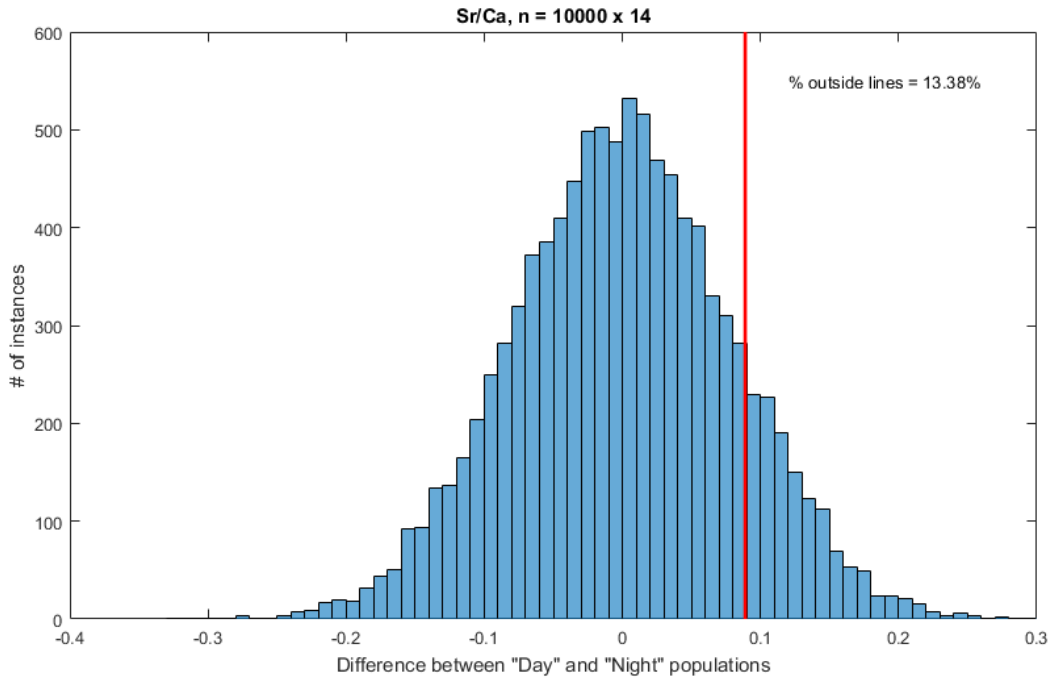

Figure 9.4. Results of Monte Carlo analysis for Sr/Ca. The number of points with a Δmean greater than the observed Δmean are 13.38%, reflecting a 13.38% possibility that the gametogenic and ontogenic Sr/Ca ratios were drawn from the same population..

9.5 Surface Images of Foraminifera Shells

9.5.1 *Helium Ion Microscope Images*

Helium ion microscope images were obtained using a Zeiss Orion Plus Helium Ion Microscope. Relevant images are displayed in Figures 9.5 to 9.7 below. These images were of a specimen that had been collected prior to gametogenesis, and so should not have any gametogenic calcite.

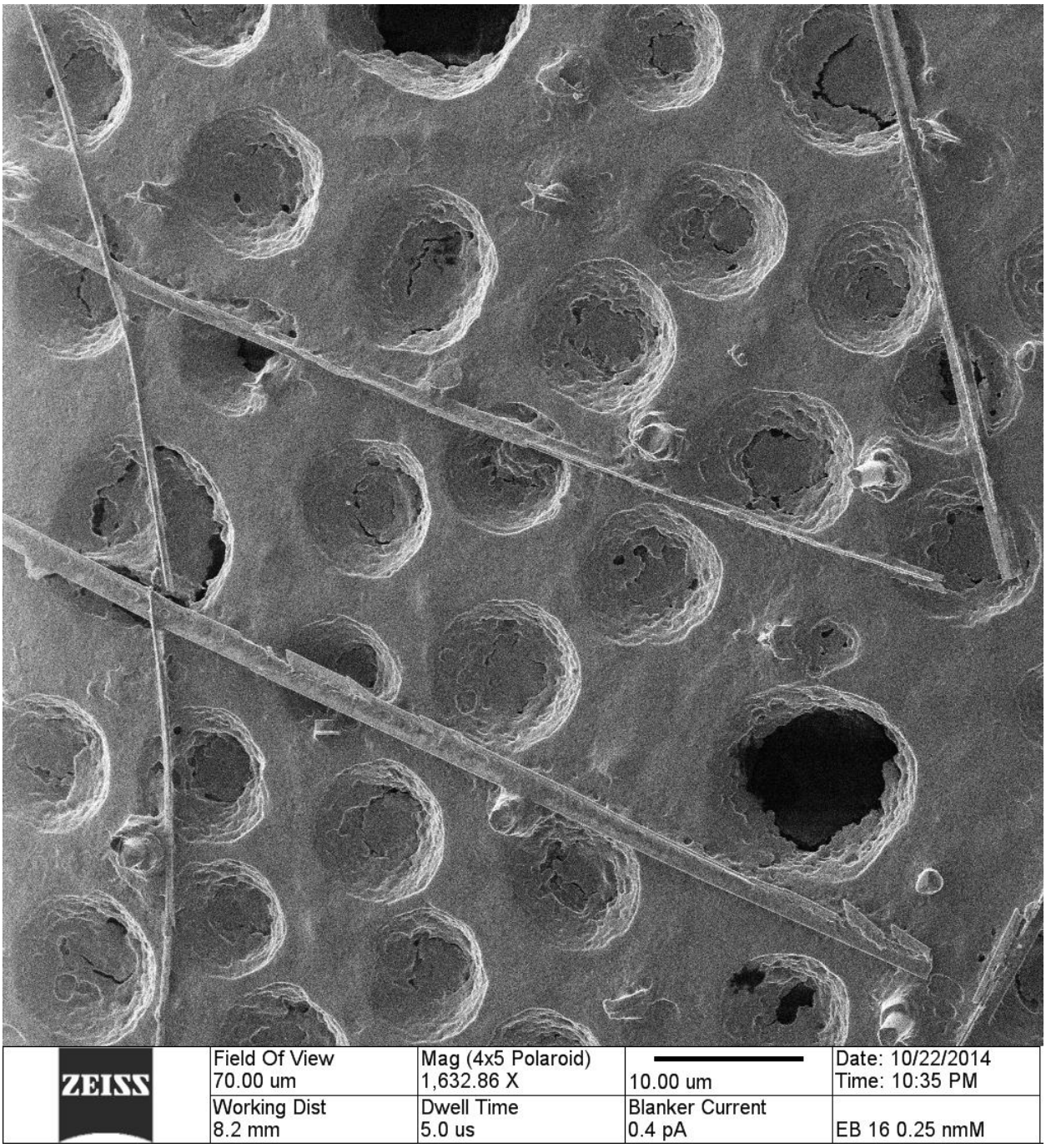

Figure 9.5. Helium ion microscope image of the surface of a foraminifer that had been collected prior to gametogenesis. Note the irregular 'terrace-like' surface in the interior of the pores.

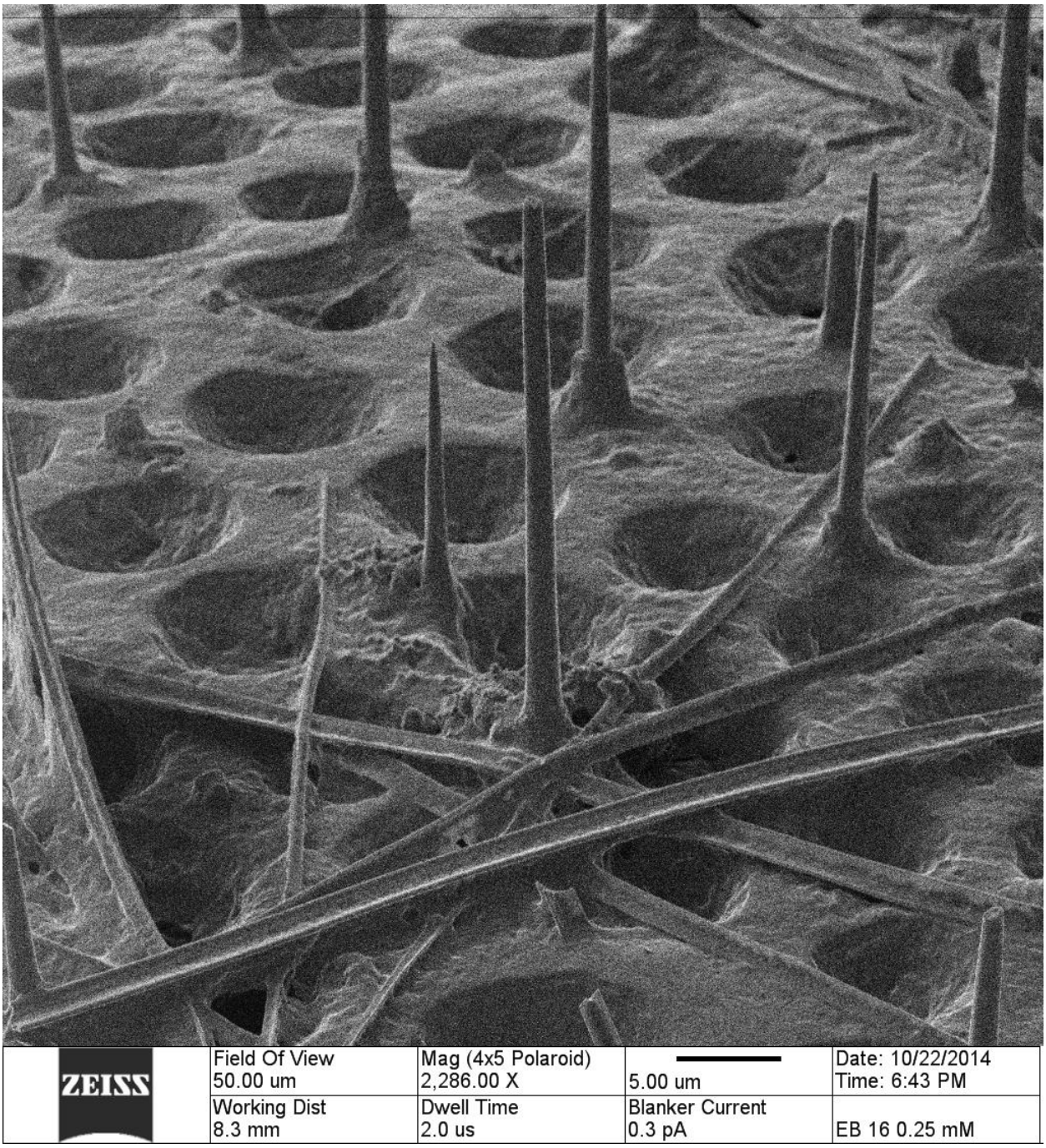

Figure 9.6. Helium ion microscope image of the surface of a foraminifer that had been collected prior to gametogenesis. Because this specimen had not undergone gametogenesis, spines were intact during collection.

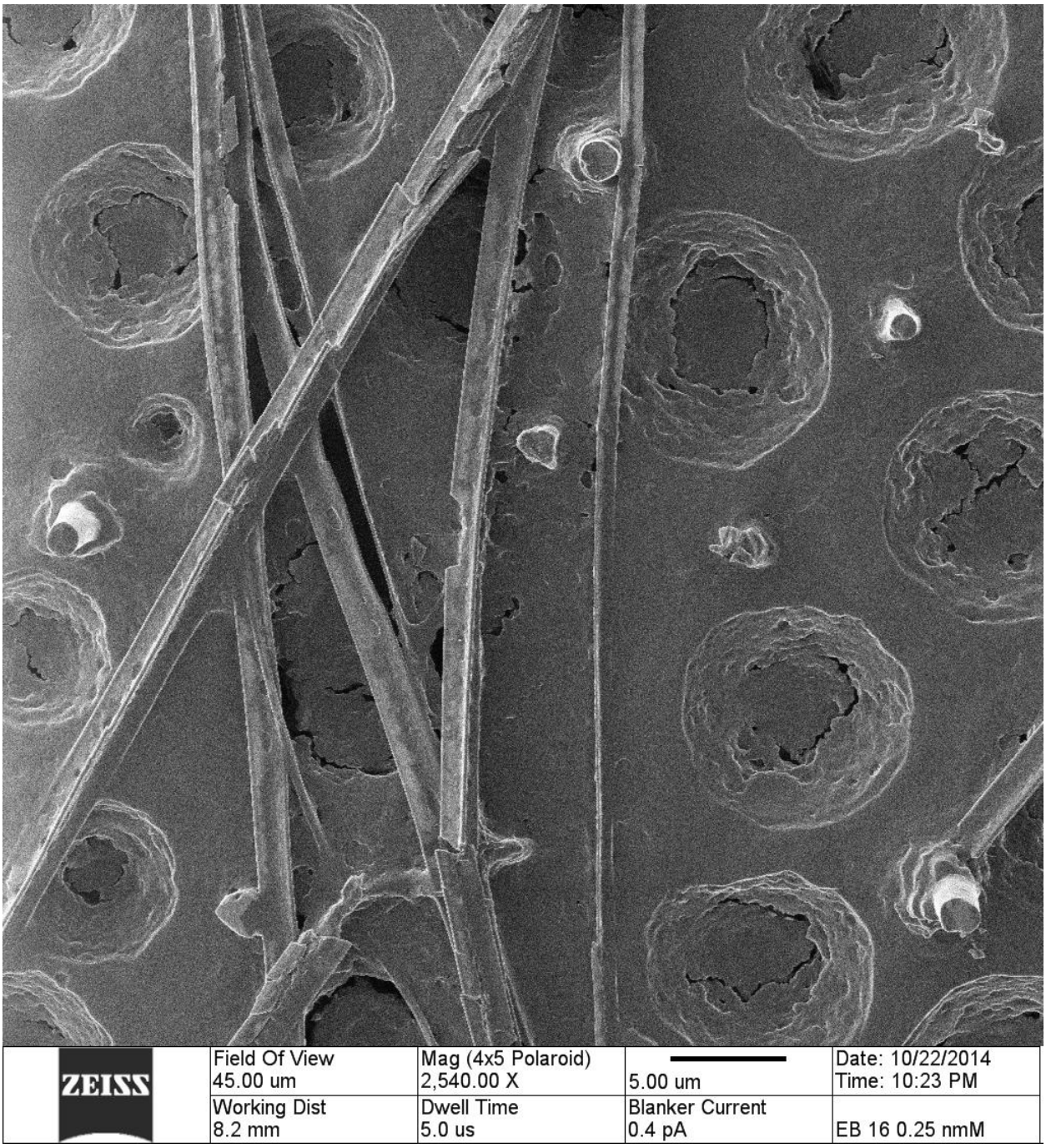

Figure 9.7. Helium ion microscope image of the surface of a foraminifer that had been collected prior to gametogenesis. Note the plugged interior of most of the pores visible on the test surface.

9.5.2 *SEM Images*

Scanning electron microscope (SEM) images were taken using a TFS Apreo-S with Lovac Scanning Electron Microscope. Images from all foraminifera are displayed below. Figures 9.8 through 9.10 show foraminifera that were not included in the gametogenic calcite experiment. Figure 9.8 depicts the natural abundance control foraminifer, which was not labeled with isotope spike but which may still have undergone gametogenesis. Figures 9.9 and 9.10 show images from the surface of foraminifera that were included in the gametogenic calcite experiment but did not take up isotope spike, even after being placed in labeled seawater. These samples may not have undergone gametogenesis, or they may have undergone gametogenesis outside of spiked seawater. Figures 9.11 to 9.14 show SEM images from the surface of foraminifera that were included in the gametogenic calcite experiment, underwent gametogenesis in labeled seawater, and took up a measurable isotope label.

9.5.2.1 Control (Unlabeled) Foraminifera

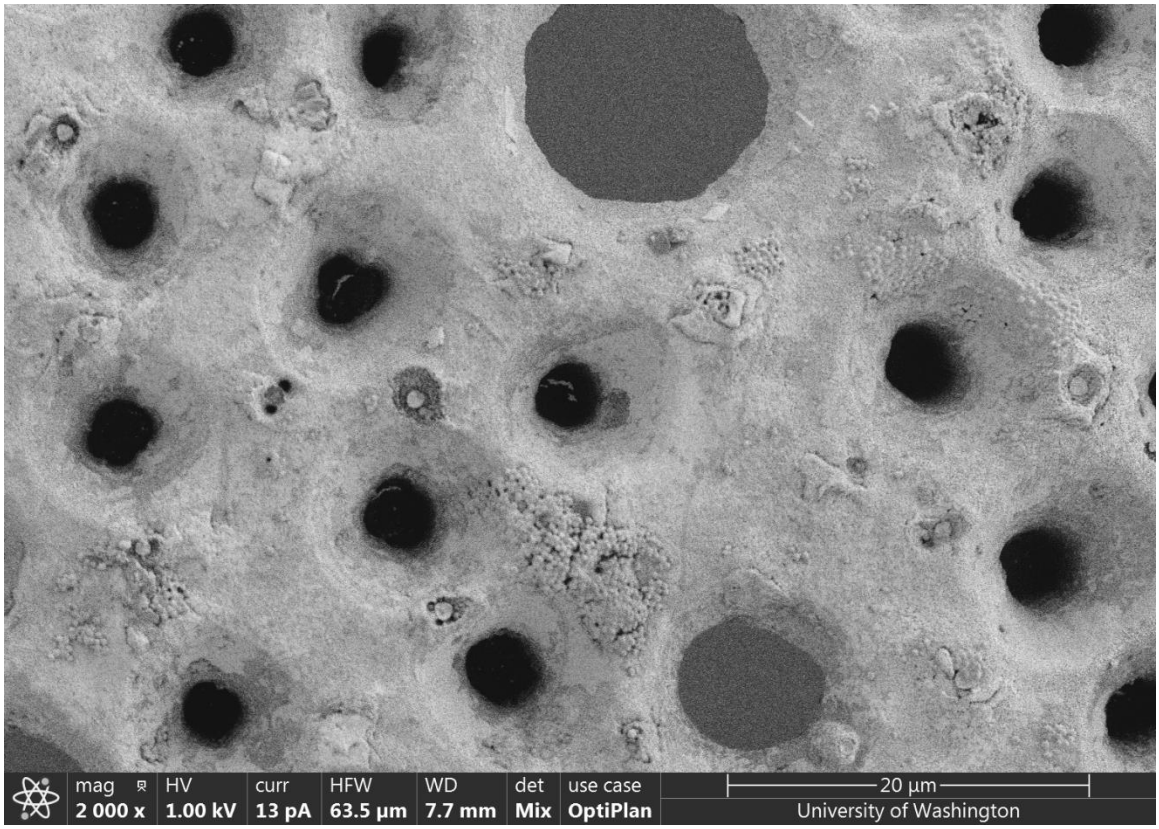

Figure 9.8. SEM image of the surface of the natural abundance control foraminifer used in this study. This sample was never placed in spike.

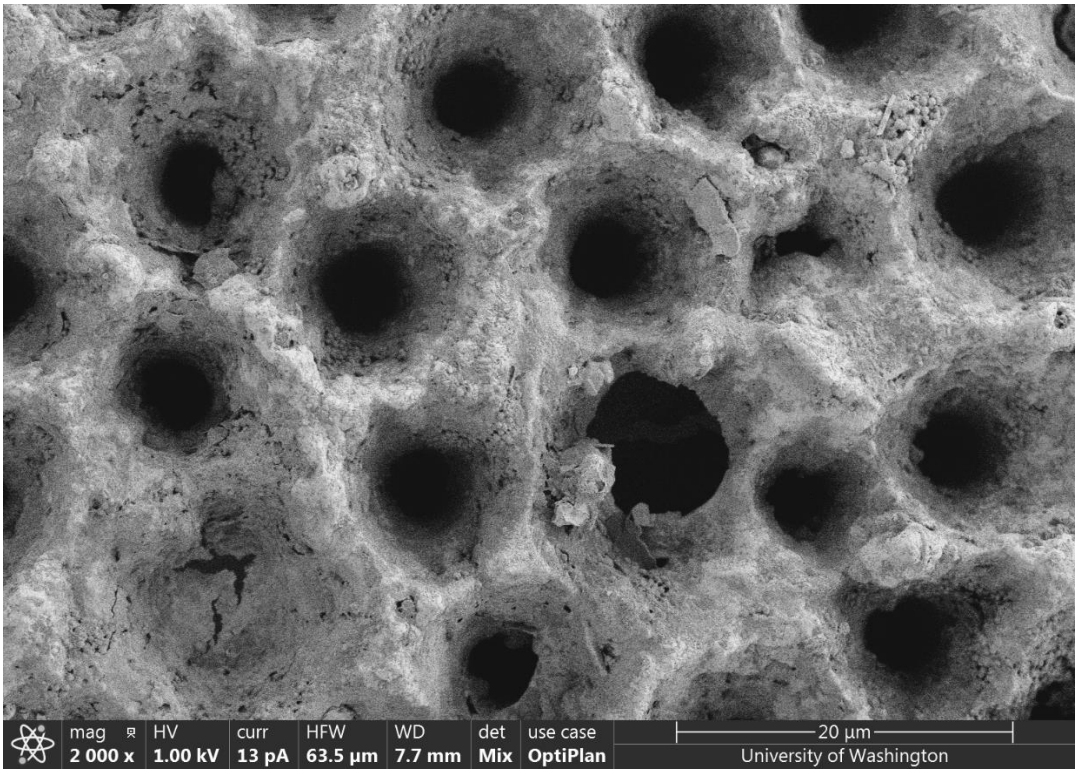

Figure 9.9. SEM image of the surface of a foraminifer (#334) that was placed in spike, but did not take up isotope label.

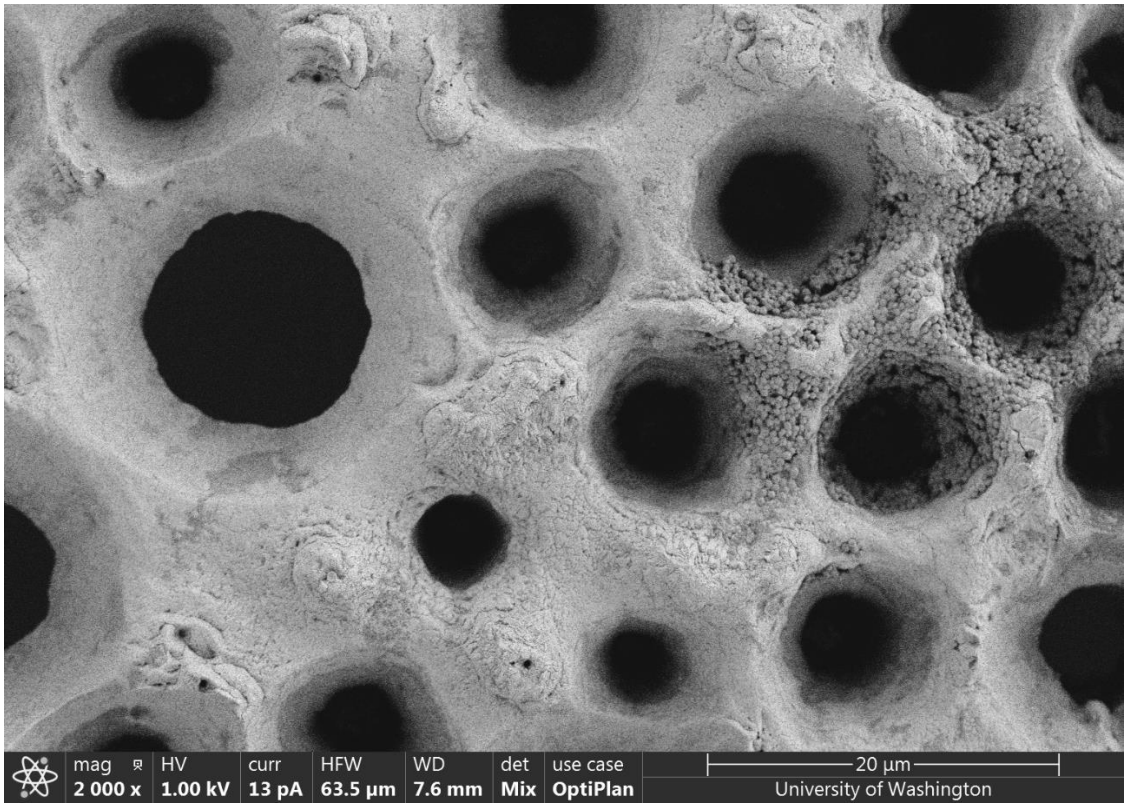

Figure 9.10. SEM image of the surface of a foraminifer (#395) that was placed in spike, but did not take up isotope label.

9.5.2.2 Labeled Foraminifera

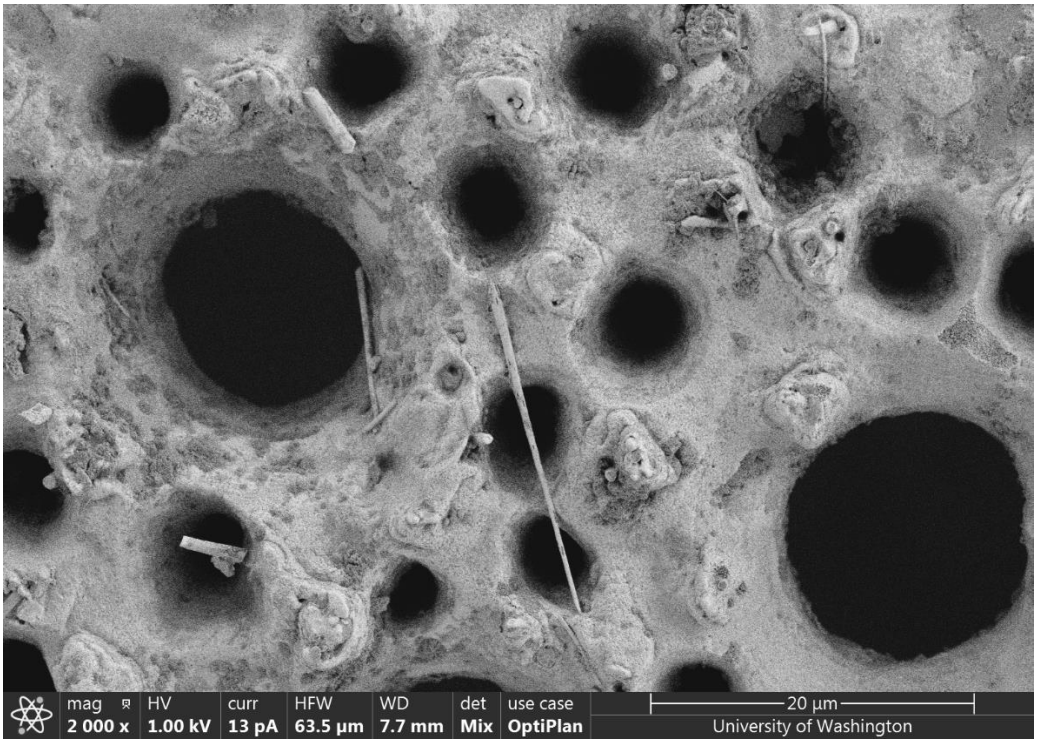

Figure 9.11. SEM image of the surface of Foram #136 (Table 9.1).

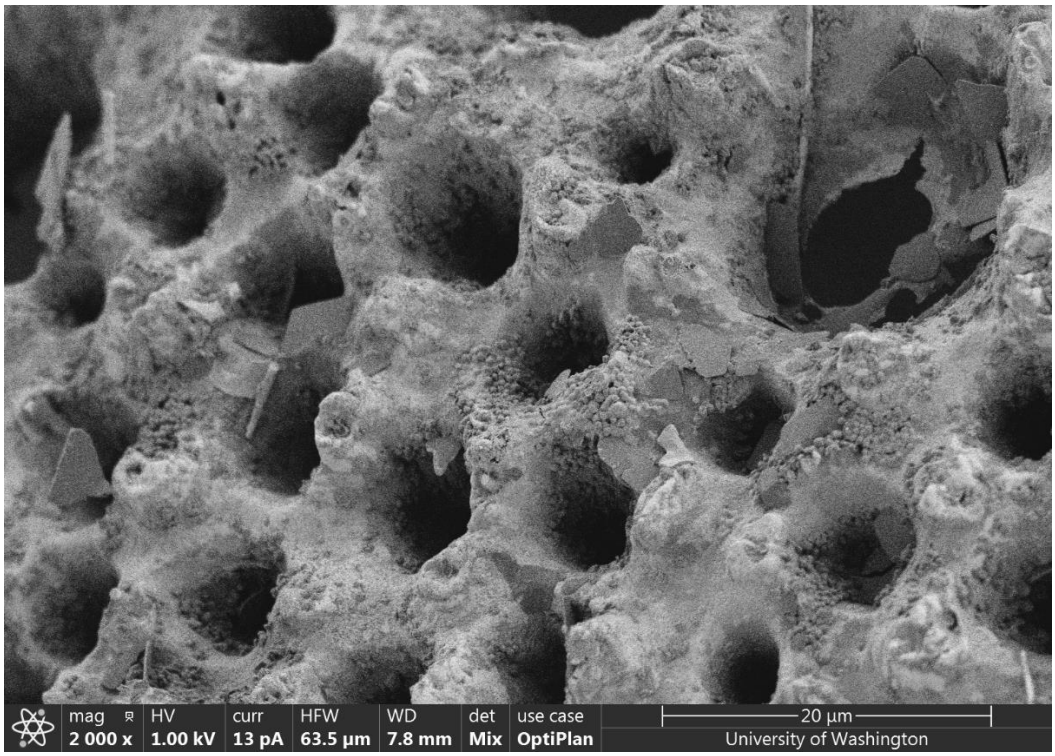

Figure 9.12. SEM image of the surface of Foram #136 (Table 9.1).

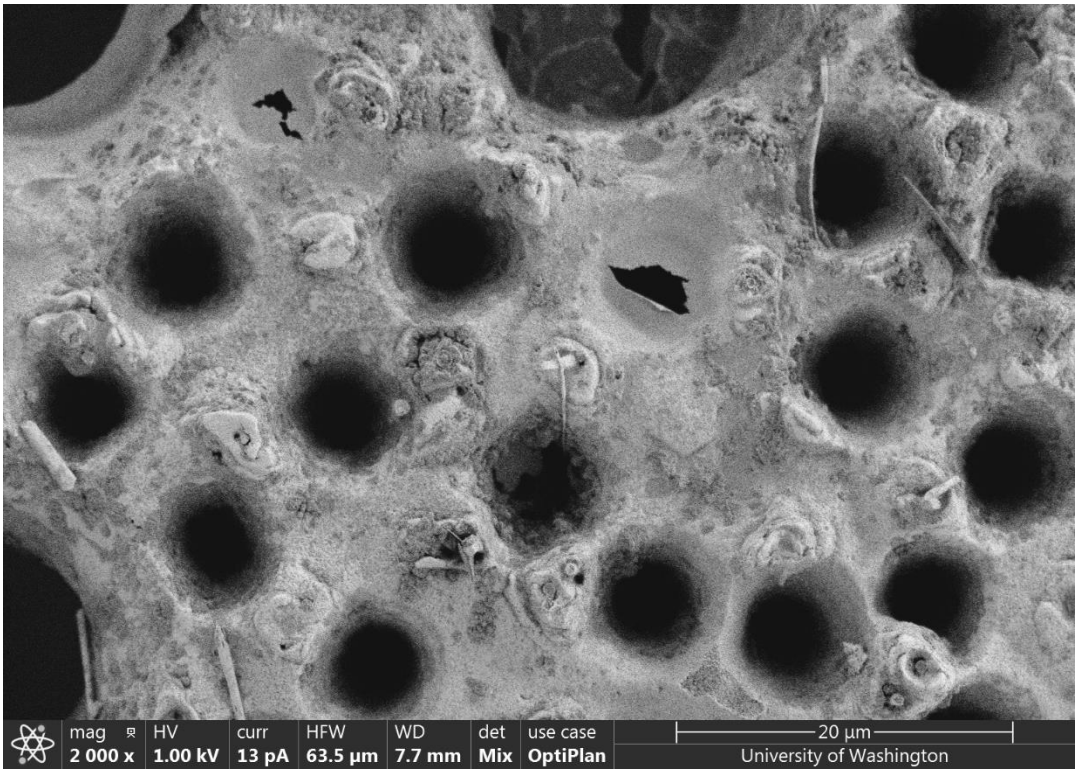

Figure 9.13. SEM image of the surface of Foram #270 (Table 9.1).

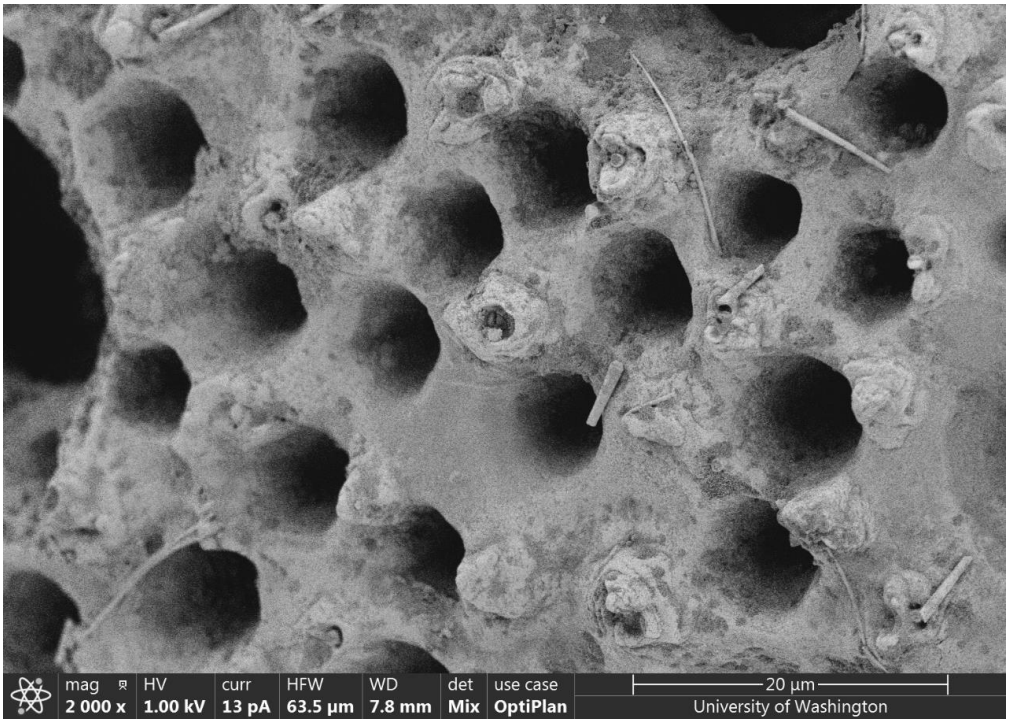

Figure 9.14. SEM image of the surface of Foram #270 (Table 9.1).

9.5.3 *ToF-SIMS Images*

Figures 9.15 and 9.16 depict ToF-SIMS images of *O. universa* that appear to show gametogenic calcification. ToF-SIMS images were obtained as part of the analysis conducted in Chapter 2.

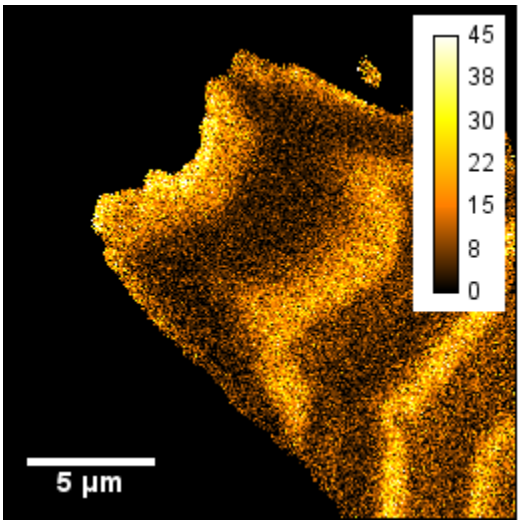

Figure 9.15. ToF-SIMS image of a Foram (#863, Table 6.1) appearing to depict gametogenic calcification. Note the high Mg band at the outer edge of the shell, which appears to cover the outer edge of the test, beginning to cover the interior of the pores to the left and right.

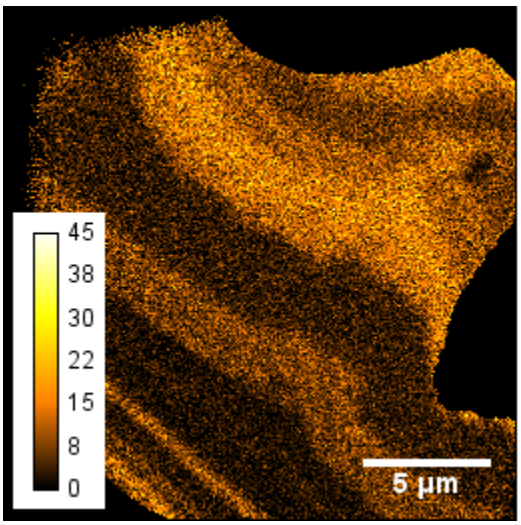

Figure 9.16. ToF-SIMS image of a Foram (#680, Table 6.1) appearing to depict gametogenic calcification. In this case, the high Mg band at the outer edge of the shell appears to cover the interior of the shallow pore to the left of the band, but not necessarily the deeper pore to the right.

VITA

Elisa Angeles Bonnin

EDUCATION

2019 **Ph.D., Oceanography**
University of Washington, Seattle, WA
Advisor: Alexander C. Gagnon
Thesis: Growth, chamber formation, and microscale heterogeneity in planktic foraminifera
Graduate Certificate in Climate Science, June 2019

2016 **Master of Science, Oceanography**
University of Washington, Seattle, WA
Advisor: Alexander C. Gagnon

2013 **Bachelor of Science in Chemistry**
University of South Carolina, Columbia SC
Summa cum Laude
With Honors from the South Carolina Honors College

RESEARCH EXPERIENCE

2013-2019 **Graduate Research Assistant**
School of Oceanography
University of Washington, Seattle, WA
Advisor: Alexander C. Gagnon

2012 **Research Intern**
Ocean Acidification Project
Smithsonian Environmental Research Center, Edgewater, MD
Advisors: Whitman Miller, Gerhardt Riedel, and Charles Gallegos

2012 **Undergraduate Researcher**
Department of Chemistry, Department of Marine Science
University of South Carolina, Columbia SC
Advisors: Timothy J. Shaw and Seth G. John

TEACHING EXPERIENCE

Teaching Assistantships

2019 The Changing Oceans Online Course Development (OCEAN 102, development)
Marine Biogeochemical Cycles (OCEAN 330)
Climatic Extremes (OCEAN 450)

2018 Marine Geology and Geochemistry (OCEAN 310)
Marine Biogeochemical Cycles (OCEAN 330)
Deep Sea Exploration (OCEAN 121)

2017 Integrative Oceanography (OCEAN 210)

2015 The Changing Oceans (OCEAN 102)

PUBLICATIONS

Bonnin, E. A., Zhu, Z., Fehrenbacher, J. S., Russell, A. D., Hönisch, B., Spero, H. J., and Gagnon, A. C. (2019). Submicron sodium banding in cultured planktic foraminifera shells. *Geochimica et Cosmochimica Acta*, *253*, 127–141. http://doi.org/10.1016/j.gca.2019.03.024

Johnson, S. C., Muller, E. A., Khatib, O., **Bonnin, E. A**., Gagnon, A. C., and Raschke, M. B. (2019). Infrared Nano-Spectroscopic Imaging in the Rotating Frame. *Optica*, *6*(4).

Branson O., **Bonnin E. A.,** Perea D. E., Spero H. J., Zhu Z., Winters M., Hönisch B., Russell A. D., Fehrenbacher J. S. and Gagnon A. C. (2016) Nanometer-Scale Chemistry of a Calcite Biomineralization Template: Implications for Skeletal Composition and Nucleation. *Proc. Natl. Acad. Sci. U. S. A.*, 201522864.

HONORS AND AWARDS

2018 Certified Science Storyteller, Massive Science Consortium

2017 Pacific Science Center, Science Communication Fellowship

2016 ASLO Ocean Sciences Meeting, Student Travel Funding

2015 SCOR/IGBP Working Group 138 Travel Funding

2014 IGERT Program on Ocean Change Associate, University of Washington, Seattle WA

2013 Egdvedt Top Scholar, University of Washington, Seattle WA

2013 Ruth Weimer Mount Mortar Board Fellowship, University of South Carolina, Columbia, SC

2010 Phi Beta Kappa, University of South Carolina, Columbia, SC

CONFERENCE PRESENTATIONS

Bonnin et al. (2018). Testing the effect of crystal growth rate on foraminiferal calcite microchemistry using Sr/Ca of individual day/night bands. Talk presented at the 2018 AGU Fall Meeting, Washington, DC.

Bonnin, et al. (2018). The effect of crystal growth rate on foraminiferal calcite geochemistry: Lessons from Sr/Ca ratios. Poster presented at the 2018 Ocean Sciences Meeting, Portland, OR.

Bonnin, et al. (2016). Systematic Sub-Micron Na/Ca Banding in *Orbulina universa* and *bilobata*. Poster presented at 2016 Ocean Sciences Meeting, New Orleans, LA.

Bonnin, et al. (2015). The influence of pH on the variability of the Mg/Ca temperature proxy and other metal/calcium ratios in planktonic foraminifera. Poster presented at the Graduate Climate Conference, Woods Hole, MA.

Bonnin, et al. (2015). Systematic Sub-Micron Na/Ca Banding in Cultured Planktic Foraminifera by SIMS. Poster presented at the AVS SIMS XX Conference, Seattle, WA.

Bonnin et al. (2015). Systematic Sub-Micron Na/Ca Banding in *Orbulina universa* and *bilobata*. Poster presented at the SCOR/IGBP Working Group 138: Planktonic Foraminifera and Ocean Changes workshop, Catalina Island, CA.

Bonnin et al. (2014). Systematic Sub-Micron Na/Ca Banding in Cultured Planktonic Foraminifera. Talk presented at the Goldschmidt Conference, Sacramento, CA.

PROFESSIONAL DEVELOPMENT

Earth and Environmental Sciences

2017 UW Program on Climate Change Summer Institute
"Population Health and Climate Change"
Friday Harbor Laboratories, Friday Harbor WA

2016 Summer School on Sustainable Climate Risk Management
Pennsylvania State University, State College PA

UW Program on Climate Change Summer Institute
"The Climate of Antarctica and the Southern Ocean"
Friday Harbor Laboratories, Friday Harbor WA

2015 UW Program on Climate Change Summer Institute
"Interactions between Terrestrial Ecosystems, Land Surface Processes and Climate"
Friday Harbor Laboratories, Friday Harbor WA

IGERT Program on Ocean Change Planning Retreat
Friday Harbor Laboratories, Friday Harbor WA

Teaching, Outreach, and Science Communication

2017 Pacific Science Center Science Communication Fellowship
Pacific Science Center, Seattle WA

2016 Young Scholar's Conference
Brown University, Providence RI

Engage Science Communication Seminar
University of Washington, Seattle WA

PROFESSIONAL SERVICE

2018 Graduate Climate Conference (GCC) Planning Committee
Logo and Pamphlet Committee Chair, Abstract Committee

2016-2019 Engage Science Communication Program Board of Directors
University of Washington, Seattle WA
Board Member

2016-2017 Hedges Visiting Scholar Planning Committee
School of Oceanography, Seattle, WA
Scheduling Committee

2016 Graduate Climate Conference (GCC) Planning Committee
Logo and Pamphlet Committee, Abstract Committee, Paleoclimate Session Chair

OUTREACH

2018 Workshop Leader, Engage Science Communication Workshop
Graduate Climate Conference, University of Washington, Seattle WA

Speaker, *'Translating Earth's historical record…'*
Ignite Seattle 37, Seattle, WA

Organizer, Written Science Communication Workshop
Share Your Science City Tour, The People's Science, Seattle WA

Workshop Leader, Engage Science Communication Workshop
Women in Genome Sciences, University of Washington, Seattle WA

Presenter, Sackler Student Symposium
Theme: "Role/Play: Collaborative Creativity and Creative Collaborations"
National Academy of Sciences, Washington DC

2017-2019 Member, Massive Science Consortium
Massive Science Inc., online

2017-2019 Science Communication Fellow
Pacific Science Center, Seattle WA

2017 Speaker, Science Talk Northwest
Oregon Museum of Science and Industry, Portland OR

2016-2018 EarthGames UW Narrative Writer and Science Advisor
University of Washington, Seattle WA

2016 Presenter, Youth Climate Action Network Action Fair
Woodland Park Zoo, Seattle WA

Workshop Leader, Engage Science Communication Workshop
Clean Energy Institute, University of Washington, Seattle WA

UW Science Now Speaker
Town Hall, Seattle WA

2014 Guest Speaker, Graduate Student Panel
Mercer Slough Environmental Education Center, Bellevue WA

Beach Naturalist
Seattle Aquarium, Seattle WA

FIELD WORK

Planktonic Foraminifera Culturing, Wrigley Marine Science Center, Catalina Island, CA
2014 Culture Season (6 weeks)
2013 Culture Season (6 weeks)

PROFESSIONAL AFFILIATIONS

2018 American Geophysical Union
2016 Earth Science Women's Network
2015 The Oceanography Society
2014 Geochemical Society